



Morisse, Clément (2015) *The structure/activity relationship of nitrobenzene hydrogenation over Pd/alumina catalysts*. PhD thesis.

<https://theses.gla.ac.uk/6384/>

Copyright and moral rights for this work are retained by the author

A copy can be downloaded for personal non-commercial research or study, without prior permission or charge

This work cannot be reproduced or quoted extensively from without first obtaining permission from the author

The content must not be changed in any way or sold commercially in any format or medium without the formal permission of the author

When referring to this work, full bibliographic details including the author, title, awarding institution and date of the thesis must be given

Enlighten: Theses

<https://theses.gla.ac.uk/>
research-enlighten@glasgow.ac.uk



University of Glasgow

PH.D. IN PHYSICAL CHEMISTRY

The structure/activity relationship of nitrobenzene hydrogenation over Pd/alumina catalysts

Author:

Clément MORISSE

Supervisor:

Dr. David LENNON

Dr. Chris MITCHELL

May 26, 2015

Abstract

The hydrogenation of nitrobenzene to form aniline is a large-scale industrial process performed using a variety of heterogeneous catalysts. One variant of the process involves the application of alumina-supported Pd catalysts. Although several 0.3 wt% Pd/Al₂O₃ formulations exhibit high aniline selectivity (ca. 98%), different grades of these catalysts favour different impurities. It is observed that the impurities arise from different reaction pathways depending on the provenance of the catalyst. In order to investigate whether the origins of impurity formation are connected to catalyst structure, a series of Pd catalysts active for this reaction have been characterised by a variety of techniques: chemisorption measurements, X-Ray Diffraction, Transmission Electron Microscopy, Temperature-Programmed Desorption and Infrared spectroscopy. The low metal loading industrial grade catalysts are challenging to characterise and required a degree of analytical refinement. Temperature-programmed infrared measurements of the probe molecule carbon monoxide revealed morphological and energetic information that could be correlated with catalytic performance. This information constitutes part of a valuable feedback loop that enables specifications for the next generation of ultra-selective nitrobenzene hydrogenation catalysts to be determined.

Acknowledgements

I would like to thank everyone that was involved in this project and to those that have helped me throughout all my years at university and beyond.

A very special thank you to Dr. David Lennon. I thank you for having faith in me from the start, for your positivity, and for your countless advices and guidance over these four years. It has kept me moving forward and stay motivated through all the ups and downs in my Ph.D. Finally, I am very grateful to Dr. Lennon for allowing me to participate in numerous Firbush meetings and conferences, the best of which took me to the Texas, USA for the 2014 ACS meeting. I will never forget my time at Glasgow. *Mille mercis David!*

Thanks to the following undergraduate project students: Kim Bova (University of Glasgow) and Laura Ascherl (University of Munich) who carried out work associated with this project, adding insight and value to many of the results. Also thank you to Robbie Warringham and Lauren Gilpin for carrying out the Bruker Spectrometer experiments and to Michael Beglan for carrying out atomic absorption measurements.

I would like to thank my industrial sponsors Huntsman Polyurethanes for providing an interesting and challenging project, and for trusting and supporting me throughout the four years. Particular thanks go to my industrial supervisor Dr. Chris Mitchell and Dr. Robert Carr for the informative meetings.

To Robbie, thanks for introducing me to the Glaswegian way of life and teaching me the scottish slang. I will be forever thankful to you. I have had an amazing time with you over the last four years. Lauren, thank you for bringing a feminine touch in the lab, it was great to have someone to talk about Beyonce with (*'although she knows nothing about hydrogenation'*)... Thank to both of you for the 'Texas Road trip 2014', it was great fun. GO HORNS! A special thank you to Andrew and Liam for not making any effort in speaking less Scottish or any slower, it definitely improved my English skills! Finally thank you Giovanni for making me a fitter person last year.

I would like to thank Ashley for putting up with my french non-sense and being the fun and supportive person that she is. Moreover, I especially thank Sebastien and Julie for being such great friends. Your support, all the phone calls about handball, work and life is much appreciated, and of course for making me the proud god-father of a wee, but beautiful *Lucie*. Finally to my Mum, Dad and brother - thank you for all the advices, support and patience through these four years. *Plein de Bisous!*

Merci à tous!

Author's declaration

I hereby declare that this thesis was composed by myself and that the work contained herein to be my own work except where otherwise indicated.

Glossary

AAS - atomic absorption spectroscopy

AN - aniline

AZO - azobenzene

AZOXY - azoxybenzene

BET surface area - Brunauer, Emmett and Teller surface area

BJH pore size distribution - Barrett-Joyner-Halenda pore size distribution

C - carbon

CHA - cyclohexylamine

CHAN - N-cyclohexylaniline

CO - carbon monoxide

CO-TPIR - CO temperature-programmed infrared

CO-IR - CO chemisorption followed by infrared

CHO - cyclohexanone

CHOL - cyclohexanol

CHOX - cyclohexanone oxime

Cu - copper

DICHA - dicyclohexylamine

DRIFT - diffuse reflectance spectroscopy

FTIR - Fourier transform infrared spectroscopy

GC - gas chromatography

H₂ - hydrogen

He - Helium

HREELS - High resolution electron energy loss spectroscopy

HYDRAZO - hydrazobenzene

IR - infrared

MDI - methyl diisocyanate

MgO - magnesium oxide

NB - nitrobenzene

NEXAFS - X-ray absorption near edge structure

Ni - Nickel

OH group - hydroxyl group

Pd - palladium

Ph-NOH - phenylhydroxylamine

Pt - platinum

TEM - transmission electron microscopy

WHSV - weight hourly space velocity

XPS - X-ray photoelectron spectroscopy

XRD - X-Ray diffraction

Contents

1	Introduction	1
1.1	Aniline Applications	1
1.2	Synthesis of Aniline	2
1.2.1	Ammonolysis of Phenol	3
1.2.2	Ammonolysis of Chlorobenzene	3
1.2.3	Ammonolysis of Benzene	4
1.3	The Catalytic Nitrobenzene Hydrogenation	4
1.3.1	Recent considerations related to industrial nitrobenzene hydrogenation	4
1.3.2	Mechanism	6
1.3.3	Adsorption of Nitrobenzene and Aniline	10
1.3.4	The Under and Over-Reduction Concepts in Nitrobenzene Hydrogenation	12
1.3.5	Activation Energy of Nitrobenzene Hydrogenation	15
1.4	Infrared Spectroscopy used in Heterogenous Catalysis	15
1.4.1	Fourier Transform Infrared Spectroscopy	18
1.5	Aims of the project	25
2	Experimental	29
2.1	Catalyst Characterisation Line	29
2.2	Reaction testing	29
2.2.1	Gas Phase hydrogenation reactor	29
2.2.2	Gas Liquid Chromatography	32
2.3	Calibration of Plug-flow reactor system	32
2.4	Characterisation	35
2.4.1	Infrared Spectroscopy	35
2.4.2	Temperature-Programmed Desorption	36
2.4.3	X-ray Powder Diffraction	37
2.4.4	Transmission Electron Microscopy	37

2.4.5	Atomic Absorption Spectroscopy	38
2.4.6	Total Surface Area measurements (BET)	38
2.4.7	CO Adsorption Isotherms	39
2.4.8	Conversion and Selectivity Calculations	40
3	Nitrobenzene hydrogenation on a commercial 5 wt % Pd/Al₂O₃ catalyst	
	- Sample 1.	41
3.1	Gas phase nitrobenzene hydrogenation	41
3.2	XRD, BET, CO chemisorptions and AAS	46
3.3	Transmission Electron Microscopy	48
3.4	CO chemisorption followed by	
	Infrared Spectroscopy	54
3.4.1	CO-IR of the 5 wt % Pd/Al ₂ O ₃ (Sample 1) using the Bruker Trans- mission system	57
3.4.2	CO-IR of the 5 wt % Pd/Al ₂ O ₃ (Sample 1) using the Bruker DRIFT system	60
3.4.3	CO-IR of the 5 wt % Pd/Al ₂ O ₃ (Sample 1) using the Nexus-Nicolet DRIFT system	62
3.5	Summary	64
4	Nitrobenzene Hydrogenation over Pelleted 0.3 wt % Pd/Al₂O₃ Catalyst	
	- Sample 2	65
4.1	0.3 wt % Pd/Al ₂ O ₃ (Sample 2) pellets as a function of temperature	66
4.2	0.3 wt % Pd/Al ₂ O ₃ (Sample 2) pellets -	
	Weight Hourly Space Velocity study	71
4.2.1	WHSV = 0.12 hour ⁻¹	73
4.2.2	WHSV = 0.3 hour ⁻¹	76
4.2.3	WHSV = 0.6 hour ⁻¹	79
4.2.4	WHSV = 1.17 hour ⁻¹	83
4.2.5	WHSV = 2.67 hour ⁻¹	86
4.2.6	Aniline Hydrogenation	94
4.2.7	Nitrobenzene and Aniline Activation Energy measurements over 0.3 wt % Pd/Al ₂ O ₃ (Sample 2, 310/2)	98
4.3	Summary	100
5	Nitrobenzene hydrogenation over two 0.3 wt % Pd/Al₂O₃ catalysts:	
	Samples 2 and 3	103
5.1	Temperature-Programmed gas phase Nitrobenzene Hydrogenation	104
5.1.1	Sample 2 (310/2)	104

5.1.2	Sample 3 (143 500)	110
5.1.3	Summary	114
5.2	Characterisation	116
5.2.1	Atomic Absorption	116
5.2.2	CO adsorption isotherms	116
5.2.3	Transmission Electron Microscopy	119
5.2.4	X-ray Powder Diffraction	122
5.2.5	Brunauer-Emmett-Teller (BET) surface area and Barrett-Joyner-Halenda (BJH) pore size	128
5.3	Summary	130
6	Infrared Spectroscopy + CO chemisorption to determine Pd particles morphology: Samples 2 and 3	133
6.1	Optimisation Characterisation Rig	133
6.1.1	CO TPIR of 5 wt % Pd/Al ₂ O ₃ (Sample 1)	133
6.1.2	CO TPD of 5 wt % Pd/Al ₂ O ₃	136
6.1.2.1	Before optimisation	136
6.1.2.2	After optimisation	138
6.1.3	CO TPIR of 5 wt % Pd/Al ₂ O ₃ (Sample 1) on Nexus DRIFT cell	140
6.1.4	CO TPIR of 5 wt % Pd/Al ₂ O ₃ (Sample 1) on Harrick DRIFT cell	143
6.1.5	CO TPIR of 5 wt % Pd/Al ₂ O ₃ (Sample 1) on Transmission cell	145
6.2	CO TPIR of the 0.3 wt % Pd/Al ₂ O ₃ (Sample 2, 310/2) catalyst	147
6.3	CO TPIR of the 0.3 wt % Pd/Al ₂ O ₃ (Sample 3, 143500) catalyst	149
6.3.1	Summary	151
7	The structure/activity relationship applied to Pd/alumina-silica catalysts (Samples 4, 5 and 6)	155
7.1	Reaction Testing	155
7.1.1	M11572 0.3 wt % Pd/Al ₂ O ₃ -30 % SiO ₂ (Sample 4) catalyst	155
7.1.2	764 0.4 wt % Pd/Al ₂ O ₃ - 1 % SiO ₂ (Sample 5) catalyst	158
7.1.3	M12340 0.3 wt % Pd/Al ₂ O ₃ - 1 % SiO ₂ (Sample 6) catalyst	162
7.2	Characterisation, XRD, BET and CO Chemisorptions.	167
7.2.1	Atomic Absorption	167
7.2.2	CO adsorption isotherms	167
7.2.3	X-ray powder Diffraction	169
7.3	CO Temperature-programmed Infrared Spectroscopy (Samples 4, 5 and 6)	174
7.3.1	M11572 0.3 wt % Pd/Al ₂ O ₃ -30 % SiO ₂ (Sample 4) catalyst	174
7.3.2	764 0.4 wt % Pd/Al ₂ O ₃ - 1 % SiO ₂ (Sample 5) catalyst	176

7.3.3	M12340 0.3 wt % Pd/Al ₂ O ₃ - 1 % SiO ₂ catalyst (Sample 6)	178
7.4	Discussion	180
8	Conclusion	182
	Appendices	186
A		187
A.1	Nitrobenzene Calibration	187
A.2	Aniline Calibration	188
A.3	Cyclohexylamine (CHA) Calibration	189
A.4	Dicyclohexylamine (DICHA) Calibration	190
A.5	Diphenylamine (DPA) Calibration	191
A.6	Azobenzene (AZO) Calibration	192
A.7	N-cyclohexylaniline (CHAN) Calibration	193

List of Figures

1.1	Aniline uses distribution in 2013	1
1.2	Polyurethane applications' distribution in 2010	2
1.3	Haber mechanism for the reduction of aromatic nitrogroups to aniline . . .	6
1.4	Reaction pathway for the reduction of nitrobenzene through dismutation of hydroxylamine	7
1.5	Direct hydrogenation route proposed by Visentin <i>et al.</i>	7
1.6	Proposed pathway for the hydrogenation of nitrobenzene to aniline on Au/TiO ₂	8
1.7	Nitrobenzene hydrogenation pathways proposed by Gelder <i>et al.</i>	9
1.8	Infrared as part of the electromagnetic spectrum	16
1.9	Different molecular vibrations recorded in Infrared Spectroscopy.	17
1.10	Schematic representation of a Spectrometer using a grating to select wave- length	18
1.11	Schematic representation of a Michelson Interferometer	18
1.12	Resulting interference pattern from variation of pathlength in a Michelson's interferometer	20
1.13	Different Infrared cell setups for heterogenous catalysis studies [1].	22
1.14	DRIFT cells - (a) Harrick vs (b) Spectra Tech. The grey shading in (b) represents the path of light throughout the sampling device.	23
1.15	Blyholder CO-Metal bonding model representation	24
1.16	Representation of the three adsorption modes of CO over Pd(111) low index plane. The palladium is represented by the grey spheres, oxygen by the red and carbon by the blue ones	25
1.17	Impurities profile from Huntsman reaction testing on Sample 2 (310/2) and Sample 3 (143 500)	27
2.1	Catalyst Characterisation line schematic.	30
2.2	Nitrobenzene hydrogenation Reaction Unit.	31
2.3	Vapour Pressure of aniline in red and Nitrobenzene in black calculated from Antoine's law.	34
2.4	Picture of the Harrick High Temperature transmission IR cell	36

2.5	Picture of the Harrick Praying Mantis IR setup	37
3.1	Nitrobenzene conversion in black and aniline selectivity in red reported from the reaction of 20 mg of catalyst 1 under feed of nitrobenzene/hydrogen/helium (NB 2.03×10^{-6} mol/min: H_2 $7.83E-04$ mol/min - H_2 :NB = 385 : 1, NB(s^{-1}) : Pd _(s) = 1 : 63)	43
3.2	Impurities selectivity reported from the reaction of 20 mg of catalyst 1 under feed of nitrobenzene/hydrogen/helium (NB 2.03×10^{-6} mol/min: H_2 $7.83E-04$ mol/min - H_2 :NB = 385 : 1, NB(s^{-1}) : Pd _(s) = 1 : 63). Dicyclohexylamine in green, N-cyclohexylaniline in purple, Cyclohexanone in blue, Cyclohexanol in red and Cyclohexylamine in black.	44
3.3	XRD pattern of the black powder 5 wt % Pd/Al ₂ O ₃ catalyst. Red drop lines represent the γ -alumina reflections.	47
3.4	Dark Field - Bright Field imaging on the 5 wt % Pd/Al ₂ O ₃ catalyst. The metal component is indicated as black particles in (a) but white particles in (b). Bar scale represents 50 nm.	49
3.5	Transmission Electron Microscopy of the 5% Pd/Al ₂ O ₃ (Sample 1) before activation. The white scale bar represents 5nm.	51
3.6	Transmission Electron Microscopy of the 5% Pd/Al ₂ O ₃ (Sample 1) before activation. The white scale bar represents 5nm here.	52
3.7	Particle size distribution of the 5 wt % Pd/Al ₂ O ₃ obtained using TEM Tecnai T20.	53
3.8	Temperature Programmed Desorption of CO in black and CO ₂ in red for the 5 wt % Pd/Al ₂ O ₃	56
3.9	Spectrum of the 5 wt % Pd/Al ₂ O ₃ chemisorbed with CO at room temperature using the Bruker Transmission system.	59
3.10	Spectrum of the 5 wt % Pd/Al ₂ O ₃ chemisorbed with CO at room temperature using the Bruker DRIFTS system.	61
3.11	Spectrum of the 5 wt % Pd/Al ₂ O ₃ chemisorbed with CO at room temperature using the Nicolet Nexus DRIFTS system.	63
4.1	Nitrobenzene conversion (green) and aniline selectivity (red) as a function of temperature during hydrogenation of nitrobenzene. 50mg of the 0.3% Pd/alumina catalyst (301/2) was used for the gas phase hydrogenation (NB 2.03×10^{-6} mol/min: H_2 7.83×10^{-4} mol/min - H_2 :NB = 385 : 1, NB(s^{-1}) : Pd _(s) = 1 : 11).	68

4.2	Impurities observed during nitrobenzene hydrogenation over 50 mg of 0.3% Pd/alumina (310/2) catalyst. By-products are N-cyclohexylaniline (CHAN) in red, Cyclohexanone (CHO) in black and Azobenzene (AZO) in blue (NB 2.03 x 10 ⁻⁶ mol/min: H ₂ 7.83 x 10 ⁻⁴ mol/min - H ₂ :NB = 385 : 1, NB(s ⁻¹) : Pd _(s) = 1 : 11).	69
4.3	Nitrobenzene hydrogenation reaction profile over 500 mg of the 0.3wt% Pd/alumina catalyst pellets (WHSV = 0.12 hour ⁻¹). Temperature was set at 100°C and nitrobenzene/hydrogen flow mixture was kept constant throughout (NB 2.03 x 10 ⁻⁶ mol/min: H ₂ 7.83 x 10 ⁻⁴ mol/min - H ₂ :NB = 385 : 1, NB(s ⁻¹) : Pd _(s) = 1 : 115).	74
4.4	Nitrobenzene hydrogenation reaction profile over 200 mg of the 0.3wt% Pd/alumina catalyst pellets (WHSV = 0.3 hour ⁻¹). Temperature was set at 100°C and nitrobenzene/hydrogen flow mixture was kept constant throughout (NB 2.03 x 10 ⁻⁶ mol/min: H ₂ 7.83 x 10 ⁻⁴ mol/min - H ₂ :NB = 385 : 1, NB(s ⁻¹) : Pd _(s) = 1 : 45).	77
4.5	Nitrobenzene hydrogenation reaction profile over 100 mg of the 0.3wt% Pd/alumina catalyst pellets (WHSV = 0.6 hour ⁻¹). Temperature was set at 100°C and nitrobenzene/hydrogen flow mixture was kept constant throughout (NB 2.03 x 10 ⁻⁶ mol/min: H ₂ 7.83 x 10 ⁻⁴ mol/min - H ₂ :NB = 385 : 1, NB(s ⁻¹) : Pd _(s) = 1 : 23).	80
4.6	Nitrobenzene hydrogenation reaction profile over 50 mg of the 0.3wt% Pd/alumina catalyst pellets (WHSV = 1.17 hour ⁻¹). Temperature was set at 100°C and nitrobenzene/hydrogen flow mixture was kept constant throughout (NB 2.03 x 10 ⁻⁶ mol/min: H ₂ 7.83 x 10 ⁻⁴ mol/min - H ₂ :NB = 385 : 1, NB(s ⁻¹) : Pd _(s) = 1 : 12).	84
4.7	Nitrobenzene hydrogenation reaction profile over 50 mg of the 0.3wt% Pd/alumina catalyst pellets (WHSV = 2.67 hour ⁻¹). Temperature was set at 100°C and nitrobenzene/hydrogen flow mixture was kept constant throughout (NB 2.03 x 10 ⁻⁶ mol/min: H ₂ 7.83 x 10 ⁻⁴ mol/min - H ₂ :NB = 385 : 1, NB(s ⁻¹) : Pd _(s) = 1 : 5).	87
4.8	Nitrobenzene Conversion reported as a function of WHSV.	91
4.9	Aniline Selectivity reported as a function of WHSV.	92
4.10	Conversion reported as a function of WHSV. In blue, CHAN, in green, Azobenzene, in red, DICHA and in black, CHA.	93
4.11	Aniline Conversion (black), DICHA selectivity (blue), CHAN selectivity (red) and CHA selectivity (green) are plotted against Temperature. Aniline was placed in a bubbler and 100 mg of the 310/2 catalyst was placed in the tubular reactor.	96

4.12	Nitrobenzene hydrogenation activation energy measurements plot on 20 mg of sieved catalyst 2 under nitrobenzene/hydrogen/helium feed (NB 2.03×10^{-6} mol/min: H ₂ 7.83×10^{-4} mol/min - H ₂ :NB = 385 : 1).	99
4.13	Aniline hydrogenation activation energy measurements plot on 100 mg of sieved catalyst 2 under Aniline/hydrogen/helium feed (AN 2.03×10^{-6} mol/min: H ₂ 7.83×10^{-4} mol/min - H ₂ :NB = 385 : 1).	99
4.14	Scheme representing the reaction testing data observed so far for the nitrobenzene hydrogenation on Pd/alumina catalysts.	102
5.1	Mass spectrum of unknown molecule collected from Sample 2.	105
5.2	Suggestion of the provenance of the Cyclohexanone Oxime (CHOX) molecule.	106
5.3	Nitrobenzene conversion (green) and aniline selectivity (blue) as a function of reaction temperature over 0.3wt% Pd/alumina (Sample 2, 310/2) catalyst. Catalyst was sieved to 500-250 microns before reaction and 20 mg was placed in the stainless steel 1/4 inch tubular reactor. nitrobenzene/hydrogen flow was kept constant throughout the reaction. Each temperature was kept for an hour before increasing by 20°C until reaching 180°C (NB 2.03×10^{-6} mol/min: H ₂ 7.83×10^{-4} mol/min - H ₂ :NB = 385 : 1, NB(s ⁻¹) : Pd _(s) = 1 : 4.5).	107
5.4	Selectivity profile (%) of the by-products produced as a function of reaction temperature over 0.3wt% Pd/alumina (Sample 2, 310/2) catalyst. Catalyst was sieved to 500-250 microns before reaction and 20 mg was placed in the stainless steel 1/4 inch tubular reactor. Nitrobenzene/hydrogen flow was kept constant throughout the reaction. Each temperature was kept for an hour before increasing by 20°C until reaching 180°C. Cyclohexanone oxime (red), N-cyclohexylaniline (green) and dicyclohexylaniline (yellow) are observed (NB 2.03×10^{-6} mol/min: H ₂ 7.83×10^{-4} mol/min - H ₂ :NB = 385 : 1, NB(s ⁻¹) : Pd _(s) = 1 : 4.5).	108
5.5	Equilibrium between cyclohexanone oxime (CHOX) and cyclohexanone (CHO).	110
5.6	Nitrobenzene conversion (green) and aniline selectivity (blue) as a function of reaction temperature over 0.3 wt % Pd/alumina (Sample 3, 143 500) catalyst. Catalyst was sieved to 500-250 microns before reaction and 20 mg was placed in the stainless steel 1/4 inch tubular reactor. Nitrobenzene/hydrogen flow was kept constant throughout the reaction. Each temperature was kept for an hour before increasing by 20°C until reaching 180°C (NB 2.03×10^{-6} mol/min: H ₂ 7.83×10^{-4} mol/min - H ₂ :NB = 385 : 1, NB(s ⁻¹) : Pd _(s) = 1 : 7.7).	111

5.7	Selectivity profile (%) of the by-products produced as a function of reaction temperature over 0.3 wt % Pd/alumina (Sample 3, 143 500) catalyst. Catalyst was sieved to 500-250 microns before reaction and 20 mg was placed in the stainless steel $\frac{1}{4}$ inch tubular reactor. Nitrobenzene/hydrogen flow was kept constant throughout the reaction. Each temperature was kept for an hour before increasing by 20°C until reaching 180°C. Cyclohexanone oxime (red), N-cyclohexylaniline (blue) and cyclohexanone (black) are observed (NB 2.03×10^{-6} mol/min: H ₂ 7.83×10^{-4} mol/min - H ₂ :NB = 385 : 1, NB(s ⁻¹) : Pd _(s) = 1 : 7.7).	112
5.8	Pulsed CO Chemisorption Isotherm on 0.3wt% Pd/alumina (Sample 2, 310/2)	117
5.9	Pulsed CO Chemisorption Isotherm on 0.3wt% Pd/alumina (Sample 3, 143 500)	118
5.10	Transmission Electron Microscopy of the 0.3 wt % Pd/alumina (Sample 2, 310/2) catalyst recorded at low magnification (left) and high magnification (right).	120
5.11	Transmission Electron Microscopy of the 0.3wt% Pd/alumina (Sample 3, 143 500) catalyst recorded at low magnification (left) and high magnification (right).	121
5.12	Temperature transformation of hydroxides or oxohydroxides to corundum via the formation of transitional alumina phases	123
5.13	X-ray Powder Diffraction pattern recorded for the 0.3 wt % Pd/alumina (310/2) catalyst. The green drop lines represent the θ -alumina phase and the red drop lines represent the δ -alumina phase	125
5.14	X-ray Powder Diffraction pattern recorded for the 0.3 wt % Pd/alumina (143 500) catalyst. The green drop lines represent the θ -alumina phase and the red drop lines represent the α -alumina phase	127
5.15	Nitrogen absorption - desorption isotherms (BET) of (a) the 0.3wt% Pd/alumina (Sample 2, 310/2) catalyst and (b) the 0.3wt% Pd/alumina (Sample 3, 143 500) catalyst	129
6.1	Temperature-Programmed Infrared Spectroscopy on 5 wt % Pd/Al ₂ O ₃ catalyst (Sample 1)	135
6.2	Temperature-Programmed Desorption of CO (in black) and CO ₂ (in red) for the 5 wt % Pd/Al ₂ O ₃ prior to optimisation of experimental methodology.	137
6.3	Temperature-Programmed Desorption of CO (in black) and CO ₂ (in red) for the 5 wt % Pd/Al ₂ O ₃	139
6.4	Temperature-Programmed Infrared Spectroscopy on the 5 wt % Pd/Al ₂ O ₃ (Sample 1).	142

6.5	Temperature-Programmed Infrared Spectroscopy on the 5 wt % Pd/Al ₂ O ₃ (Sample 1) on Harrick DRIFT cell as showed in Chapter 1	144
6.6	Temperature-Programmed Infrared Spectroscopy on the 5 wt % Pd/Al ₂ O ₃ (Sample 1) on Transmission cell as shown in Chapter 1	146
6.7	Temperature-Programmed Infrared Spectroscopy for CO chemisorption on 0.3 wt % Pd/Al ₂ O ₃ (Sample 2, 310/2).	148
6.8	Temperature-Programmed Infrared Spectroscopy fro CO chemisorption on 0.3 wt % Pd/Al ₂ O ₃ (Catalyst 3, 143 500).	150
7.1	Nitrobenzene conversion (black) and aniline selectivity (red) as a function of reaction temperature over 0.3 wt % Pd/alumina-Silica (M11572) catalyst. Catalyst was sieved to 500-250 microns before reaction and 20 mg was placed in the stainless steel 1/4 inch tubular reactor. Nitrobenzene/hydrogen flow was kept constant throughout the reaction. Each temperature was kept for an hour before increasing by 20°Cuntil reaching 160°C (NB 2.03 x 10 ⁻⁶ mol/min: H ₂ 7.83 x 10 ⁻⁴ mol/min - H ₂ :NB = 385 : 1, NB(s ⁻¹) : Pd _(s) = 1 : 3.2).	157
7.2	Nitrobenzene conversion (black) and aniline selectivity (red) as a function of reaction temperature over 0.4 wt % Pd/alumina-Silica (764) catalyst. Catalyst was sieved to 500-250 microns before reaction and 20 mg was placed in the stainless steel 1/4 inch tubular reactor. Nitrobenzene/hydrogen flow was kept constant throughout the reaction. Each temperature was kept for an hour before increasing by 20°Cuntil reaching 180°C (NB 2.03 x 10 ⁻⁶ mol/min: H ₂ 7.83 x 10 ⁻⁴ mol/min - H ₂ :NB = 385 : 1, NB(s ⁻¹) : Pd _(s) = 1 : 6.8).	159
7.3	Selectivity profile (%) of the by-products produced as a function of reaction temperature over 0.4 wt % Pd/alumina-Silica (764) catalyst. Catalyst was sieved to 500-250 microns before reaction and 20 mg was placed in the stainless steel 1/4 inch tubular reactor. Nitrobenzene/hydrogen flow was kept constant throughout the reaction. Each temperature was kept for an hour before increasing by 20°Cuntil reaching 180°C. Cyclohexylamine (black), cyclohexanone (red) N-cyclohexylaniline (blue) and dicyclohexylaniline (green) are observed.	160

7.4	Nitrobenzene conversion (black) and aniline selectivity (red) as a function of reaction temperature over 0.3 wt % Pd/alumina-Silica (M12340) catalyst. Catalyst was sieved to 500-250 microns before reaction and 20 mg was placed in the stainless steel 1/4 inch tubular reactor. Nitrobenzene/hydrogen flow was kept constant throughout the reaction. Each temperature was kept for an hour before increasing by 20°C until reaching 160°C (NB 2.03×10^{-6} mol/min: H ₂ 7.83×10^{-4} mol/min - H ₂ :NB = 385 : 1, NB(s ⁻¹) : Pd _(s) = 1 : 3.7).	164
7.5	Selectivity profile (%) of the by-products produced as a function of reaction temperature over 0.3 wt % Pd/alumina-Silica (M12340) catalyst. Catalyst was sieved to 500-250 microns before reaction and 20 mg was placed in the stainless steel 1/4 inch tubular reactor. Nitrobenzene/hydrogen flow was kept constant throughout the reaction. Each temperature was kept for an hour before increasing by 20°C until reaching 180°C. Cyclohexylamine (black), cyclohexanone (red) N-cyclohexylaniline (blue) and dicyclohexylaniline (green) are observed.	165
7.6	Pulsed CO Chemisorption Isotherm on Pd/alumina-Silica catalysts 4, 5 and 6.	168
7.7	X-ray Powder Diffraction pattern recorded for the 0.3 wt % Pd/alumina-30%Silica (M11572) catalyst. The red drop lines represent the reference γ -alumina diffractogram.	170
7.8	X-ray Powder Diffraction pattern recorded for the 0.3 wt % Pd/Al ₂ O ₃ - 1% SiO ₂ (M12340) catalyst. The red drop lines represent the δ -alumina main reflections and the green drop lines the θ -alumina.	172
7.9	X-ray Powder Diffraction pattern recorded for the 0.4 wt % Pd/Al ₂ O ₃ - 1% SiO ₂ (764) catalyst. The red drop lines represent the δ -alumina main reflections and the green drop lines the θ -alumina.	173
7.10	Temperature-Programmed Infrared Spectroscopy on 0.3 wt % Pd/Al ₂ O ₃ - 30% SiO ₂ (M11572).	175
7.11	Temperature-Programmed Infrared Spectroscopy on 0.4 wt % Pd/Al ₂ O ₃ - 1% SiO ₂ (764).	177
7.12	Temperature-Programmed Infrared Spectroscopy on 0.3 wt % Pd/Al ₂ O ₃ - 1% SiO ₂ (M12340).	179
A.1	Nitrobenzene calibration plot.	187
A.2	Aniline calibration plot.	188
A.3	Cyclohexylamine calibration plot.	189
A.4	Dicyclohexylamine calibration plot.	190
A.5	Diphenylamine calibration plot.	191

A.6	Azobenzene calibration plot.	192
A.7	N-cyclohexylaniline calibration plot.	193

List of Tables

1.1	List of catalyst used during the project	26
2.1	Antoine's coefficients for Nitrobenzene and Aniline.	33
2.2	Absorbance recorded for different Pd standard solution analysed.	38
3.1	Table of Dispersions for CO Pulsed Chemisorptions obtained on the 5 wt % Pd/Al ₂ O ₃ catalyst (Sample 1).	46
3.2	XRD assignments for the 5 wt % Pd/alumina catalyst based on the gamma-alumina main reflections.	48
3.3	Interspacing distances for the Pd metal and Pd oxide.	50
3.4	Summary of Spectral assignments for CO chemisorption on Pd crystallites	57
4.1	Weight Hourly Space Velocity (hour ⁻¹) reported for the different mass of catalyst used in the 1/2inch fixed-bed reactor. Nitrobenzene flow and hydrogen content remained constant throughout.	72
5.1	Mass Measurement of the Cyclohexanone Oxime (CHOX)	105
5.2	Actual Metal Loading From Atomic Absorption Spectroscopy measurements	116
5.3	Table of Dispersions for CO Pulsed Chemisorptions.	116
5.4	Assignments of the 310/2 catalyst diffraction pattern	124
5.5	Assignments of the 143 500 catalyst diffraction pattern	126
5.6	BET and BJH measurements.	128
7.1	Actual Metal Loading From Atomic Absorption Spectroscopy measurements	167
7.2	Table of Dispersions for CO Pulsed Chemisorptions.	167
7.3	XRD assignments for the M11572 catalyst based on the gamma-alumina main reflections.	171
7.4	XRD assignments for the 764 and M12340 catalyst based on the main reflections of θ and δ -alumina transition phases.	171
A.1	Nitrobenzene calibration data obtained manual injection on GC.	187
A.2	Aniline calibration data obtained manual injection on GC.	188
A.3	Cyclohexylamine calibration data obtained manual injection on GC.	189

A.4	Dicyclohexylamine calibration data obtained manual injection on GC. . . .	190
A.5	Diphenylamine calibration data obtained manual injection on GC.	191
A.6	Azobenzene calibration data obtained manual injection on GC.	192
A.7	N-cyclohexylaniline calibration data obtained manual injection on GC. . .	193

Chapter 1

Introduction

1.1 Aniline Applications

Aniline is a capital chemical building block used massively in many different industries especially for the manufacture of polymers. The most famous industrial outputs include methyl diphenyl diisocyanate (MDI) synthesis as shown in **Figure 1.1 and Scheme 1.1**, which can then be used for polyurethane applications (**Figure 1.2**) such as polyaniline (PANI) polymers used to provide semiconductor manufacturers [2]. The aniline demand as a feedstock for these industries is constantly growing, especially as the Chinese market increases [3].

Global Aniline Consumption by End Use Sector in 2013

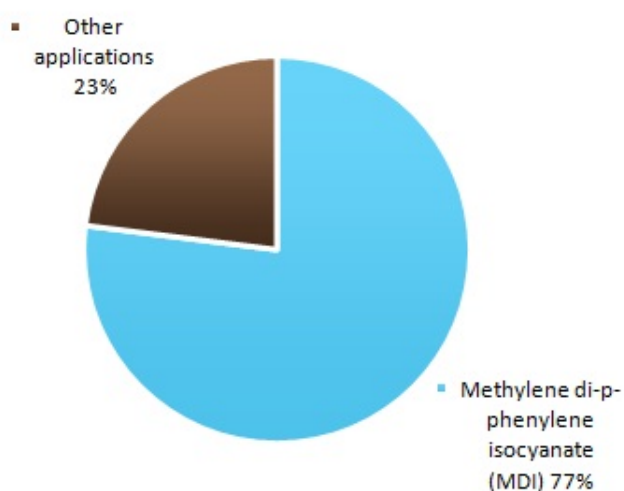


Figure 1.1: Aniline uses distribution in 2013 [3].

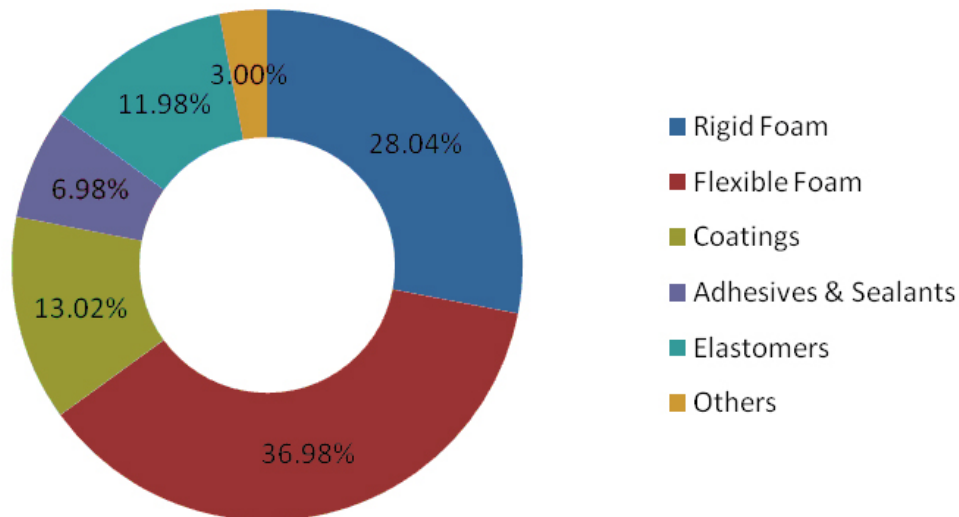
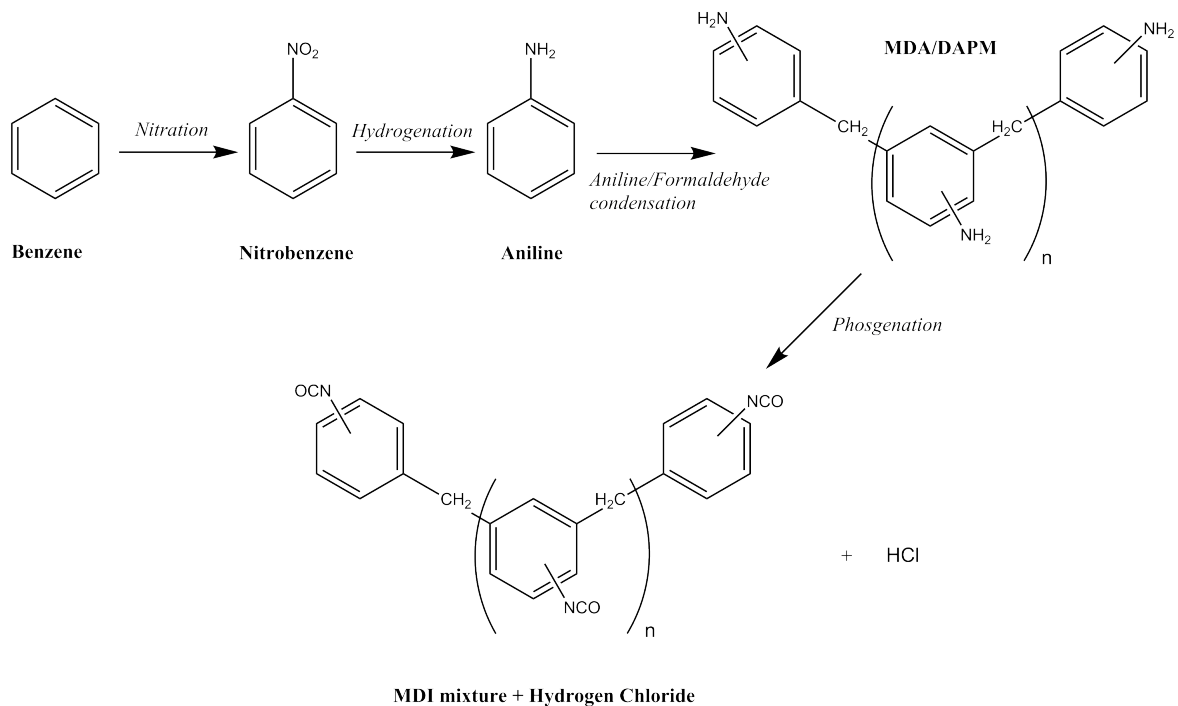
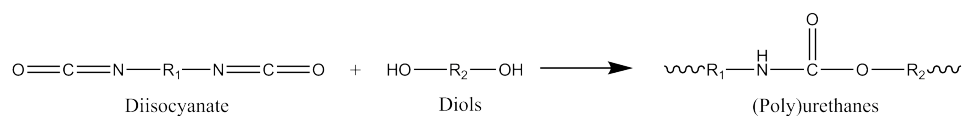


Figure 1.2: Polyurethane applications' distribution in 2010 [4]



Scheme 1.1: Schematic representation of the methyl-diisocyanate production from benzene [5]



Scheme 1.2: Formation of polyurethane from the reaction between diols and diisocyanates [5]

1.2 Synthesis of Aniline

Several starting products are available to synthesise aniline at a large scale and nitrobenzene is at the moment the most favorable and most frequently used. Most of the nitroben-

zene produced worldwide goes straight in to aniline production [4], which is used in the methyl diisocyanate (MDI) process as described in **Scheme 1.1**. MDI is then used in conjunction with diols to produce the polyurethane polymer as shown in **Scheme 1.2**.

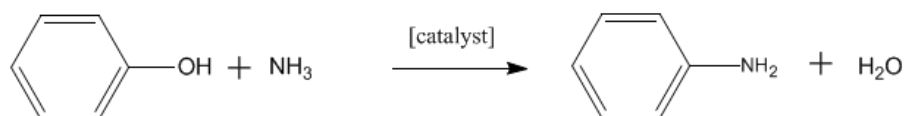
The initial aniline production process was named after his creator and is called the Bechamp reaction. Antoine Bechamp used this reaction to reduce nitronaphthalene and nitrobenzene in 1854 [6]. The reaction was previously used to produce large amounts of aniline by reducing the nitro aromatic group. This reaction involves mixing iron and water in the presence of hydrochloric acid in order to reduce the nitro group into an amine. The common yield obtained is 90% to 95%. As a means of producing aniline, this reaction has been replaced by the catalytic nitrobenzene hydrogenation but the Bechamp reaction is still used by Bayer in West Virginia as a way to produce iron oxide pigment from the iron oxide sludge [7].

The catalytic nitrobenzene hydrogenation is used by the majority of the chemical companies where the selectivity to aniline, under mild conditions with a three molar equivalent hydrogen supply in presence of a suitable catalyst, is around 98-99%. Many different metals can be used effectively as a catalyst so that this reaction has now become a standard test for hydrogenation catalysts [8].

Despite the fact that nitrobenzene hydrogenation is seen as the most efficient technique to get highly pure aniline in large quantities, a few other methods have also been used by industry.

1.2.1 Ammonolysis of Phenol

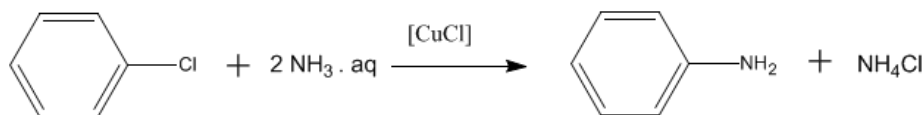
This Halcon/Scientific design has been operated by Mitsui Petrochemicals since the 1970's to produce aniline. This process operates at 200 bar and 425°C with a catalyst (which can sometimes be supported on a zeolite) and combined with different metallic co-catalysts [6]. As shown in **Scheme 1.3**, a large ammonia excess gives 98% conversion and 87-90% selectivity towards aniline.



Scheme 1.3: Amination of Phenol

1.2.2 Ammonolysis of Chlorobenzene

Dow chemicals operated the Kanto Electrochemical Co. process for aniline until 1966. This involved reacting chlorobenzene with two equivalents of ammonia at 180-220°C under 60-75 bar in the presence of CuCl and NH₄Cl (also called 'Niewland catalyst') [6].

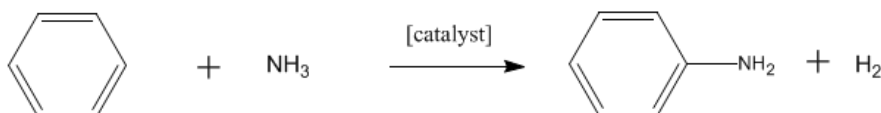


Scheme 1.4: Amination of Chlorobenzene

The aniline selectivity obtained was 91%.

1.2.3 Ammonolysis of Benzene

This reaction has been designed and used by Du Pont to avoid the nitrobenzene production step by reacting benzene and ammonia together under severe conditions. Indeed, the reaction temperature is 350°C and the pressure is set up at 300 bar to obtain a low conversion (13%), but it proved to be a highly aniline selective process (97%) [6]. However, catalyst regeneration and low conversion appear to stop further large scale production.



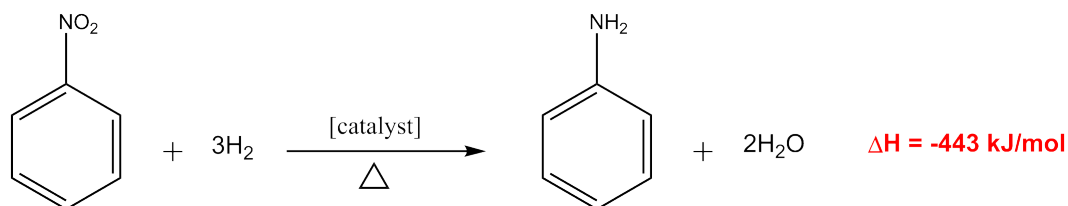
Scheme 1.5: Amination of Benzene

1.3 The Catalytic Nitrobenzene Hydrogenation

1.3.1 Recent considerations related to industrial nitrobenzene hydrogenation

The hydrogenation of nitrobenzene to produce aniline is a high value business for the worldwide manufacture of MDI [5]. Aniline has been produced quantitatively and successfully via different catalytic processes in the last few decades, but the rise of energy costs has forced changes in plant design [9, 10]. As a result, an alumina-supported catalyst used in a trickled bed reactor was introduced recently by Huntsman Polyurethanes in order to take advantage of the high exothermicity of the nitrobenzene hydrogenation ($\Delta H = -443 \text{ kJ/mol}$) [11]. They designed the new reactor to additionally obtain high pressure steam during the reaction. In parallel, Abo-Ghander *et al.* [12, 13] and Rahimpour *et al.* [14, 15] have shown interest in novel integrated thermally fluidized bed which couples with the dehydrogenation of ethylbenzene to styrene with the hydrogenation of nitrobenzene to aniline. This coupled reactor was designed to overcome the thermodynamic limitation on the dehydrogenation of ethylbenzene to styrene. As a result, the enhancement in conversion of ethylbenzene and yield of styrene were considerable. These studies

showed that nitrobenzene hydrogenation could be used to produce high value chemicals and when operated in optimum conditions, it will also generate considerable amounts of heat. Indeed, Maria *et al.* have studied the variability of operating conditions within a fixed-bed catalytic reactor for vapour-phase nitrobenzene hydrogenation [16] where they reported the parametrical effect on the temperature sensitivity inside the reactor for different inlet and cooling agent temperature. They found that above a certain temperature, the system was sustainable and that heat transfer could be used efficiently.



Scheme 1.6: Catalytic Nitrobenzene Hydrogenation [11]

Industrially, steam is commonly used to transfer heat and drive turbines to produce a considerable amount of electricity [17]. As a consequence of the increase in energy cost, the production of electricity via steam propelled turbines has soared in the last decade, where it is now more common to see new plants feature self-sufficient processes, or where they provide heat to other unit operations. To avoid corrosion and other significant problems related to saturated steam, superheated steam can be used for the steam inflow. Where saturated steam has a high heat transfer capacity ($U = 1160 \text{ W/m}^2\cdot\text{K}$) and can cause problems due to the presence of water, superheated steam has a significantly lower heat capacity ($U = 92 \text{ W/m}^2\cdot\text{K}$) because it is dry. It also has a high internal energy which can be used through mechanical expansion against turbine blades. As opposed to superheated steam, saturated steam is incompressible due to the presence of the water droplets; but to avoid any mechanical fault, the gas used needs to remain compressible hence the use of superheated steam. The Rankine cycle is a thermodynamic concept based on the Carnot heat engine principle that predicts the performance of steam engines. The model was developed using mechanical work generated or consumed by the turbine and the pump, and the heat given and taken out the system. As a result, a temperature vs entropy diagram can be generated and the superheated Rankine cycle indicates what temperature the inlet flow must be (just below 400°C) to operate with superheated steam. It is our understanding that economical and design reasons dictate the nitrobenzene hydrogenation conditions nowadays.

1.3.2 Mechanism

A reaction mechanism for nitrobenzene hydrogenation was first introduced by Haber in 1898 [18]. This mechanism agreed that the nitrogroup was first reduced to aniline through nitrosobenzene and hydroxylamine intermediates. The formation of the latter compound is thought to constitute the rate determining the step. Phenylhydroxylamine (Ph-NHOH) is a reactive compound and quite unstable, so it is able to form either aniline or produce azoxybenzene and azobenzene, which can then ultimately lead on to aniline as well. The Haber Mechanism is shown here in **Figure 1.3**.

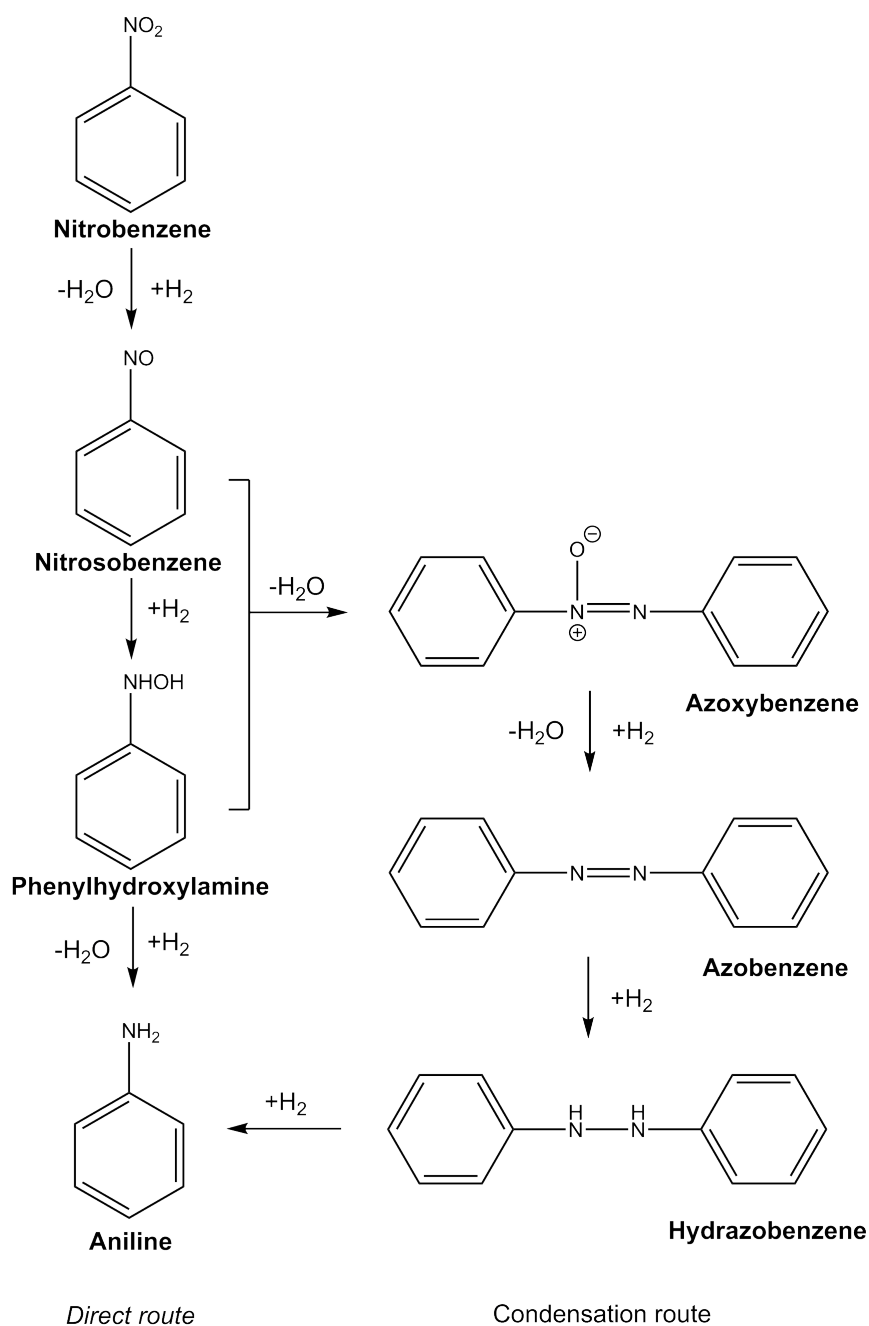


Figure 1.3: Haber mechanism for the reduction of aromatic nitrogroups to aniline [18]

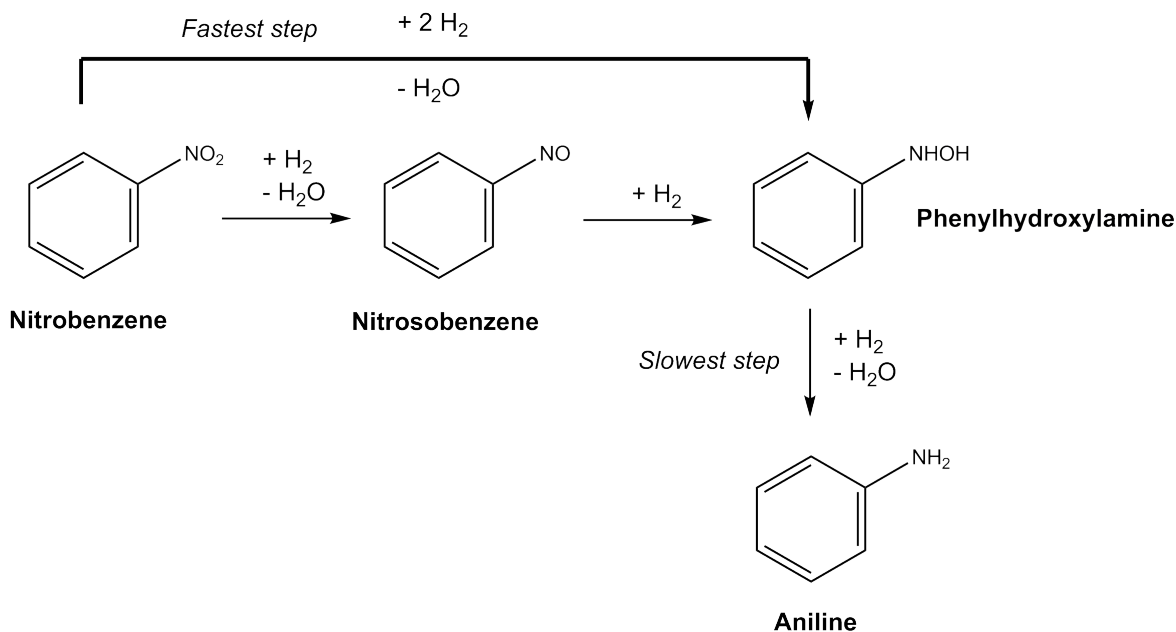


Figure 1.6: Proposed pathway for the hydrogenation of nitrobenzene to aniline on Au/TiO₂ [22]

supported on carbon or alumina. From their study, they proposed a renewed detailed reaction pathway concerning the hydrogenation of nitrobenzene to aniline. The study suggested that the formation of an adsorbed species, named Ph-NOH, which permits further hydrogenation with adsorbed hydrogen to lead to aniline, or a hydrogenolysis route which leads to the formation of azoxybenzene. Nitrosobenzene was introduced as a reactant and the rate to aniline formation dropped when compared to nitrobenzene on the Pd/C catalyst; hence nitrosobenzene was ruled out being an intermediate.

When Haber proposed the mechanism for the hydrogenation of nitro aromatics, he also suggested that aniline could be further reduced to cyclohexylamine and other derivatives [18]. The reactivity of aniline hydrogenation over platinum group metals particles was studied by Freifelder *et al.* in 1962 and Greenfield in 1964 [25, 26]. Of the rhodium, ruthenium, platinum and palladium tested, ruthenium was seen to be the most active metal to carry out the hydrogenation of aromatic amines to alicyclic amines [27, 28]. Cobalt could also be used to hydrogenate aniline as reported by Winans in 1940 [29]. He found that the ring hydrogenation occurs at temperature of 200-300°C depending on the activity of the catalyst to give cyclohexylamine, which was then followed by the autoalkylation to give dicyclohexylamine.

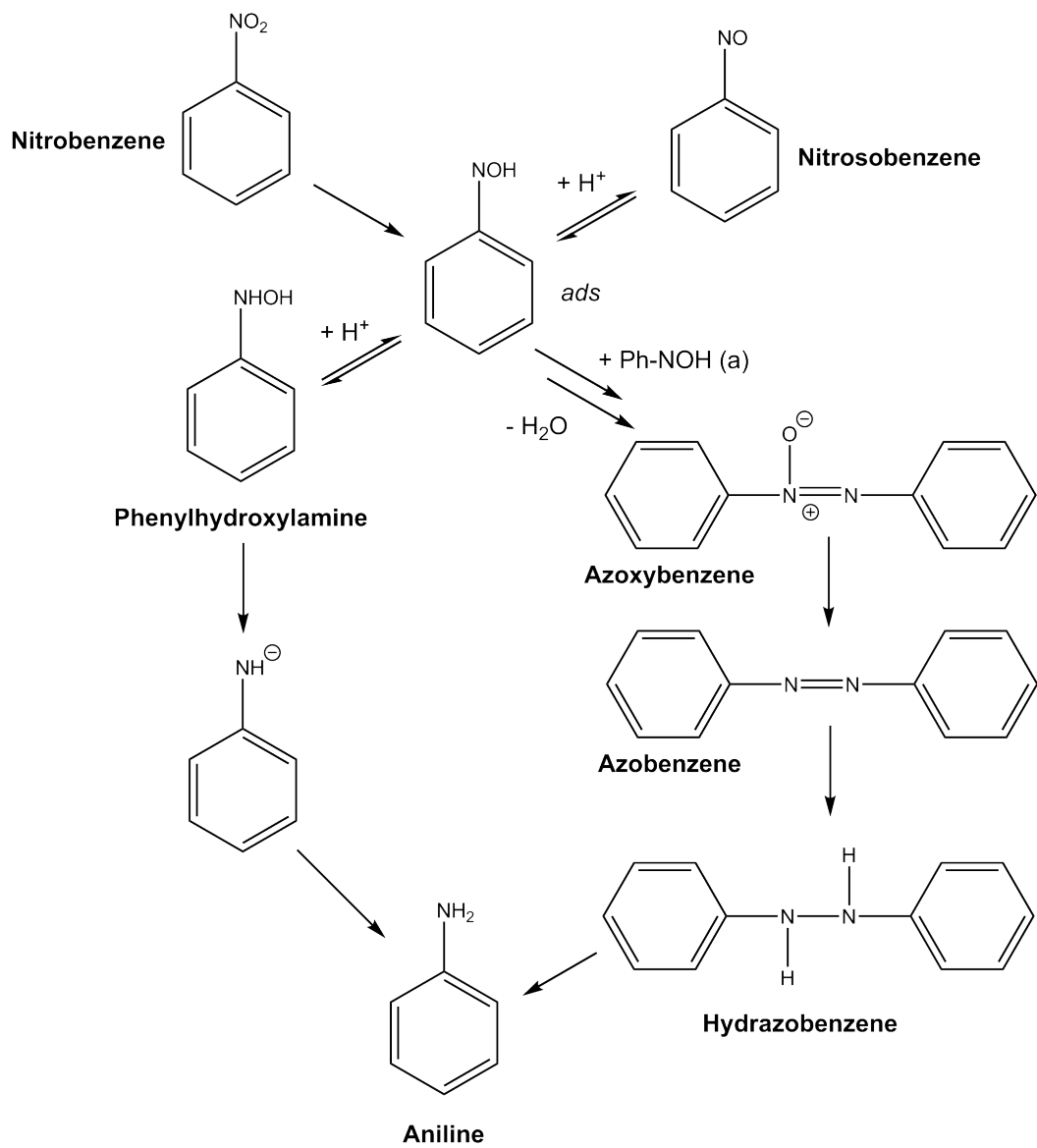


Figure 1.7: Nitrobenzene hydrogenation pathways proposed by Gelder *et al.* [24]

The work by Pitara *et al.* in 1996 highlighted the influence of the pH while reacting nitrobenzene with hydrogen over Pt/C catalyst in the liquid phase [30]. In a neutral solution, the reaction is totally selective to aniline, whereas, when the reaction mixture is acidic, the selectivity towards aniline drops to 30%. The latter can be explained by a further hydrogenation of aniline to cyclohexylamine and dicyclohexylamine. This behaviour can be explained by the difference between the modes of adsorption at the surface of the catalyst.

Narayanan *et al.* studied the hydrogenation of aniline over alumina-supported cobalt and nickel catalysts [31, 32]. Both catalysts produced cyclohexylamine, N-phenylcyclohexylamine and dicyclohexylamine, although the Ni catalyst was found to be more active when using similar metal loading.

Mink *et al.* studied the reactivity of gas phase aniline over a nickel catalyst as well [33]. The primary product obtained was cyclohexylamine, which adsorbed strongly onto the catalytic surface and lead to the formation of dicyclohexylamine and the hydrogenolysis reaction. More recently, Kim *et al.* looked at synthesizing alicyclic amines from nitroarenes using ruthenium catalysts. They reported different selectivities depending on the reaction conditions and formulations of catalysts used. All reactions underwent the following steps: Nitro reduction, ring hydrogenation, which sometimes continued on to N-alkylation.

1.3.3 Adsorption of Nitrobenzene and Aniline

Early work on nitro-compound adsorption on catalyst surfaces was published in 1967 by Nelson et al [34]. They studied the adsorption on the surface of MgO powder using electron spin resonance and reflectance spectrophotometry. Adsorption of nitrobenzene at the surface was performed under air conditions and heated to 200°C, after their first attempt failed at room temperature. Nelson *et al.* suggested that the nitrobenzene ion must lie flat on the surface and to avoid hindered rotation. Furthermore, rotation decreased with low temperature, and/or by adding a nitrobenzene group to the aromatic ring. Electron spin resonance data suggest that the MgO electron donor support induced a distortion to the adsorbed molecule which could then increases the planarity.

Adsorption of nitrobenzene and aniline on different materials was investigated further in the 1990s. Meijers *et al.* studied the adsorption of nitro and amino compounds on cobalt oxide in 1994 using IR spectroscopy [35]. The cobalt catalyst sample was placed into an IR cell under vacuum and dosed with nitrobenzene aliquots. Spectrum was obtained after adsorption and with any increase in temperature. The reactivity of the three cobalt oxides was enhanced by their surface hydroxyl groups. Some Lewis acid sites are believed to play a role as well, but possibly the most interesting observation is the pure cobalt oxide sample, where part of the hydrogen used during activation remained stored on the surface. This enabled reduction of the nitro group and further ring reduction to give

aniline and cyclohexylamine respectively [36]. Ponec *et al.* concluded that nitrobenzene was bound through the phenyl ring which lies parallel to the surface, and that aniline is bound by hydrogen bonding between the amino group and a surface OH group. This suggestion leaves the phenyl ring pointing away from the surface. Chen *et al.* investigated the adsorption of nitrobenzene on a Cu (110) surface using FTIR [37]. Adsorption of nitrobenzene was first carried out at low temperature which was then heated to 28°C. The IR results showed strong NO₂ modes compared with the phenyl ring because of the related parallel adsorption of the ring towards the surface of the adsorbent [38]. Thereby, adsorption of nitrobenzene at low temperature is believed to happen through adsorption of nitro group preferentially. In parallel, Near Edge X-ray Absorption Fine Structure (NEXAFS) studies of phenyl adsorption on Cu (111) showed that the aromatic ring was aligned away from the surface plane by an angle of $43 \pm 5^\circ$ [39]. Other studies using High Resolution Electron Energy Loss Spectroscopy (HREELS) estimated this angle to be approximately 30 degrees [40]. At higher temperatures, they suggested a decomposition of the adsorbed nitrobenzene into a nitro free molecule, *i.e.* benzene. This emphasises the fact that the C-N bond must weaken enough to be ruptured before further reduction of the aromatic ring.

Aniline adsorption on Cu(110) has been investigated by Davies *et al.* for the oxidation of aniline [41, 42]. The nitro group is a better electron donor compared to the amino group, this could explain why they stated and observed that aniline and its derivatives were adsorbed through the pi bonding occurring from the phenyl aromatic ring. Huang *et al.* studied the kinetics and adsorption of aniline and derivatives on Ni(111) using XPS, NEXAFS, and fluorescence spectroscopy [43, 44, 45, 46, 47, 48, 49]. Experiments were performed using gas phase aniline where several analytical techniques were carried out to provide an understanding of aniline adsorption process and hydrogenation to cyclohexylamine, N-cyclohexylaniline and dicyclohexylamine. The data obtained showed that aniline adsorption underwent the same process shown previously, where the aniline is found to bond to the nickel surface through nitrogen's lone electron pair at low temperatures. In addition, at the same temperature, NEXAFS data indicated that aniline was tilted away 55 degrees from the surface plane. This is consistent with the fact that lone pair donation is the dominant adsorption mode. At 365 K, adsorbed hydrogen is believed to play an important role because it keeps the C-N bond in a favorable orientation for the reaction by stabilizing the amino hydrogens and hydrogenating the ring.

Huang *et al.* investigated aniline hydrogenation on the Pt(111) surface where they attempted to correlate the surface configuration to the selectivity/activity [50]. This study showed the same tendency, namely the aniline adsorption pattern at low temperature is nearly parallel to the surface. Whereas, increasing temperature showed that this pattern is no longer stable and that the ring was found to be tilted away from the surface. For

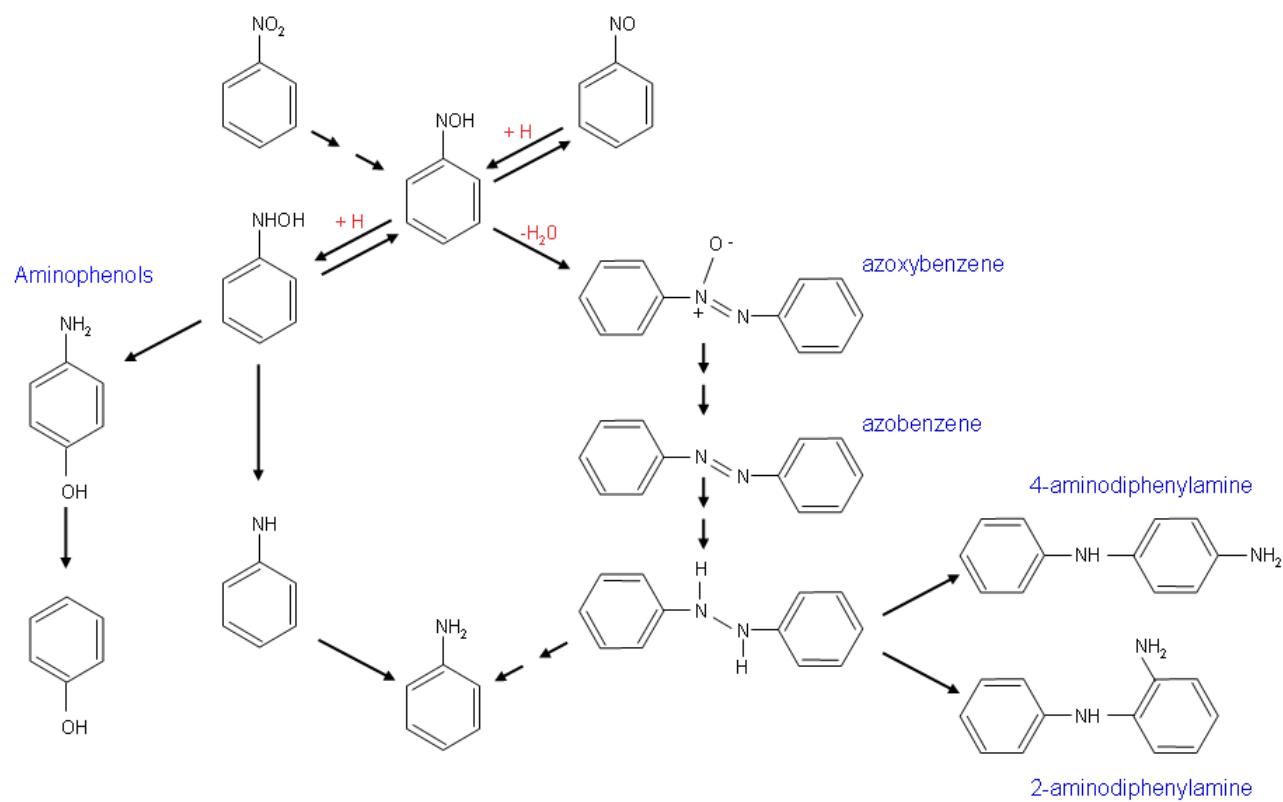
Pt(111), calculations using NEXAFS estimated an angle around 30 degrees for the maximum tilt possible. Whatever the adsorption pattern is, these results showed that aniline adsorption is believed to be weaker than the nitrobenzene.

1.3.4 The Under and Over-Reduction Concepts in Nitrobenzene Hydrogenation

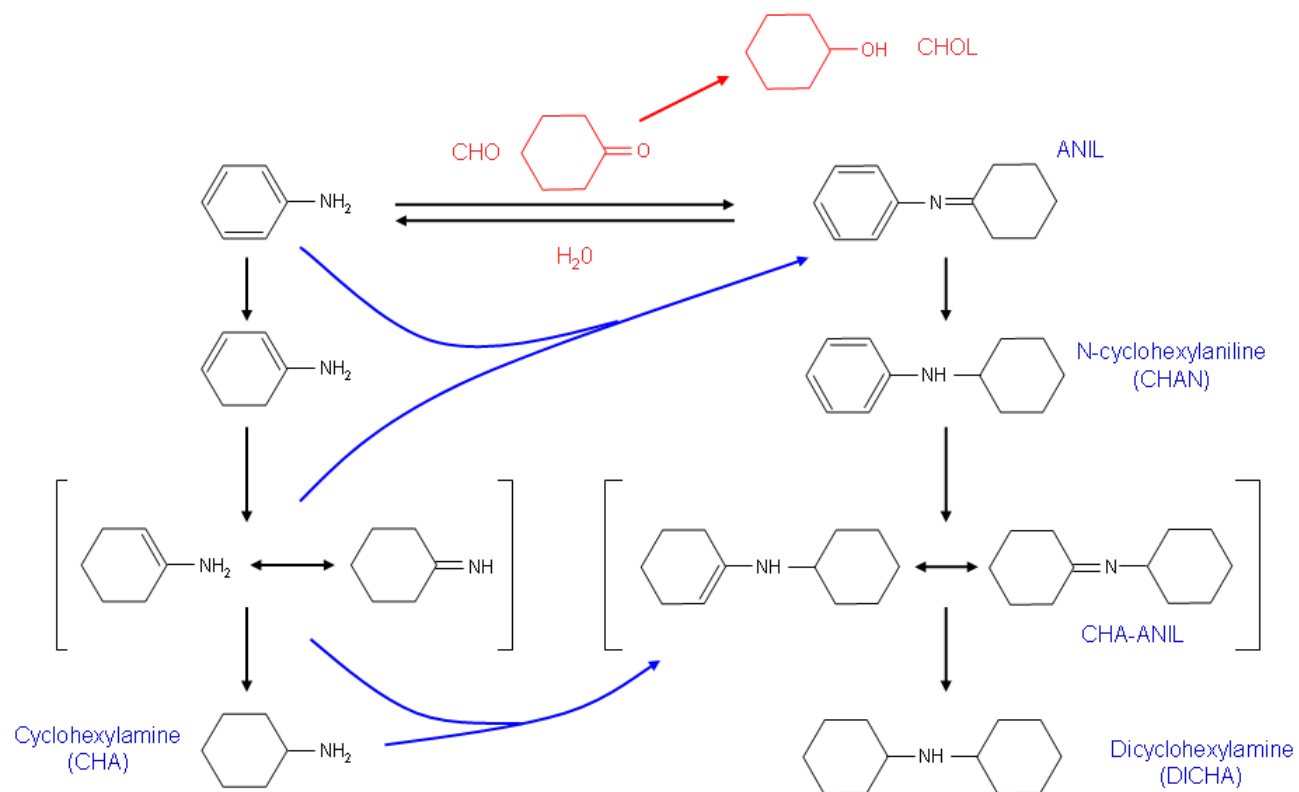
Following Gelder's work [51], with industrial testing and the understanding of the nitrobenzene hydrogenation mechanism (**Section 1.3.2**), Huntsman Polyurethanes provided an extensive scheme composed of two parts which are presented in **Schemes 1.7 and 1.8** [11].

The '*under-reduction*' scheme, **Scheme 1.7** includes the understanding of the nitrobenzene hydrogenation as reported by Haber [18] and Gelder [24]. It includes all products obtained between the reduction of nitrobenzene to the production of aniline. Note the adsorbed intermediate discussed by Gelder *et al.*

The '*over-reduction*' scheme, **Scheme 1.8** reports the over-hydrogenation steps of aniline in the catalytic reactor. It provides an understanding of the different species such as dicyclohexylamine and N-cyclohexylaniline, but also note that the scheme accounts for results obtained in liquid phase in the presence of aniline and water, which should be dealt with cautiously.



Scheme 1.7: Reaction mechanism pathway proposed by Huntsman as the "under-reduction" branch of the catalytic nitrobenzene hydrogenation [11].



Scheme 1.8: Reaction mechanism pathway proposed by Huntsman as the "over-reduction" branch of the catalytic nitrobenzene hydrogenation [11].

1.3.5 Activation Energy of Nitrobenzene Hydrogenation

Other studies were performed on non-metallic surfaces such as TiO₂, kaolin and silver supported on TiO₂, at room temperature and ambient pressure using successively Pd/Rh, colloidal Pt and Ni. They observed an activation energy of 50-62 kJ/mol for an order of reaction of 0 and 1. But the activation energy dropped to 0-6 kJ/mol when hydrogen diffusion through the solvent determined the rate [52, 53, 54, 55]. Still in the liquid phase, Metcalfe and Rowden worked on a Pd-Ag alloy using butanol as a solvent. They observed an activation energy from 21 to 105 kJ/mol [56]. Rihani *et al.* considered the hydrogenated nitrobenzene in the gas phase between 275 and 350°C, over Ni and Cu catalysts [57]. A comparable study was also performed by Gharda and found an activation energy of 69 kJ/mol [58].

On the other hand, Stoessel studied the hydrogenation of aromatic nitro compounds and established an enthalpy of reaction around 560 kJ/mol [59]. Yeong *et al.* calculated an enthalpy of reaction value of 545 kJ/mol [60]. Nitrobenzene hydrogenation is an exothermic reaction with a low activation energy which therefore makes this reaction feasible at low temperature and atmospheric pressure.

1.4 Infrared Spectroscopy used in Heterogenous Catalysis

Infrared Spectroscopy uses infrared light which has a higher wavelength and a lower frequency than visible light as shown in **Figure 1.8**. An infrared beam consists of photons that are able to excite structure, molecules, lattices, bonds. Indeed, if the frequency (ν) and the energy (E) of the photon matches a fundamental vibration of the molecule and cause resonance, the molecule can absorb energy from the photon [61]. This interaction results in an infrared absorption band.

The infrared section of the electromagnetic spectrum is usually divided into three regions:

the high energy Near-IR from 14000 to 4000 cm⁻¹,

the Mid-IR from 4000 to 400 cm⁻¹,

the Far-IR from 400 to 10 cm⁻¹.

Each region has a different discrete wavenumber range which results in discrete energy bands as shown in **Equation 1.1**.

$$E = h\nu = \frac{hc}{\lambda} = hc\bar{\nu} \quad (1.1)$$

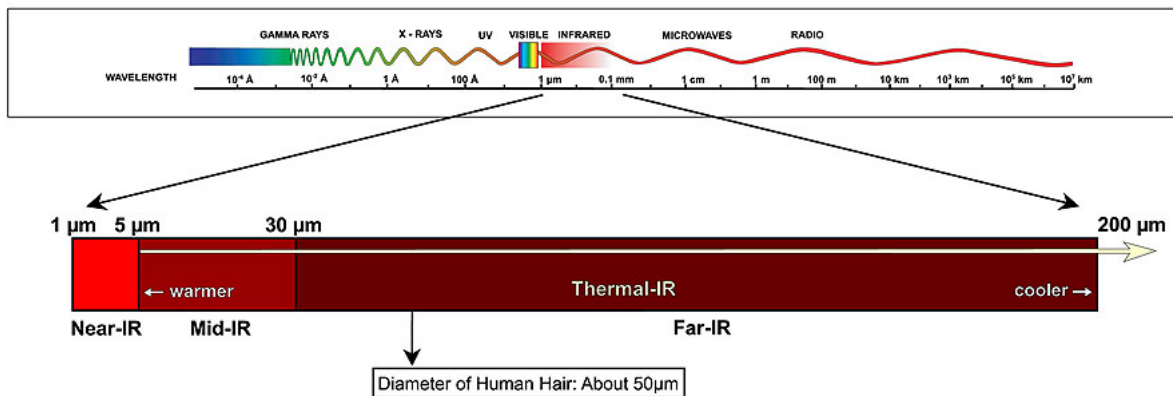
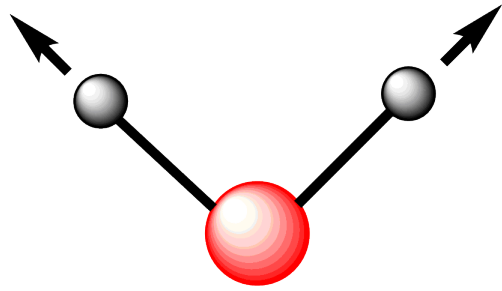
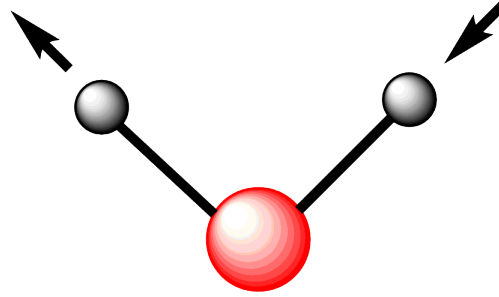


Figure 1.8: Infrared as part of the electromagnetic spectrum [62]

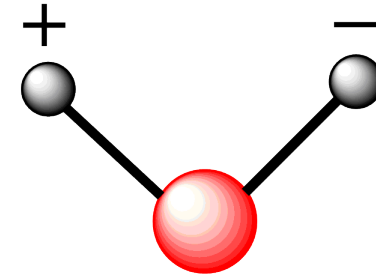
As stated earlier, molecular vibrations using infrared is possible when the energy and frequency of the beam matches one of the fundamental vibrations of the functional group present on a sample. However, this is not the unique condition to obtain a vibration with IR. Indeed, infrared is useful when a functional group has a dynamic dipole moment. For example, nitrogen is IR inactive while carbon monoxide is IR active [63]. IR spectroscopy can be used to analyse a wide variety of molecules and materials in liquid, solid and gas phase. This technique has become one of the most popular techniques used in heterogeneous catalysis, as first used by Eischens in 1958 [64]. Additionally, there is an extensive database of information available regarding the type of vibrations possible as seen in **Figure 1.9**. It therefore allows for a better understanding of complex systems such as: liquid batch reactions and co-adsorption of gases at the surface of a catalyst. Although infrared spectroscopy is a powerful technique, the real breakthrough came with the use of Fourier transform spectrometers using an interferometer which replaced monochromatic spectrometers which were deemed too long to operate [63].



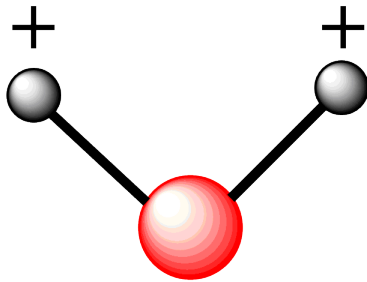
ν_s - Symmetrical stretching



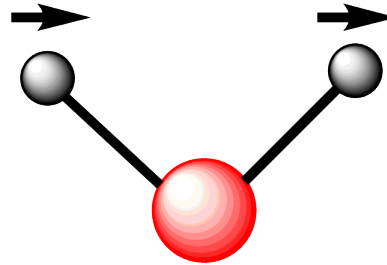
ν_{as} - Antisymmetrical stretching



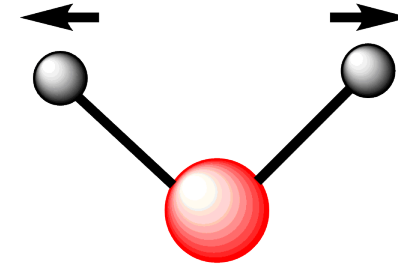
τ - Twisting
(deformation out-of-plane)



ω - Wagging
(deformation out-of-plane)



ρ - Rocking
(deformation in-plane)



δ_s - Scissoring
(deformation in-plane)

Figure 1.9: Different molecular vibrations recorded in Infrared Spectroscopy [65].

1.4.1 Fourier Transform Infrared Spectroscopy

The use of Fourier Transform IR Spectroscopy is well established but before the introduction of the Michelson interferometer in the spectrometer, monochromators were used to select a narrow range of wavelengths useful to the experiment as shown in **Figure 1.10**. The monochromator used is known as a grating. A diffraction grating for infrared consists of a series of close, evenly spaced lines positioned on an optical flat aluminised glass. For coverage of the mid-IR spectra region at least two gratings are required [61, 63]. Therefore the loss of energy due to radiation hitting side of the grating walls was considerable and the total of energy allowed through the sample was attenuated. As a consequence, it was therefore very time-consuming to obtain a well-resolved spectra.

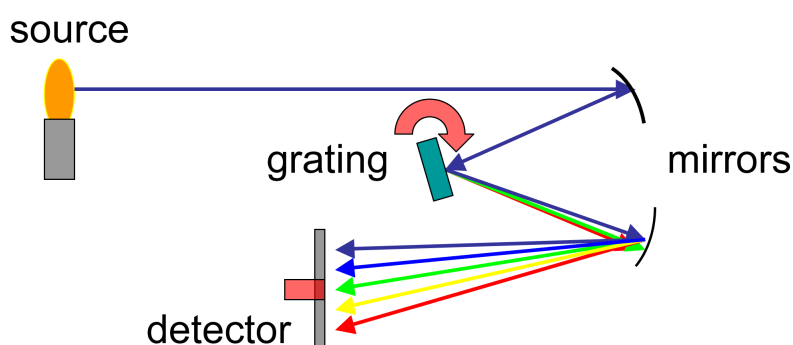


Figure 1.10: Schematic representation of a Spectrometer using a grating to select wavelength.

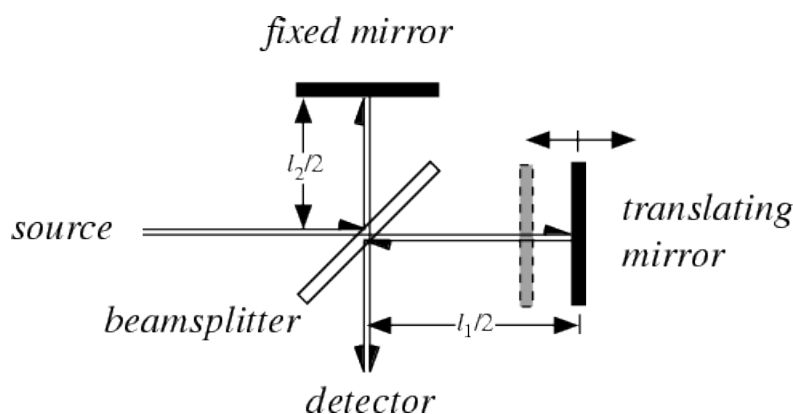


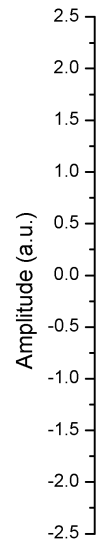
Figure 1.11: Schematic representation of a Michelson Interferometer [66].

IR spectrometers nowadays use Fourier Transform spectrometry which enables an acquisition of all the frequencies simultaneously [63]. This revolution was possible due to the development of the Michelson's interferometer represented schematically in **Figure 1.11**. The interferometer is a piece of apparatus which consists of a beamsplitter, a fixed mirror and a translating mirror positioned perpendicular to each other. The beamsplitter transmits and reflects the beam into two equal beams. As shown in

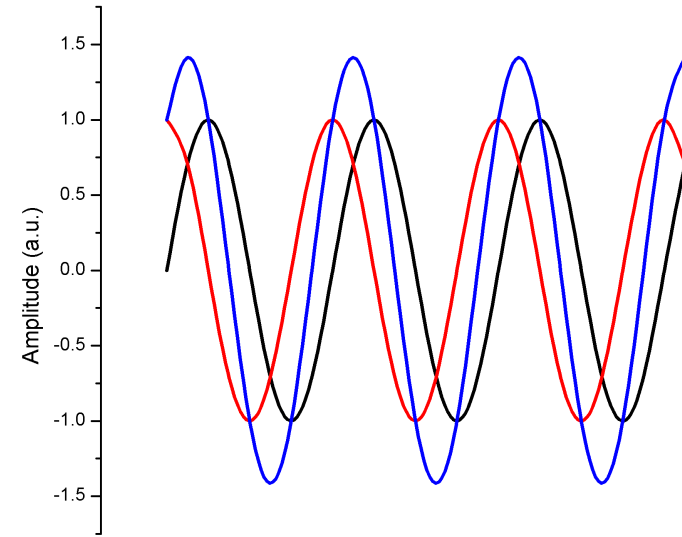
Figure 1.11, one half of the signal (S_2) is reflected to the fixed mirror and the other half (S_1) is transmitted to the translating mirror. As a consequence, the path of S_2 is unchanged whereas the S_1 pathlength can be altered by moving the mirror. The resulting difference of pathlength between the two beams S_1 and S_2 is known as the retardation and is calculated with **Equation 1.2** .

$$retardation = 2 \times \left(\frac{l_1}{2} - \frac{l_2}{2} \right) \quad (1.2)$$

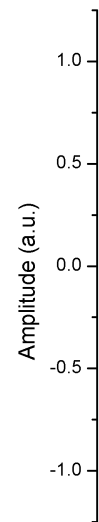
Three different combinations of resulting interferences are displayed in **Figure 1.12**. When the beamsplitter is equidistant from both the moving and fixed mirror, both signals are *in-phase* and constructive interference occurs, as shown in **Figure 1.12a**. **Figure 1.12c** demonstrates the opposite phenomenon called deconstructive interference. In this case, the retardation is equal to a full wavelength and the resulted signal is a flat 0 line. When the retardation is equal to half a wavelength as shown in **Figure 1.12b**, the resultant signal in blue is obtained. This enables to scan from 400 to 4000 cm^{-1} in a few seconds.



(a) No retardation.



(b) half-wavelength retardation.

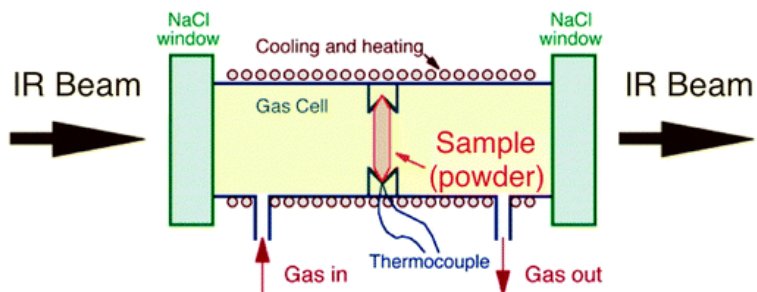


(c) one complete wavelength retardation.

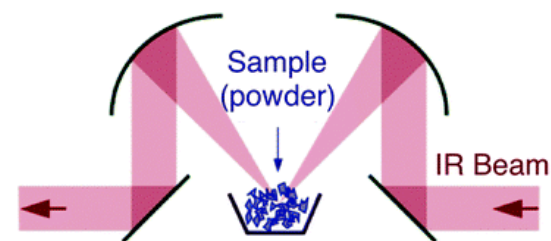
Figure 1.12: Resulting interference pattern from variation of pathlength in a Michelson's interferometer. (a) represents a constructive pattern and (c) a deconstructive pattern [66].

Of the four techniques shown in **Figure 1.13** reproduced from the paper from Zaera[1], two of the techniques are commonly used in heterogeneous catalysis. Transmission-IR and DRIFT have been used extensively to monitor catalytic surfaces under different conditions. Transmission-IR cells usually require the catalyst to be pressed into a wafer-disc or sprayed onto an infrared transparent surface or mesh. The deposition of catalyst onto a IR-transparent surface can be non-reproducible because of the preparation process and the uncertainty in the exact sample mass deposited. Where pressing a disc of a known mass of catalyst into a circular wafer can be seen to be reproducible, one needs to ensure that the mass is kept as low as possible to avoid blocking the transmission of the signal. Moreover, pressing a disc to a couple of tonnes per cm^2 can be quite dramatic for a catalyst where the pressure could lead to collapse of the structure (i.e. zeolites) or cause a phase change of the support (i.e. mixed oxide support). Finally, the transmission setup is qualitative for high loading catalysts (ie. $> \text{Metal } 1\% \text{ w/w}$) but fails to detect important features in lower loads [67].

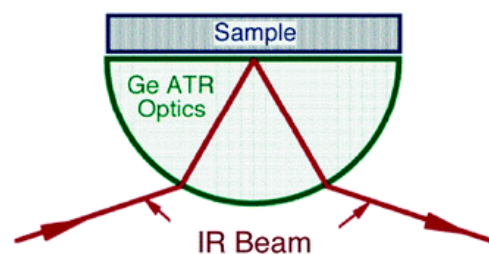
Diffuse Reflectance Infrared Fourier Transform (DRIFT) cells are much easier to use because the catalyst is usually placed in a ceramic cup at the bottom of the cell and the IR-beam is directed towards the cup and signal collected using multiple mirrors. The beam is usually transmitted to the catalyst, absorbed, then reflected back to the collecting mirrors, which focus the signal to the IR detector. The extended path length of the beam through the sample is advantageous because it enables the study of low metal loading catalysts and allow for monitoring of a low concentrated chemisorbed species at the surface of the material. However, in certain cases, a specular reflectance can occur (mirror effect) and has been reported to distort the signal. Another advantage of using DRIFT cells is that it is possible to optimise the optical arrangement of the cell to increase the detection limit thus improving the focus of the reflected signal. The choice of DRIFT cells used for our catalysts seems appropriate and will be discussed further in **Chapter 3**.



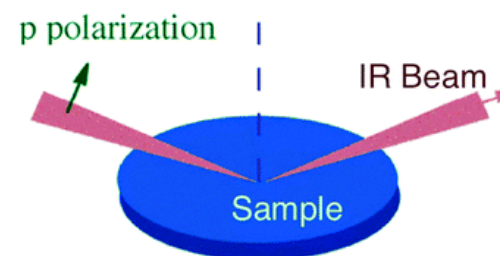
Transmission (TIR)



Diffuse-Reflectance
(DRIFTS)

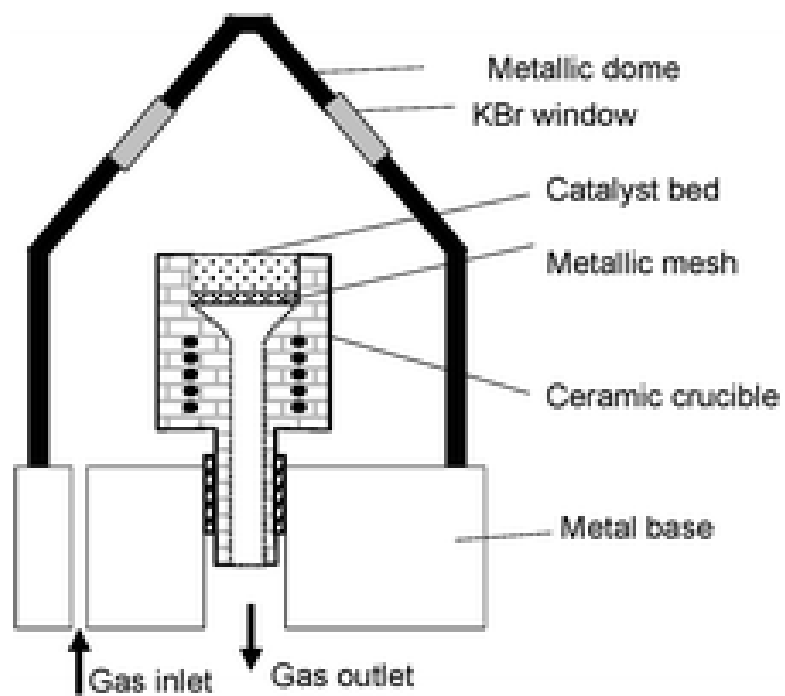


Attenuated Total Reflection
(ATR)

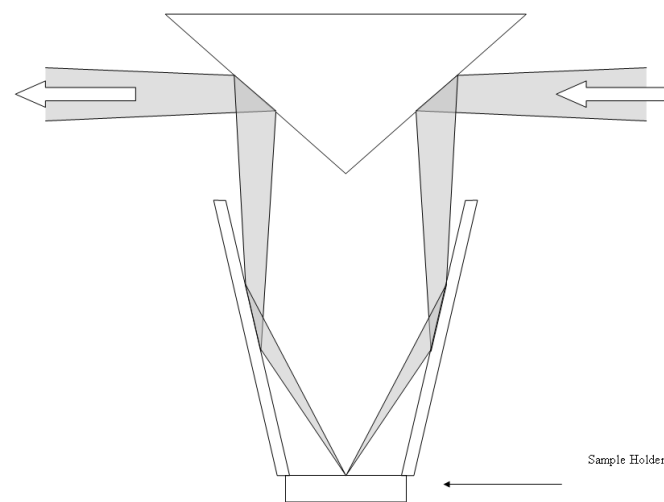


Reflection-Absorption
(RAIRS)

Figure 1.13: Different Infrared cell setups for heterogenous catalysis studies [1].



(a) Schematic representation of the Harrick Praying Mantis(R) cell.



(b) Schematic Representation of the Nexus Spectra Tech Smart collector.

Figure 1.14: DRIFT cells - (a) Harrick vs (b) Spectra Tech. The grey shading in (b) represents the path of light throughout the sampling device.

Carbon monoxide is IR active because of its strong dipole moment which results in an intense band at 2143 cm^{-1} [68, 69]. The chemisorption of CO at the surface of metal particles was first reported by Eischens in 1958 and opened a new era in understanding the behaviour of such particles. He reported that the different bands observed described two types of chemisorption. Above 2000 cm^{-1} , the CO is linearly chemisorbed to the metal surface, whereas below 2000 cm^{-1} , the CO is found to be chemisorbed to 2 or 3 Pd atoms. These assumptions were based on previous calibrations carried out on $\text{Fe}_2(\text{CO})_9$ complexes that matched the wavenumbers observed at the surface of metal such as Ni, Cu, Pd, Pt [70].

The shift in wavenumber between the gas and chemisorbed CO can be better explained using the Blyholder model [71]. It describes the adsorption onto a metal surface using the sigma and pi bonding concepts. First, the sigma interaction occurs due to an overlap of a filled sigma orbital of the carbon atom with an empty sigma orbital from the metal, which then triggers a transfer of an electron from the CO molecule to the metal centre. Secondly, the partially-filled d-orbital of the metal interact with the empty pi-antibonding orbital of the CO which results in pi back-donating transfer of an electron. However, the transfer of an electron towards the antibonding orbital of the CO leads to a reduction of the CO bond strength, which explains the shift observed between CO gas phase and chemisorbed CO.

This model accounts for the linearly chemisorbed CO as it considers that only one metal atom binds to the CO, nevertheless, many studies state the threefold and two-fold pattern chemisorption for wavenumbers below 2000 cm^{-1} [72, 73]. Different metal low index planes lead to different atom arrangements, thus different chemisorption patterns. It is believed that the packing in fcc (111) plane results in different chemisorbed species [74].

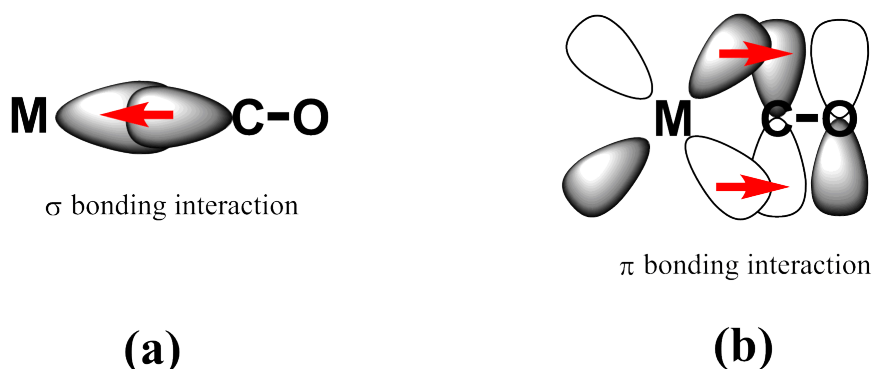


Figure 1.15: Blyholder CO-Metal bonding model representation [75]

Although CO has been used for decades to probe catalyst morphology [77, 78, 79, 72], initially, only one type of bonding on the surface could be identified, *i.e.* bridged or linear [78]. However after the pioneering work of Bradshaw and Hoffmann on single crystal

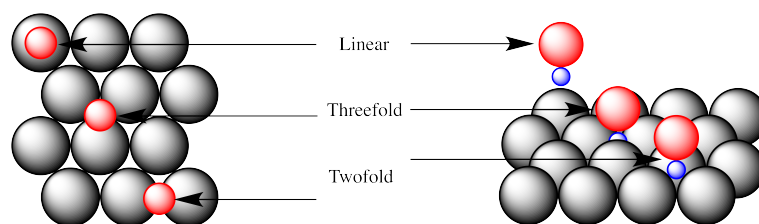


Figure 1.16: Representation of the three adsorption modes of CO over Pd(111) low index plane. The palladium is represented by the grey spheres, oxygen by the red and carbon by the blue ones [76].

surfaces in 1978 [80], a more detailed analysis of the metal crystallites could be made. Not only could the type of bonding be identified, but the particular surface planes could also be determined. Until the work of Freund et al, all the assignments for CO on palladium crystallites were relatively undisputed, however recent work has suggested that the band at $1970\text{-}1982\text{ cm}^{-1}$ was not solely due to bridge bonded CO on Pd(100), but that it could be due to bridge bonded CO on particle edges [81]. Although the evidence is well presented, care must be taken when comparing real catalysts with model catalysts as (i) the spectra are taken in a different way and (ii) they can also be taken at different temperatures and CO bonds in a different way at different temperatures on different single crystal faces [74, 82]. Thus CO chemisorption followed by infrared spectroscopy is an extremely useful probe of surface morphology, but one must be aware of the experimental conditions under which the spectra were acquired.

1.5 Aims of the project

A number of alumina-supported Pd catalyst samples have been selected to rationalise the range of pathways accesible in this transformation. Catalyst samples 2-6 were provided by Huntsman Polyurethanes. Sample 1 (5 wt% Pd/Al₂O₃) is a commercial grade catalyst that was used as a reference material in this work. These are listed below:

A new industrial trickle-bed reactor has been designed to take advantage of the high exothermicity of the nitrobenzene hydrogenation [11]. In fact, the new process is capable of generating high pressure steam as a side reaction, which can then be used to provide heat or feed turbines, which can be used to generate electricity for the industrial complex.

Historically at the plant, the nitrobenzene hydrogenation has been performed in a liquid slurry with a nickel catalyst but the re-design of the reactor has forced the use of a new catalyst. Huntsman Polyurethanes have recently supplemented an aniline production facility with a Pd/Al₂O₃ catalyst which is intended to react in a liquid-gas-solid triple phase reactor at high temperatures (240-260°C). Pd catalysts are extensively used for hy-

	Catalyst	Provenance	Code
Sample 1	5 wt % Pd/Al ₂ O ₃	Alfa Aesar	11713
Sample 2	0.3 wt % Pd/Al ₂ O ₃	Johnson Matthey	310/2
Sample 3	0.3 wt % Pd/Al ₂ O ₃	BASF	143 500
Sample 4	0.3 wt % Pd/Al ₂ O ₃ - 30% SiO ₂	Johnson Matthey	M11572
Sample 5	0.4 wt % Pd/Al ₂ O ₃ - 1% SiO ₂	Johnson Matthey	764
Sample 6	0.3 wt % Pd/Al ₂ O ₃ - 1% SiO ₂	Johnson Matthey	M12340

Table 1.1: List of catalyst used during the project

drogenation reactions [83], and it is not surprising that Hunstman is capable of operating their reactor in a high conversion and high selectivity (above 99%). However, few ppm of by-products are being generated during the reaction, and although it is common in industrial processes to produce impurities in low amounts alongside the main reaction, these by-products seem to be produced differently with the use of similar catalyst formulations as shown in **Figure 1.17**. The concepts of over-reduction and under-reduction are introduced in **Section 1.3.4**. It therefore becomes impossible to predict the outcome of the reaction and design an appropriate setup which is able to purify the product mixture.

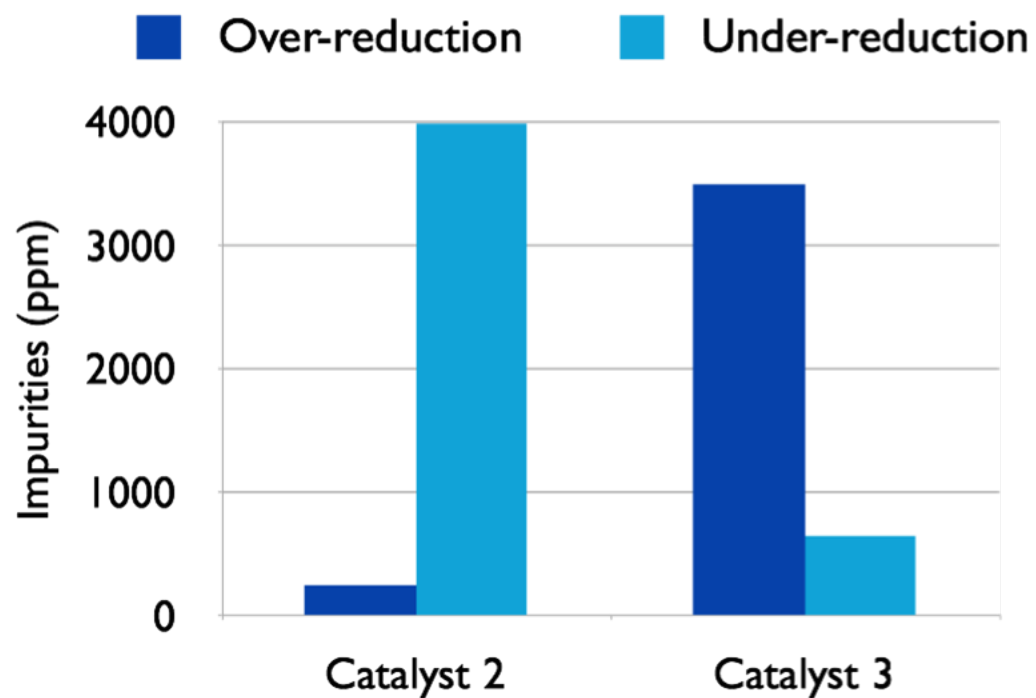


Figure 1.17: Impurities profile from Huntsman reaction testing on Sample 2 (310/2) and Sample 3 (143 500) obtained in a trickle bed reactor with 20-30 bar pressure and at a temperature of 215-260°C. Over-reduction and under-reduction were previously discussed in **Section 1.3.4** [11]

It is of high importance to study the structure/activity relationship of nitrobenzene hydrogenation over representative alumina-supported Pd catalysts in order to understand the morphological aspect of the catalyst which governs the impurity production. In developing a deep understanding of this relationship, it may be possible to optimise the preparation of the catalyst used in order to meet the industrial requirements.

The project is therefore aimed at developing the structure/activity relationships of nitrobenzene hydrogenation over Pd/alumina catalysts. In order to do so, the project will be divided into three main components:

1. Reaction testing (gas-phase in tubular-reactor) of the catalysts,
2. Physical characterisation (BET, TEM, CO isotherm and XRD),
3. Morphological study using CO chemisorption followed by IR spectroscopy,
4. Correlation of reactor performance with Pd crystallite morphology.

In summary, this project seeks to determine the product distribution in the hydrogenation of nitrobenzene to form aniline over a range of supported Pd catalysts operating at elevated temperatures (30-200°C). Two prototype catalysts (Samples 2 and 3) are studied in particular detail. Temperature-programmed infrared spectroscopy of chemisorbed CO adsorbed onto the catalyst surfaces is used to determine the morphology of the Pd crystallites. Hence the correlation of the product distribution with catalyst morphology can be determined with respect to the structure/activity relationship concerning by-product selectivity. This model is under consideration at the industrial complex as part of a process intensification initiative for the large scale manufacture of aniline as a feedstock for isocyanate synthesis.

Chapter 2

Experimental

2.1 Catalyst Characterisation Line

In order to assess Pd particle size and dispersion of the Pd/Al₂O₃ samples, a characterisation line was used to perform CO adsorption isotherms. The line was set to pulse known aliquots of pure CO at the surface of an activated Pd/alumina catalyst. The set-up is shown in **Figure 2.1**.

2.2 Reaction testing

2.2.1 Gas Phase hydrogenation reactor

Catalysts will be tested for nitrobenzene hydrogenation reaction using a tubular fixed bed reactor feed with nitrobenzene and/or aniline in a gas phase using helium as a carrier gas, as illustrated in **Figure 2.2**. The unit is composed of Swagelok 1/8 stainless tubing to avoid any oxidation or undesired side reactions, moreover those lines are trace-heated to maintain a constant vapour pressure of nitrobenzene all the way to the GLC gas sampling valve as shown here in **Figure 2.2**. The reaction-testing unit is composed of a tubular reactor, a split tube furnace, a temperature control box, two thermocouples, a bubbler (dreschel bottle, hotplate and oil bath), a helium dilution line and, finally, a gas-liquid chromatograph which characteristics will be discussed in **Section 2.2.2**.

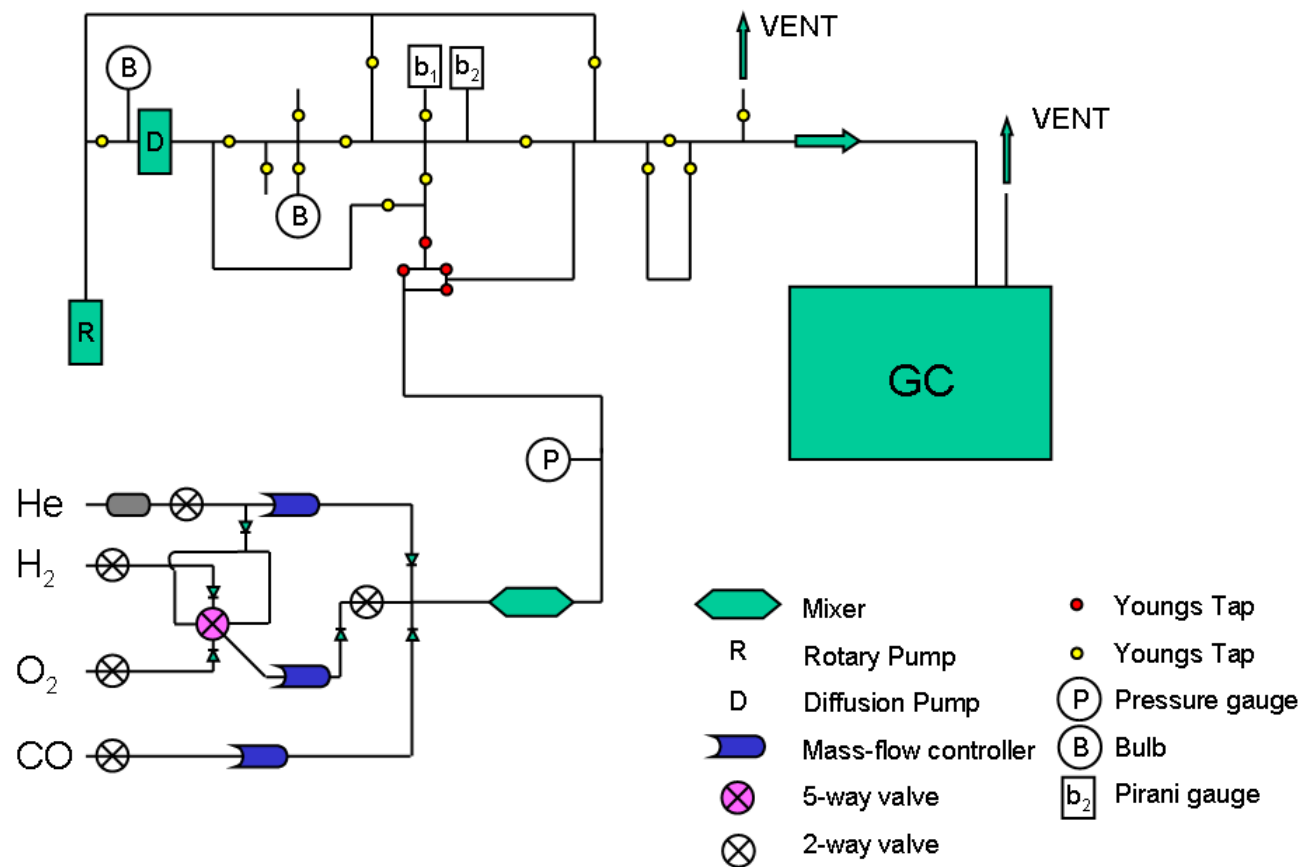


Figure 2.1: Catalyst Characterisation line schematic.

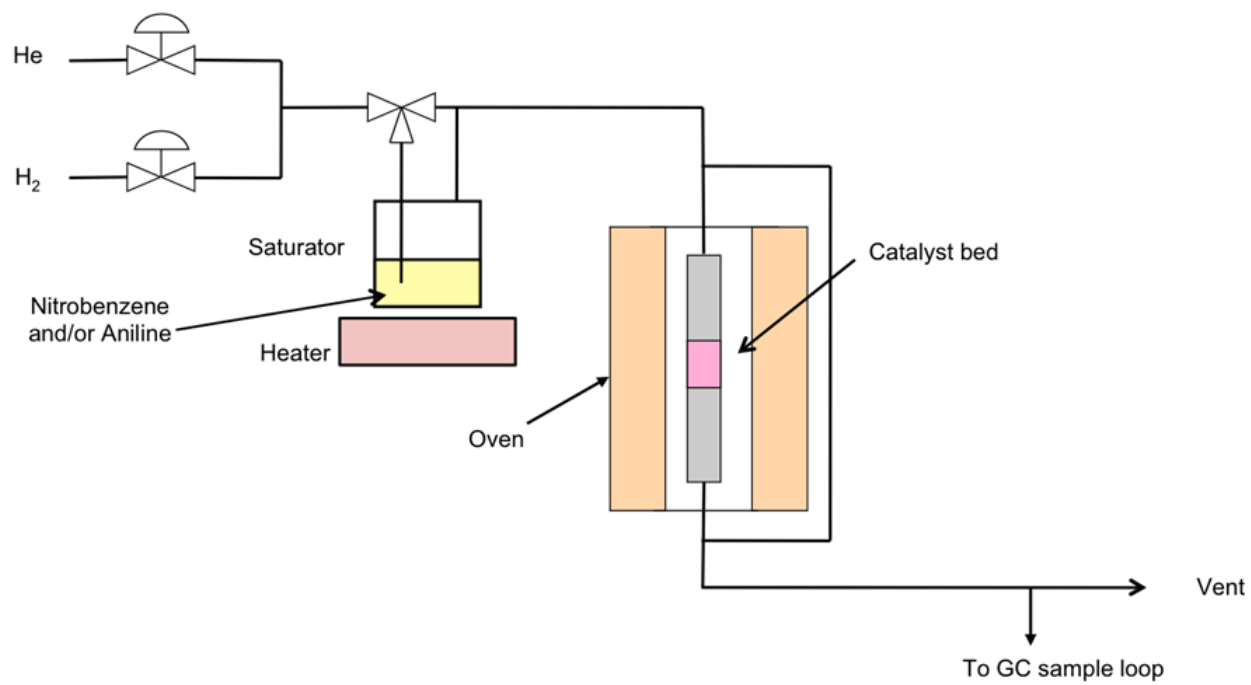


Figure 2.2: Nitrobenzene hydrogenation Reaction Unit.

The tubular reactor consisted of a 50 mm long 316-stainless steel tube, fitted with Swagelok connections at the top and bottom to fix it into place and assure correct sealing. A stainless steel mesh disc is positioned nearly at the middle of the tubular reactor to position the catalyst at the centre of the reactor. The catalyst is placed into the tube using a bed of carborundum (silicon carbide) both above and below the catalyst sample to position the catalyst bed at the middle of the furnace and close to the thermocouple. This thermocouple enables controlling and monitoring the reaction temperature profile using a control box (DMG controls). The single zone split tube furnace is from LCP Elements Ltd. With an internal diameter of 25 mm and a length of 418 mm to encase the entire length of the tube, the diameter permits use of 1/4 and 1/2 inch tubing as reactor. Tests concerning which reactor is most efficient for performing this reaction will be established. During operation, quartz wool (Fisher Scientific) is placed at the top and bottom of the furnace cavity to prevent heat loss and ensure effective heat distribution throughout the whole reactor. It is noteworthy to say that carborundum is really important to improve heat exchange in the reactor and avoid any condensation before the catalytic bed. Brooks mass flow controllers (5850 TR series) are used to supply gas through the reactor. The reactor is also equipped with a by-pass, which allows analysis of the feed prior any experiment without being in contact with the catalyst. Baseline values (A_0) were obtained flowing the mixture He/H₂/nitrobenzene through this by-pass. The oven is capable of heating from room temperature to 1200°C, and is controlled by a PID controller (WEST 6400).

2.2.2 Gas Liquid Chromatography

Identification of the reaction products were obtained by gas liquid chromatography (GLC) by comparison of their retention time against known standards. Analysis will be performed considering the same apparatus as used by Huntsman Polyurethanes. An Agilent GC 6850 series II fitted with a flame ionization detector (FID), which was controlled by chemstation software provided by Agilent. The column used for analysis is Durabond DB-17 capillary column (30 m, 0.250 mm, 0.5 μ m). A calibration of the entire reaction product involved in nitrobenzene hydrogenation was performed to ensure that any retention peak would have a response factor.

2.3 Calibration of Plug-flow reactor system

The gas/liquid feed was calibrated before reaction was carried out. Mass flow controllers connected to an analogue controlbox (Brooks model 5878) were calibrated using either hydrogen or helium gas flowing through a burette equipped with a soapy solution. Calibration of the GC was performed injecting manually known standard solutions diluted in

cyclohexane or acetone depending on the product solubility in those solvents.

The bubbler temperature was set at 45°C for the reaction. By using Antoine’s law **Equation 2.1** below, we were able to assess the concentration expected and prepare the solutions accordingly.

$$\log(P_{(bar)}) = A - \frac{B}{C + T_{(K)}} \quad (2.1)$$

The three constants A, B and C have been determined experimentally [84]. Values for nitrobenzene and aniline are tabulated in **Table 2.1** below.

	Nitrobenzene	Aniline
A	4.21553	4.34541
B	1727.592	1661.858
C	-73.438	-74.048

Table 2.1: Antoine’s coefficients for nitrobenzene and aniline [84].

Using **Equation 2.1** and the values in **table 2.1**, we obtain the plot observed here, **figure 2.3**.

The calibration plots for the different for the reactant and products observed during the reaction can be seen in **Appendix A**.

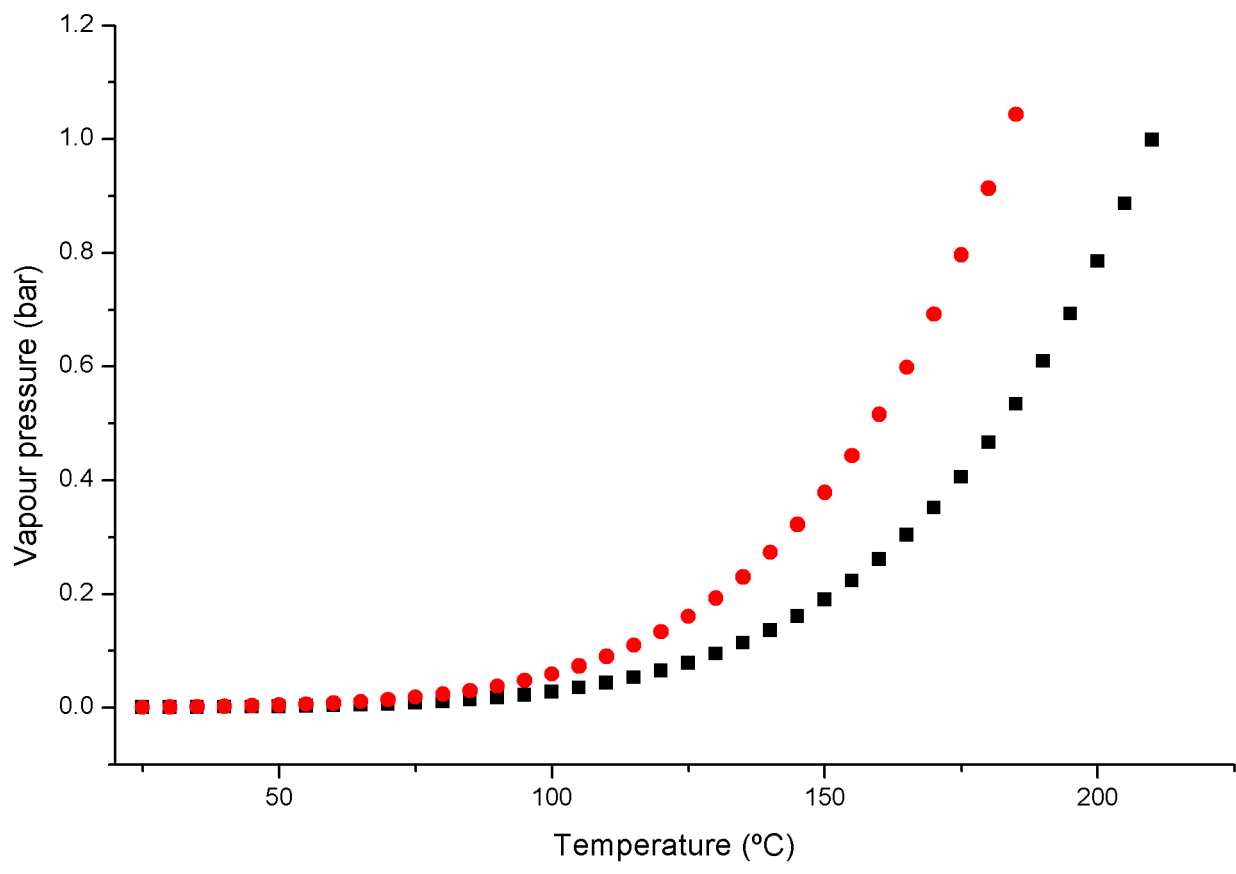


Figure 2.3: Vapour Pressure of aniline in red and Nitrobenzene in black calculated from Antoine's law.

2.4 Characterisation

2.4.1 Infrared Spectroscopy

The majority of the infrared experiments were performed using a Nicolet Nexus FTIR spectrometer (model number: 470/670/870) fitted with a high D* MCT detector. Experiments were carried out in absorbance mode, using a SpectraTech Smart diffuse reflectance cell and environmental chamber, using a typical sample size of ca. 50 mg. The optical set-up of the cell is shown in **Figure 1.14b**. The sample cell is connected to a gas manifold that provides control of flow gases into the infrared cell and allows aliquots of gas molecules to be passed over the catalyst. The catalyst sample stands in a ceramic cup fitted with a temperature controller in order to set up variable temperature experiments up to 1173 K. The catalyst were activated *in-situ* under a He/H₂ flow (35/15 ml/min). Temperature was first maintained at 110°C for 30 min, then at 200°C for 30 min before hydrogen was switched off. Hydrogen was allowed to desorb for 30 min at 200°C before cooling down to 25°C. A background spectrum was recorded post-activation at 25°C. Pure CO (CK gas 99%) was then sampled and a few Torr were passed through the IR cell [85]. The cell was then purged using helium for at least 10 min, which corresponds to the period needed to expel of any non-chemisorbed CO from the chamber. Spectra were recorded (512 scans, resolution 4 cm⁻¹) at 25°C and took approximately 10 minutes. All spectra were background subtracted, which means that the sample spectra is subtracted with the post-activation spectra recorded before CO was introduced. No other signal treatment was performed. For desorption experiments, the cell containing the catalyst was heated under He flow. Each temperature was maintained for 10 minutes before cooling down to room temperature where a spectrum was recorded.

The same experiment was performed using a different spectrometer (Bruker Vertex 70 FTIR) and two other infrared cells.

The Bruker spectrometer was also fitted with a high D*MCT detector. Of the two cells used with this device, one was a IR transmission cell (Harrick Scientific), which enabled measurements up to 450°C and one a DRIFT cell (Harrick, Praying Mantis reaction chamber). The optical setup for the transmission cell is straightforward; the catalyst is pressed into a disc of 13 mm diameter, which represents a mass of around 20 mg using a press. The thin wafer is then placed at the centre of the transmission, which is equipped with two KBr windows. Hence the IR beam goes through the wafer at a 90° angle and is transmitted directly to the detector. A picture of the cell is shown in **Figure 2.4**.

The Harrick DRIFT cell used on the Vertex system differs from the Spectra tech cell presented above. Although the sample is contained in a ceramic cup containing approximately 50 mg as well, the optic is rather different as shown in **Figures 2.5 and 1.14b**. In the Praying Mantis setup, the IR beam is reflected on three mirrors before hitting the



Figure 2.4: Picture of the Harrick High Temperature transmission IR cell

sample surface and three times again before being analysed by the detector - as seen in **Figure 2.5**. The Spectra Tech DRIFT cell allows a much simpler beam pathway as seen in **Figure 1.14b**; indeed, the beam is reflected once before the sample and once after. Added to that, the IR chamber cell of the Spectra Tech cell is much more confined than the Harrick DRIFT cell as seen in **Figures 1.14a and 1.14b**; the resulting differences observed during the CO temperature-programmed infrared carried out on these three cells will be discussed in **Chapters 3 and 6**.

2.4.2 Temperature-Programmed Desorption

Temperature-Programmed Desorption (TPD) experiments were performed using 0.5g of catalyst contained in a quartz reactor (500 mm length, 1/4 inch diameter) packed with quartz wool. The reactor was located in a single zone split tube furnace (LPC Elements, DMG Controls). A mass spectrometer (MKS microvision plus) was used to analyse the outlet gases through pulses and desorption of CO via a capillary line and metal-sintered precision leak. The catalyst samples were activated using a 35:15 ml/min mixture of He:H₂ and the temperature was allowed to ramp by 3°C/min from RT to 200°C. After 30 min at 200°C, H₂ was shut off and the temperature was kept for another 60 min before cooling down to room temperature. Saturation of samples with CO were performed via

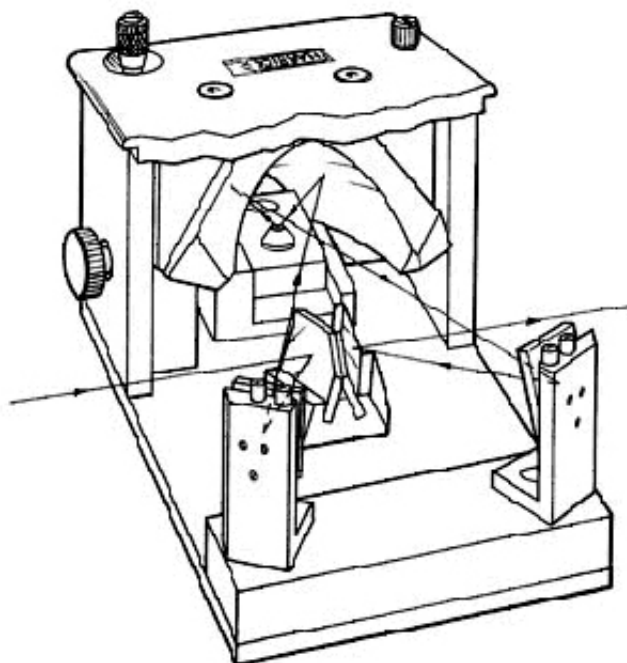


Figure 2.5: Picture of the Harrick Praying Mantis IR setup

1-2 torr CO pulses ($V = 6.8\text{ml}$, 1.05 torr, 3.43×10^{-7} mol). Desorption was then carried out using the a temperature ramp of $15^\circ\text{C}/\text{min}$ [86].

2.4.3 X-ray Powder Diffraction

Diffractograms were recorded with a Siemens D5000 diffractometer using CuK_α (1.5418 Å) radiation in Bragg-Brentano geometry in the range 2θ 5-80°. The source has an accelerating voltage of 40 kV with an intensity of 40 mA. XRD patterns were monitored by a scan rate of $0.02^\circ/\text{s}$.

2.4.4 Transmission Electron Microscopy

More and more, literature related to characterisation of catalysts show that use of TEM is really a breakthrough in correlating structure to some assumption like crystal face orientation, dispersion, metal particle size and element mapping of the surface. In general, the detection and resolution of the metal particles is possible provided that there is sufficient contrast between metal and support. This contrast depends on how electrons are scattered by each elements and materials, thereby; resolution can be improved using proper sample thickness and knowing previously which elements is analysed.

The microstructure of the catalyst samples were studied by a Tecnai T20 microscope, with an accelerating voltage of 220 keV, fitted with a Gagan image filter. TEM samples of Pd/alumina catalysts are prepared first by grounding in a mortar and pestle before being dispersed in methanol. This suspension was then dropped on a micron scale carbon

grid (300 μm mesh grid, Agar scientific) and dried to obtain a sample thinner than 100 microns capable of fitting in the TEM for further analysis.

2.4.5 Atomic Absorption Spectroscopy

Standard Pd (mg.L^{-1})	Absorbance
0	0
5	0.240
10	0.383
15	0.465

Table 2.2: Absorbance recorded for different Pd standard solution analysed.

In catalysis, Atomic Absorption Spectrometry (AAS) is often used post-preparation to ensure the loading of the metal supported on a given catalyst. The catalyst is dissolved in a strong acid solution, then atomized. Nowadays, samples are atomized using flames or graphite tubes. Next, a lamp that emits the spectrum of the analyte is shone through and absorbance is recorded via a detector [87]. Palladium loading was measured by AAS using a Perkin Elmer Analyst 100 instrument. The wavelength was 244.8 nm with background correction. Standard solutions were prepared by dilution from a 1000 mg/L (Sigma Aldrich) Pd/hydrochloric acid commercial stock solution. An accurate weight of approximately 0.1 g of material was carefully transferred to a 50 mL beaker. 5 mL of aqua regia was added and a watch glass placed on top. The beaker was placed on a hotplate and boiled for approximately 30 minutes. The watch glass was removed to allow the fumes to evaporate and the beaker was allowed to cool before 5 mL of water was added to reduce the acid strength. The solution was then filtered through a hardened filter paper into a 25 mL volumetric flask with washing and made to the mark. A blank was carried through this procedure as well. Calibration standard solutions were analysed and tabulated here in **Table 2.2**.

2.4.6 Total Surface Area measurements (BET)

Activity and selectivity of catalysts are often linked with pore size distribution and surface area. There are different methods used to measure surface area but the most widely used is the isothermal adsorption of nitrogen. Here, the Brunauer, Emmett and Teller (BET) method was used to measure the total surface area of the catalysts on a Micromeritics ASAP 2400 gas adsorption analyser using a static barometric method. 0.5 g of the “as-received” samples were placed into a glass tube and outgassed at 413 K over-night in flowing nitrogen. The nitrogen absorption experiments were carried out at 77 K. The

entire surface of the catalyst, including the metal and the porous support material were quantified using the nitrogen adsorption and desorption isotherm [88].

2.4.7 CO Adsorption Isotherms

The process of chemisorption can be used in a quantitative manner to calculate the total amount of metal that is available for reaction, assuming that a monolayer of the adsorbate is formed. This is known as the dispersion of the catalyst and is normally expressed as a percentage of the total metal atoms. In the case of a supported metal catalyst, the dispersion is the total number of surface metal atoms; the equation for which is shown below.

When using supported metal catalysts, there are several molecules selected to use for adsorbates. These include carbon monoxide, oxygen, hydrogen and nitric oxide. In all these cases, it is important to know:

- What is the metal to adsorbate stoichiometry?
- Does the molecule dissociatively adsorb?
- Does the support play any part in the adsorption, *i.e.* is there spillover, or does the support play an active role in adsorption?

It is believed that carbon monoxide chemisorbs onto the surface of palladium with little or no dissociation so this makes it an ideal molecule to use for chemisorption measurements. Pulsed chemisorption studies were performed by placing a known mass of catalyst (ca. 250mg) into the reactor and reducing it in a flowing 40% H₂/He mix for 1 hour at 200°C after a temperature ramp of 3°C/min up to 200°C. Pulses of a known volume of CO were passed over the catalyst using helium as a carrier gas. The point of saturation was monitored using a thermal conductivity detector (Thermo Finnigan Ultra GC). Saturation point was determined when three peaks of equal area were observed on the integrator. Since the volume and pressure of gas passed over were known, it was possible to calculate the dispersion of the catalyst assuming a 1:2 ratio of CO:Pd [89]. The dispersion of a catalyst can be used to estimate particle size, provided certain assumptions are made, namely that the particles are all of the same size and are spherical. From these assumptions, dispersion may be expressed as [85]:

$$D = \frac{6A}{\rho S_a N_a d} \times 100 \quad (2.2)$$

$$d = \frac{109}{D} \quad (2.3)$$

Where:

D = Dispersion (%)

A = Atomic weight (106.92 g.mol⁻¹)

ρ = Density of metal (12.02x10⁻²¹ g.nm⁻³)

S_a = Average surface area occupied by one active atom (0.0806 nm²)

N_a = Avogadro number

d = Average particle diameter (nm)

2.4.8 Conversion and Selectivity Calculations

The conversion and selectivity data that will be presented in this thesis have been calculated using **Equations 2.4 and 2.5** [90]. The values were taken from gas chromatography as peak area, then converted in number of moles using the calibration reported in **Section 2.2.2** to account for the difference of the response factor of the different molecules monitored by a flame ionisation detector as explained in **Section 2.2.2**.

$$\text{Conversion}_{\text{nitrobenzene}} (\%) = \frac{n_{\text{nitrobenzene}}(t)}{n_{\text{nitrobenzene}}(0)} \times 100 \quad (2.4)$$

$$\text{Selectivity}_{\text{aniline}} (\%) = \frac{n_{\text{aniline}}(t)}{n_{\text{aniline}} - n_{\text{nitrobenzene}}(0)} \times 100 \quad (2.5)$$

Chapter 3

Nitrobenzene hydrogenation on a commercial 5 wt % Pd/Al₂O₃ catalyst - Sample 1.

A commercially available 5 wt % Pd/Al₂O₃ (Alfa Aesar 11713) was chosen to test the feasibility of the nitrobenzene hydrogenation reaction and the different characterisation techniques before studying the industrial grade 0.3 wt % Pd/Al₂O₃ (Samples 2 and 3). The as-received catalyst is a dark-grey powder consisting of palladium deposited on γ -alumina which was reduced post-preparation. While many publications state different catalysts being highly active and selective for the nitrobenzene hydrogenation to aniline, few display the selectivity profile and the inner characteristics of the catalysts used. This section aims to introduce the concept of the loss of selectivity in the nitrobenzene hydrogenation in parallel with the morphological study of the active sites present at the surface of a standard Pd/Al₂O₃ catalyst.

3.1 Gas phase nitrobenzene hydrogenation

Nitrobenzene hydrogenation was carried out as specified in **Section 2.2**. After reduction, the temperature was set at 60°C and allowed to react overnight in order to reach a permanent reaction state. Temperature was then sequentially increased by an increment of 20°C up to a maximum temperature of 180°C. The results for the nitrobenzene hydrogenation performed on the continuous flow plug-reactor using the standard 5 wt % Pd/Al₂O₃ are shown in **Figures 3.1 and 3.2**. The reaction feed was composed of Nitrobenzene/hydrogen/helium (NB 2.03 x 10⁻⁶ mol/min: H₂ 7.83E-04 mol/min - H₂:NB = 385 : 1), with a large excess of hydrogen. The large excess was selected so that the hydrogenation pathways at the selected reaction conditions were accessible. A reduced hydrogen supply could also emphasize deactivation pathways which are not a major focus

of this study.

Firstly, the catalyst shows a very high (>99%) nitrobenzene conversion all the way through the range of temperature. This can easily be explained by the hydrogen being introduced in large excess, a low vapour pressure of nitrobenzene and a rather high palladium loading. Secondly, the selectivity towards aniline decreases with increasing temperature, with 90% at 60°C and only 20% at 180°C. The loss of selectivity observed is steady and seen to be caused by formation of by-products such as cyclohexylaniline ($C_6H_{11}NH_2$,CHA), cyclohexanol ($C_6H_{11}OH$,CHOL), cyclohexanone ($C_6H_{10}O$,CHO), dicyclohexylamine ($C_{12}H_{22}NH$,DICHA) and N-cyclohexylaniline ($C_{12}H_{16}NH$,CHAN). At 60°C, the loss of selectivity is due to the formation of the DICHA and CHAN compounds derived from the further hydrogenation of the aniline produced [31, 32]. As the temperature increases from 80°C to 120°C, DICHA is obtained in larger quantities with CHAN staying constant throughout the change of temperature. Another compound is detected between 80 and 120°C, cyclohexylaniline (CHA), as a result of the ring hydrogenation of aniline [91, 33, 92]. This last compound stands as an intermediate between aniline, N-cyclohexylaniline and dicyclohexylamine. While the CHAN intermediate remains constant with increasing temperature, the number of moles of the CHA intermediate grows substantially. Between 140°C and 180°C, by-products follow the same trend, where an increase in DICHA and CHA is observed, while CHAN slightly decreases. Additionally, one should note that the amount of DICHA and CHA compared to CHAN is quite high. This is indicative of the difference in rate of reaction from aniline to cyclohexylaniline, N-cyclohexylaniline and dicyclohexylamine. Finally, cyclohexanone is recorded in small amounts from 140°C and is seen to slightly increase with temperature. Surprisingly, only a few publications on the catalytic nitrobenzene hydrogenation mention the aniline derived by-products caused by a further hydrogenation of the ring to form CHA, CHAN and DICHA [93, 94]. One study in the liquid phase does however discuss how the pH gives rise to impurities as part of the catalytic nitrobenzene hydrogenation [33].

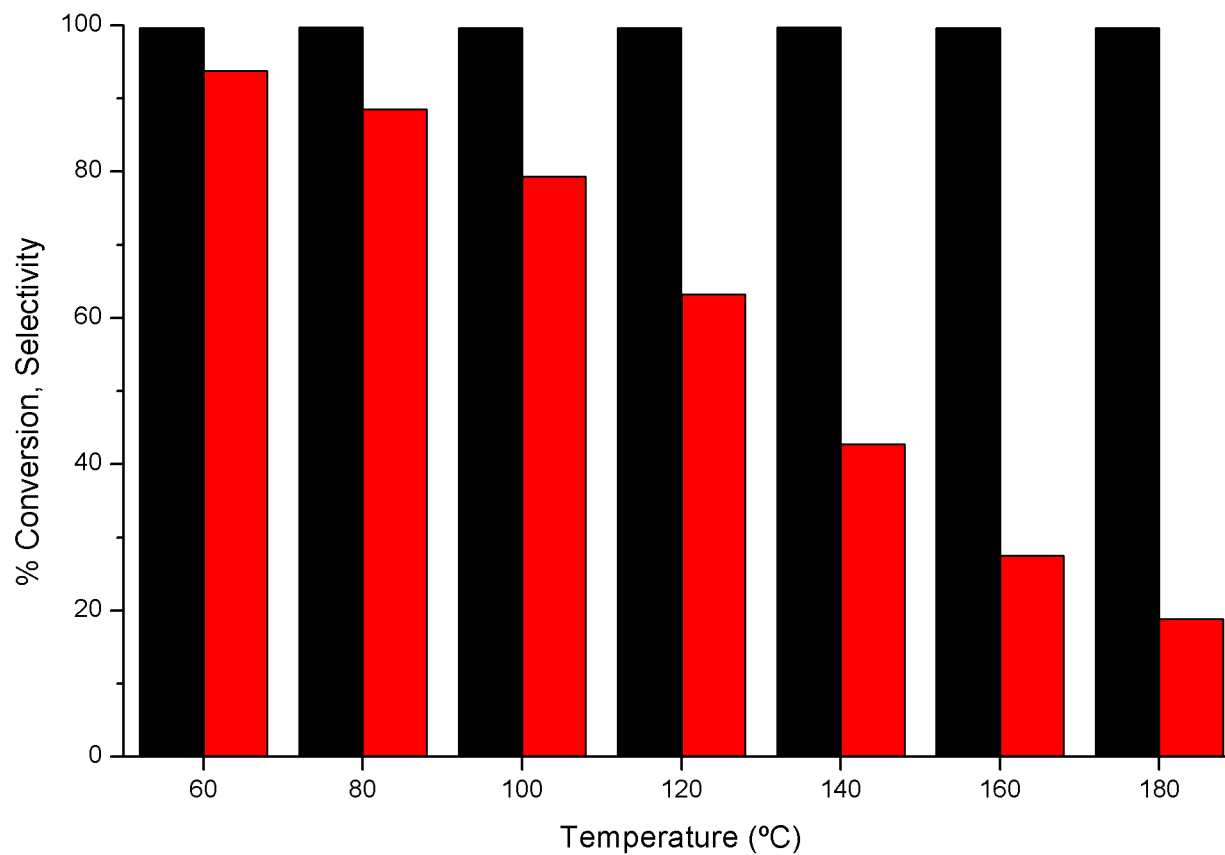


Figure 3.1: Nitrobenzene conversion in black and aniline selectivity in red reported from the reaction of 20 mg of catalyst 1 under feed of nitrobenzene/hydrogen/helium (NB 2.03×10^{-6} mol/min: H_2 $7.83E-04$ mol/min - H_2 :NB = 385 : 1, NB(s^{-1}) : Pd(s) = 1 : 63)

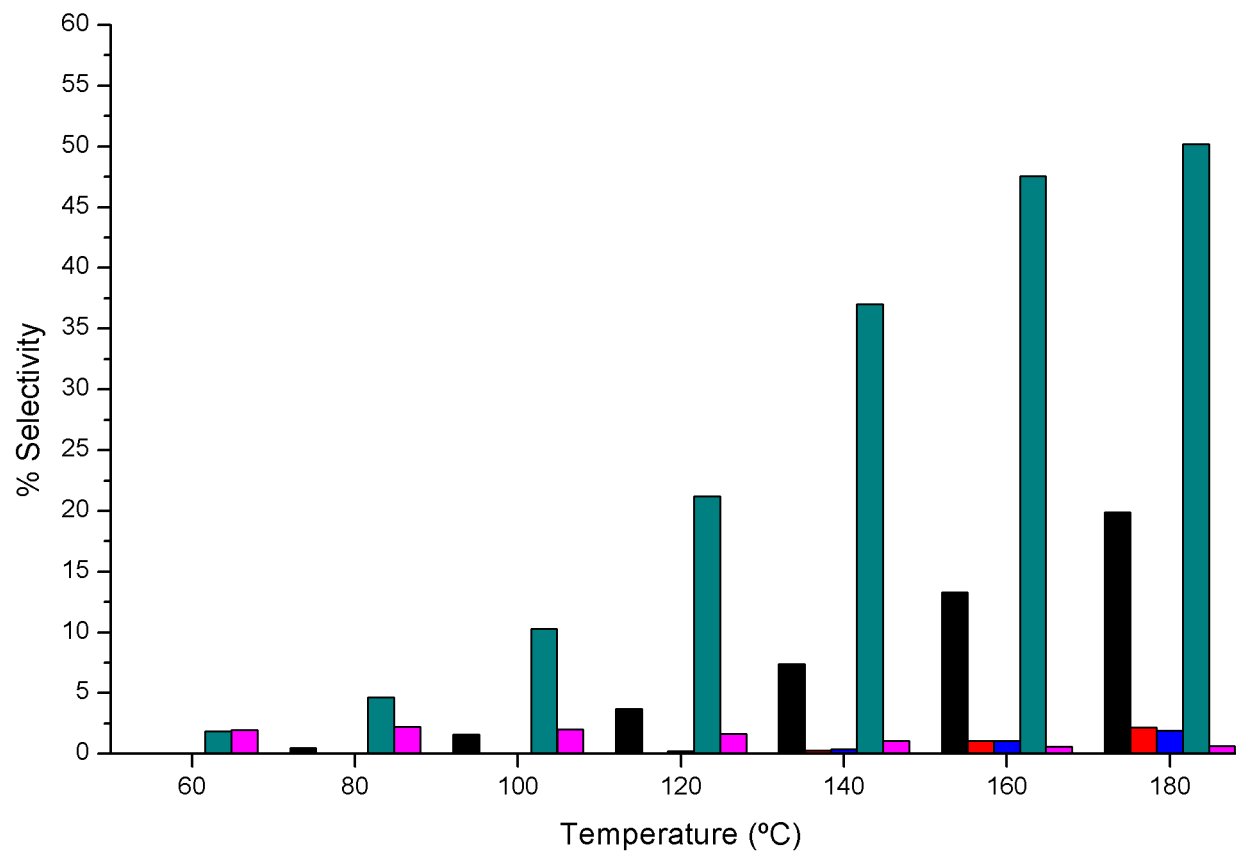
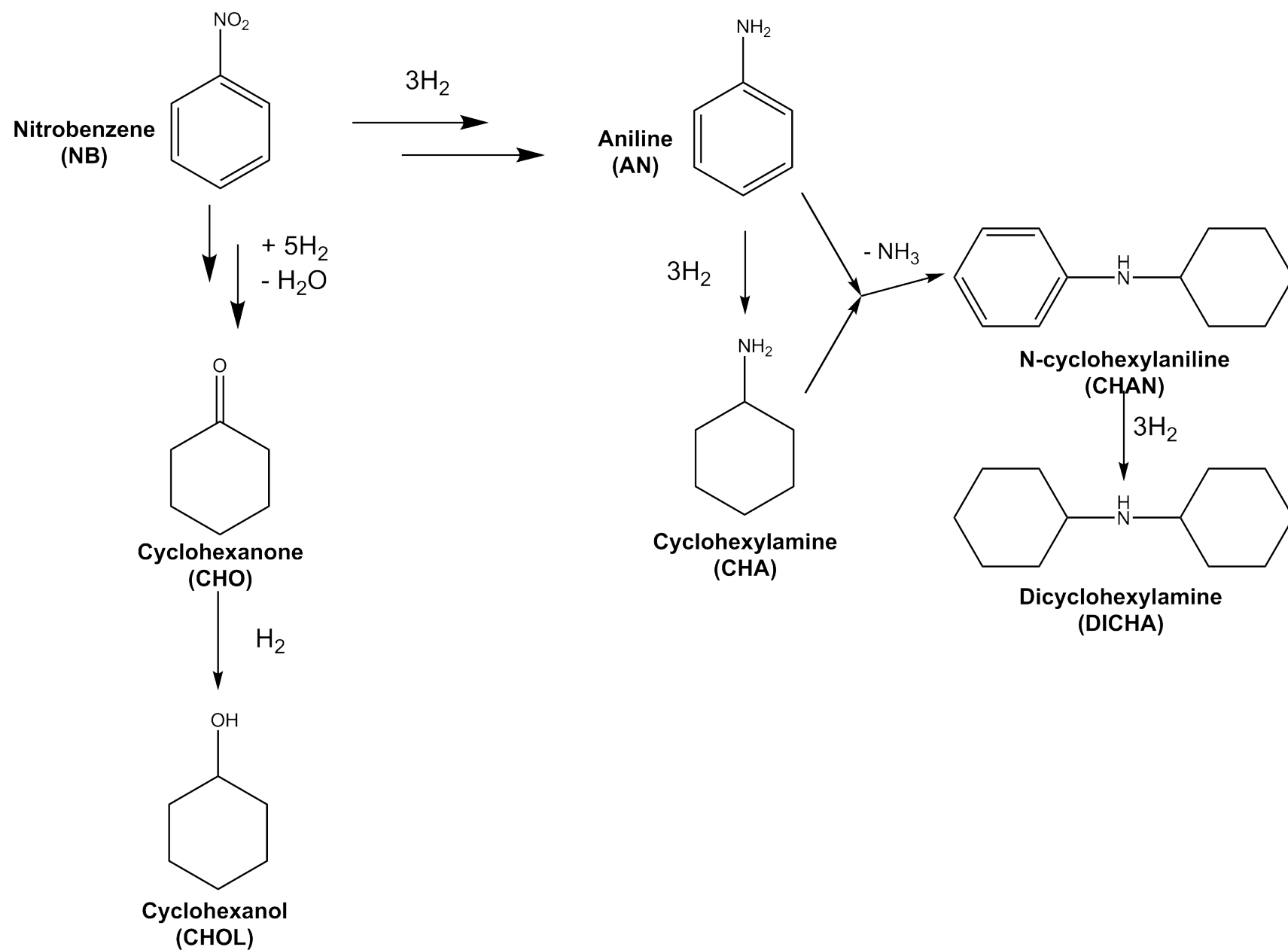


Figure 3.2: Impurities selectivity reported from the reaction of 20 mg of catalyst 1 under feed of nitrobenzene/hydrogen/helium (NB 2.03×10^{-6} mol/min: H_2 $7.83E-04$ mol/min - H_2 :NB = 385 : 1, NB(s^{-1}) : Pd(s) = 1 : 63). Dicyclohexylamine in green, N-cyclohexylaniline in purple, Cyclohexanone in blue, Cyclohexanol in red and Cyclohexylamine in black.



Scheme 3.1: Reaction scheme as observed using the 5 wt % Pd/Al₂O₃ catalyst in nitrobenzene hydrogenation.

3.2 XRD, BET, CO chemisorptions and AAS

X-ray powder diffraction was carried out to determine what type of alumina was present as a support. **Figure 3.3** shows the diffractogram of the as-received 5 wt % Pd/Al₂O₃ catalyst before reaction. The pattern observed in **Figure 3.3** is indicative of a gamma-alumina. The BET experiment indicates that the surface area is 140 ± 10 m²/g. As detailed in **Section 2.4.7**, CO adsorption isotherms was also performed on the catalyst to determine the dispersion of the palladium and to estimate the particle size at the surface of the catalyst. The catalyst was analysed using Atomic Absorption Spectroscopy to verify the amount of Palladium present on the catalyst as described in **Section 2.4.5**. It was found that there is 4.3 ± 0.3 wt % of palladium present in the catalyst.

CO uptake (mol CO / g catalyst)	Dispersion (%)	Particle size (nm)	BET (m ² .g ⁻¹)	AAS g _{Pd} / g _{catalyst}
5.0×10^{-5}	21.3	5.1	140	4.3 ± 0.3
5.1×10^{-5}	21.7	5.0		

Table 3.1: Table of Dispersions for CO Pulsed Chemisorptions obtained on the 5 wt % Pd/Al₂O₃ catalyst (Sample 1).

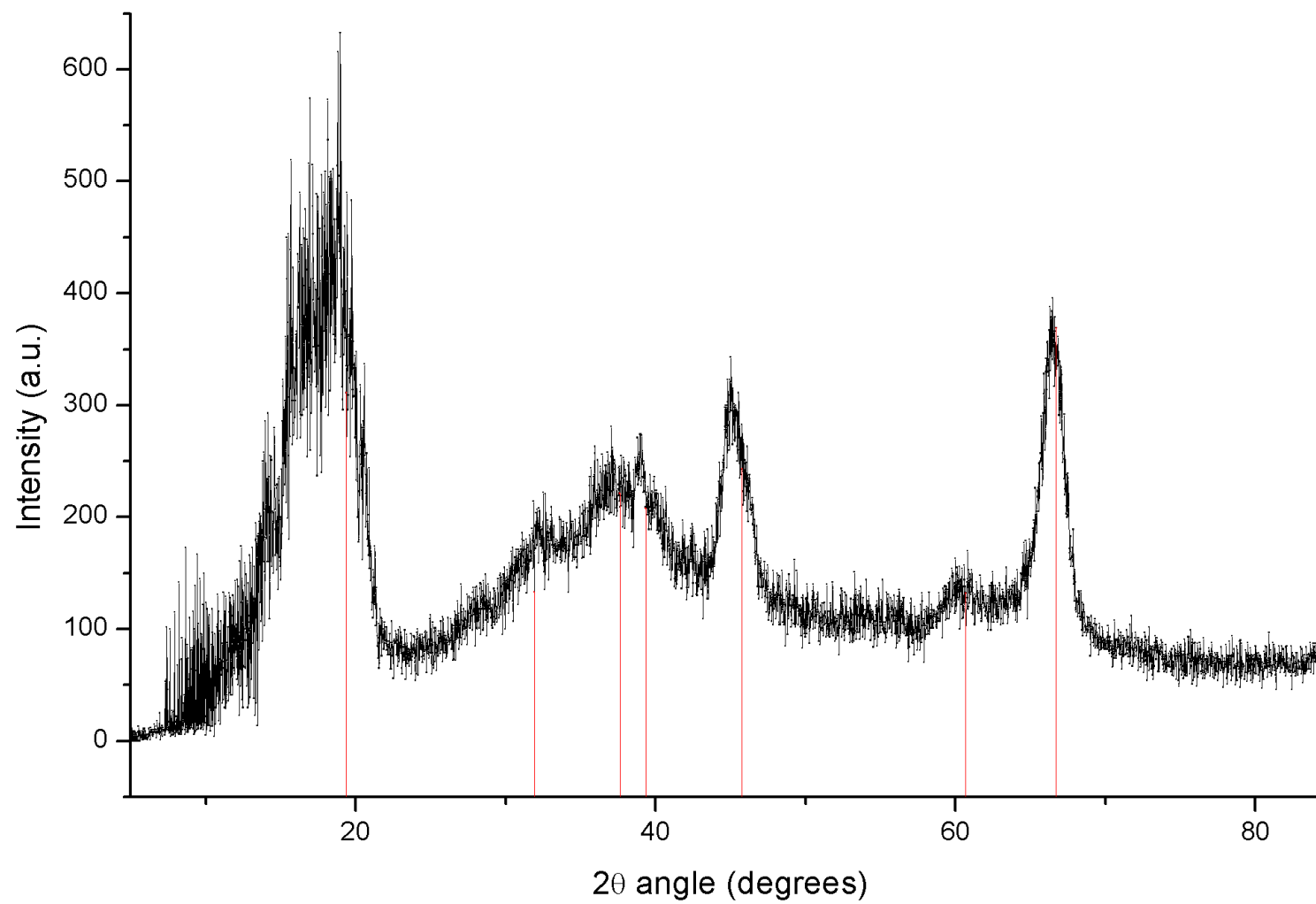


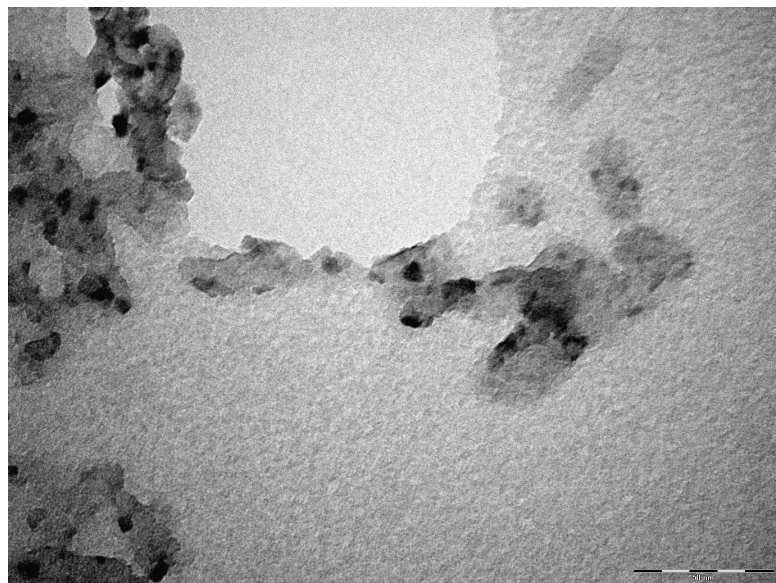
Figure 3.3: XRD pattern of the black powder 5 wt % Pd/Al₂O₃ catalyst. Red drop lines represent the γ -alumina reflections [95].

Gamma-alumina		
2 Θ Angle (degrees)	d spacing (\AA)	h k l
37.618	2.38918	311
39.358	2.28746	222
45.765	1.981	400
60.679	1.52497	511
66.721	1.40078	440

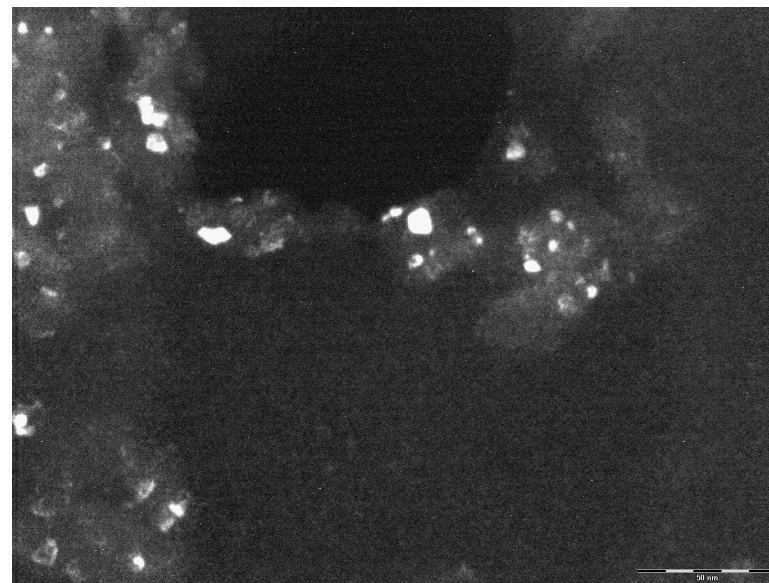
Table 3.2: XRD assignments for the 5 wt % Pd/alumina catalyst based on the gamma-alumina main reflections [95].

3.3 Transmission Electron Microscopy

The microstructure of the 5 wt % Pd/Al₂O₃ catalyst was analysed using Transmission Electron Microscopy as detailed in **Section 2.4.4**. The TEM images presented here were all recorded on the as-received catalyst before any activation and/or reaction. As discussed in the section above, we expected the majority of the catalyst to be gamma-alumina based with well dispersed palladium particles throughout the surface measuring around at 5 nm.



(a) Bright Field Imaging



(b) Dark Field Imaging

Figure 3.4: Dark Field - Bright Field imaging on the 5 wt % Pd/Al₂O₃ catalyst. The metal component is indicated as black particles in (a) but white particles in (b). Bar scale represents 50 nm.

Figure 3.4a shows a broad view of the catalyst surface. At this magnification, we can observe a large alumina cluster on which we can distinguish multiple small black dots. This area was analysed using the dark field / bright field imaging technique to ensure that the black dots were correlated to palladium particles. It is a simple technique that consists of tilting the beam so that a different diffraction of the electron beam through the sample can be obtained. It is widely understood that in the bright field imaging the contrast is obtained via absorbance of the light and the dark field is obtained from light scattered. Alumina and palladium having a different electronic structure so this simple tilt is often enough to distinguish them from each other. **Figure 3.5** displays a large black particle exhibiting a high crystalline pattern. It was possible to measure the interplanar spacing also called d-spacing which is then used to determine the low index plane. Given that palladium crystal is Face Cubic Centered, the interplanar spacing (d) is expressed as follows:

$$d_{hkl} = \frac{a}{\sqrt{h^2 + k^2 + l^2}} \quad (3.1)$$

$$d_{hkl} = \frac{a}{\sqrt{h^2 + k^2 + l^2 \left(\frac{a^2}{c^2}\right)}} \quad (3.2)$$

Pd ⁰ - FCC	
a = b = c = 3.880 Å	α = β = γ = 90°
d(100) = 3.880 Å	
d(111) = 2.250 Å	
PdO – Tetragonal	
a = b = 3.043 Å	c = 5.336 Å α = β = γ = 90°
d(100) = 3.043 Å	
d(001) = 2.309 Å	
d(111) = 5.753 Å	

Table 3.3: Interspacing distances for the Pd metal and Pd oxide [96].

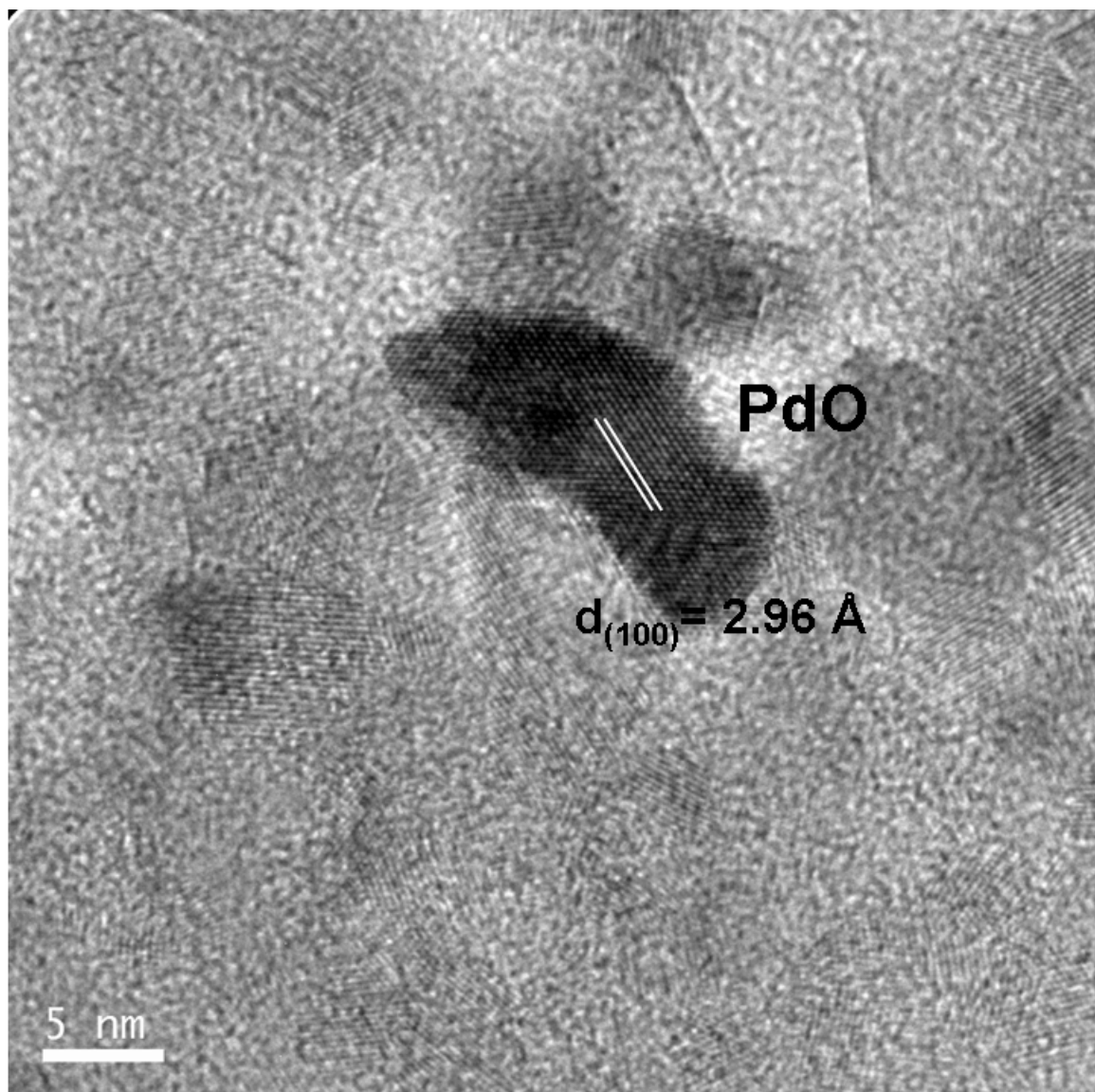


Figure 3.5: Transmission Electron Microscopy of the 5% Pd/Al₂O₃ (Sample 1) before activation. The white scale bar represents 5nm.

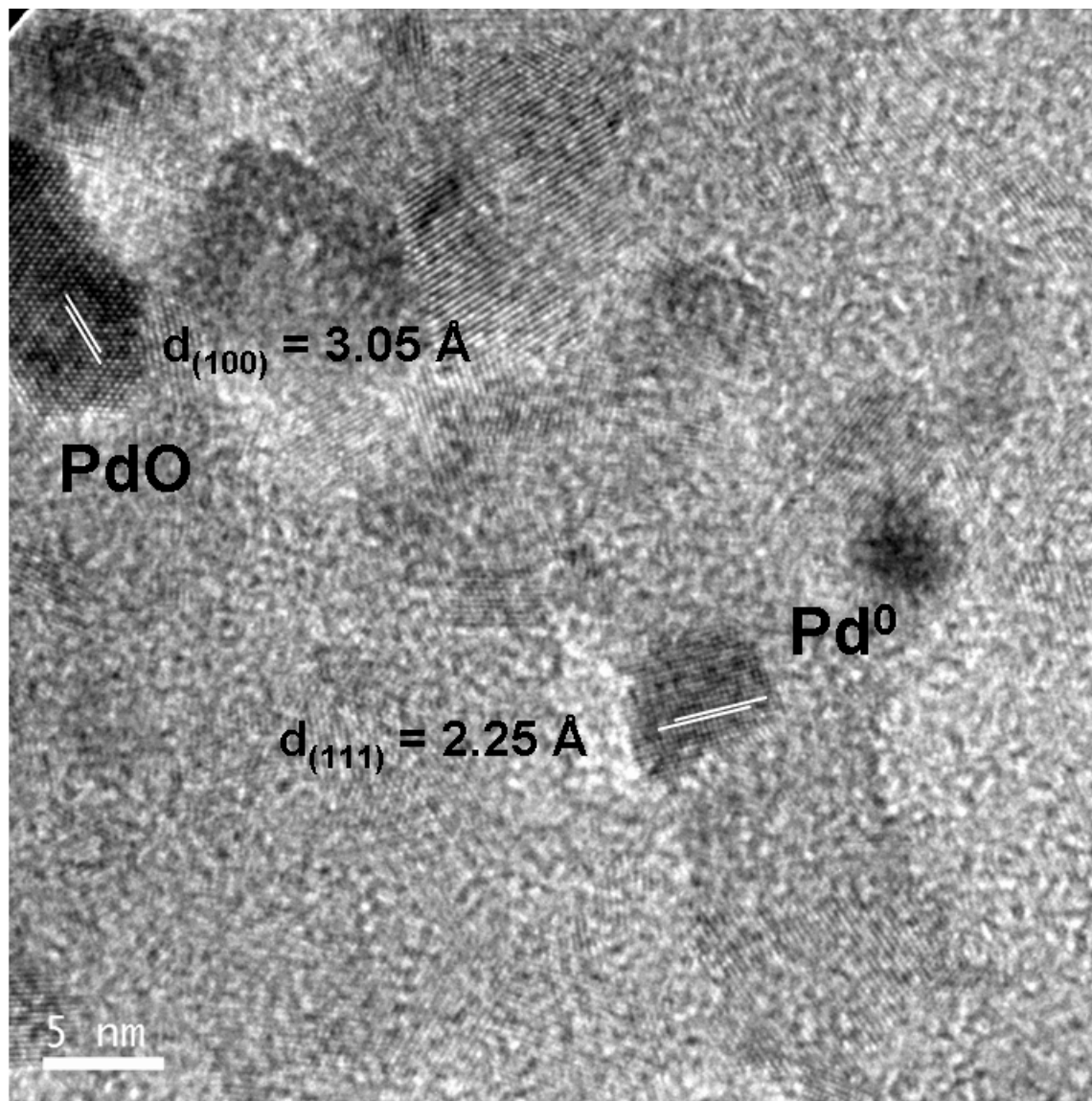


Figure 3.6: Transmission Electron Microscopy of the 5% Pd/Al₂O₃ (Sample 1) before activation. The white scale bar represents 5nm here.

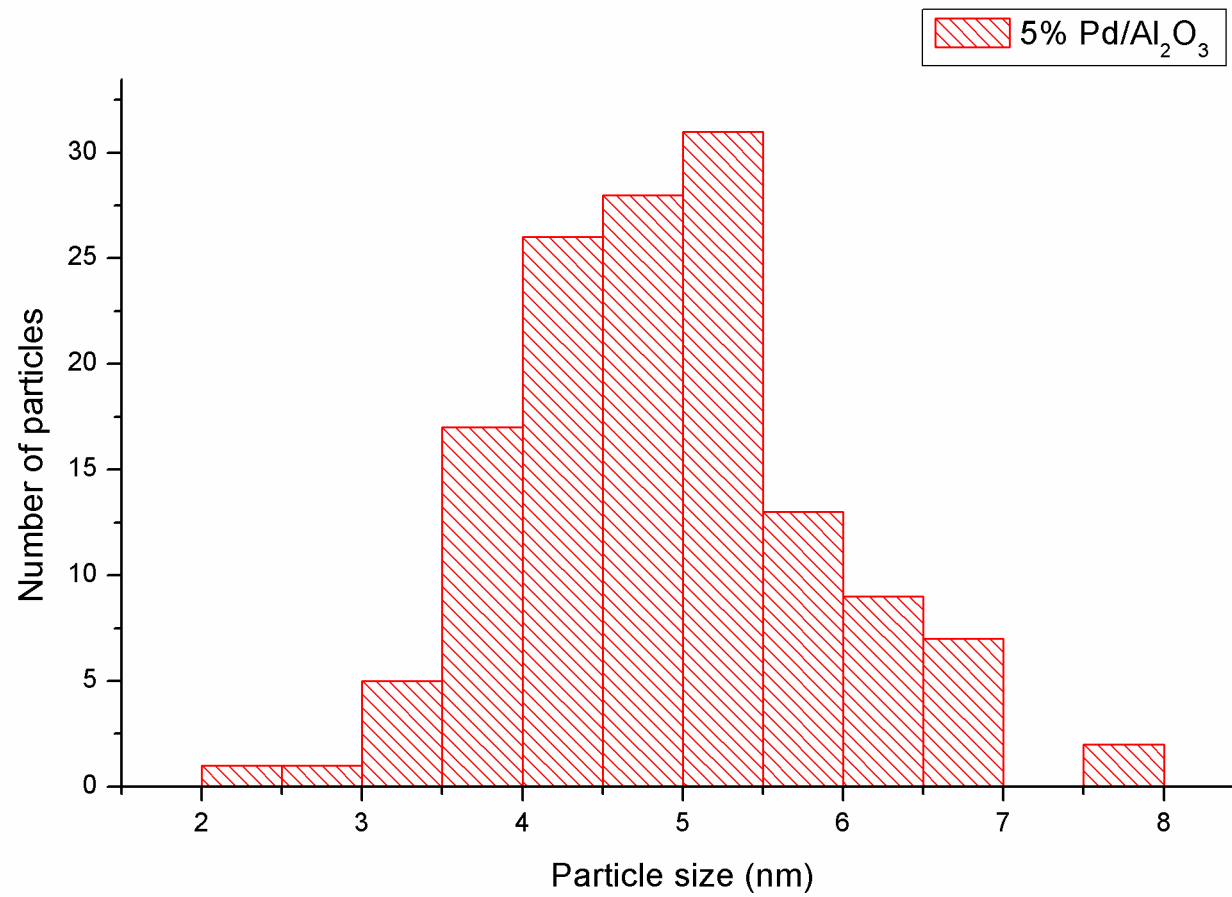


Figure 3.7: Particle size distribution of the 5 wt % Pd/Al₂O₃ obtained using TEM Tecnai T20.

TEM images were analysed using imaging software to measure the interplanar spacing with the best resolution possible. Here in **Figure 3.5**, the particle seen at the centre is believed to be palladium oxide. **Figure 3.6** displays two other palladium particles, one seen to be metallic palladium and one palladium oxide. In fact, the presence of metallic palladium before reduction is unusual but possible due to the high energy of the electron beam used. It was reported in the literature that the palladium particles (111) low index plane is seen in large quantities when looking at supported catalysts. Images not included here have been examined to measure more than 100 palladium particles. As a consequence, **Figure 3.7** displays a particle size distribution histogram for the 5 wt % Pd/Al₂O₃ catalyst. The mean Pd particle size is around 5 nm, a value consistent with the CO adsorption isotherm measurements (**Section 3.2**).

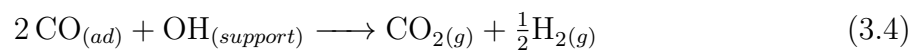
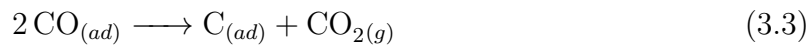
In summary, the 5 wt % Pd/Al₂O₃ catalyst is composed of a gamma-alumina supporting highly dispersed palladium particles, with a mean particle size of 5 nm.

3.4 CO chemisorption followed by Infrared Spectroscopy

CO chemisorbs to the palladium metal in different ways: linear, two-fold hollow and three-fold hollow. It is assumed that over Pd/alumina catalysts, the shift of the adsorbed bands is truly informative. Indeed, work by Lear *et al.* over different types of Pd/alumina catalysts enabled the correlation of morphology of palladium to the chemisorbed bands observed. Supported catalyst particles are usually well described by simple geometric structures such as spheres or hemispheres [97]. TEM shows the 5 wt % Pd/Al₂O₃ catalyst to be comprised of particles, some of which exhibit a distinct hexagonal structure, consistent with cubo-octahedra. Van Hardeveld and Hartog established the relationship between metal particle size and crystallite morphology [98]. Investigations on model alumina-supported palladium catalysts have been able to refine the description of adsorption sites on well-defined nanoparticles [97]. Later studies led by McInroy *et al.* [99] and Morisse *et al.* revealed how the understanding of the palladium particles morphology could lead to structure/activity relationships in selective hydrogenation reactions and help in the optimisation of a new range of catalysts [85].

To ensure that our system was leak-free and able to chemisorb CO at the surface of the catalyst, effectively we operated a CO TPD experiment reported in **Figure 3.8**. The mass spectrometry signal for mass 28 and 44 which respectively accounted for CO and CO₂ were recorded alongside the progression of the linear temperature ramp. We observe desorption of CO then CO₂ at higher temperatures. The pattern observed is consistent with previous CO TPD performed on Pd/alumina [86]. As for the production of CO₂,

it arises from three reactions: the Boudouart reaction, the oxidation of CO by hydroxyl groups on the metal-surface interface and the decomposition of carbonates present on the alumina surface [100]. The TPD observed in **Figure 3.8** indicates that the system can be used to chemisorb CO safely and this can be followed using infrared spectroscopy.



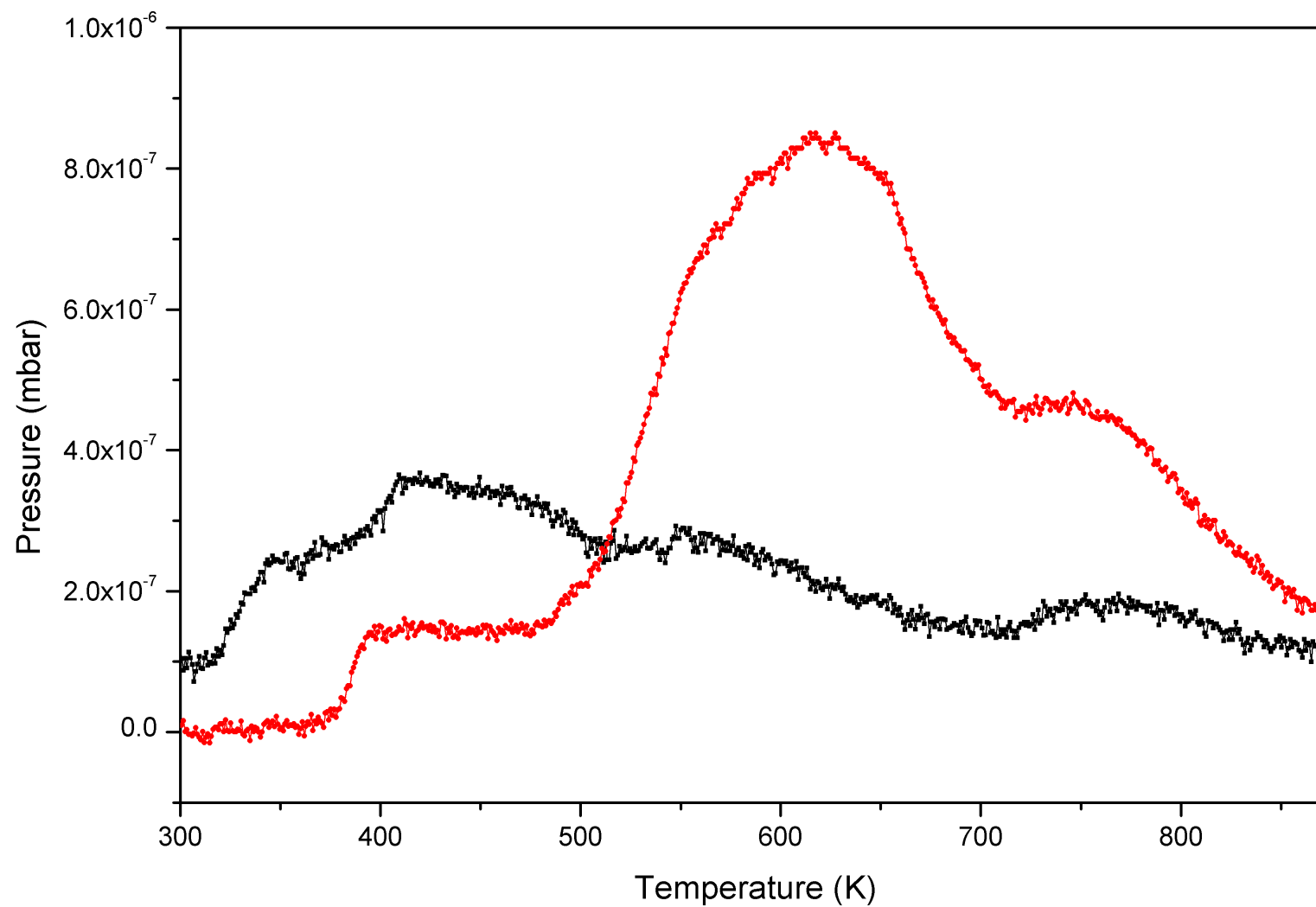


Figure 3.8: Temperature Programmed Desorption of CO in black and CO₂ in red for the 5 wt % Pd/Al₂O₃.

Lear *et al.* have made a number of precise assignments for CO chemisorption on Pd/Al₂O₃ catalysts using the DRIFT technique [85]. This work will make use of that database to make deductions on Pd crystallite morphology of the catalysts under examination here (Sample 1). However, McDougall and co-workers have previously highlighted the differences found between DRIFT-derived spectra and the more traditional technique of transmission IR [101]. McDougall suggests that the sensitivity for transmission cell and DRIFT cells are different because of the beam pathway and the sampling method used. They felt that both methods should be used in conjunction and not against each other. Later work by Meunier and co-workers made comparable statements [102]. Thus, in an attempt to calibrate the DRIFT approach adopted here, the 5% Pd/Al₂O₃ reference catalyst will also be examined using transmission spectroscopy. Such a joint approach was previously used by McInroy and co-workers to examine methanol adsorption of an η -alumina catalyst [103].

Mode of adsorption	Description
μ_1	Linear CO on corners and edges Pd(100)/(111)
μ_2	Two-fold CO adsorption geometry on Pd(100)
μ_3	Three-fold CO adsorption geometry on Pd(111)

Table 3.4: Summary of Spectral assignments for CO chemisorption on Pd crystallites

DRIFT technique can lead to distortion of spectrum depending of the geometry of the cell, the size of the sample particle, the homogeneity of the sample and the packing of the sample as described by Dent and Chalmers [61]. In order to verify that the analytical conditions for the DRIFT experiment will not result in distortion of the spectrum, we decided in a first instance to test it against a transmission analytical setup. A transmission setup for IR analysis of catalyst does not lead to distortion and have been widely used for probing catalytic surfaces in the past. Therefore, in the following section, we compared the use of a transmission cell (**Figure 2.4**) on a Bruker spectrometer against a DRIFT cell (**Figure 1.14a**). Finally we compared two DRIFT cell which have two distinct different geometry on wo spectrometers. The Praying Mantis cell used with the Bruker spectrometer (**Figure 1.14a**) was then compared to the Nexus Spectra Tech smart collector cell (**Figure 1.14b**). One 5 wt % Pd/Al₂O₃ catalyst was used for the three analysis and probed in the same way with CO.

3.4.1 CO-IR of the 5 wt % Pd/Al₂O₃ (Sample 1) using the Bruker Transmission system

The infrared spectroscopy results from CO chemisorption using the transmission cell on the 5 wt % Pd/Al₂O₃ are shown in **Figure 3.9**. The chemisorption was carried out

as mentioned in **Section 2.4.1**. The scan of the chemisorbed CO at the surface of the catalyst after activation is shown in **Figure 3.9**. The saturated spectrum displays three characteristics bands for the chemisorption of CO at the surface a Pd/alumina catalyst [85]. The band at 2055 cm^{-1} is attributed to CO linearly bound on the Pd crystallites. The two other features are attributed to two-fold and three fold chemisorbed CO over Pd low index planes as shown previsouly in **Figure 1.16**. The band at 1974 cm^{-1} is assigned to μ_2 bridge bonded CO on Pd (100) and the band at 1907 cm^{-1} is assigned to μ_3 bridge bonded CO on Pd (111). The fact that the band at 1974 cm^{-1} is more intense than the band at 1907 cm^{-1} suggests that there is a large amount of intensity stealing occurring [104]. This is due to the two frequencies active modes being close enough to allow coupling to occur which causes a transfer of intensity from the low frequency mode to its higher frequency counterpart.

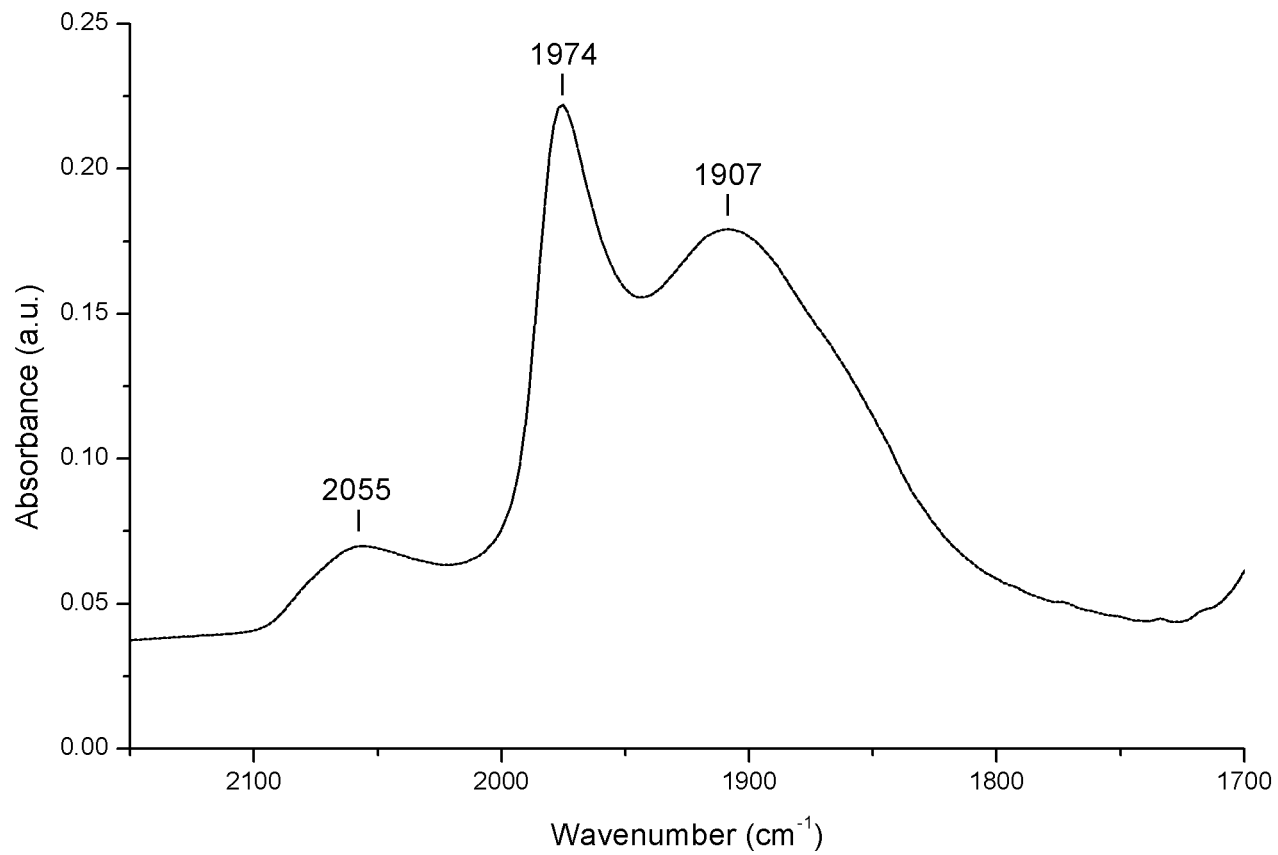


Figure 3.9: Spectrum of the 5 wt % Pd/Al₂O₃ chemisorbed with CO at room temperature using the Bruker Transmission system.

3.4.2 CO-IR of the 5 wt % Pd/Al₂O₃ (Sample 1) using the Bruker DRIFT system

The infrared spectroscopy results from the chemisorption using the Harrick Praying Mantis® Diffuse Reflectance Infrared Fourier Transform cell on the 5 wt % Pd/Al₂O₃ are shown in **Figure 3.10**. The chemisorption was carried out as mentioned in **Section 2.4.1**.

The scan of the chemisorbed CO at the surface of the catalyst after activation is shown in **Figure 3.10**. The saturated spectrum displays three characteristic bands for the chemisorption of CO at the surface a Pd/alumina catalyst [85]. The band at 2065 cm⁻¹ is attributed to CO linearly bound on the Pd crystallites. The two other features are attributed to two-fold and three fold chemisorbed CO over Pd low index planes. The band at 1980 cm⁻¹ is assigned to μ_2 bridge bonded CO on Pd (100) and the band at 1915 cm⁻¹ is assigned to μ_3 bridge bonded CO on Pd (111).

Spectra presented in **Figure 3.9 and 3.10** were recorded using the same spectrometer and MCT detector. The difference between the two spectra lies in the type of cell used, on one side we have a transmission experiment and on the other, a diffuse reflectance cell. The path length of the beam through the sample is much greater with DRIFT than transmission [101]. There is a shift of ~ 10 cm⁻¹ between the two experiments, but the main difference lies in the intensity and ratio between the three bands. The intensity of the DRIFT experiment for the μ_2 bridge bonded CO on Pd (100) band is much more intense than the two other. Nevertheless, the differences between the spectra can be understood with respect to the characteristics of the two distinct sampling geometries and it is concluded with reference to **Figure 3.10**, that the DRIFT measurements conform to the required optical parameters, including minimal interference from specular reflected light [63, 61].

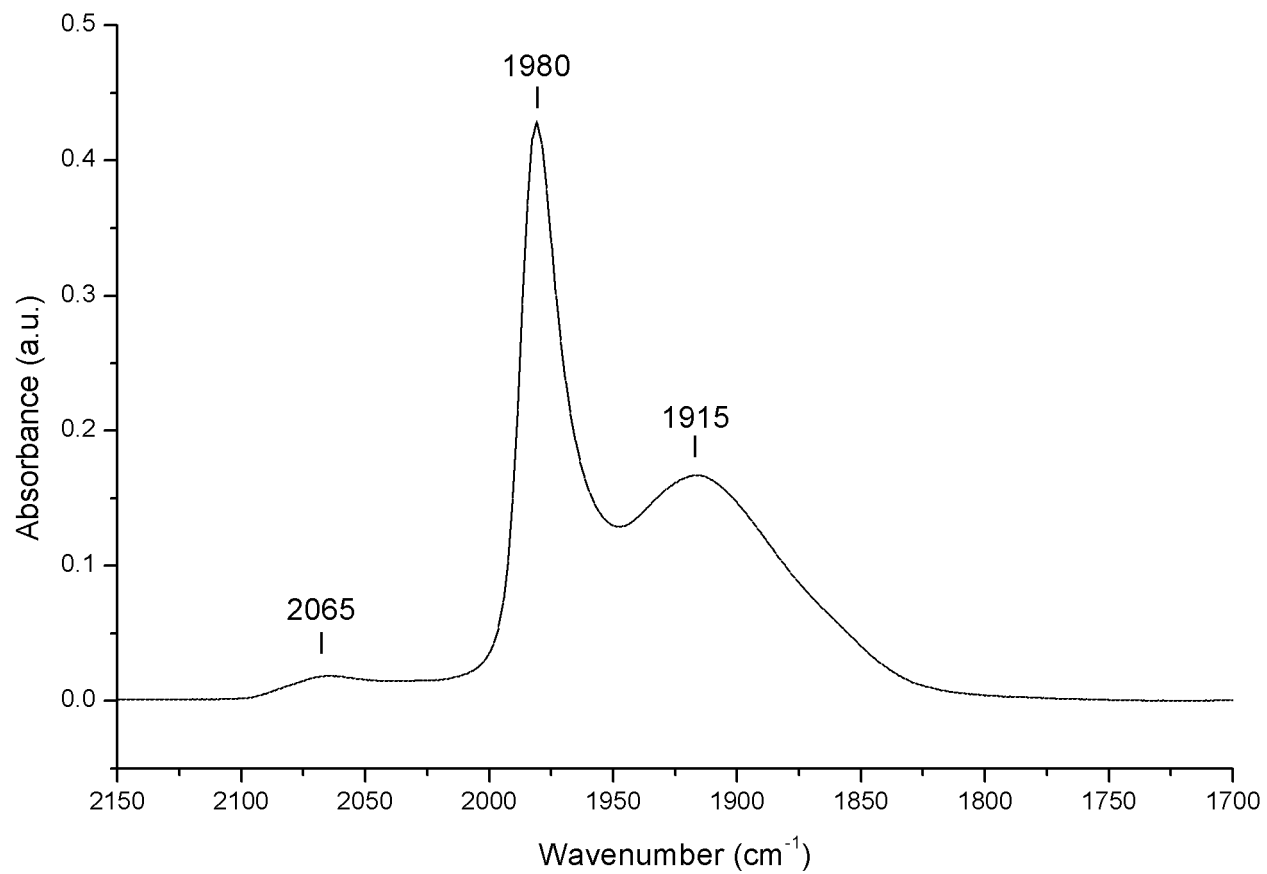


Figure 3.10: Spectrum of the 5 wt % Pd/Al₂O₃ chemisorbed with CO at room temperature using the Bruker DRIFTS system.

3.4.3 CO-IR of the 5 wt % Pd/Al₂O₃ (Sample 1) using the Nexus-Nicolet DRIFT system

The DRIFT option on a Nicolet Nexus FTIR spectrometer has the preferred sampling arrangement as it exhibits the greatest sensitivity. The Bruker Vertex arrangement was used to check the DRIFT and transmission spectra as it has the unique capability to record both DRIFT and transmission modes of operation.

The infrared spectroscopy results from the chemisorption using the Spectra-Tech Diffuse Reflectance Infrared Fourier Transform cell on the 5 wt % Pd/Al₂O₃ is shown in **Figure 3.11**. The chemisorption was carried out as mentioned in **Section 2.4.1**.

The scan of the chemisorbed CO at the surface of the catalyst after activation is shown in **Figure 3.11**. The saturated spectrum displays four characteristic bands for the chemisorption of CO at the surface a Pd/alumina catalyst [85]. The shoulder at 2080 cm⁻¹ indicates that a small amount is chemisorbed linearly on the corner site of the palladium crystal. The band at 2057 cm⁻¹ is attributed to CO linearly bound on the Pd edge (100)/(111) crystallites. The two other features are attributed to two-fold and three fold chemisorbed CO over Pd low index planes. The band at 1980 cm⁻¹ is assigned to μ_2 bridge bonded CO on Pd (100) and the band at 1909 cm⁻¹ is assigned to μ_3 bridge bonded CO on Pd (111).

The differences observed between the two DRIFT cells mainly arose because of the optical configuration difference. The Harrick cell as seen in **Figure 1.14a**, has no mirrors around the sampling cup so therefore allow the full range of transmitted, reflected and absorbed beams to be collected and focused to the detector, as opposed to the Spectra-tech cell. The Nexus one presented in **Figure 1.14b**, features a sampling cup placed in the middle of a concave golden plated mirror that gathers and focuses all type of reflections back to the detector. Hence the gain in intensity and resolution with the Spectra-Tech cell is superior to the Harrick transmission and DRIFT cell.

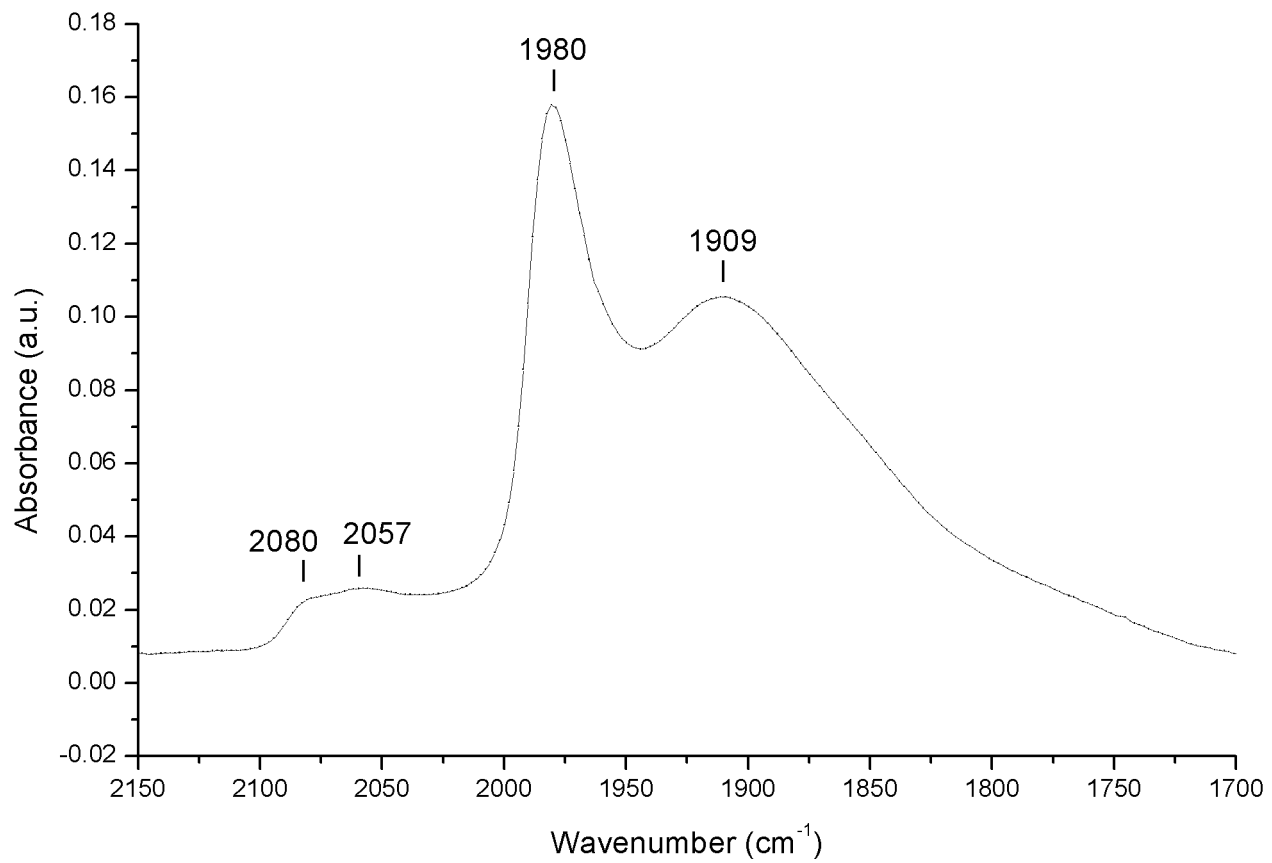


Figure 3.11: Spectrum of the 5 wt % Pd/Al₂O₃ chemisorbed with CO at room temperature using the Nicolet Nexus DRIFTS system.

3.5 Summary

A commercially available 5 wt % Pd/Al₂O₃ catalyst has been used to study the gas phase hydrogenation of nitrobenzene. The following statements can be made.

- Aniline produced during the nitrobenzene hydrogenation can be further reduced to cyclohexylamine, N-cyclohexylaniline and dicyclohexylamine. This leads to a substantial loss in selectivity at higher temperatures.
- Cyclohexanone was also produced alongside the aniline. It is believed that this compound is not produced through an aniline-derived process but it requires further investigation to assess the reaction pathway responsible for it.
- The 5 wt % Pd/Al₂O₃ was deemed a homogeneous and well dispersed catalyst supported by a gamma-alumina.
- The CO chemisorption followed by IR spectroscopy has been used to determine the precise morphology of Pd crystallites at the surface of Pd/alumina samples. The same experiment carried out on the 5 wt % Pd/Al₂O₃, using three different systems, highlighted the difference between transmission and diffuse reflectance spectroscopy. Within the diffuse reflectance spectroscopy experiments, the geometry of the optical configuration of the cell is amongst the most important characteristic to consider. For species like linear CO which reside on corner sites, an optical setup allowing the full range of reflectance to be collected and focused to the detector appeared to make an impact. Indeed, others IR spectrometer/IR cell arrangements did not allow the detection of the corner site feature.

Chapter 4

Nitrobenzene Hydrogenation over Pelleted 0.3 wt % Pd/Al₂O₃ Catalyst - Sample 2

As discussed in **Chapter 3**, nitrobenzene (NB) hydrogenation over 20 mg of a 5 wt % Pd/Al₂O₃ (Sample 1) led to a drastic loss in selectivity with increasing temperature. The relatively high Pd concentration in the presence of a high H₂(gas) concentration favours hydrogenation, including the hydrogenation of aniline (AN), which leads to production of down-stream compounds. Thus aniline was further reduced to cyclohexylamine (CHA), N-cyclohexylaniline (CHAN) and di-cyclohexylamine (DICHA), where up to 80% of the aniline was hydrogenated.

For obvious economical reasons, industry would rather use less palladium at the surface of their catalysts without compromising the activity and selectivity required. As a consequence, low loading catalysts have been prepared using 0.3-0.4 wt % palladium deposited on the outer surface of egg-shell type alumina support to give pellets. Such pellets are made to be resistant to sintering and attrition.

In order to compare our reaction data to the industrial trickle bed-reactor, we first decided to react the catalyst in its pellet form in a 1/2 inch tubular reactor as detailed in **Section 2.2**. The literature on nitrobenzene hydrogenation using different types of catalyst is extensive and states the use of diverse reactors [12, 105, 106, 94, 107, 108, 109, 110, 111, 112, 113, 114]. Before discussing the structure/activity relationship, we must first establish a range of reaction conditions that meet the requirements and enable us to distinguish the differences in selectivity between the catalysts.

4.1 0.3 wt % Pd/Al₂O₃ (Sample 2) pellets as a function of temperature

Sample 2 is one of the two samples that have been proposed as candidate catalysts for the new Vanguard process developed by Huntsman Polyurethanes [10]. 50 mg of the 310/2 catalyst pellets were placed in a 1/2 inch reactor and reduced as mentioned in **Section 2.2**. The temperature was allowed to cool down to 80°C before introducing the nitrobenzene/hydrogen mixture (NB 2.03×10^{-6} mol/min: H₂ 7.83×10^{-4} mol/min - H₂:NB = 385 : 1) into the reactor. This was then increased every two hours by increments of 20°C up to 200°C. Conversion of nitrobenzene was calculated according to **Equation 2.4** and is reported in **Figure 4.1**.

Conversion, represented in blue, is seen to be 81, 87 and 85% respectively for 80, 100 and 120°C. Throughout these temperatures, the selectivity to aniline in red, is observed as 100%. No loss in selectivity is observed up until we increase the temperature beyond 120°C.

From 140°C to 200°C, the conversion decreases gradually from 81% to 55% and we observe a loss in aniline selectivity from 99% to 92-93% at 200°C. In general, with increasing temperature, the nitrobenzene conversion and selectivity towards aniline decreases. The feed of nitrobenzene/hydrogen/helium remained constant throughout the temperature ramp and the experiment was carried out without any regeneration or change of catalyst between the different temperatures. It is thought that the loss of conversion found with increasing temperature, could be due to:

- An increase in the speed of diffusion in and out of the catalytic material,
- Deactivation of the catalyst via coking, phase change of the transition alumina, sintering and/or fouling by the impurities produced.
- Competitive adsorption between nitrobenzene and the impurities produced that have bigger molar mass and flatter adsorption pattern.
- Increasing rate of desorption of nitrobenzene on increasing temperature.

The loss of selectivity can be explained simply by an increase of chemical activity of the nitrobenzene hydrogenation coupled with a very active catalyst operating in a hydrogen rich regime. The plot of the selectivity as a function of temperature is shown in **Figure 4.2**. Up to 120°C, the selectivity towards aniline is 100%. However by increasing the temperature from 140°C to 200°C, by-products are observed that increase with temperature. At 140°C, alongside the aniline produced, N-cyclohexylaniline and azobenzene appeared with

less than 0.5% selectivity for each. As discussed in **Chapter 3**, the n-cyclohexylaniline (CHAN) is obtained via the reduction of the aniline chemisorbed at the surface of the catalyst and is classed as an aniline-derived by-product. To the contrary, as discussed in **Chapter 1**, azobenzene is a nitrobenzene-derived by-product and is obtained through the adsorbed phenylhydroxylamine subsequently giving azoxybenzene which then leads to azobenzene. This reaction pathway was proposed by Jackson *et al.* [24] and discussed in **Chapter 1**. At 160°C, we observe an increase of the N-cyclohexylaniline to 1% selectivity while the azobenzene remains constant. The increase of temperature to 180°C leads to an increase of the N-cyclohexylaniline (CHAN) up to 3% and 2% for the Azobenzene (AZO). Moreover, cyclohexanone (CHO) is present in low quantities (0.2%). The provenance of the cyclohexanone within the nitrobenzene hydrogenation over a catalyst has not been fully explained in the literature but will be discussed further in **Chapter 5**. Surprisingly, when the temperature is set at 200°C, the cyclohexanone (CHO) continues to increase but the N-cyclohexylaniline (CHAN) and azobenzene (AZO) production decreases. The overall loss of selectivity at 200°C is less than that found at 180°C. To sum up, the loss of selectivity with increasing temperature is due to the production of side-products originating from the different mechanism pathways discussed previously in **Section 1.3.2**. Observations made are laid out in **Scheme 4.1**

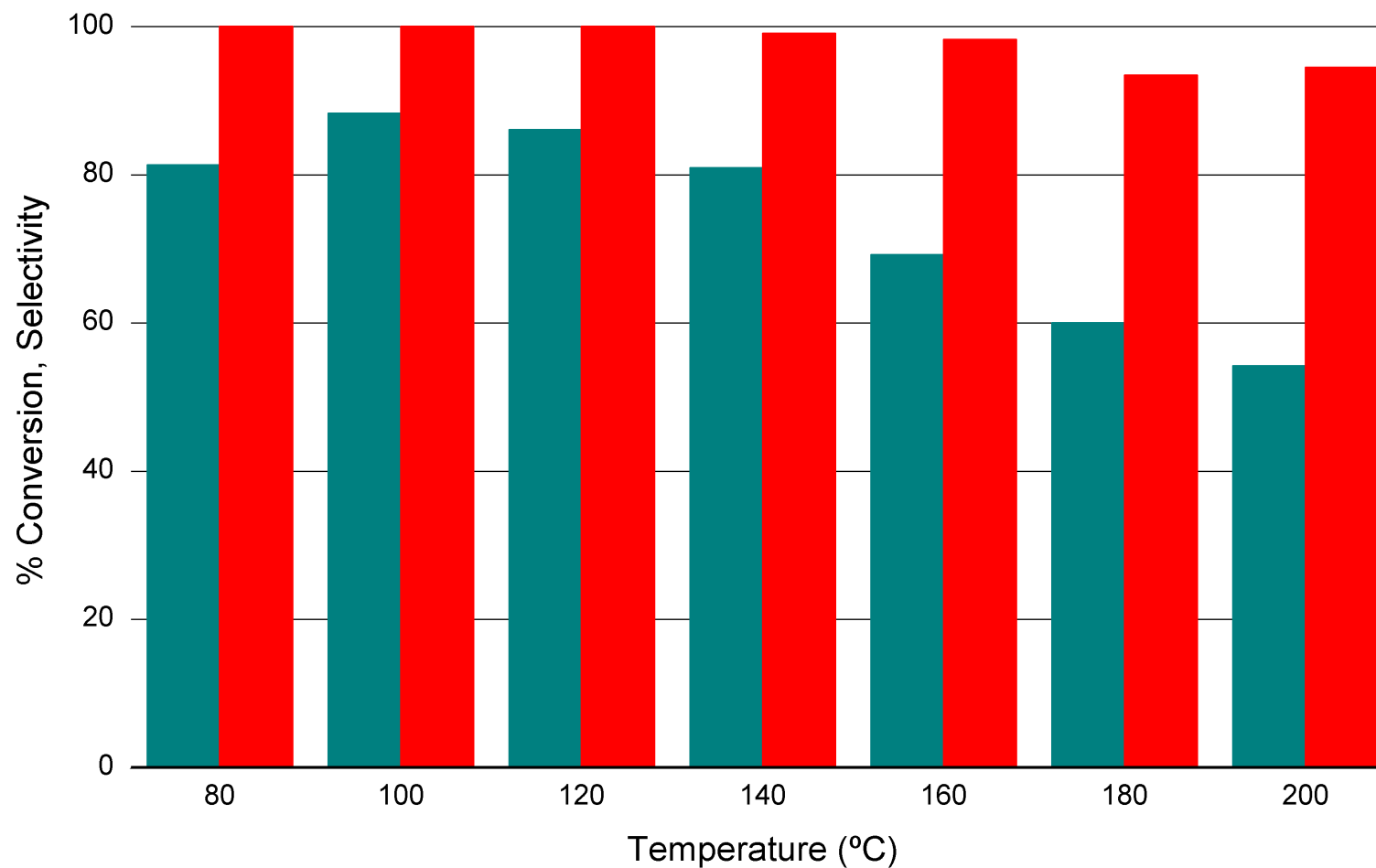


Figure 4.1: Nitrobenzene conversion (green) and aniline selectivity (red) as a function of temperature during hydrogenation of nitrobenzene. 50mg of the 0.3% Pd/alumina catalyst (301/2) was used for the gas phase hydrogenation (NB 2.03×10^{-6} mol/min: H₂ 7.83×10^{-4} mol/min - H₂:NB = 385 : 1, NB(s⁻¹) : Pd_(s) = 1 : 11).

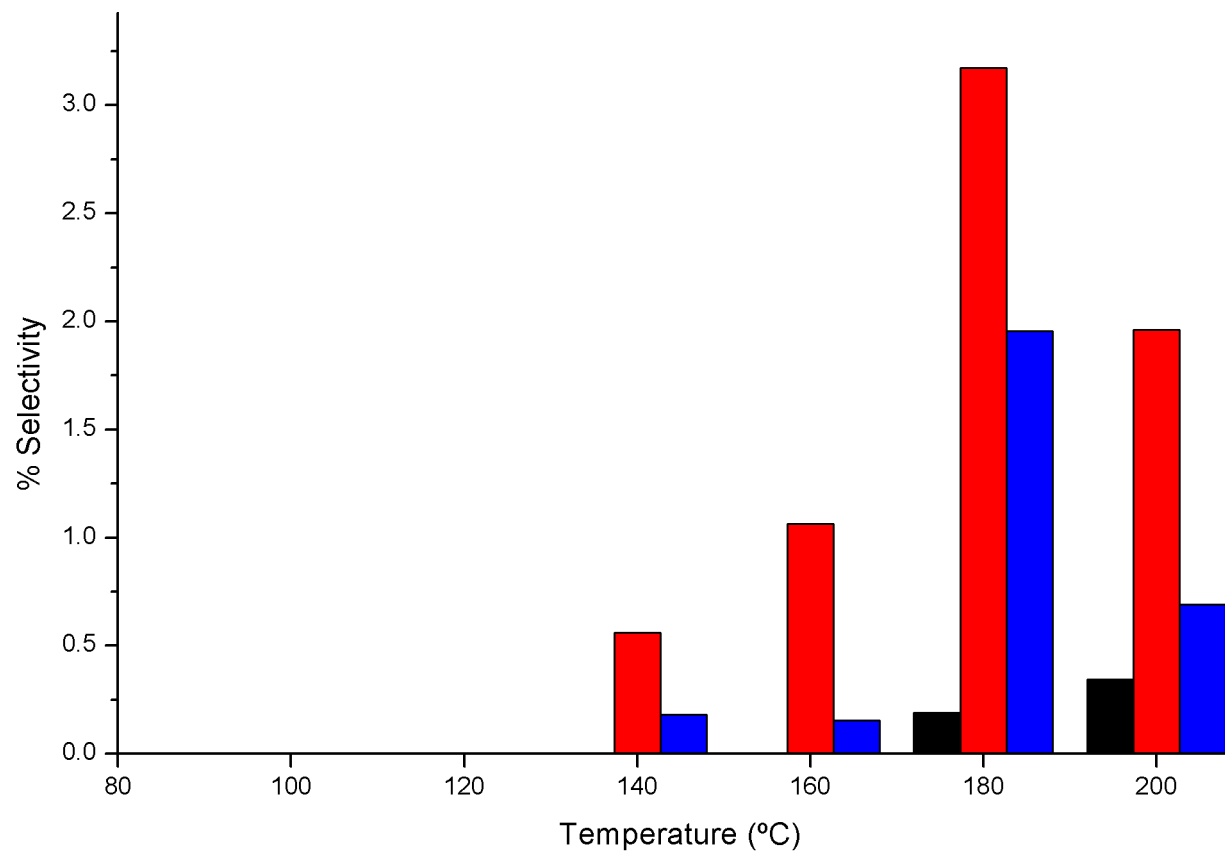
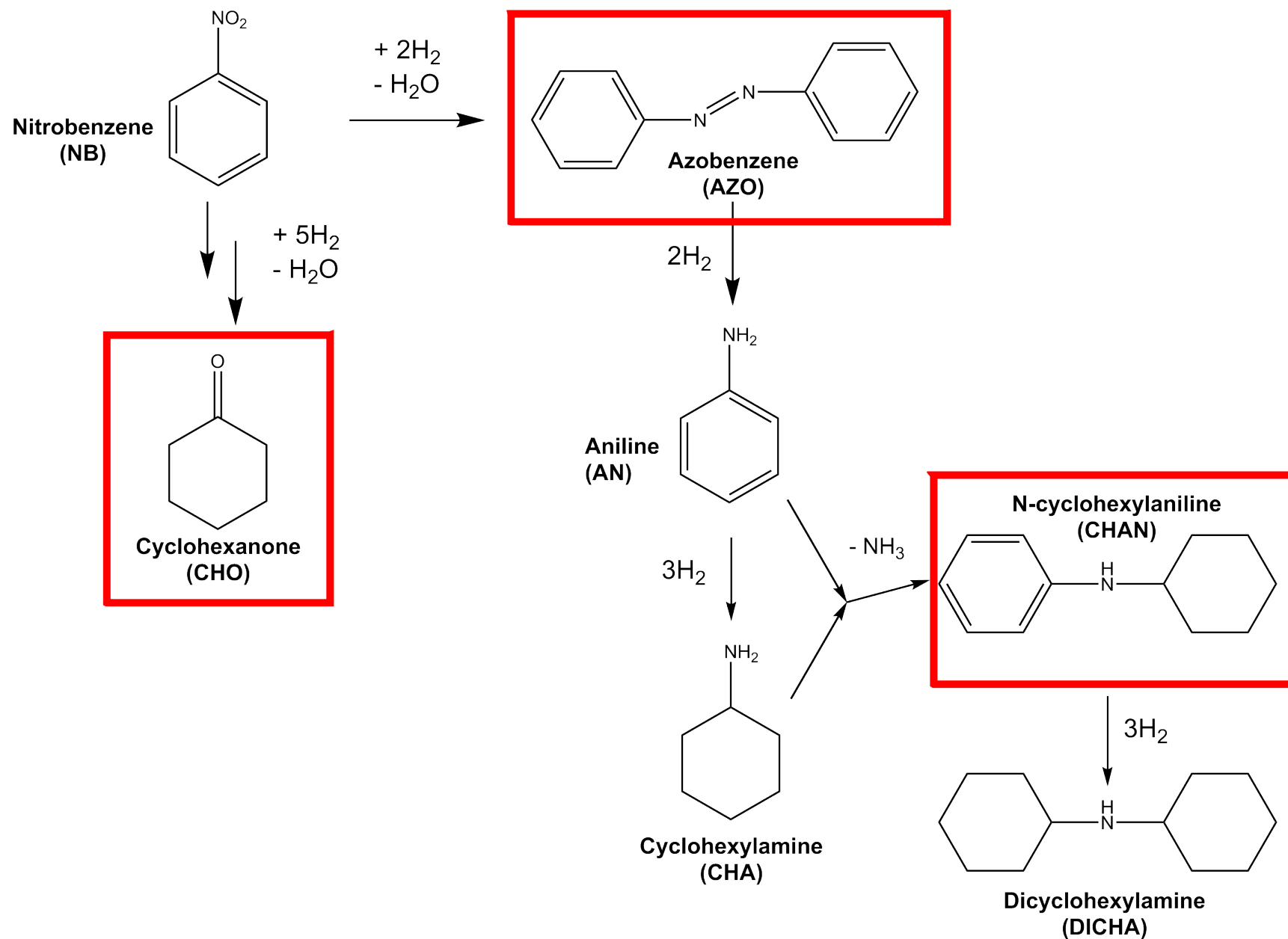


Figure 4.2: Impurities observed during nitrobenzene hydrogenation over 50 mg of 0.3% Pd/alumina (310/2) catalyst. By-products are N-cyclohexylaniline (CHAN) in red, Cyclohexanone (CHO) in black and Azobenzene (AZO) in blue (NB 2.03×10^{-6} mol/min: H₂ 7.83×10^{-4} mol/min - H₂:NB = 385 : 1, NB(s⁻¹) : Pd_(s) = 1 : 11).



Scheme 4.1: Nitrobenzene hydrogenation scheme as observed when reacting nitrobenzene and hydrogen over catalyst 2 (pellets). Red square highlight the impurities produced during the process.

4.2 0.3 wt % Pd/Al₂O₃ (Sample 2) pellets - Weight Hourly Space Velocity study

Following results obtained in **Section 4.1**, 100°C was chosen as the optimal reaction conditions for our system. At this temperature, nitrobenzene conversion and aniline selectivity on pellets is maximised. The experiment described previously was carried out using 50 mg of the 310/2 pellet catalyst. The temperature was varied while keeping the other parameters constant. The aim of this section is to discuss the influence of the space velocity in the plug-flow reactor when hydrogenating nitrobenzene on the 310/2 pellets. The space velocity is often used to define, industrially or academically, the reactor volumes of feed that can be treated in a unit time. This parameter is useful when needed to compare results from reactors of the same type but of different sizes, and is found to be very useful when scaling-up lab experiment into industrial applications. There are three type of space velocities: Liquid Hourly Space Velocity (LHSV), Gas hourly Space Velocity (GHSV) and Weight Hourly Space Velocity (WHSV). The use of one over another is mainly due to the type of feed used. For example, LHSV is used with liquid feed. Here, the feed is composed of vaporised liquid nitrobenzene, helium and hydrogen. So Weight Hourly Space Velocity (WHSV) has been used and calculated as follows - **equation 4.1** [90].

$$\text{WHSV} = \frac{F_{\text{nitrobenzene}}}{m_{\text{catalyst}}} \quad (4.1)$$

Where:

- WHSV (hour^{-1})
- $F_{\text{nitrobenzene}}$ is expressed in ($\text{g}/\text{hour}^{-1}$)
- m_{catalyst} is expressed in (g)

By varying the mass of catalyst and keeping the other parameters constant throughout each experiment, we obtained the range of WHSV values as presented in **Table 4.1**. Metal surface area was determined from CO adsorption isotherm measurements - see **Section 5.2.2**. This enabled the nitrobenzene exposure rate with respect to surface Pd atoms to be reported: NB(s^{-1}) : Pd(s).

Catalyst Mass (<i>mg</i>)	Feed Mass Flow (<i>g/h</i>)	WHSV (<i>hour</i> ⁻¹)	NB(<i>s</i> ⁻¹) : Pd(<i>s</i>)
23		2.67	1 : 5
52.5		1.17	1 : 12
102.4	0.0615	0.6	1 : 23
199.7		0.30	1 : 45
503.4		0.12	1 : 115

Table 4.1: Weight Hourly Space Velocity (*hour*⁻¹) reported for the different mass of catalyst used in the 1/2inch fixed-bed reactor. Nitrobenzene flow and hydrogen content remained constant throughout.

4.2.1 WHSV = 0.12 hour⁻¹

Figure 4.3 represents the molar profile recorded during the nitrobenzene hydrogenation over 500 mg of the 310/2 pellets. All the way through the reaction, no nitrobenzene was detected because it was fully converted over the catalytic bed as shown in **Figure 4.8**. Once, the reaction reached a steady state, the selectivity towards aniline (shown in **Figure 4.3**) dropped to 80% after 200 min and remained constant. The loss of selectivity is due to production of by-products as discussed earlier in **Chapter 3**. Here, the impurities formed are Dicyclohexylamine (DICHA), N-cyclohexylaniline (CHAN) and Cyclohexylamine (CHA). The CHA appears slightly later than the others because as CHA increases to its maximum value, CHAN reaches a peak value and its selectivity slightly decreases once the CHA production is constant. Only aniline-derived by-products are observed here but they are found in substantial amount as the catalyst lost its selectivity by 20%.

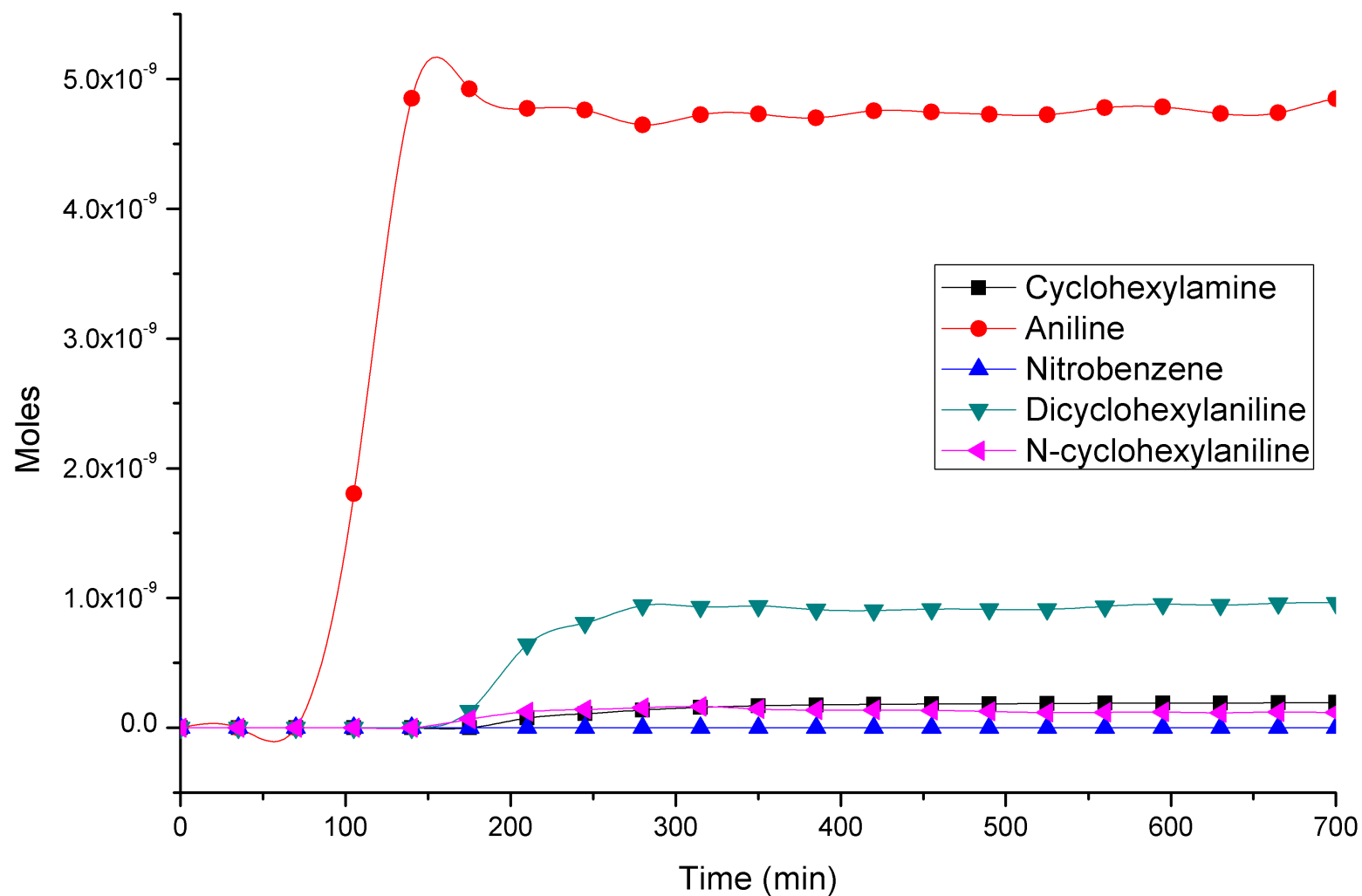


Figure 4.3: Nitrobenzene hydrogenation reaction profile over 500 mg of the 0.3wt% Pd/alumina catalyst pellets ($\text{WHSV} = 0.12 \text{ hour}^{-1}$). Temperature was set at 100°C and nitrobenzene/hydrogen flow mixture was kept constant throughout (NB $2.03 \times 10^{-6} \text{ mol/min}$; H_2 $7.83 \times 10^{-4} \text{ mol/min}$ - $\text{H}_2:\text{NB} = 385 : 1$, $\text{NB}(\text{s}^{-1}) : \text{Pd}(\text{s}) = 1 : 115$).

4.2.2 WHSV = 0.3 hour⁻¹

Figure 4.4 represents the molar profile recorded during the nitrobenzene hydrogenation over 200 mg of the 310/2 pellets. All the way through the reaction, no nitrobenzene was detected because it was fully converted over the catalytic bed as shown in **Figure 4.8**. Once, the reaction reached a steady state, the selectivity towards aniline (shown in **Figure 4.4**) dropped to 90% after 200 min and remained constant. The loss of selectivity is due to the production of by-products as discussed earlier in **Chapter 3** and **Section 4.2.1**. Here, the impurities formed are Dicyclohexylamine, N-cyclohexylaniline and Cyclohexylamine. The CHA appears slightly later than the others because as CHA increases to its maximum value, CHAN peaks and its selectivity was found to slightly decrease when the CHA production became constant. This behaviour was previously observed with the 500 mg experiment but the amount of impurities was found to be lower which led to an increase of the aniline selectivity. The use of 200 mg of catalyst gave an increase in the space velocity at the surface of the 310/2 catalyst, thereby lowering the aniline derived by-product formation. Impurities observed during this experiment are highlighted in **Scheme 4.3**.

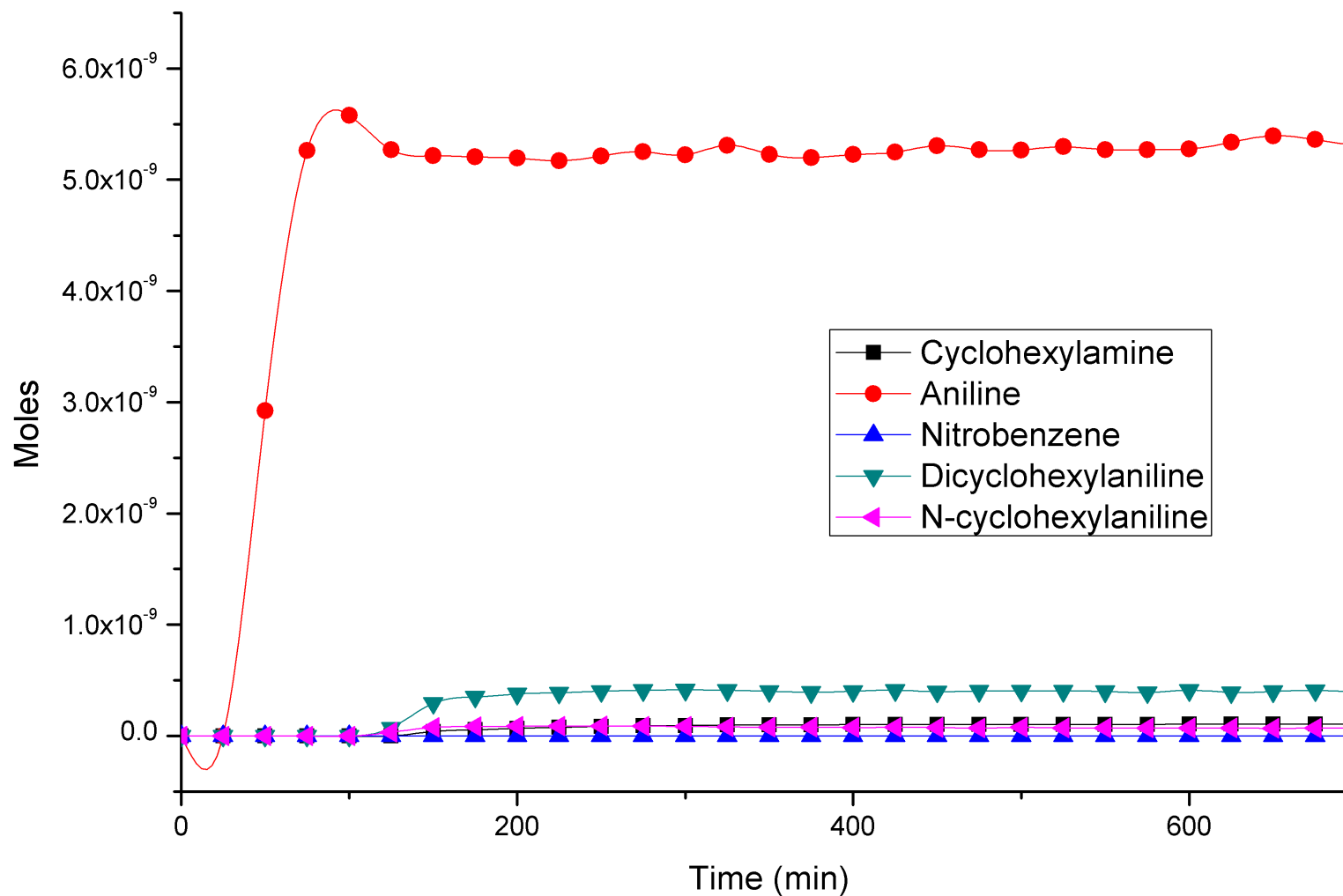
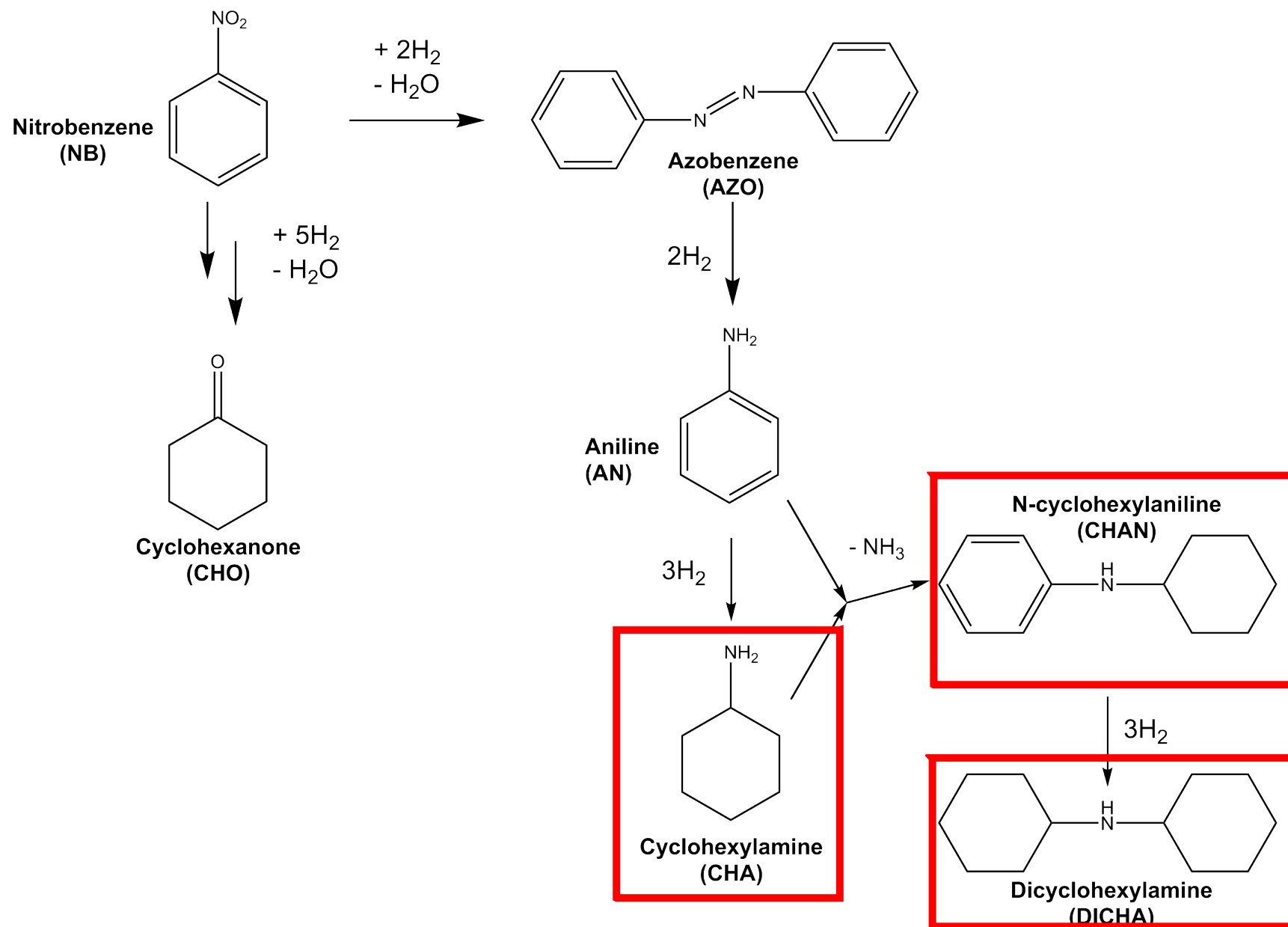


Figure 4.4: Nitrobenzene hydrogenation reaction profile over 200 mg of the 0.3wt% Pd/alumina catalyst pellets ($\text{WHSV} = 0.3 \text{ hour}^{-1}$). Temperature was set at 100°C and nitrobenzene/hydrogen flow mixture was kept constant throughout (NB $2.03 \times 10^{-6} \text{ mol/min}$; H_2 $7.83 \times 10^{-4} \text{ mol/min}$ - $\text{H}_2:\text{NB} = 385 : 1$, $\text{NB}(\text{s}^{-1}) : \text{Pd}_{(\text{s})} = 1 : 45$).



Scheme 4.3: Reaction observed for $\text{WHSV} = 0.3 \text{ hour}^{-1}$. Red square highlight the impurities produced during the process.

4.2.3 WHSV = 0.6 hour⁻¹

Figure 4.5 represents the molar profile recorded during the nitrobenzene hydrogenation over 100 mg of the 310/2 pellets. No nitrobenzene was detected because during the reaction it was fully converted over the catalytic bed as shown in **Figure 4.8**. Once the reaction reached a steady state, the selectivity towards aniline (shown in **Figure 4.5**) dropped to 96% after 200 min and remained constant. The loss of selectivity is due to production of by-products as discussed in **Chapter 3, Section 4.2.1** and **Section 4.2.2**. Here, the impurities formed are Dicyclohexylamine (DICHA), N-cyclohexylaniline (CHAN) and Cyclohexylamine (CHA). As opposed to the 500 and 200 mg experiment, CHA production remained unseen throughout the experiment except for a few data points which were detected in ppm concentrations. Again, these conditions favoured the aniline-derived chemistry at the surface of the 310/2 catalyst. Impurities observed during this experiment are highlighted in **Scheme 4.4**.

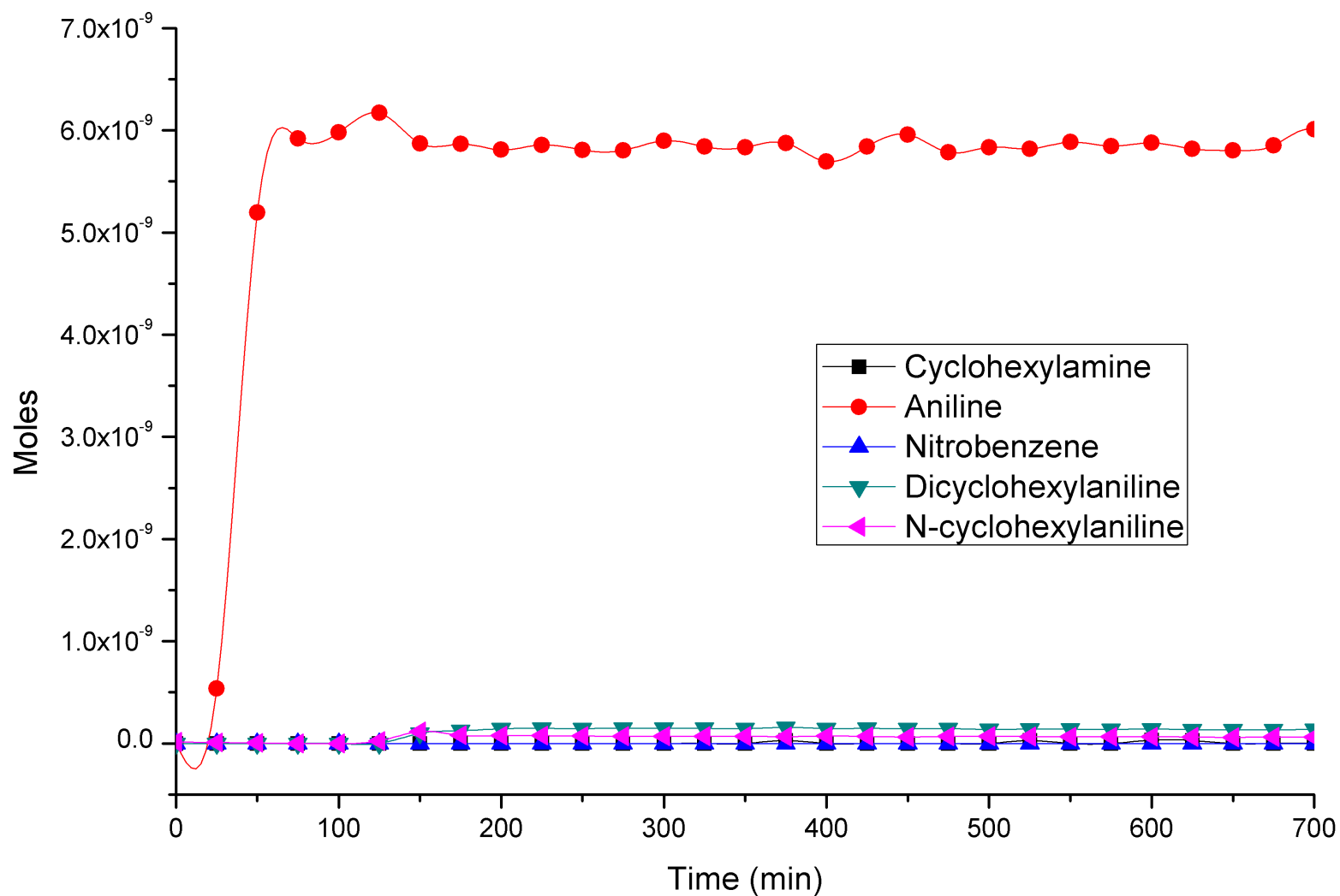
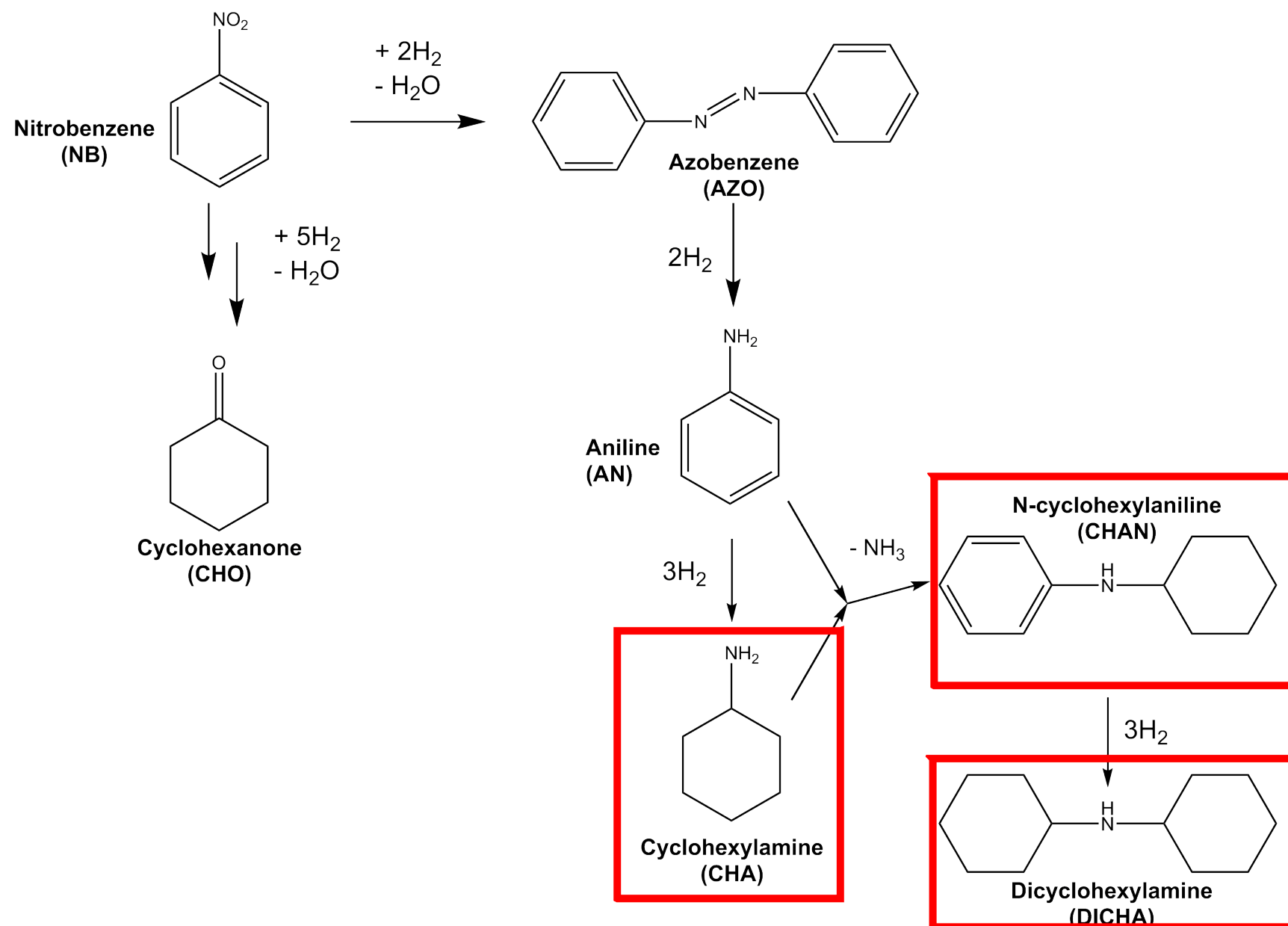
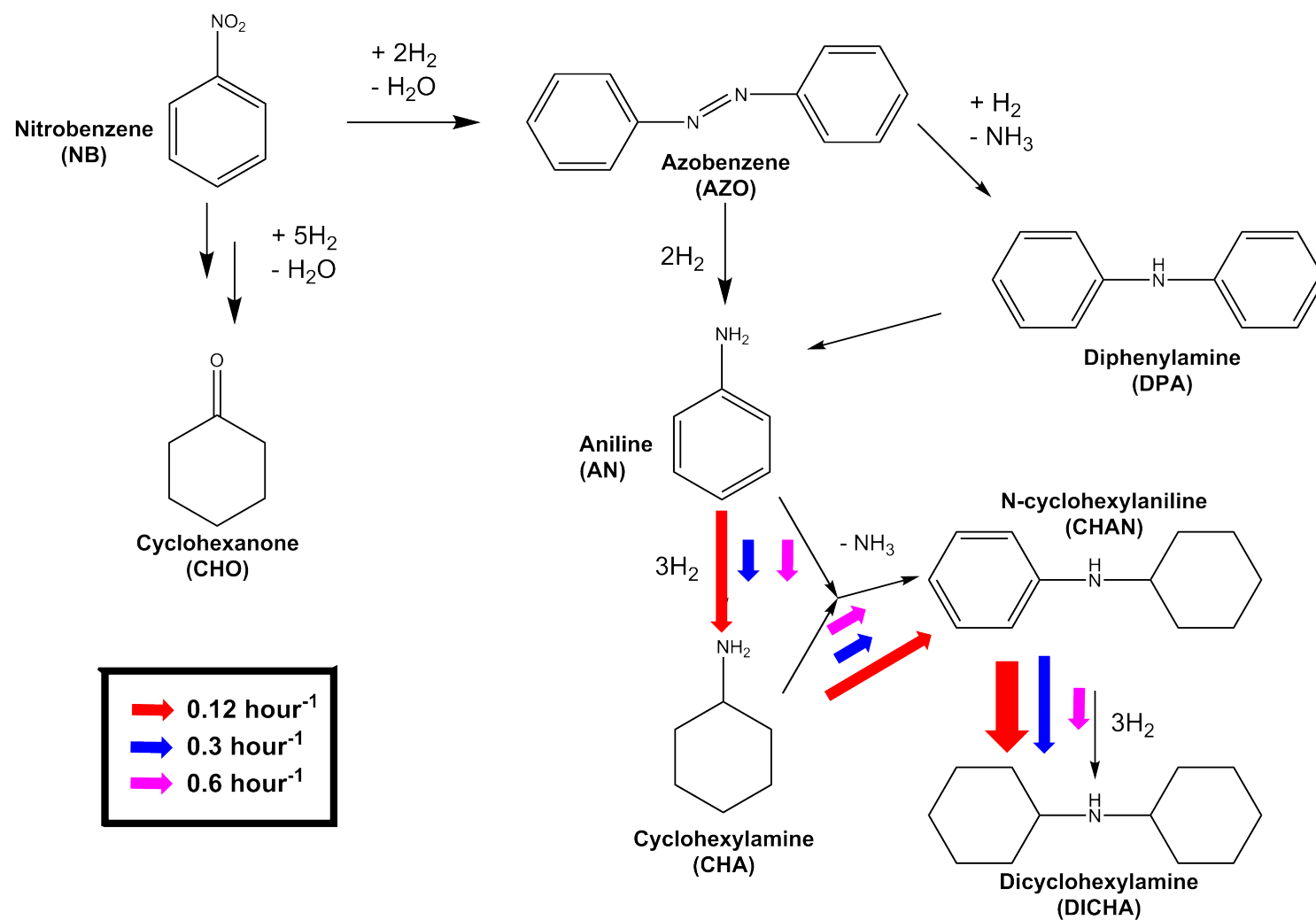


Figure 4.5: Nitrobenzene hydrogenation reaction profile over 100 mg of the 0.3wt% Pd/alumina catalyst pellets ($\text{WHSV} = 0.6 \text{ hour}^{-1}$). Temperature was set at 100°C and nitrobenzene/hydrogen flow mixture was kept constant throughout (NB $2.03 \times 10^{-6} \text{ mol/min}$; H_2 $7.83 \times 10^{-4} \text{ mol/min}$ - $\text{H}_2:\text{NB} = 385 : 1$, $\text{NB}(\text{s}^{-1}) : \text{Pd}(\text{s}) = 1 : 23$).



Scheme 4.4: Reaction observed for $WHSV = 0.6 \text{ hour}^{-1}$. Red square highlight the impurities produced during the process.



Scheme 4.5: Nitrobenzene hydrogenation reaction scheme for catalyst mass of 500, 200 and 100 mg respectively WHSV of 0.12, 0.3 and 0.6 hour^{-1} . The size of the coloured arrows is a qualitative indication of degree of by-product formed at a particular WHSV.

4.2.4 WHSV = 1.17 hour⁻¹

Figure 4.6 represents the molar profile recorded during the nitrobenzene hydrogenation over 50 mg of the 310/2 pellets. Alongside the detection of aniline, it was possible to record unreacted nitrobenzene in the gas reaction mixture which resulted in an overall conversion of 87% which decreased slightly over time as indicated in **Figure 4.8**. Once the reaction reached a steady state, the selectivity towards aniline (shown in **Figure 4.6**) dropped to 96% and slowly rose to 98% after 700 min. The loss of selectivity is due to the production of by-products as discussed earlier in **Section 4.2.1**, **Section 4.2.2**, **Section 4.2.3** and **Chapter 3**. Here, the impurities formed are dicyclohexylamine (DICHA), N-cyclohexylaniline (CHAN), Cyclohexylamine (CHA) and Azobenzene (AZO). The formation of azobenzene occurred through the condensation route as discussed in **Section 1.3.2** and is part of the nitrobenzene-derived by product. At the start of the reaction, no impurities were produced and only aniline and nitrobenzene were detected. After about one hour, azobenzene alongside N-cyclohexylaniline appeared in low concentrations. Azobenzene disappeared from the gas mixture not long after and both N-cyclohexylaniline and dicyclohexylaniline remained present and constant throughout the rest of the reaction. The increase of the space velocity to 1.17 hour⁻¹ induced for the first time the production of a nitrobenzene-derived by-product at the surface of the catalyst. Nevertheless, azobenzene quickly disappeared and only CHAN and DICHA remained visible during the remainder of the reaction. Impurities observed during this experiment are highlighted in **Scheme 4.6**.

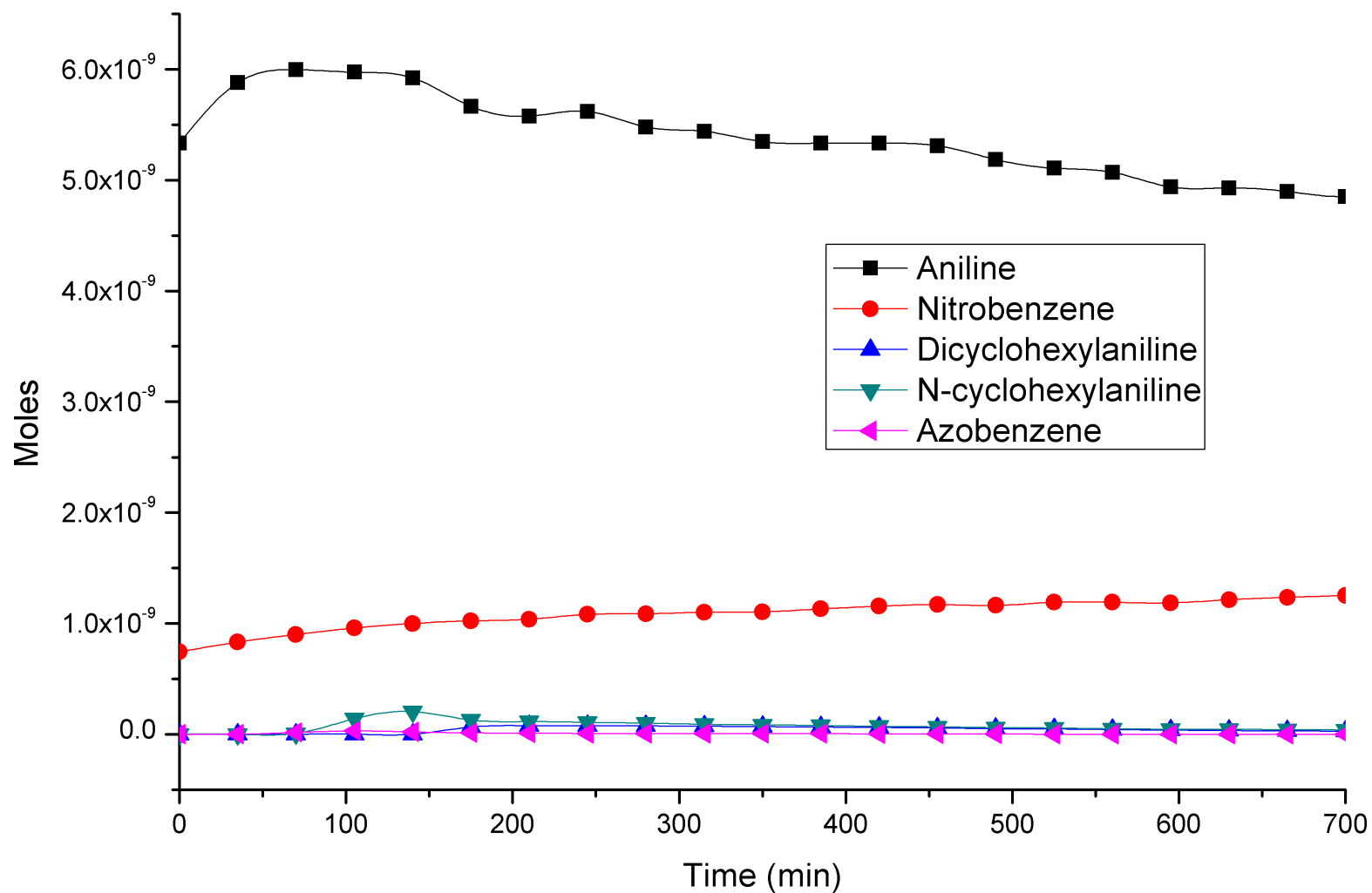
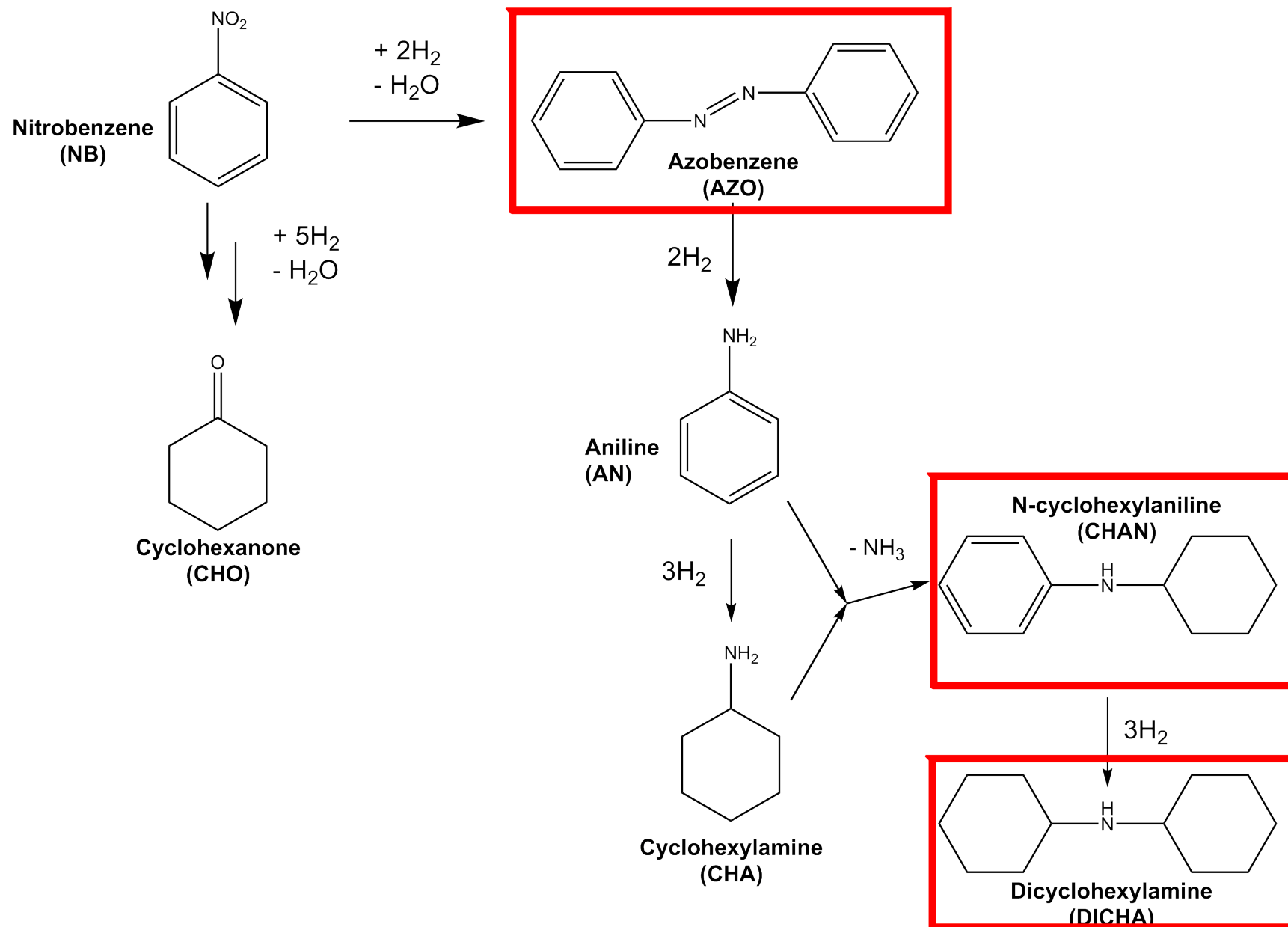


Figure 4.6: Nitrobenzene hydrogenation reaction profile over 50 mg of the 0.3wt% Pd/alumina catalyst pellets (WHSV = 1.17 hour⁻¹). Temperature was set at 100°C and nitrobenzene/hydrogen flow mixture was kept constant throughout (NB 2.03 x 10⁻⁶ mol/min: H₂ 7.83 x 10⁻⁴ mol/min - H₂:NB = 385 : 1, NB(s⁻¹) : Pd_(s) = 1 : 12).



Scheme 4.6: Reaction observed for $WHSV = 1.17 \text{ hour}^{-1}$. Red square highlight the impurities produced during the process. This figure demonstrates an interesting deviation from the lower space velocities.

4.2.5 WHSV = 2.67 hour⁻¹

Figure 4.7 represents the molar profile recorded during the nitrobenzene hydrogenation over 25 mg of the 310/2 pellets. Alongside the detection of aniline, it was possible to record unreacted nitrobenzene in the gas reaction mixture which decreased with time and settled around 65% as indicated in **Figure 4.8**. Once the reaction reached a steady state, the selectivity towards aniline (shown in **Figure 4.7**) was observed to be approximately 99%. Once again, the loss of selectivity is due to the production of by-products as discussed earlier in **Section 4.2.1**, **Section 4.2.2**, **Section 4.2.3**, **Section 4.2.5** and **Chapter 3**. Here, the impurities formed are dicyclohexylamine (DICHA), N-cyclohexylaniline (CHAN), cyclohexylamine (CHA), azobenzene (AZO) and diphenylamine (DPA). As discussed in **Section 1.3.2** and **Section 4.2.4**, azobenzene is produced through the condensation route of the Haber mechanism and as is diphenylamine [24]. Hence diphenylamine can also be classified as a nitrobenzene-derived by-product. At the start of the experiment, CHAN, AZO and DPA are found to peak, then decrease and reside at low concentration levels but remain constant throughout the reaction. It should be noted that DICHA is not produced under these conditions and that aniline was reduced to CHAN, with no production of either DICHA or CHA. In summary, not only aniline-derived by-products were detected, but also diphenylamine and azobenzene observed as a consequence of the reaction of nitrobenzene via the condensation route. Impurities observed during this experiment are highlighted in **Scheme 4.7**.

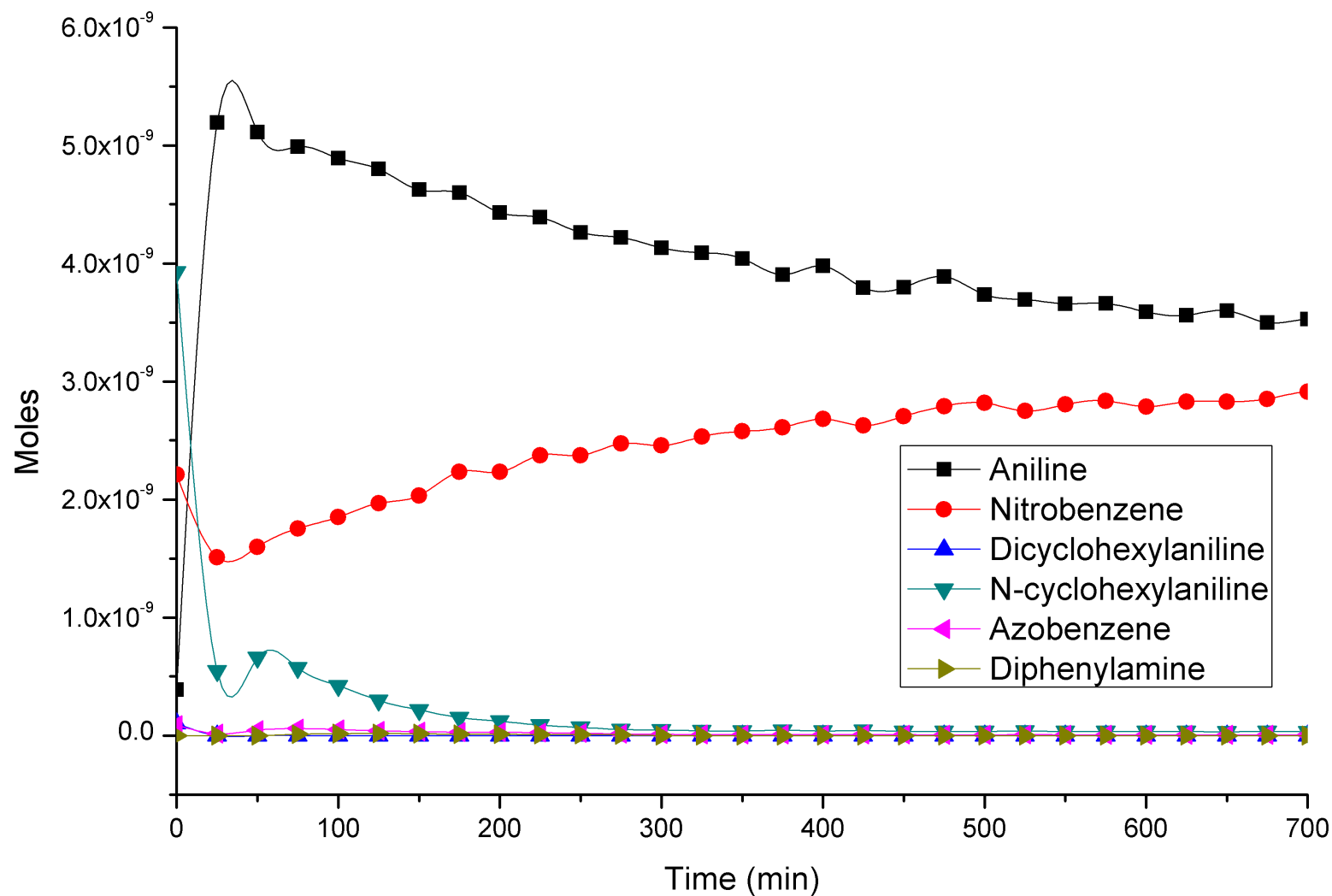
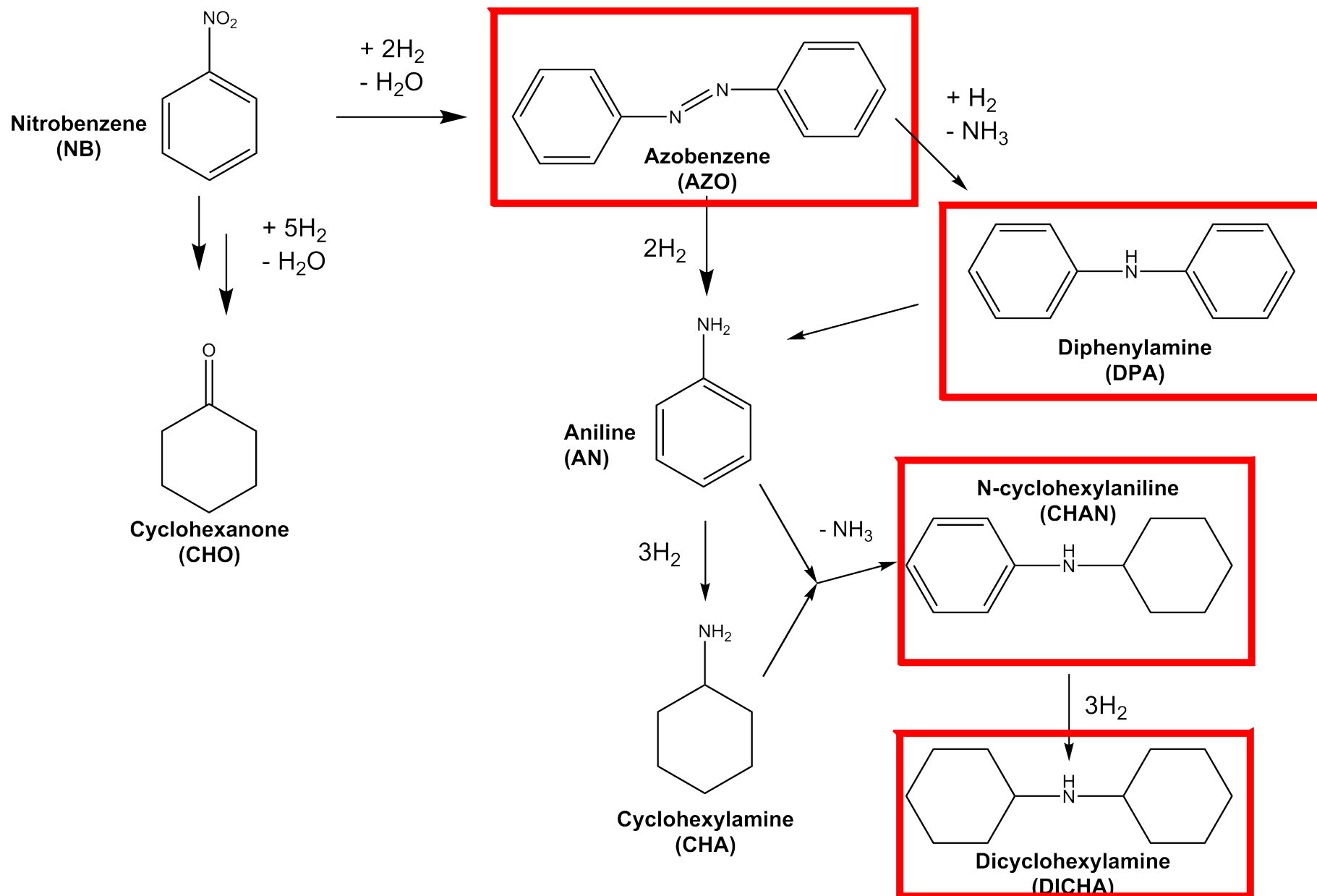
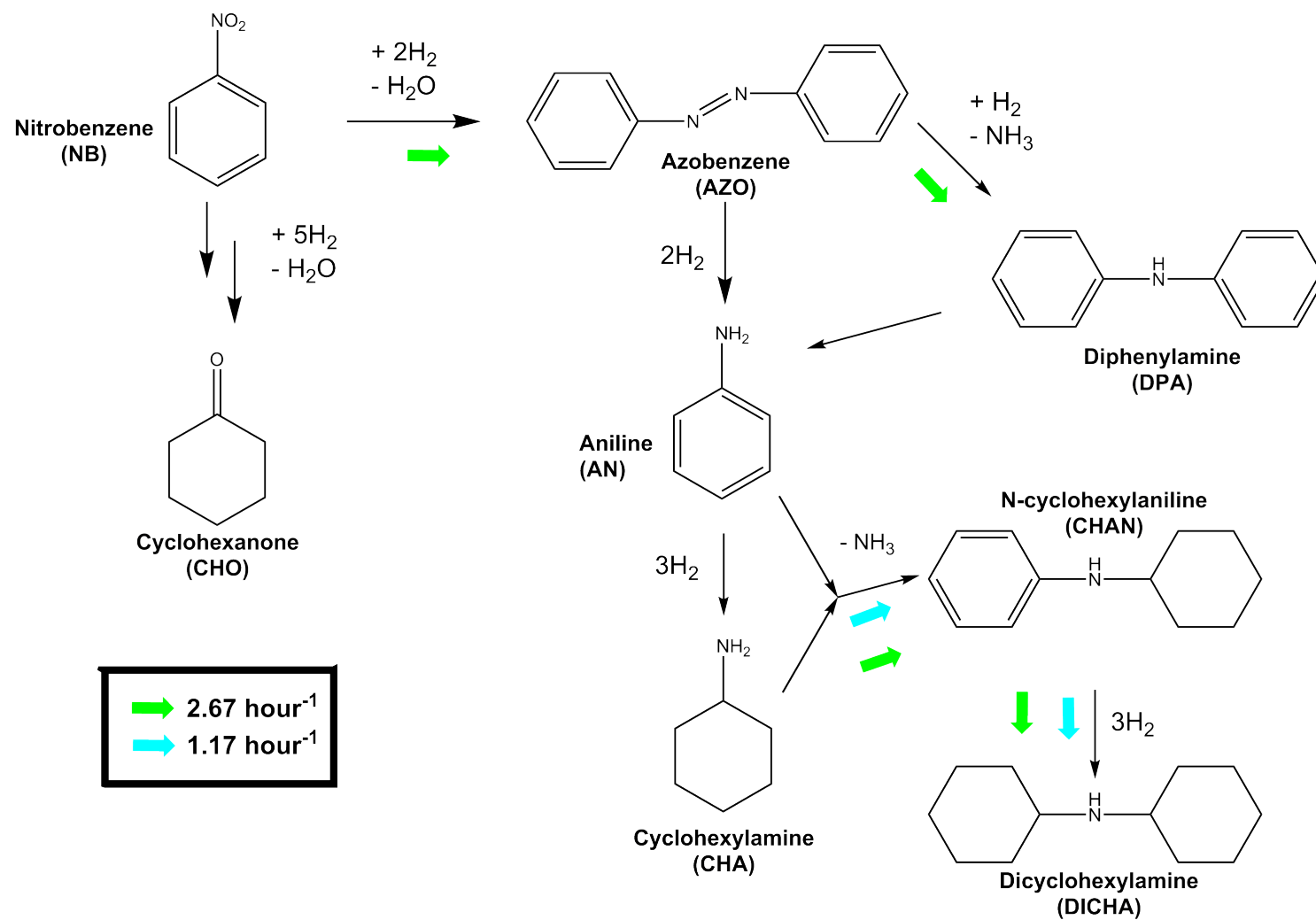


Figure 4.7: Nitrobenzene hydrogenation reaction profile over 50 mg of the 0.3wt% Pd/alumina catalyst pellets ($WHSV = 2.67 \text{ hour}^{-1}$). Temperature was set at 100°C and nitrobenzene/hydrogen flow mixture was kept constant throughout (NB $2.03 \times 10^{-6} \text{ mol/min}$: H_2 $7.83 \times 10^{-4} \text{ mol/min}$ - $\text{H}_2:\text{NB} = 385 : 1$, $\text{NB}(\text{s}^{-1}) : \text{Pd}_{(s)} = 1 : 5$).



Scheme 4.7: Reaction observed for $\text{WHSV} = 2.67 \text{ hour}^{-1}$. Red square highlight the impurities produced during the process.



Scheme 4.8: Nitrobenzene hydrogenation reaction scheme for catalyst mass of 50 and 25 mg respectively WHSV of 1.17 and 2.67 hour^{-1} .

Figure 4.8 indicates that below 50 mg of catalyst ($WHSV = 1.17 \text{ hour}^{-1}$), the reaction conditions do not allow for all of the nitrobenzene to be reacted over the catalyst. **Figure 4.9** reports aniline selectivity as a function of space velocity. To conclude, the higher the catalyst mass, the lower the selectivity towards aniline. Mass 20, 50 and 100 mg gave a relatively high selectivity to aniline but higher masses of 200 and 500 mg gave a considerable loss in selectivity.

Finally, **Figure 4.10** reports the selectivity observed for different space velocity values (where the mass of catalyst was different) and show that after 800 min of reaction, all signals for reactants and products seem to have stabilised. The link between the mass of catalyst and the loss of selectivity is also highlighted in **Figure 4.10** where the higher the mass, the higher the loss of selectivity. Furthermore, the impurities produced are more aniline-derived when the mass is higher. At low mass, nitrobenzene-derived chemistry was monitored as well where there is a clear link between the contact time (proportional to the mass of catalyst in the reactor) and the products obtained. Indeed, with increasing mass of catalyst, it seems that more downstream products are obtained (bottom of **Scheme 4.14**), whereas, at low contact time, upstream products (top of **Scheme 4.14**) are more favourable.

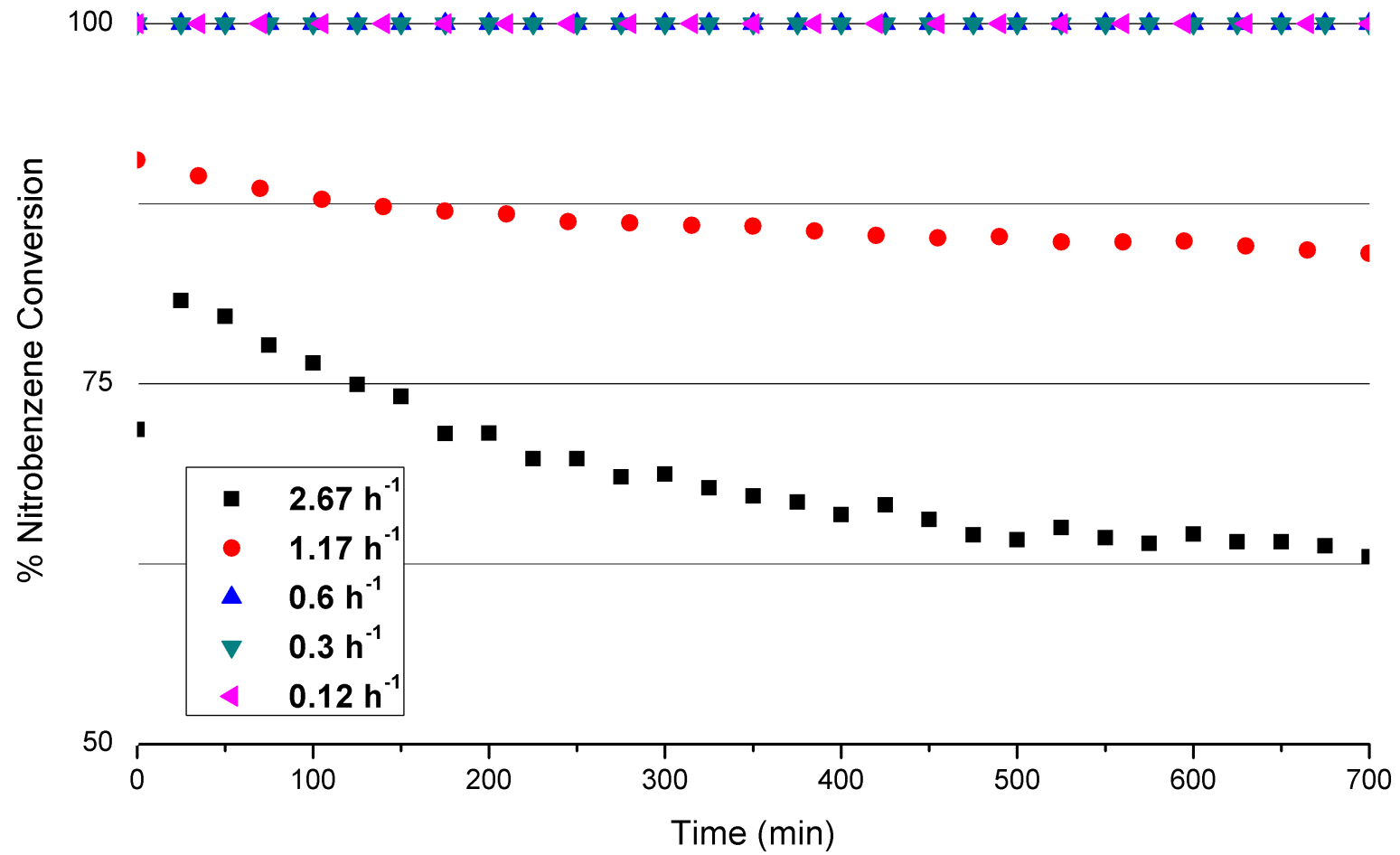


Figure 4.8: Nitrobenzene Conversion reported as a function of WHSV.

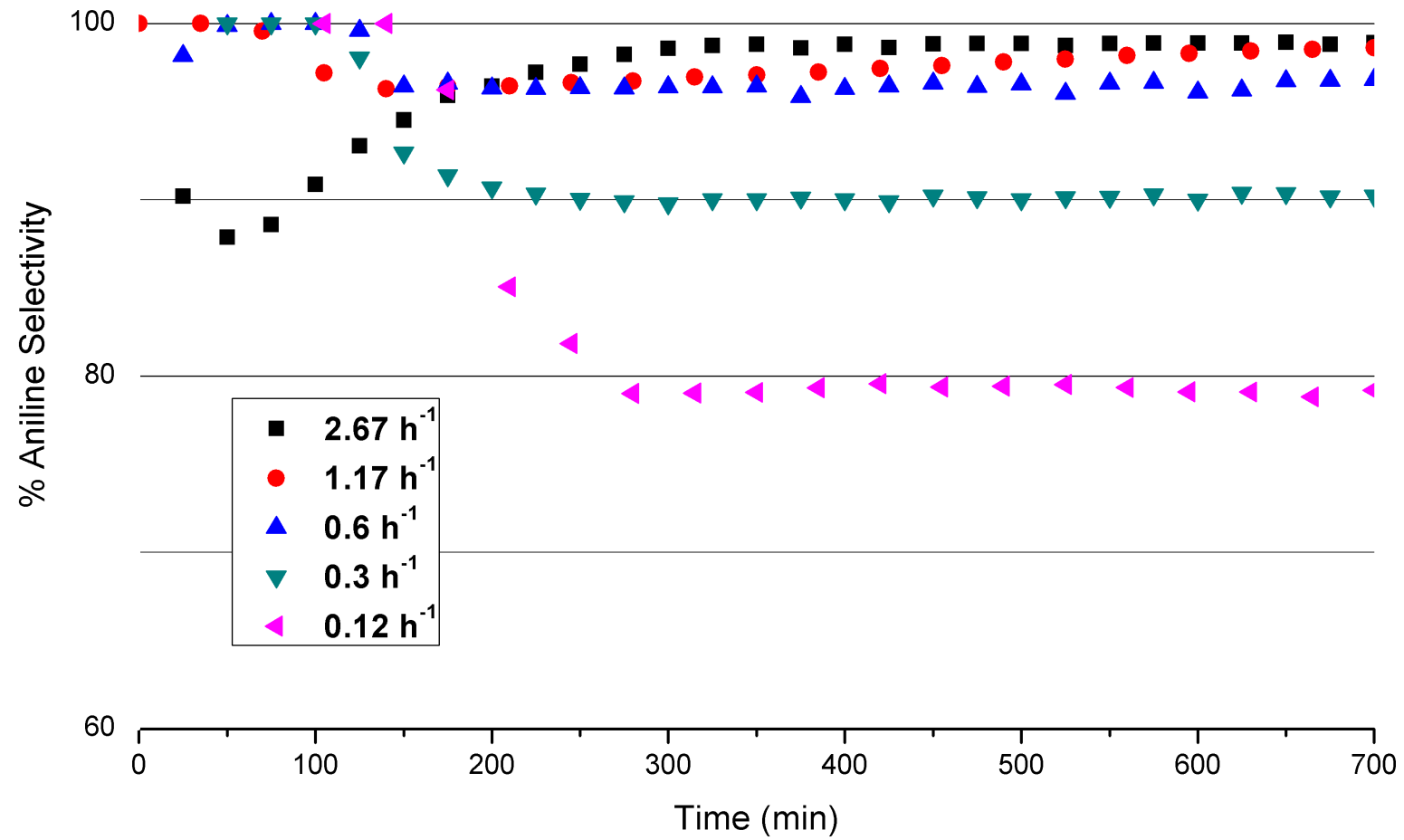


Figure 4.9: Aniline Selectivity reported as a function of WHSV.

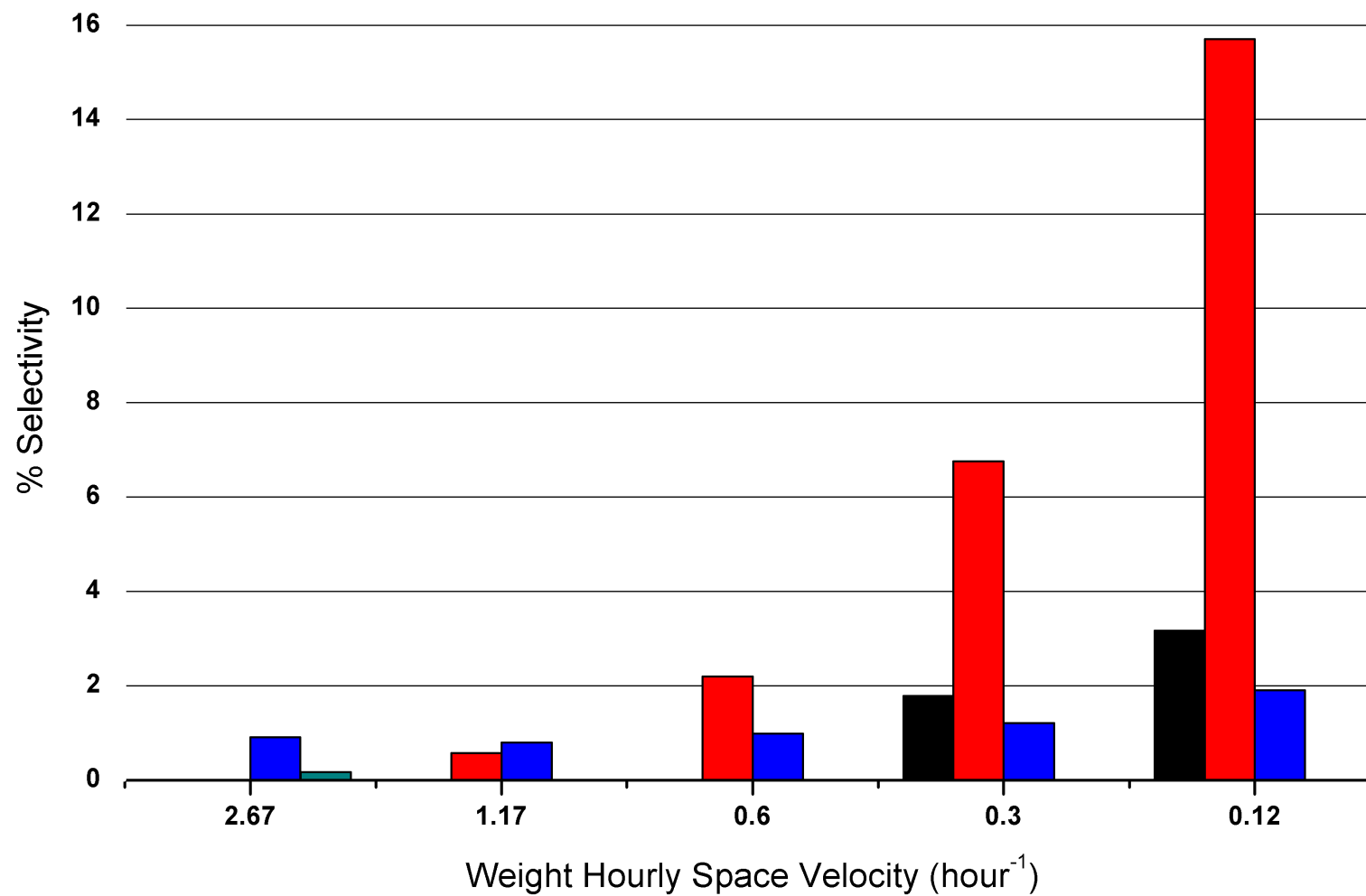


Figure 4.10: Conversion reported as a function of WHSV. In blue, CHAN, in green, Azobenzene, in red, DICHHA and in black, CHA.

4.2.6 Aniline Hydrogenation

The hydrogenation of aniline as part of a nitrobenzene reduction process has not been reported frequently in the literature but was recorded recently by Rubio-Marques [93]. However, Mink [33], Aranyi [91] and Echigoya [92] have all studied the catalytic hydrogenation of aniline and reported the production of cyclohexylamine (CHA), N-cyclohexylaniline (CHAN) and dicyclohexylamine (DICHA) production as part of the process. It is believed that under reducing conditions and in the presence of an active catalyst, hydrogenation of the unsaturated ring occurs first to produce CHA, which is then capable of adsorbing aniline onto the surface of catalyst to give rise of CHAN. Finally CHAN which contains one unsaturated ring and one saturated ring is readsorbed onto the surface by the unsaturated ring and is then hydrogenated to give the final DICHA product. A scheme outlining this sequence of concurrent/consecutive process is shown in **Figure 4.14**.

In order to comprehend the space velocity influence on the production of aniline-derived by-products, an aniline hydrogenation experiment on the Sample 2 (310/2, 100 mg) sieved catalyst (500-250 μm) in a $1/4$ inch tubular reactor was carried out. As discussed in **Section 1.3.3**, the strength of adsorption of aniline at the surface of Pd/Al₂O₃ catalyst is thought to be smaller than nitrobenzene, so using more catalyst (100 mg) to obtain a conversion at low temperature seemed like a logical step. Moreover, where the nitrobenzene activation energy has been reported in **section 1.3.5** to be around 40 kJ/mol, the aniline activation energy was reported being higher. Hence, the catalyst was reacted from 30°C to 150°C by increment of 10°C every 2 hours.

The aniline hydrogenation conversion and product selectivities are reported in **Figure 4.11**. Firstly, the conversion of aniline at 30°C is 2% which gradually increased up to 10% at 100°C. The conversion observed at 120 and 140°C was 31 and 35% respectively. When comparing these conversions against those achieved when reacting nitrobenzene with less catalyst present in the reactor, it is evident that the activation energy for aniline hydrogenation is larger than nitrobenzene, but not much larger. Secondly, the selectivity profile observed throughout the temperature ramp is surprising. In fact, at low temperature (30°C) we obtain 100% selectively to the final product DICHA. With increasing temperature, CHAN appears alongside DICHA, where the selectivity towards DICHA decreases with increasing selectivity towards CHAN up to 100°C. This behaviour is surprising because one would expect that the increase of temperature would drive the concurrent/consecutive reaction to the last step but it does exactly the opposite here. One possible explanation is the fact that the reaction is under diffusion control rather than kinetic control. The apparent activation energy was calculated and a value of 25 kJ/mol was obtained which is consistent with the fact that the reaction is under diffusion-

control. From 100°C to 150°C, the selectivity of DICHA was found to be around 1-2% when the CHAN selectivity decreased from 98% to 75%. The reason for this loss of CHAN selectivity can be accredited to the increasing production of CHA in the reaction mixture (observed up to 23% at 150°C).

Considering the production of DICHA at low temperature with a selectivity of 100%, it is evident that the consecutive reduction of CHA to CHAN to DICHA is extremely fast and that neither of the two steps is a limiting factor. At low temperature, the aniline conversion of 2% indicates that the majority of the catalytic surface/bulk is saturated with aniline and only a fraction is reduced to DICHA. With increasing temperature, one would expect an increase in diffusion and activity. Indeed the conversion increases, therefore hydrogenation of the aniline ring will lead to more CHA production which would lead to a rapid transformation to CHAN then DICHA. Considering that an increase of temperature led to an increase of CHA being produced, CHA would react straight away with the adsorbed aniline to form CHAN. CHAN being composed of an unsaturated ring and a saturated ring, we would expect its strength of adsorption to be lower than aniline. With increasing temperature, the desorption of CHAN would be faster than aniline. DICHA being composed of two saturated phenyl rings would suggest that its adsorption on the surface will be highly improbable.

Following this assumption, it is likely that the strength of adsorption of the four components would be from highest to lowest:

1. Aniline (AN)
2. N-cyclohexylaniline (CHAN)
3. Cyclohexylamine (CHA)
4. Dicyclohexylamine (DICHA)

Therefore, it would explain the production of DICHA at low temperatures. Where the release of CHAN relates to increasing temperature and the turnover with DICHA is due to competitive adsorption. Finally, the increase of conversion with temperatures mean that less aniline is able to stay adsorbed on the surface, so the turnover frequency to CHA increases, hence the loss of selectivity to CHAN and the gain to CHA. The scheme for the aniline hydrogenation in the $1/4$ reactor is displayed in **Scheme 4.9**.

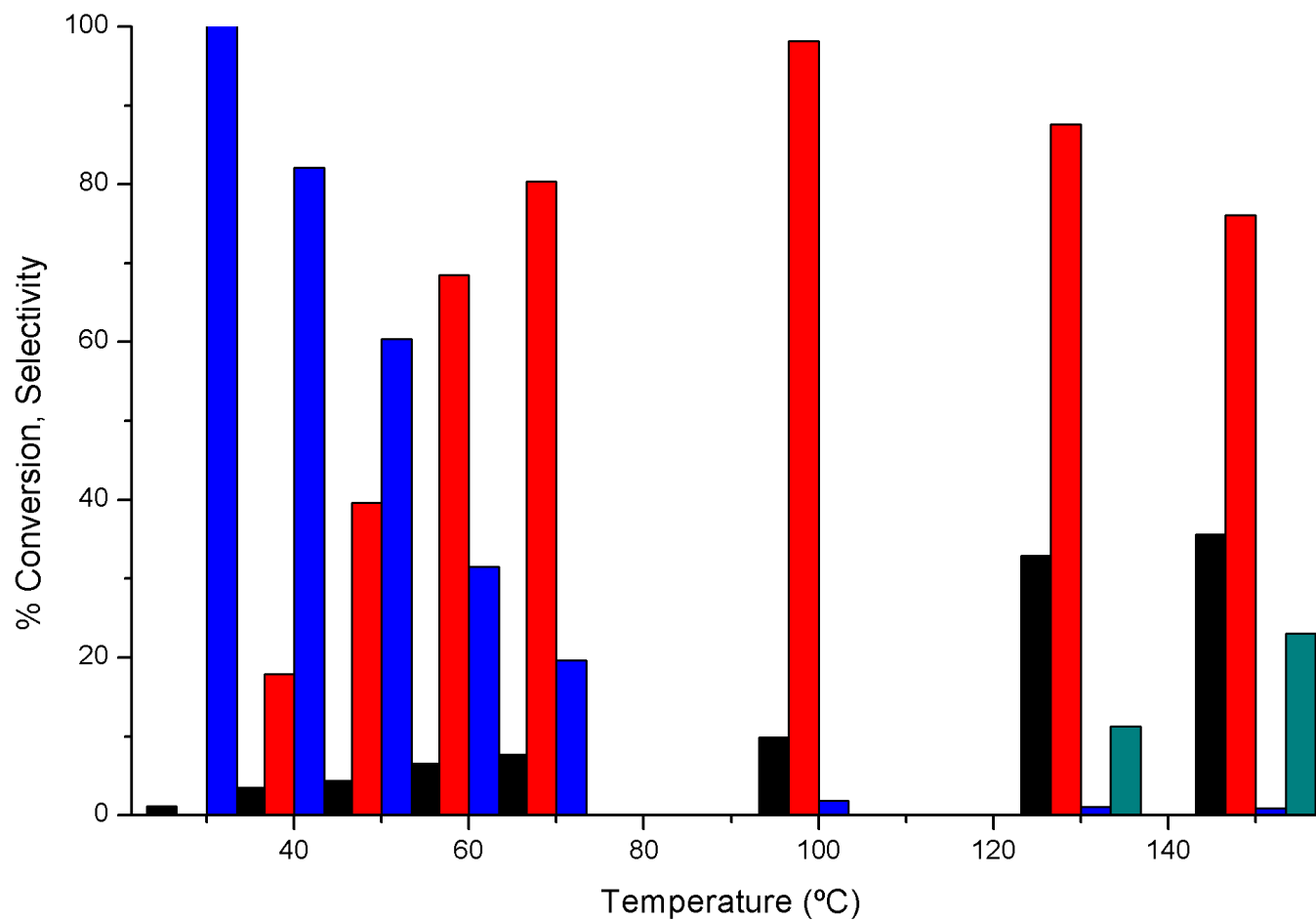
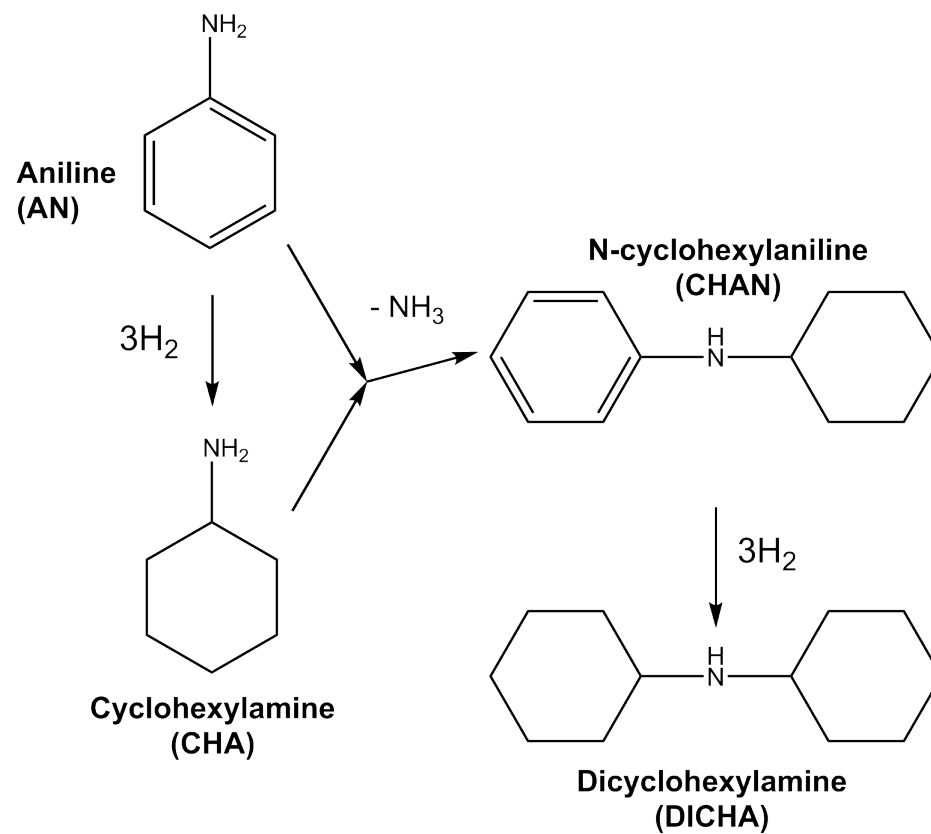


Figure 4.11: Aniline Conversion (black), DICHA selectivity (blue), CHAN selectivity (red) and CHA selectivity (green) are plotted against Temperature. Aniline was placed in a bubbler and 100 mg of the 310/2 catalyst was placed in the tubular reactor.



Scheme 4.9: Aniline Conversion (black), DICHA selectivity (blue), CHAN selectivity (red) and CHA selectivity (green) are plotted against Temperature. Aniline was placed in a bubbler and 100 mg of the 310/2 catalyst was placed in the tubular reactor.

4.2.7 Nitrobenzene and Aniline Activation Energy measurements over 0.3 wt % Pd/Al₂O₃ (Sample 2, 310/2)

Following the difficulties encountered when trying to hydrogenate aniline at low temperature, the activation energy for both nitrobenzene and aniline was measured. The measurement for nitrobenzene hydrogenation is shown in **Figure 4.12** and was carried out using 20 mg of sieved sample 2 and the same reaction procedure as discussed in **Section 2.2**. At low temperature, the apparent activation energy for nitrobenzene was 62 kJ/mol which indicates that it was in a kinetic regime. However, with increasing temperature, the activation energy decreased to 31 kJ/mol which possibly indicates a shift towards diffusion control. When trying to replicate the measurement with 20 mg of sample 2 for the aniline hydrogenation, it was impossible to get any reactivity. So, it was therefore decided that an increase in the mass of catalyst was necessary. Using the same experimental conditions as detailed above but with 100 mg of sieved sample 2, aniline conversion was attainable. Apparent activation energy for the aniline hydrogenation is shown in **Figure 4.13**. The two first points taken at low temperatures (30 and 40°C) and gave an activation energy of 89 kJ/mol, whereas after 50°C it was found decreased to 15 kJ/mol and 5.5 kJ/mol at high temperature. This value indicates that the aniline hydrogenation under these conditions is kinetically driven at low temperature but progresses to a diffusion limited regime at higher temperature.

The values for the activation energy of nitrobenzene hydrogenation in the literature are reported between 40 and 105 kJ/mol [57, 8] so is in agreement with the above result. Although very few publications relate to the activation energy of aniline, it was seen to exhibit a comparable activation energy to that of nitrobenzene hydrogenation over this catalyst. Sokol'skij *et al.* have studied aniline hydrogenation in liquid phase over a deposited ruthenium and rhodium catalysts and reported an activation energy of 50 ± 10 kJ/mol [115]. Aniline hydrogenation was also studied in a trickle bed reactor and the author reported an apparent activation energy of 53 kJ/mol and a true activation energy of 165 kJ/mol [116].

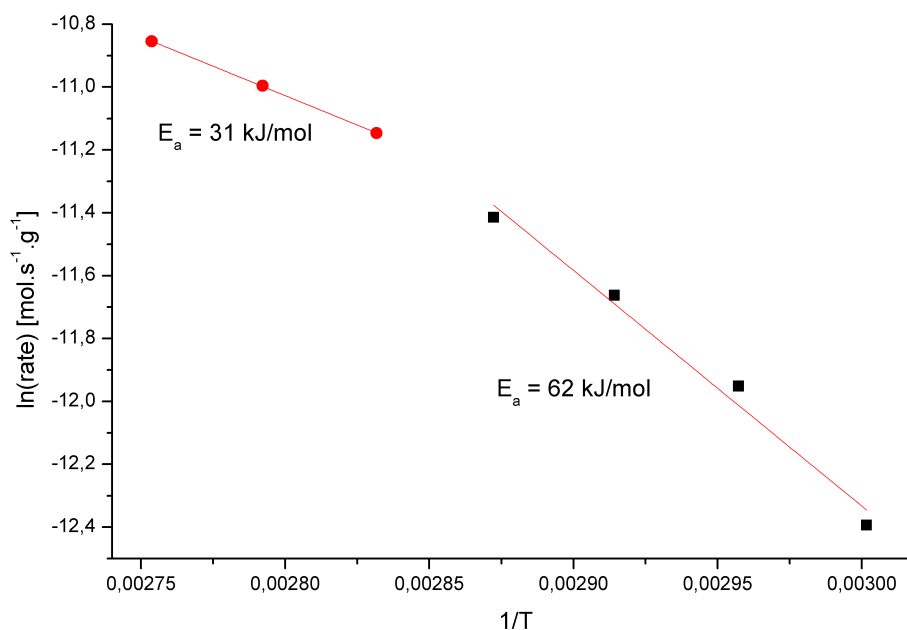


Figure 4.12: Nitrobenzene hydrogenation activation energy measurements plot on 20 mg of sieved catalyst 2 under nitrobenzene/hydrogen/helium feed (NB 2.03×10^{-6} mol/min: H₂ 7.83×10^{-4} mol/min - H₂:NB = 385 : 1).

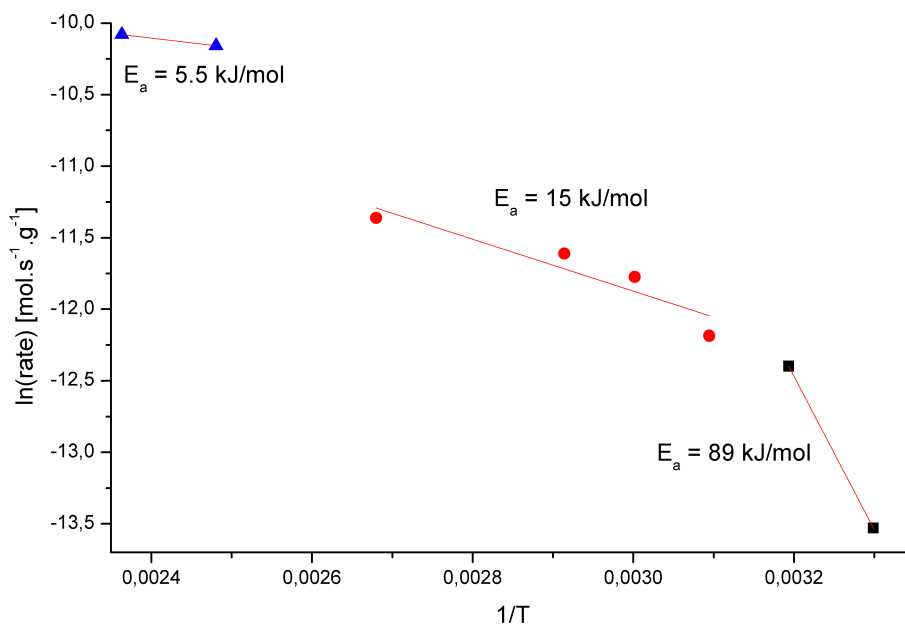


Figure 4.13: Aniline hydrogenation activation energy measurements plot on 100 mg of sieved catalyst 2 under Aniline/hydrogen/helium feed (AN 2.03×10^{-6} mol/min: H₂ 7.83×10^{-4} mol/min - H₂:NB = 385 : 1).

4.3 Summary

An industrial grade 0.3 wt % Pd/Al₂O₃ (Sample 2, 310/2) catalyst, prepared in the form of pellets was sent by Huntsman Polyurethanes and used as a reference catalyst. The previous chapter discussed the feasibility of nitrobenzene hydrogenation on our rig and the use of the different characterisation techniques used in the project. As part of the study, the first objective was to reproduce some reaction testing obtained in a fixed-bed reactor under ambient pressure.

In order to do so, understanding of the reactivity of the as-received sample under our conditions had to be established so that the conditions could be fine tuned in the future to obtain a sub-100% conversion with a high aniline selectivity of 98-99%. Firstly, the as-received catalyst (pellets) was used without further treatment (grinding) in a 1/2 inch tubular reactor. The temperature and catalyst mass was varied to obtain interesting results:

- During a temperature ramp, nitrobenzene conversion displayed a volcano plot type of behaviour, showing a maximum conversion of 100% at 100°C.
- As the temperature was increased to 180-200°C, the aniline selectivity was lost due to the production of aniline derived-byproducts (as observed in **Chapter 3**). The by-products observed were different to the 5 wt % Pd/alumina catalyst, and included the formation of azobenzene and cyclohexanone at high temperature using the pellet catalyst.
- The mass of catalyst was varied to study the influence of space velocity on the conversion and selectivity. Conversion of nitrobenzene was complete until the contact time was reduced by using 50 and 20 mg of catalyst in the reactor. The selectivity was the best for 20 mg of catalyst and the worst for 500 mg.
- The use of high mass of catalyst (high contact time) generated aniline-derived by-products such as CHA, CHAN and DICHA.
- When the contact time between nitrobenzene and the catalyst is extended with a higher mass of catalyst, the aniline produced during the reaction reacts further. This trend can be reduced when using a smaller mass of catalyst which allows nitrobenzene to be reduced to aniline, thus preventing it from reacting further to produce impurities.
- The origin of aniline-derived by-products was investigated using aniline as a feed and the sieved catalyst in a 1/4 inch reactor. The reaction was carried out on the same catalyst by applying the same temperature ramp as in **section 4.1**. Results

indicate that temperature has an influence on the desorption and adsorption of the reactant and products, which can then explain the turnover seen around 100°C.

- Activation measurements were partially compromised by a temperature induced transition towards a diffusion controlled regime. Nevertheless, at low conversions, an activation energy for nitrobenzene hydrogenation of 62 kJ/mol was observed whereas aniline hydrogenation exhibited an E_a value of 54 kJ/mol. These values are thought to indicate that nitrobenzene and aniline exhibit comparable activation energies over catalyst 2.

The results observed in **Chapter 4** improved the nitrobenzene hydrogenation scheme taken from Haber and Gelder [18, 24]. A modified version of the reaction scheme is presented here in **Figure 4.14**.

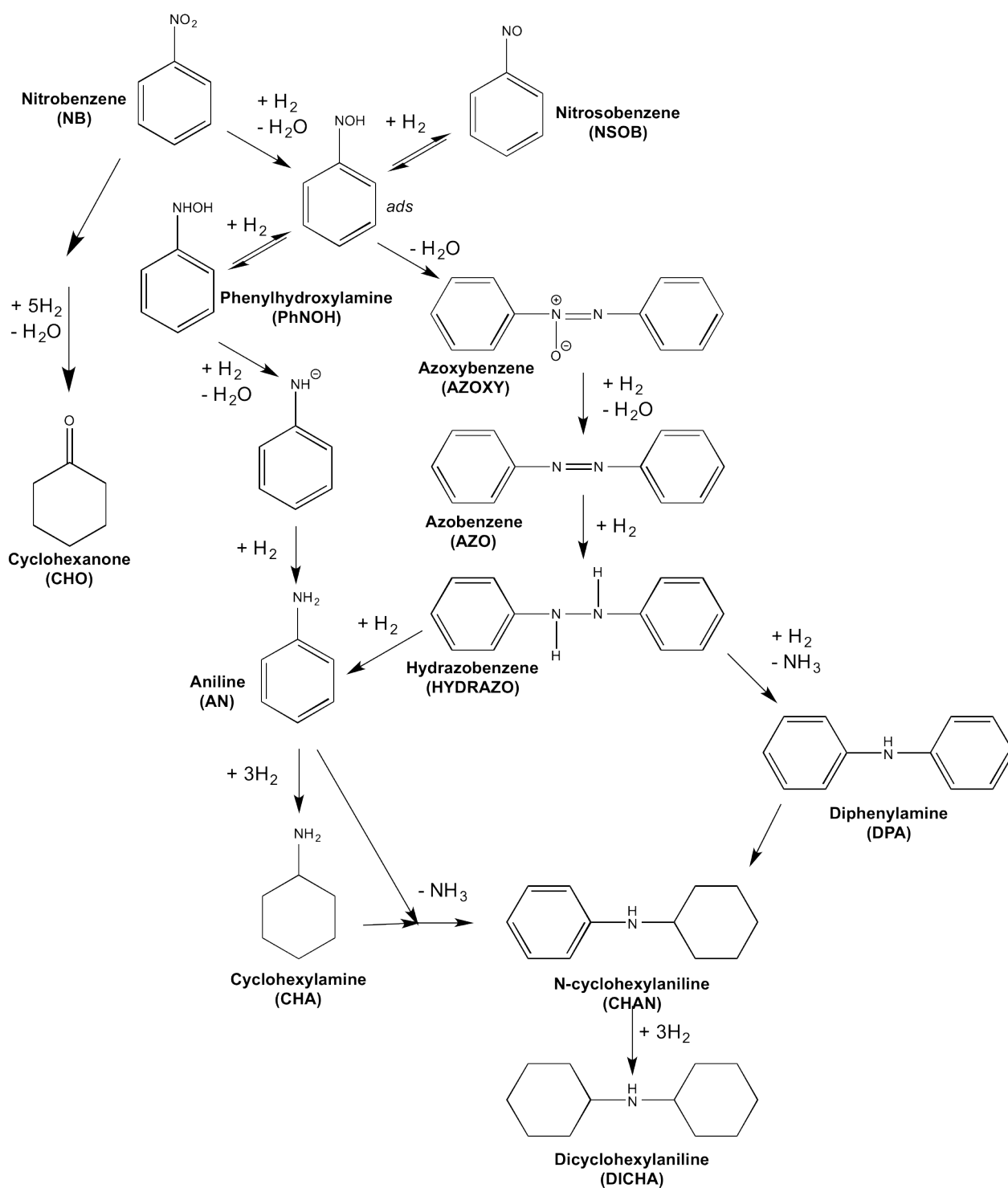


Figure 4.14: Scheme representing the reaction testing data observed so far for the nitrobenzene hydrogenation on Pd/alumina catalysts.

Chapter 5

Nitrobenzene hydrogenation over two 0.3 wt % Pd/Al₂O₃ catalysts: Samples 2 and 3

The structure/activity relationships of the 0.3 wt % Pd/alumina required a deeper understanding of the reactivity before characterising their morphology. In **Chapter 4**, optimal reaction conditions for the nitrobenzene hydrogenation over our lab-scale tubular-reactor were discussed. Two 0.3 wt % Pd/Al₂O₃ supplied by Huntsman Polyurethanes have been tested using a fixed-bed reactor under different conditions. Where, the rig at the industrial complex was fed with a liquid mixture of nitrobenzene, aniline, water and hydrogen (120 excess) and reacted under 20-30 bar pressure at around 230-260°C. These conditions are dictated by the plant engineers as discussed in **Chapter 1**. The experimental results of two 0.3 wt % Pd/Al₂O₃ prototype catalysts are presented in **Figure 1.17**. The plot presents the fraction of 'over-reduction' seen in **Figure 1.8** and 'under-reduction' seen in **Figure 1.7** product formed during the nitrobenzene hydrogenation over the industrial reactor. The two catalysts considered for the study were made by two different companies: Johnson Matthey and BASF. Superficially, they possess the same specifications and yet produce different by-product distributions. Understanding the origins of this difference in selectivity traits is at the heart of this thesis. Catalyst 2 (310/2) and Catalyst 3 (143 500) selectivity profiles are shown here in **Figure 1.17**. Although those 2 catalysts have the same formulation (0.3 wt % Pd/Al₂O₃), they produce different reaction impurities as seen in **Figure 1.7** and **Figure 1.8**. For an industrial process it is mandatory to foresee any type of impurities that could arise during the process so that purification and cleaning treatment can be designed before to avoid huge losses. In general, it could be assumed that two catalysts with equivalent formulation should behave in the same manner, however the preparation process is known to affect the morphology of the catalyst. Therefore, one needs to assess the relationship between the morphology of a Pd/alumina catalyst

and its activity. This chapter will aim to characterise and test these two catalysts with the 1/4 inch reactor in comparable conditions to those studied in **Chapter 4**.

5.1 Temperature-Programmed gas phase Nitrobenzene Hydrogenation

The catalysts were sieved to 500-250 microns and placed in a 1/4 inch tubular stainless-steel reactor then activated as detailed in **Section 2.2**. The temperature was allowed to cool down to 60°C, then the nitrobenzene/helium/hydrogen feed (NB 2.03×10^{-6} mol/min: H₂ 7.83×10^{-4} mol/min - H₂:NB = 385 : 1) was introduced into the reactor. The reaction was allowed to settle overnight at 60°C before the analysis was started. With the exception of the temperature, the reaction conditions remained constant throughout and 20 mg of sieved catalyst was used.

5.1.1 Sample 2 (310/2)

Results for the nitrobenzene hydrogenation carried out on the 310/2 (0.3 wt % Pd/Al₂O₃) catalyst are shown in **Figure 5.3 and 5.4**. The conversion of nitrobenzene shows a high conversion throughout the temperature-programmed reaction as displayed in **Figure 5.3**. At 60°C, conversion is set at 78% which then increased to 86% at 120°C. With the continuous increase of temperature, the conversion decreases and reaches 74% at 180°C. The nitrobenzene conversion profile forms a volcano plot and exhibits optimal conversion at 120°C. The selectivity towards aniline is shown here in **Figure 5.4**. Throughout the temperature program (60-180°C), the selectivity remains very high falling above 99%. However, there is a general trend that sees the loss of selectivity towards aniline with the increase of temperature. This loss is the direct consequence of the production of by-products detected alongside nitrobenzene and aniline, and is shown in **Figure 5.4**. At low temperatures, only one product was detected which disappeared by increasing the temperature from 60 to 80°C. This compound was unknown and the peak found on the chromatogram was located between the peaks corresponding to aniline and nitrobenzene. Identification of this potential intermediate is considered below.

The molar mass and the retention time of all the products detected suggested that the unknown was of a similar molecular weight to nitrobenzene and aniline. All the possible known options as depicted by Haber [18], were injected and analysed using GC but none were successfully identified/matched. The rig was then transformed and a condensation apparatus fitted before the exhaust. By operating the right catalyst (Sample 3) at 60°C over 48 hours under the right conditions, we successfully collected enough liquid to operate a GCMS analysis of the reaction mixture.

The results shown in **Figure 5.1** and **Table 5.1** indicate that the unknown is cyclohexanone oxime ($C_6H_{11}NO$). It is believed to originate from the phenylhydroxylamine in the presence of an excess of hydrogen as explained by Egberink *et al.* [117]. In the presence of a carbonyl and an amino alcohol, these react together to form a hydroxylamine, which in acidic conditions gives an oxime. The mechanism discussed in **Section 1.3.2** shows that phenylhydroxylamine is a common intermediate of the direct hydrogenation route as proposed by Haber [18], so it is possible that cyclohexanone oxime occurs through the phenylhydroxylamine intermediate as shown in **Figure 5.2**.

M/Z	%	Composition
41.1	18	C_2H_3N
42.1	6.8	C_2H_4N
54	11	C_3H_4N
55.1	10	C_4H_7
59.1	7.9	C_2H_5NO
67.1	6.1	C_4H_5N
68.1	6.1	C_4H_6N
69.1	4.5	C_4H_7N
72.1	6.6	C_4H_8O
81.1	4.5	C_6H_9
96.1	3.5	$C_6H_{10}N$
98.2	4.5	C_5H_8NO
113	11	$C_6H_{11}NO$

Table 5.1: Mass Measurement of the Cyclohexanone Oxime (CHOX) [118]

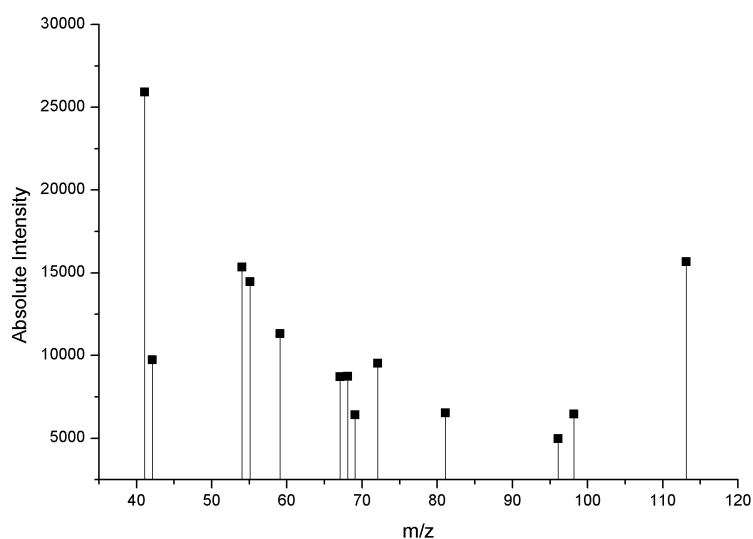


Figure 5.1: Mass spectrum of unknown molecule collected from Sample 2.

After the formation of the cyclohexanone oxime at $60^\circ C$, the increase of temperature to $80^\circ C$ leads to a selectivity of 100% towards aniline. Upon this temperature increase, appearance of N-cyclohexylaniline occurs at 100 and $120^\circ C$ with a gradual rise in quantity

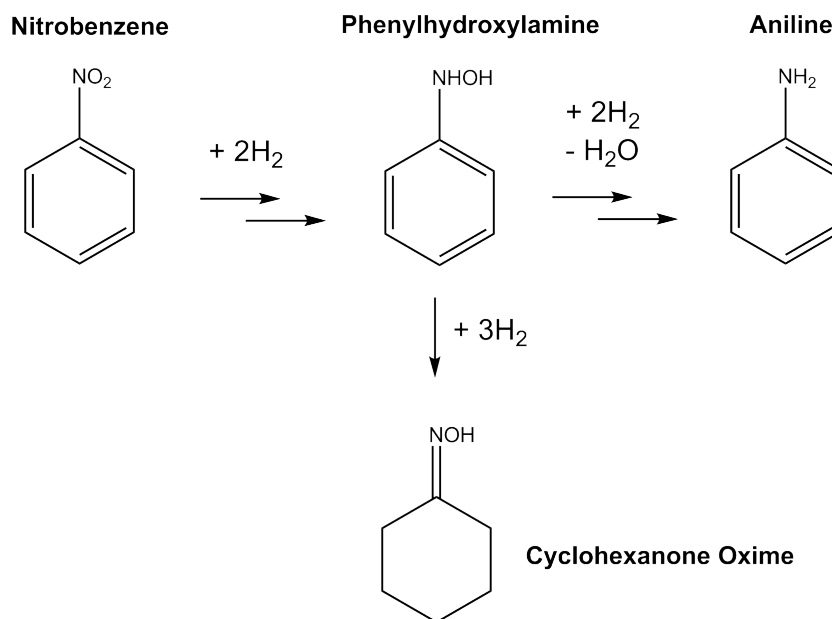


Figure 5.2: Suggestion of the provenance of the Cyclohexanone Oxime (CHOX) molecule.

(0.12 to 0.25%) in CHAN selectivity. Alongside the formation of CHAN, dicyclohexylamine appeared in a much lower quantity between 140 and 180°C. At high temperatures, the loss of selectivity to aniline is due to further hydrogenation leading to CHAN and DICHA as discussed earlier in **Chapters 3 and 4**.

The formation of cyclohexanone oxime as part of the catalytic nitrobenzene hydrogenation was poorly described in the literature until Corma *et al.* [119] published a study in 2014 concerning the synthesis of cyclohexanone oxime (CHOX) from nitrobenzene using a bifunctional catalyst. CHOX was formed from nitrobenzene with a 97% yield in a one-pot reaction catalysed by gold and palladium nanoparticles on carbon. The reaction was carried out at 60°C (the temperature at which we witnessed the formation of CHOX in our continuous flow reactor) in the presence of a catalytic amount of AuPd/C and hydroxylamine hydrochloride. Corma states that the aniline produced is further reduced to produce the N-cyclohexylaniline (CHAN) which in liquid phase forms an equilibrium with N-cyclohexylideneaniline ($\text{C}_{12}\text{H}_{15}\text{N}$, ANIL). In the presence of a catalytic amount of hydroxylamine, the imine (ANIL) undergoes a hydrogenolysis to produce cyclohexanone oxime (CHOX) and hydrochloric acid. In the presence of water, the CHOX obtained can be oxidised to cyclohexanone.

This study correlates and justifies the observation and assumption made previously and enables further development of the nitrobenzene reaction scheme further as seen in **Figure 5.4**.

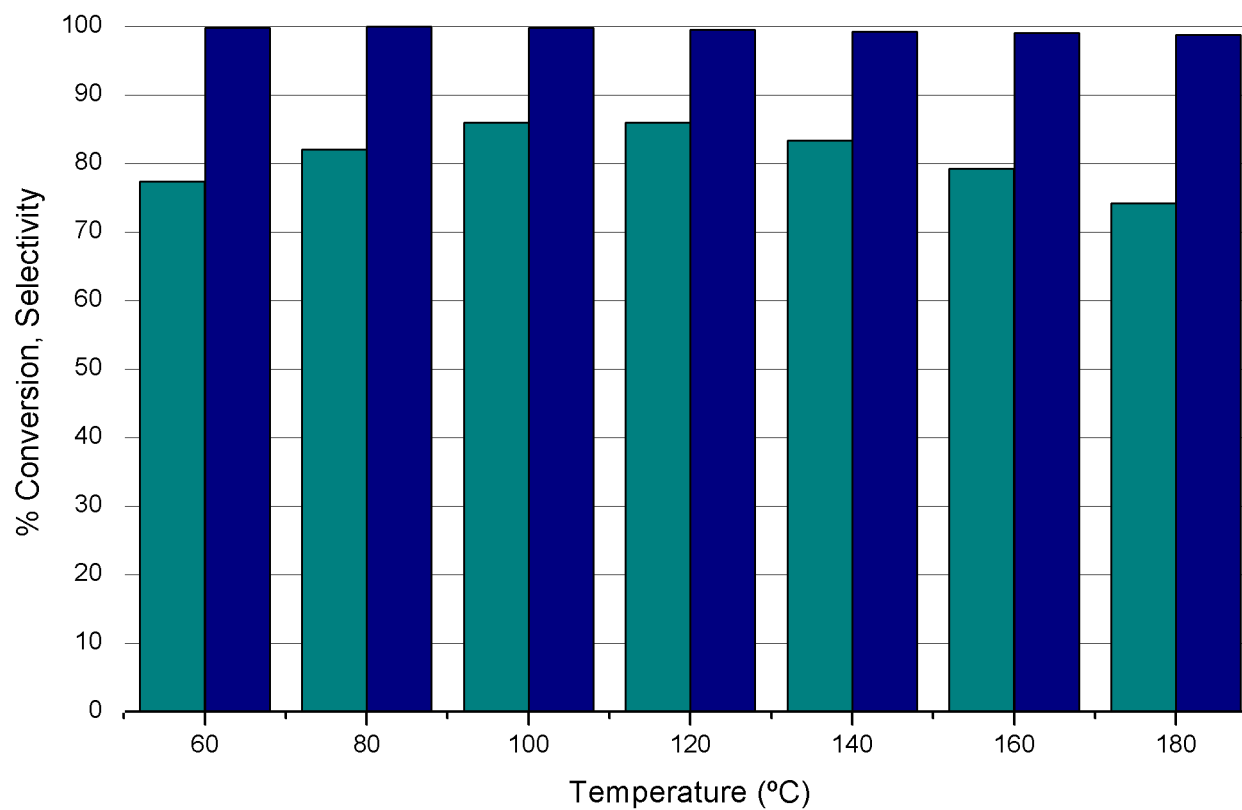


Figure 5.3: Nitrobenzene conversion (green) and aniline selectivity (blue) as a function of reaction temperature over 0.3wt% Pd/alumina (Sample 2, 310/2) catalyst. Catalyst was sieved to 500-250 microns before reaction and 20 mg was placed in the stainless steel 1/4 inch tubular reactor. nitrobenzene/hydrogen flow was kept constant throughout the reaction. Each temperature was kept for an hour before increasing by 20°C until reaching 180°C (NB 2.03×10^{-6} mol/min: H₂ 7.83×10^{-4} mol/min - H₂:NB = 385 : 1, NB(s⁻¹) : Pd_(s) = 1 : 4.5).

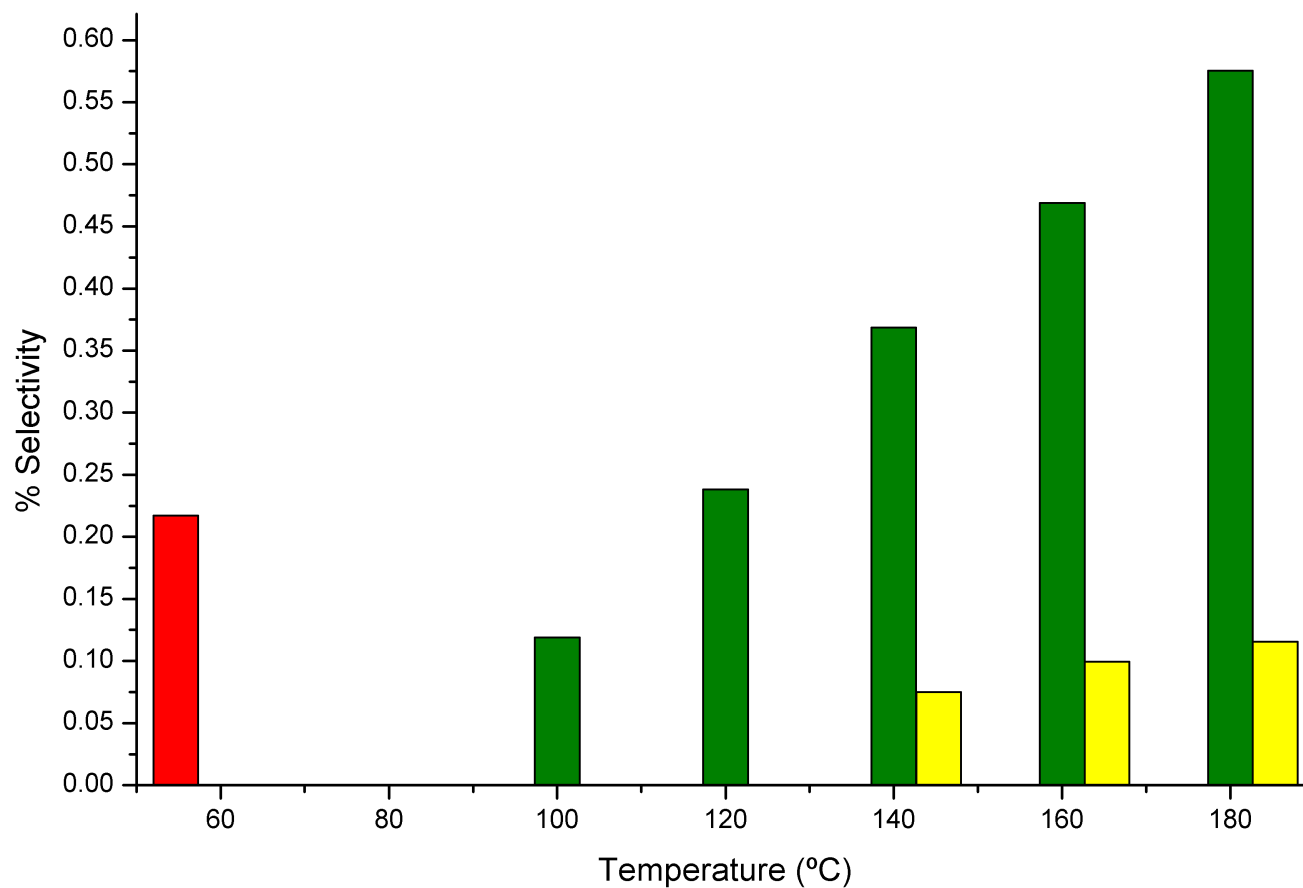
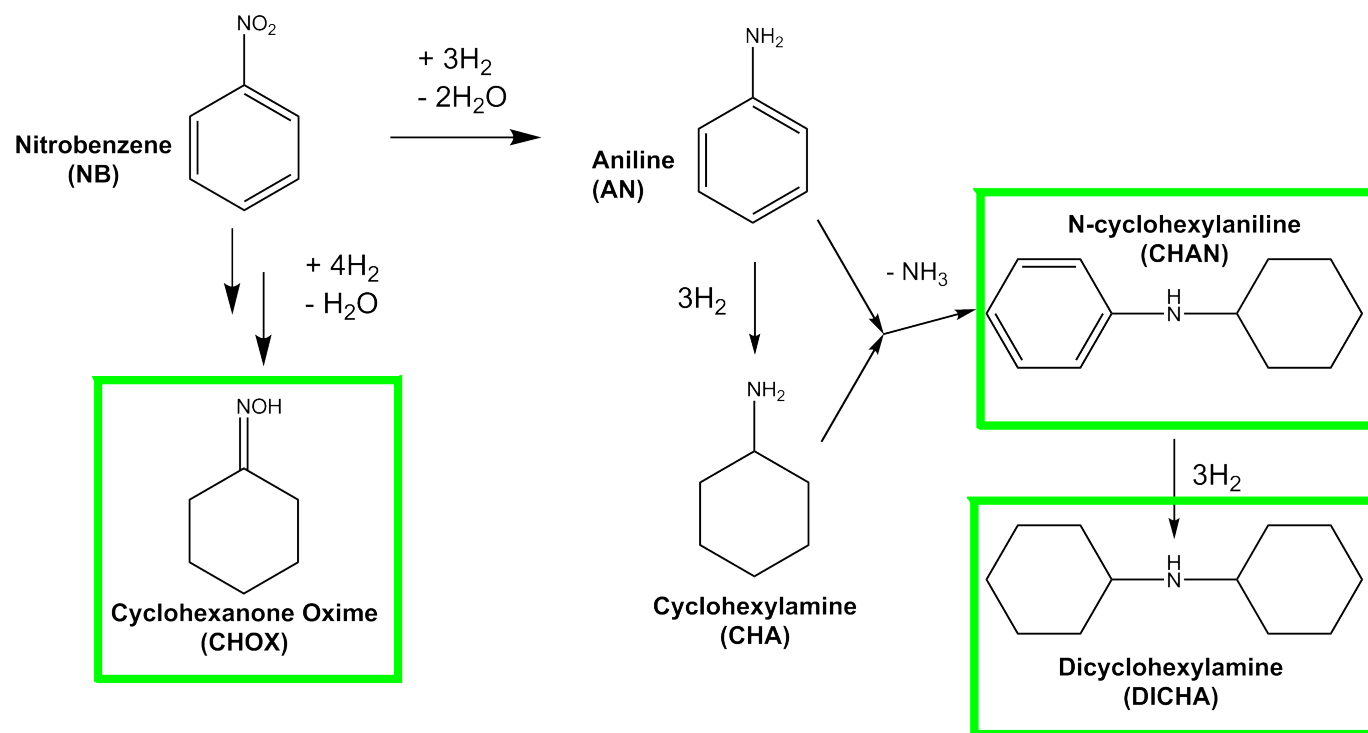


Figure 5.4: Selectivity profile (%) of the by-products produced as a function of reaction temperature over 0.3wt% Pd/alumina (Sample 2, 310/2) catalyst. Catalyst was sieved to 500-250 microns before reaction and 20 mg was placed in the stainless steel 1/4 inch tubular reactor. Nitrobenzene/hydrogen flow was kept constant throughout the reaction. Each temperature was kept for an hour before increasing by 20°C until reaching 180°C. Cyclohexanone oxime (red), N-cyclohexylaniline (green) and dicyclohexylaniline (yellow) are observed (NB 2.03×10^{-6} mol/min: H_2 7.83×10^{-4} mol/min - H_2 :NB = 385 : 1, NB(s^{-1}) : Pd(s) = 1 : 4.5).



Scheme 5.1: Observed scheme of nitrobenzene hydrogenation in a fixed-bed tubular reactor observed with catalyst 2 (310/2).

5.1.2 Sample 3 (143 500)

Results for the nitrobenzene hydrogenation carried out using the 0.3 wt % Pd/Al₂O₃ (Sample 3, 143 500) catalyst and are shown in **Figures 5.6 and 5.7**. The conversion of nitrobenzene shows a mild conversion throughout the temperature-programmed reaction as displayed in **Figure 5.6**. At 60°C, conversion is set at 58% and increases to 64% at 120°C. With the continuous increase of temperature, the conversion remains constant until 180°C. The selectivity towards aniline is shown in **Figure 5.6**. Throughout the temperature program (60-180°C), the selectivity remains above 99%. A loss is the direct consequence of the production of by-products detected alongside nitrobenzene and aniline as shown in **Figure 5.7**. At 60°C, cyclohexanone oxime (CHOX) was detected and the amount of CHOX was found to decrease with increasing temperature up to 120°C. Further CHOX was not detected after 120°C. However at 100°C, azobenzene was recorded and found to increase with the temperature program. In parallel, after CHOX disappeared, cyclohexanone was monitored at 140°C and rose with the temperature as well. This is shown in **Figure 5.7**.

The turnover between CHOX and CHO with an increase in temperature suggests that there is a correlation/dependency between the two compounds. As a matter of fact, Egberink *et al.* pointed out that an equilibrium exists between cyclohexanone and cyclohexanone oxime as shown in **Figure 5.5** [117]. Considering that there are 2 moles of water produced per mole of aniline produced (**Section 1.3.2**), the conditions are favourable to shifting the equilibrium towards the production of cyclohexanone (**figure 5.5**).

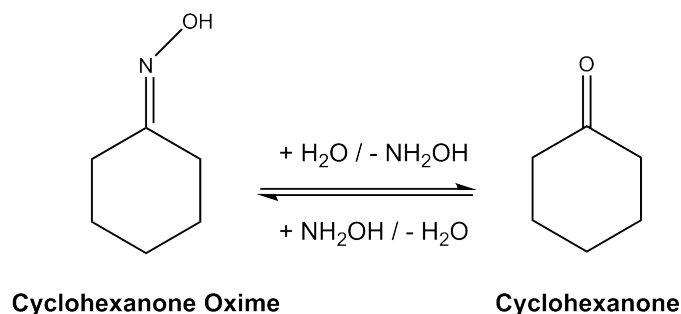


Figure 5.5: Equilibrium between cyclohexanone oxime (CHOX) and cyclohexanone (CHO).

The 0.3 wt % Pd/Al₂O₃ (Sample 3, 143 500) catalyst exhibits the production of nitrobenzene derived-product as discussed earlier and favours the production of cyclohexanone oxime and cyclohexanone. The production of azobenzene may be due to the different adsorption strength of the intermediates at the surface of the catalyst.

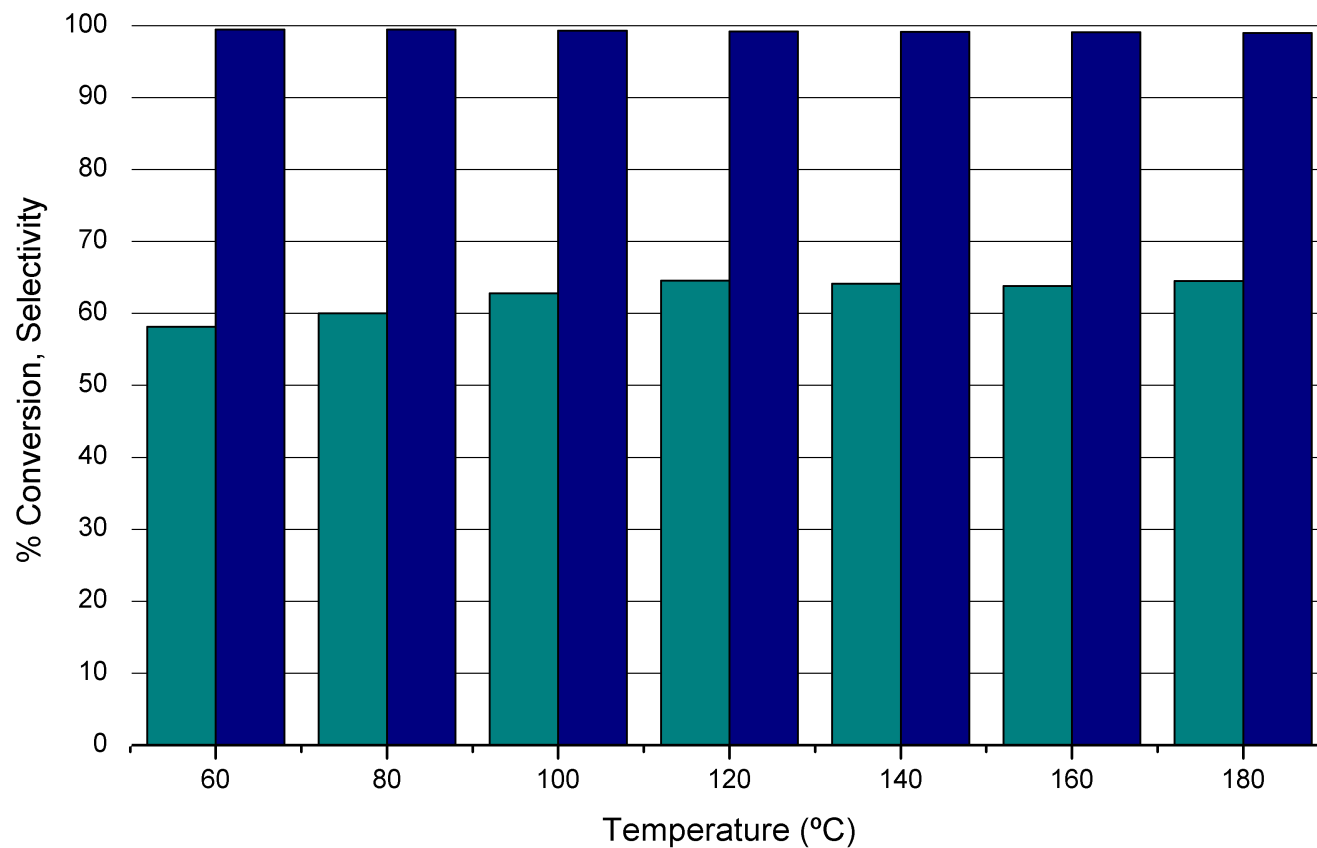


Figure 5.6: Nitrobenzene conversion (green) and aniline selectivity (blue) as a function of reaction temperature over 0.3 wt % Pd/alumina (Sample 3, 143 500) catalyst. Catalyst was sieved to 500-250 microns before reaction and 20 mg was placed in the stainless steel 1/4 inch tubular reactor. Nitrobenzene/hydrogen flow was kept constant throughout the reaction. Each temperature was kept for an hour before increasing by 20°C until reaching 180°C (NB 2.03×10^{-6} mol/min: H₂ 7.83×10^{-4} mol/min - H₂:NB = 385 : 1, NB(s⁻¹) : Pd_(s) = 1 : 7.7).

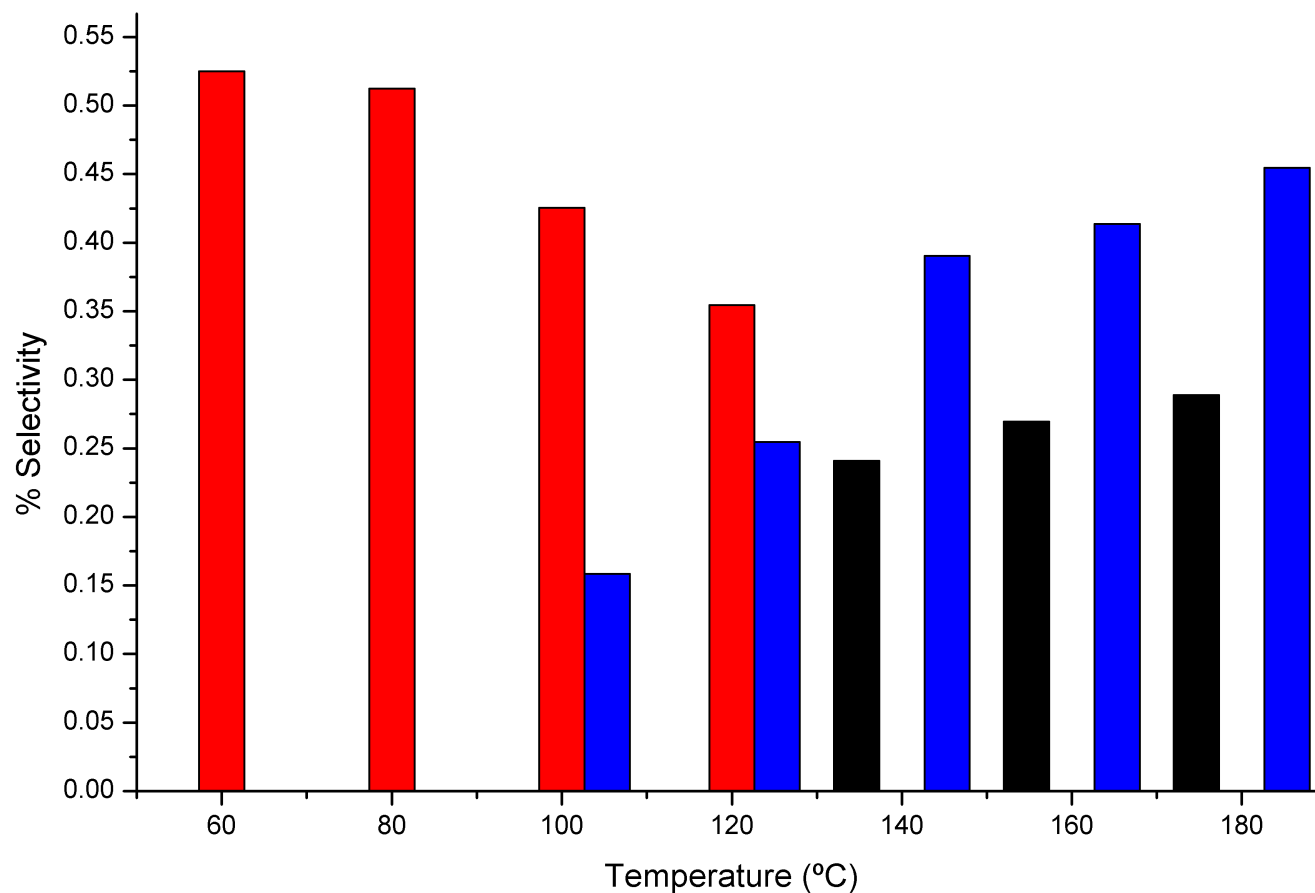
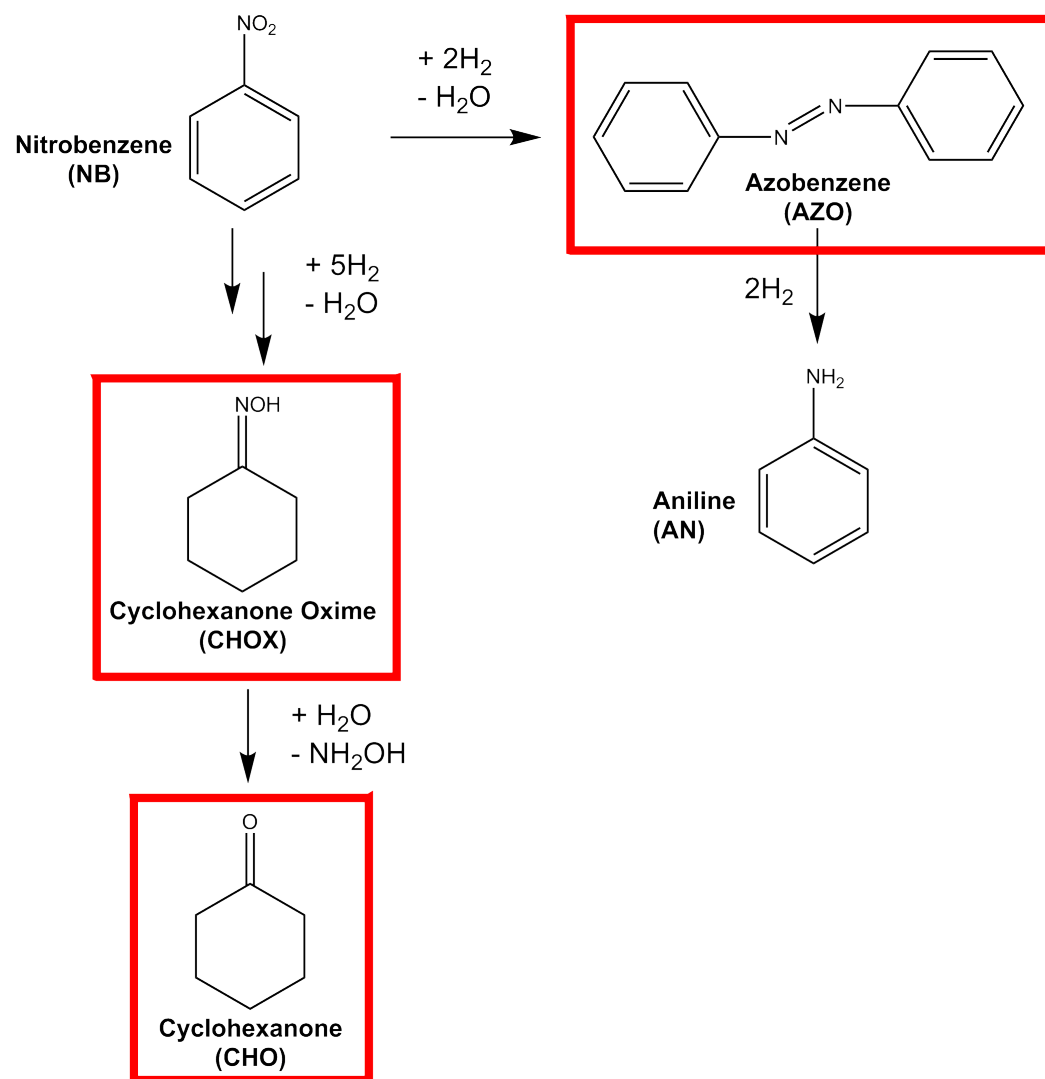


Figure 5.7: Selectivity profile (%) of the by-products produced as a function of reaction temperature over 0.3 wt % Pd/alumina (Sample 3, 143 500) catalyst. Catalyst was sieved to 500-250 microns before reaction and 20 mg was placed in the stainless steel $\frac{1}{4}$ inch tubular reactor. Nitrobenzene/hydrogen flow was kept constant throughout the reaction. Each temperature was kept for an hour before increasing by 20°C until reaching 180°C. Cyclohexanone oxime (red), N-cyclohexylaniline (blue) and cyclohexanone (black) are observed (NB 2.03×10^{-6} mol/min: H₂ 7.83×10^{-4} mol/min - H₂:NB = 385 : 1, NB(s⁻¹) : Pd_(s) = 1 : 7.7).



Scheme 5.2: Observed scheme of nitrobenzene hydrogenation in a fixed-bed tubular reactor observed with catalyst 3 (143 500).

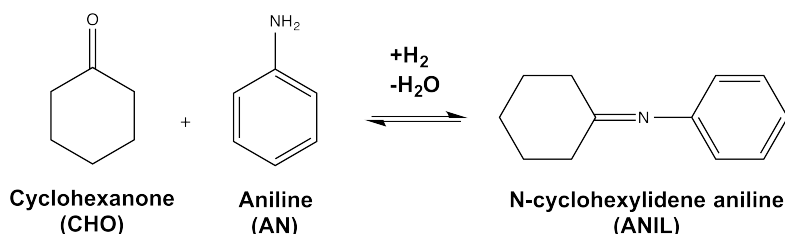
5.1.3 Summary

The reaction testing of both 0.3 wt % Pd/Al₂O₃ (Samples 2 and 3) gave interesting observations.

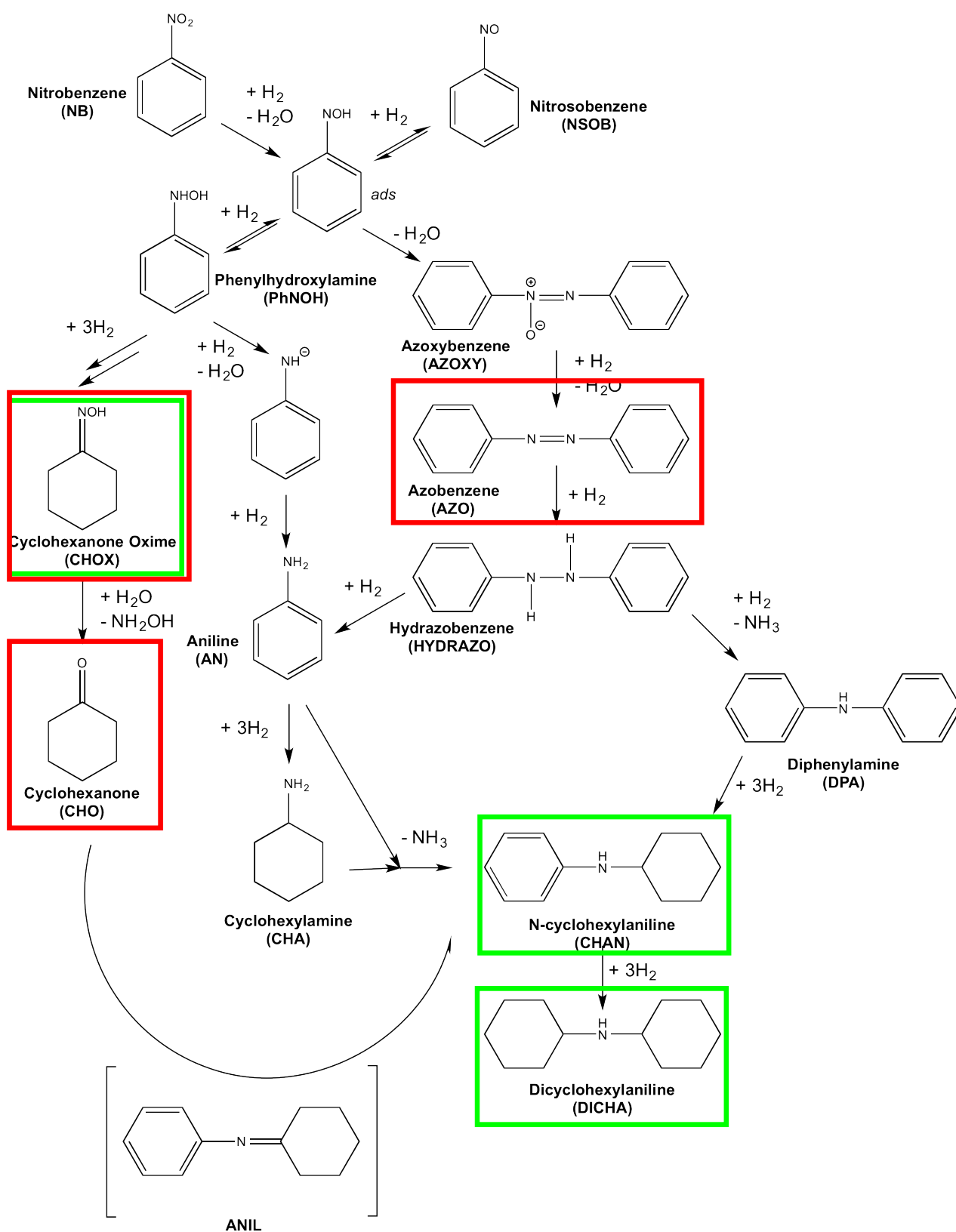
1. Sample 2 gave a higher conversion than Sample 3.
2. Both catalysts exhibited high selectivity towards the aniline product (>99%).
3. The loss of selectivity for both catalysts increased with temperature but remained relatively low (less than 1%).
4. At low temperature, both catalysts led to the production of cyclohexanone oxime, where catalyst 3 produced more.
5. With increasing temperature, the catalysts carried out different chemistry using the same reaction conditions. Catalyst 2 clearly exhibited aniline-derived chemistry, whilst catalyst 3 led to nitrobenzene-derived chemistry and the production of cyclohexanone arose from one of the nitrobenzene hydrogenation direct route intermediates.

The scheme presented hereafter displays the N-cyclohexylideneaniline (ANIL) as an intermediate between the cyclohexanone (CHO) and N-cyclohexylaniline (CHAN). In an industrial environment, the ANIL compound is formed in a homogeneous reaction between cyclohexanone (CHO) and aniline (AN), as presented hereafter in **Scheme 5.3**. Finally, the lab-scale reaction testing of the catalysts met the industrial requirement. Two catalysts with the same formulation provided different impurities originating from different reaction route as displayed earlier in this chapter in **Figure 1.17**, laid out in **Scheme 5.4**.

Therefore, a thorough characterisation of the catalysts surface is mandatory.



Scheme 5.3: Scheme for the formation of N-cyclohexylidene aniline (ANIL) in a solution of aniline (AN) and cyclohexanone (CHO).



Scheme 5.4: Nitrobenzene hydrogenation scheme showing in red the impurities produced while operating catalyst 3 and catalyst 2 in green.

5.2 Characterisation

5.2.1 Atomic Absorption

Catalyst	Actual Weight % Loading
0.3 wt % Pd/Al ₂ O ₃ (Sample 2, 310/2)	0.31±0.03
0.3 wt % Pd/Al ₂ O ₃ (Sample 3, 143 500)	0.25±0.03

Table 5.2: Actual Metal Loading From Atomic Absorption Spectroscopy measurements

The value for the 143 500 catalyst was found to be lower than the advertised loading. This could be attributed to the palladium not being properly leached from the support during the preparation stage of the solution.

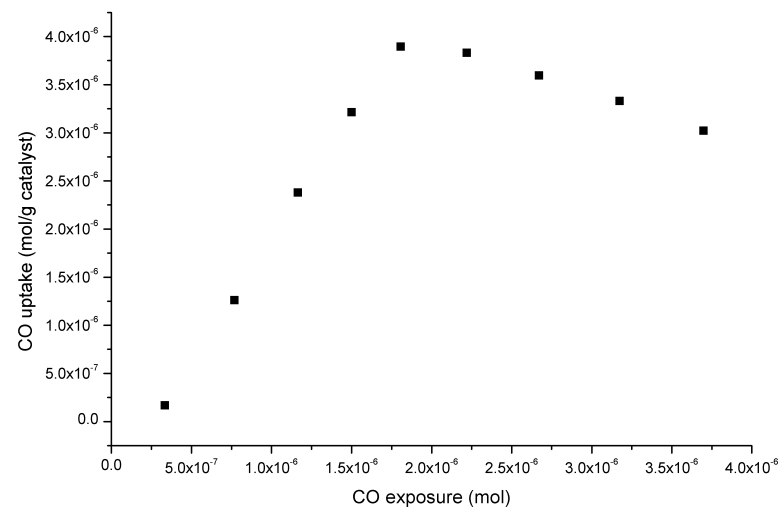
5.2.2 CO adsorption isotherms

CO chemisorption was carried out as discussed in **Section 2.4.7** considering the stoichiometry CO:Pd to be 1:2. CO isotherm plots for the 0.3 wt % Pd/Al₂O₃ (310/2) are shown in **Figures 5.8a and 5.8b**. CO isotherm plots for the 0.3 wt % Pd/Al₂O₃ (143 500) are shown in **Figures 5.9a and 5.9b**. All saturation values and subsequent calculated dispersion and estimated particle size are presented here in Table 2.

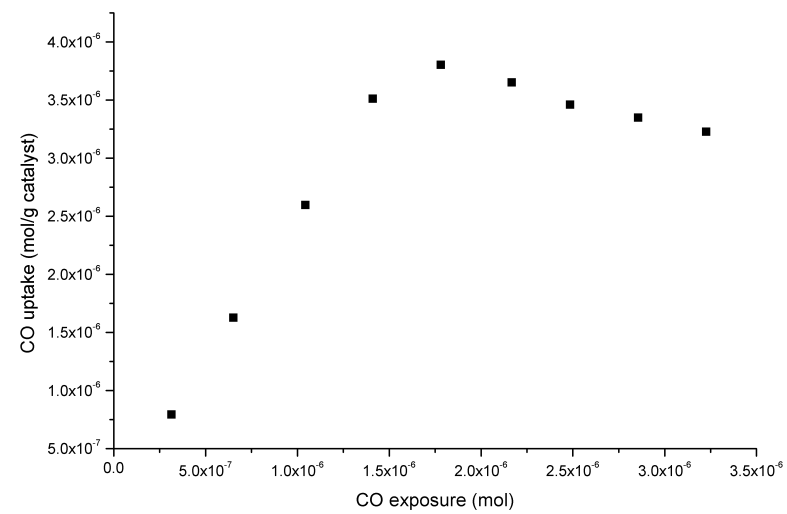
Catalyst		CO uptake (mol CO / g catalyst)	Dispersion (%)	Particle size (nm)
Sample 2, 310/2	1	3.89 x 10 ⁻⁶	27.6	3.9
	2	3.80 x 10 ⁻⁶	26.7	4
Sample 3, 143 500	1	6.84 x 10 ⁻⁶	48.5	2.2
	2	6.67 x 10 ⁻⁶	47.3	2.3

Table 5.3: Table of Dispersions for CO Pulsed Chemisorptions.

It is obvious from the results that the palladium particles morphology at the surface of both catalysts is different and needs further investigation. As discussed earlier in **Chapter 1**, a difference in particle size and hence morphology can lead to drastic changes in catalyst selectivity [99, 120].

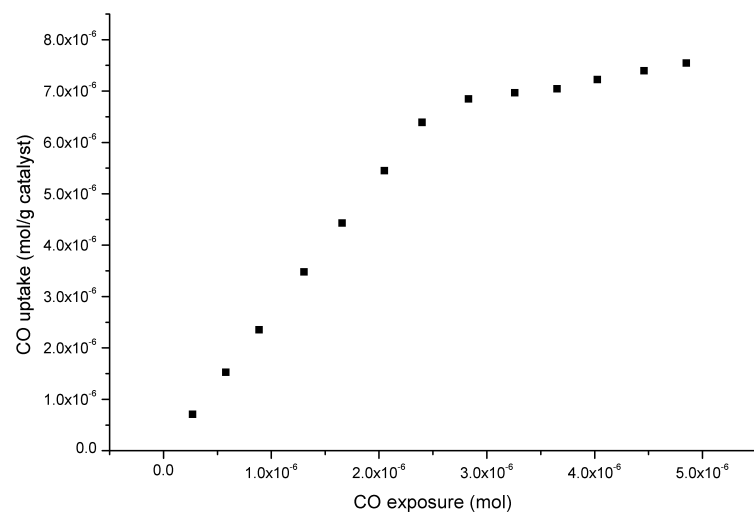


(a)

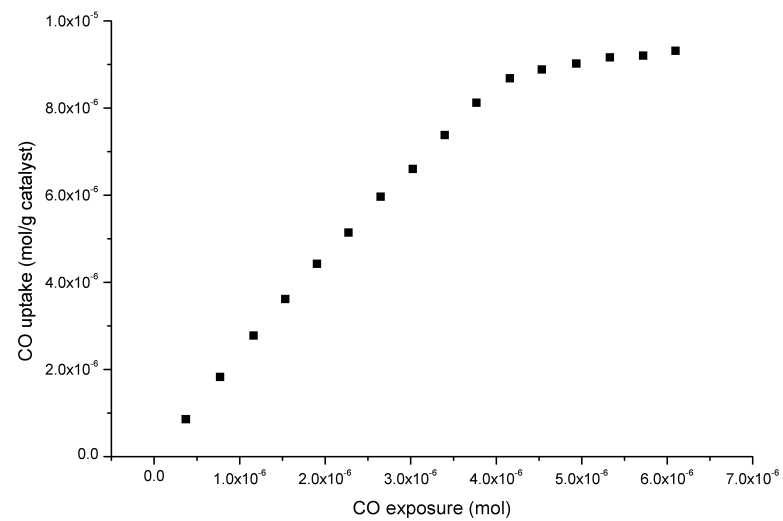


(b)

Figure 5.8: Pulsed CO Chemisorption Isotherm on 0.3wt% Pd/alumina (Sample 2, 310/2)



(a)



(b)

Figure 5.9: Pulsed CO Chemisorption Isotherm on 0.3wt% Pd/alumina (Sample 3, 143 500)

5.2.3 Transmission Electron Microscopy

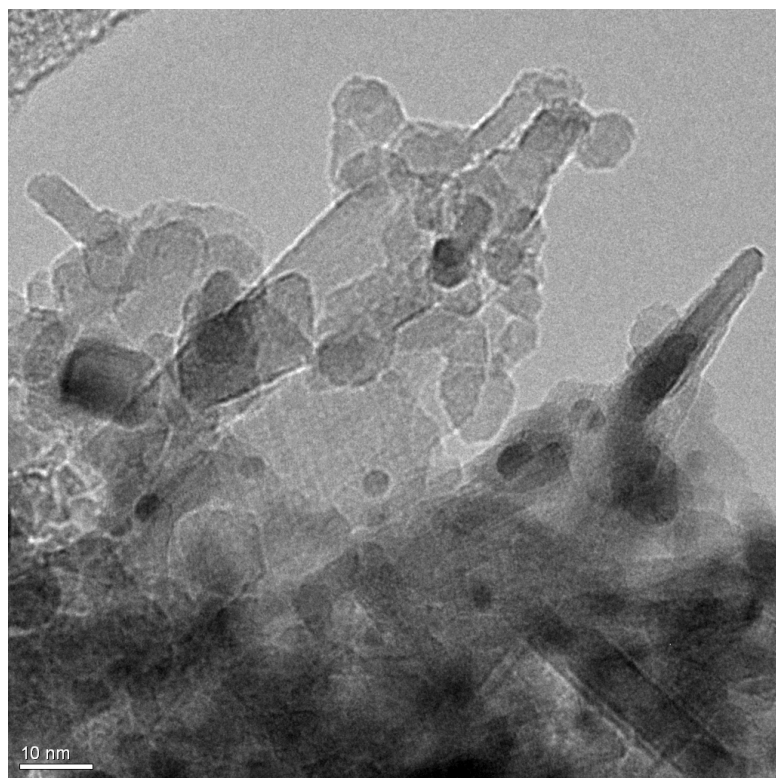
TEM pictures of the 310/2 catalyst are shown in **Figures 5.10a and 5.10b**. The catalyst 143 500 catalyst is shown in **Figures 5.11a and 5.11b**. All micrographs were taken on non-activated samples.

Considering the AAS and CO pulse chemisorption measurements, some palladium crystallites should be detectable but the loading and dispersion could make them difficult to spot. Moreover, one should note that TEM imaging is a 2D representation of a 3D object. So care should be taken when trying to explain geometry and structure. It was however possible to monitor some particles on both catalysts.

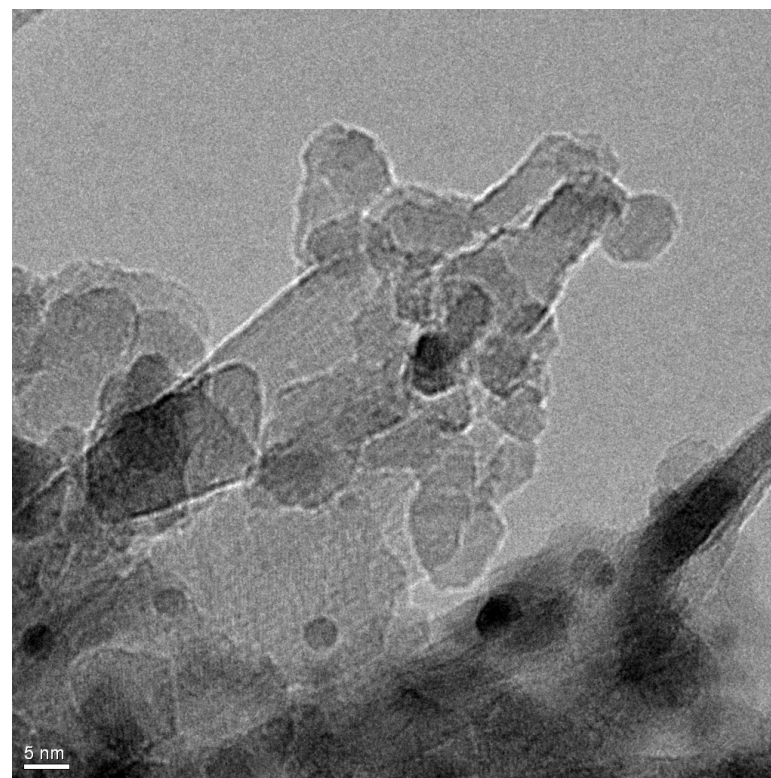
Figure 5.10a shows the alumina support randomly organised with a few darker circular shaped particles visible which can be attributed to palladium. By increasing the magnification, **Figure 5.10b** shows that there are three, round shaped palladium particles present which are each around 4 nm in size. This is consistent with the CO pulse chemisorption carried out in **Section 5.2.2** (the white bar scale represents 5 nm).

Figure 5.11a displays a large alumina particle which shows multiple holes and black particles. **Figure 5.11b** was obtained after further magnification. It was then possible to distinguish clear palladium particles which are highly dispersed on the surface of the support. Moreover, the shape of the particle seems to be different to catalyst 2, where they have a oblical/prismatic shape. It was now possible to measure the particle more accurately, but it was found that depending of their orientation we can distinguish two different dimensions where one side measured at around 2 nm and the other 4nm.

These observations are broadly consistent with the mean Pd particle size as determined by CO adsorption isotherm measurements.

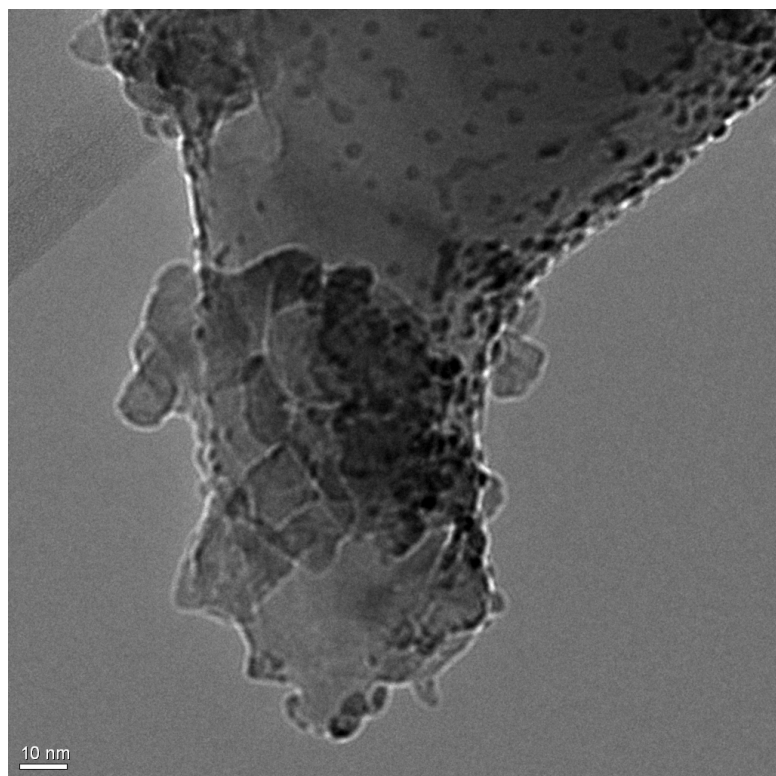


(a)

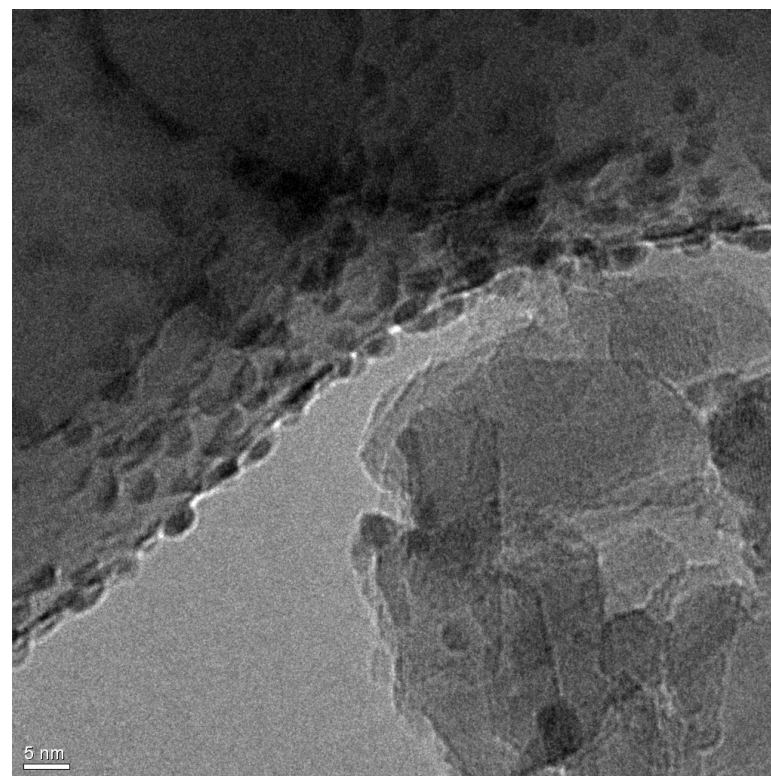


(b)

Figure 5.10: Transmission Electron Microscopy of the 0.3 wt % Pd/alumina (Sample 2, 310/2) catalyst recorded at low magnification (left) and high magnification (right).



(a)



(b)

Figure 5.11: Transmission Electron Microscopy of the 0.3wt% Pd/alumina (Sample 3, 143 500) catalyst recorded at low magnification (left) and high magnification (right).

5.2.4 X-ray Powder Diffraction

The powder X-ray diffraction patterns obtained for the catalyst 2 (0.3 wt % Pd/Al₂O₃, 310/2) are presented in **Figure 5.13**. First, the XRD was unable to detect the palladium particles which is consistent with the estimated particle size recorded in **Sections 5.8 and 5.10**. As a result, the diffraction pattern is totally dominated by the alumina support. The diffractogram displays an amorphous character, but with the help of literature and the XRD database, peaks could be assigned to δ -alumina [121, 122] which closely overlapped with θ -alumina. As shown in the **Table 5.4**, the diffraction pattern indicates that the alumina used is a δ/θ and originates from Boehmite (AlOOH) as shown in **Figure 5.12** [121, 123].

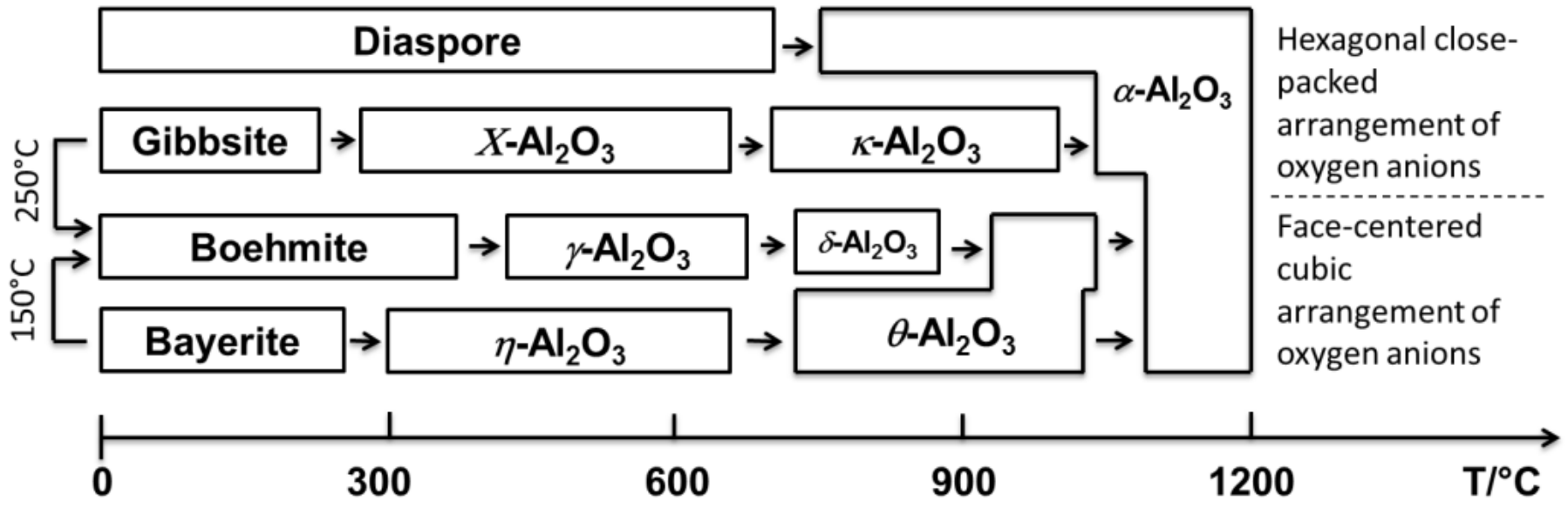


Figure 5.12: Temperature transformation of hydroxides or oxohydroxides to corundum via the formation of transitional alumina phases [123].

The diffractogram presented in **Figure 5.14** was carried out on the catalyst 3 (0.3 wt % Pd/Al₂O₃, 143 500). With the previous catalyst, no detection of palladium particles was possible, due to the size of the particles. The sharp reflections are indicative of a high degree of long range order within alumina. The transition alumina used for this catalyst was assigned to α -alumina. There was also an additional contribution, which arose from the θ -alumina which can be explained using to the phase diagram presented in **Figure 5.12**.

The supports used for both catalysts are clearly different so will therefore exhibit different behaviours. A high surface area for the first catalyst should be expected with an average pore distribution, a small surface area with larger pores is expected for the second catalyst. The second catalyst support should prove to be more durable and resistant to severe reaction conditions.

2 Θ Angle (degrees)	Theta		Delta	
	d spacing (\AA)	h k l	d spacing (\AA)	h k l
31.44	2.82737	400		
32.74	2.729	202	2.73067	222
36.8	2.44529	111		
39	2.3121	401		
39.52			2.28062	226
45.12	2.02006	311		
45.52			1.99028	400
46.84			1.94955	0.0.12
47.5			1.90956	318
50.72	1.79866	510		
57.38	1.62049	203		
60.06	1.54207	313		
63.98	1.45505	020		
64.18			1.44991	440
66.77			1.39986	4.0.12
67.14	1.38721	712		

Table 5.4: Assignments of the 310/2 catalyst diffraction pattern. The green drop lines represent θ -alumina and the red the δ -alumina [95].

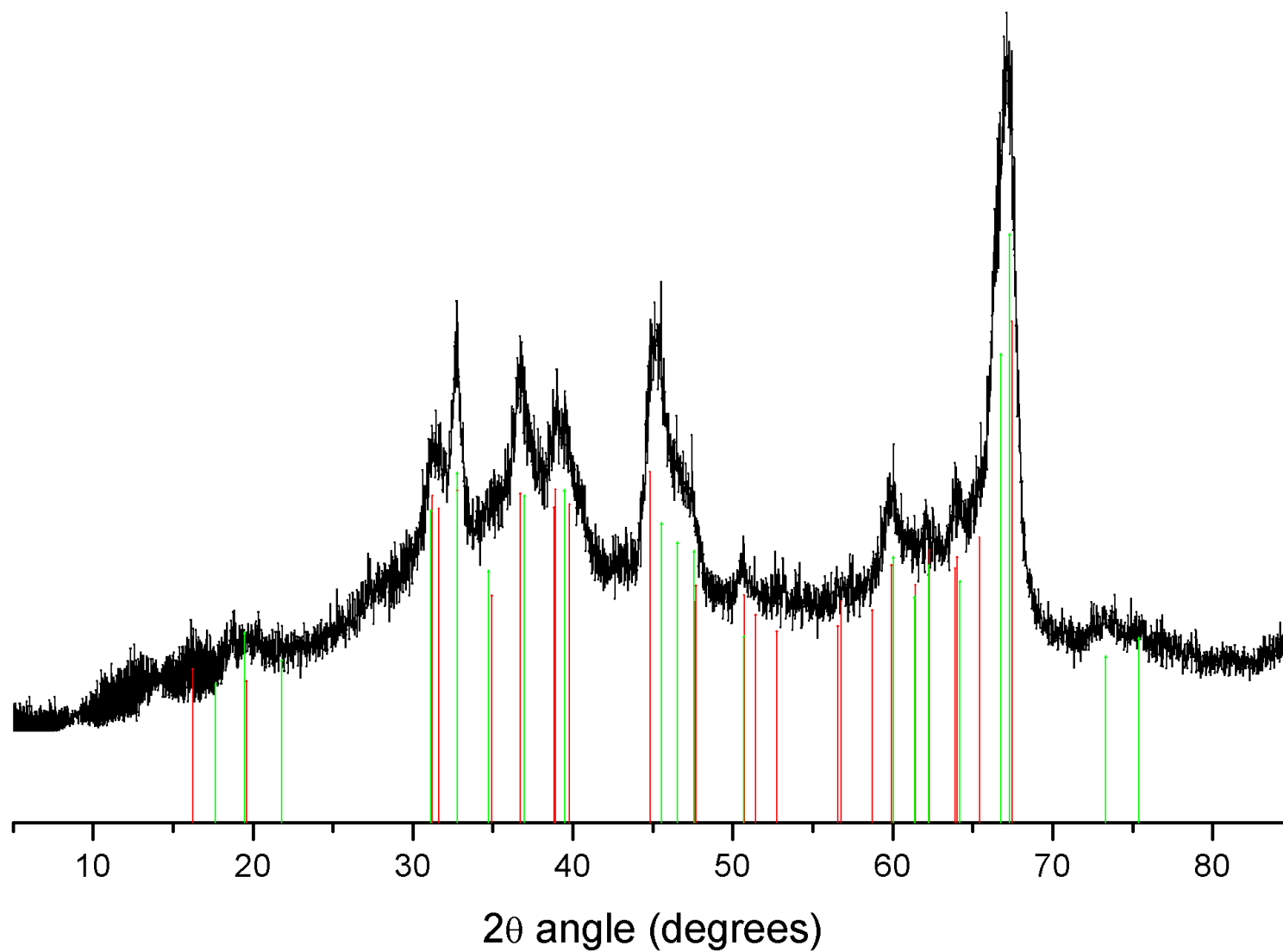


Figure 5.13: X-ray Powder Diffraction pattern recorded for the 0.3 wt % Pd/alumina (310/2) catalyst. The green drop lines represent the θ -alumina phase and the red drop lines represent the δ -alumina phase [95].

2 Θ Angle (degrees)	Alpha		Theta	
	d spacing (\AA)	h k l	d spacing (\AA)	h k l
19.599			4.52579	201
25.577	3.47998	012		
31.62			2.82737	400
32.79			2.72904	202
34.951			2.56509	111
35.151	2.55099	104		
36.723			2.44529	111
37.778	2.3794	110		
38.819			2.31795	401
39.804			2.26283	402
41.678	2.16533	006		
43.355	2.08537	113		
44.832			2.02006	311
46.18	1.96417	202		
47.703			1.90494	600
50.715			1.79866	510
51.433			1.77521	602
52.553	1.73999	024		
52.751			1.73392	403
56.568			1.62565	203
57.501	1.60147	116		
58.731			1.57082	113
59.743	1.54661	211		
59.937			1.54207	313
61.133	1.51474	122		
61.304	1.51092	018		
61.409			1.5086	603
62.307			1.48899	113
64.03			1.453	20
65.421			1.42544	800
66.521	1.40452	124		
67.461			1.38721	712
68.212	1.37375	030		
70.419	1.33601	125		
74.303	1.27549	208		
76.876	1.23909	1.0.10		
77.238	1.23418	119		
80.703	1.1897	220		
83.22	1.15999	306		
84.36	1.1472	223		

Table 5.5: Assignments of the 143 500 catalyst diffraction pattern. The red drop lines represent the α -alumina and the green ones, the θ -alumina [95].

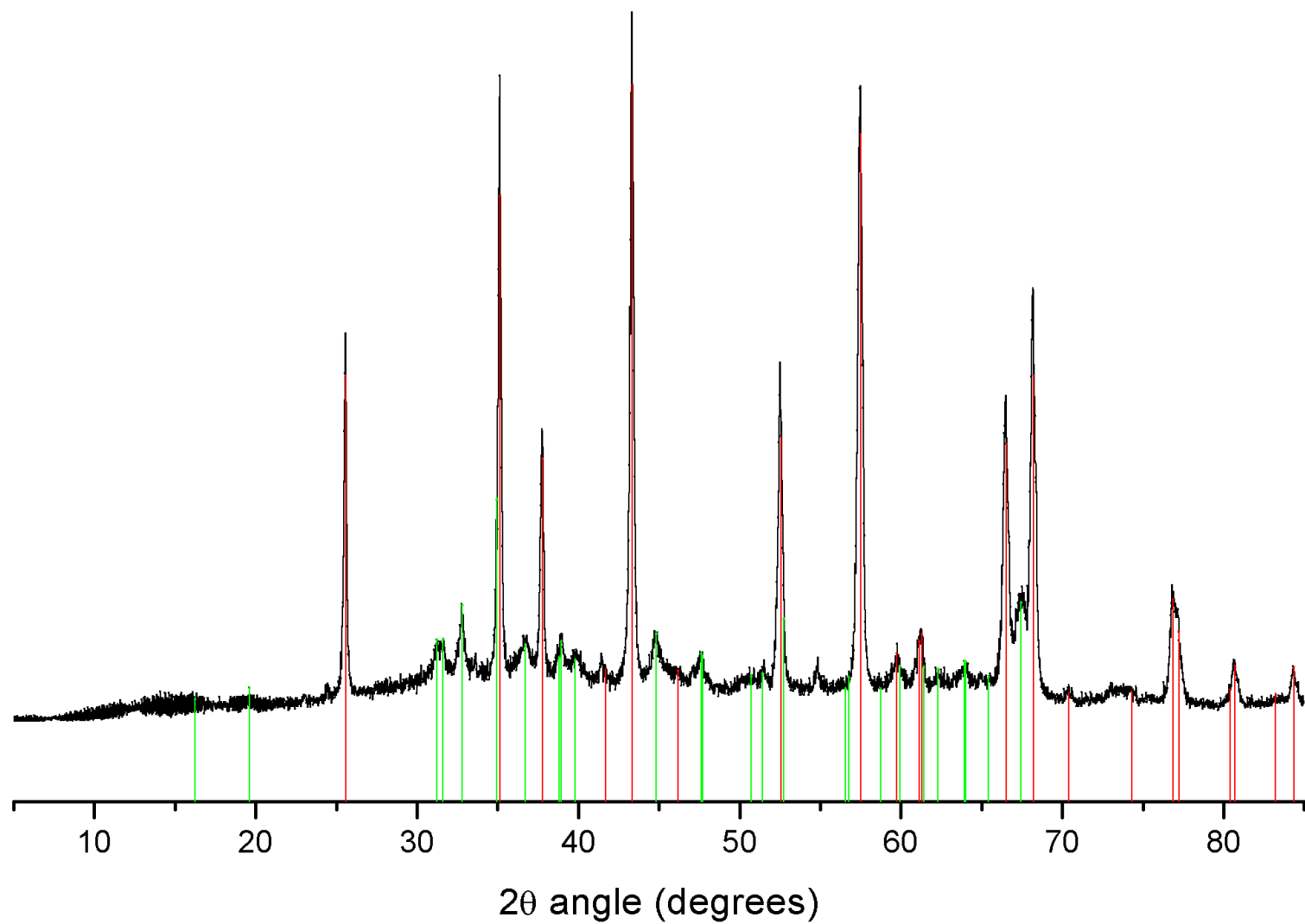


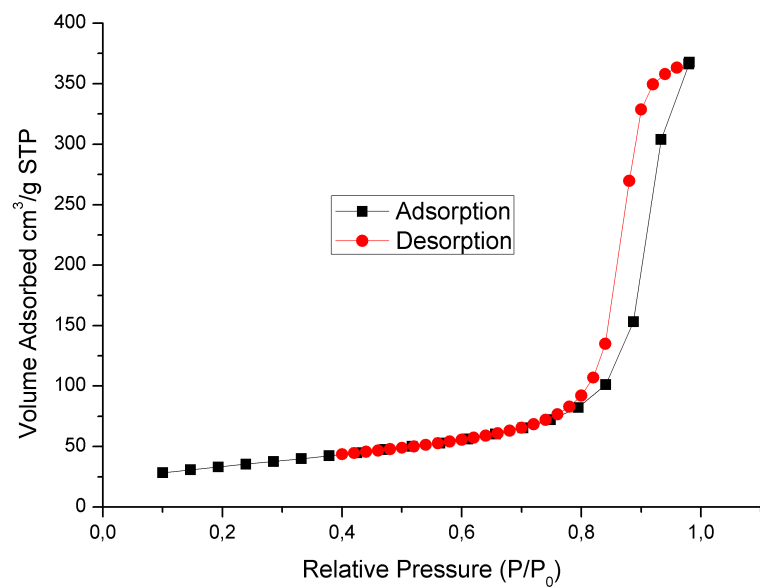
Figure 5.14: X-ray Powder Diffraction pattern recorded for the 0.3 wt % Pd/alumina (310/2) catalyst. The green drop lines represent the θ -alumina phase and the red drop lines represent the δ -alumina phase [95].

5.2.5 Brunauer-Emmett-Teller (BET) surface area and Barrett-Joyner-Halenda (BJH) pore size

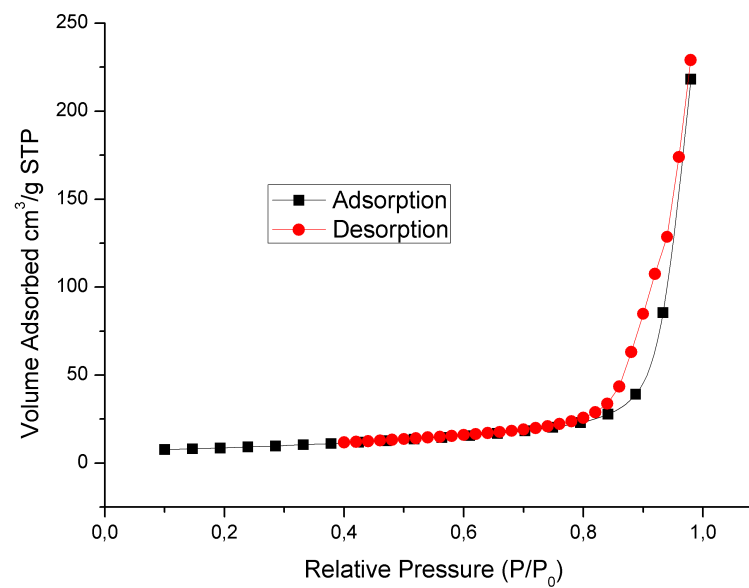
Nitrogen adsorption isotherms obtained for catalysts 2 (310/2) and 3 (143 500) are shown respectively in **Figures 5.15a and 5.15b**, where the values are reported in **Table 5.6**. These surface area values are consistent with the XRD assignments made previously, namely $120 \text{ m}^2 \cdot \text{g}^{-1}$ for a δ/θ -alumina and $30 \text{ m}^2 \cdot \text{g}^{-1}$ for an α -alumina support. These are within the areas expected for these particular types of support [121].

Catalysts	Sample 2, 310/2	Sample 3, 143 500
BET surface area ($\text{m}^2 \cdot \text{g}^{-1}$)	120.1	30.28
Average Pore Diameter (Å)	189.4	442.9
BJH pore size (Å)	146.9	254.1

Table 5.6: BET and BJH measurements.



(a)



(b)

Figure 5.15: Nitrogen absorption - desorption isotherms (BET) of (a) the 0.3wt% Pd/alumina (Sample 2, 310/2) catalyst and (b) the 0.3wt% Pd/alumina (Sample 3, 143 500) catalyst

5.3 Summary

The hydrogenation of two 0.3 wt % Pd/Al₂O₃ catalysts (Samples 2 and 3) with the same formulation were examined. Both catalysts were tested under the same conditions and characterised using the same techniques.

The reaction testing showed that:

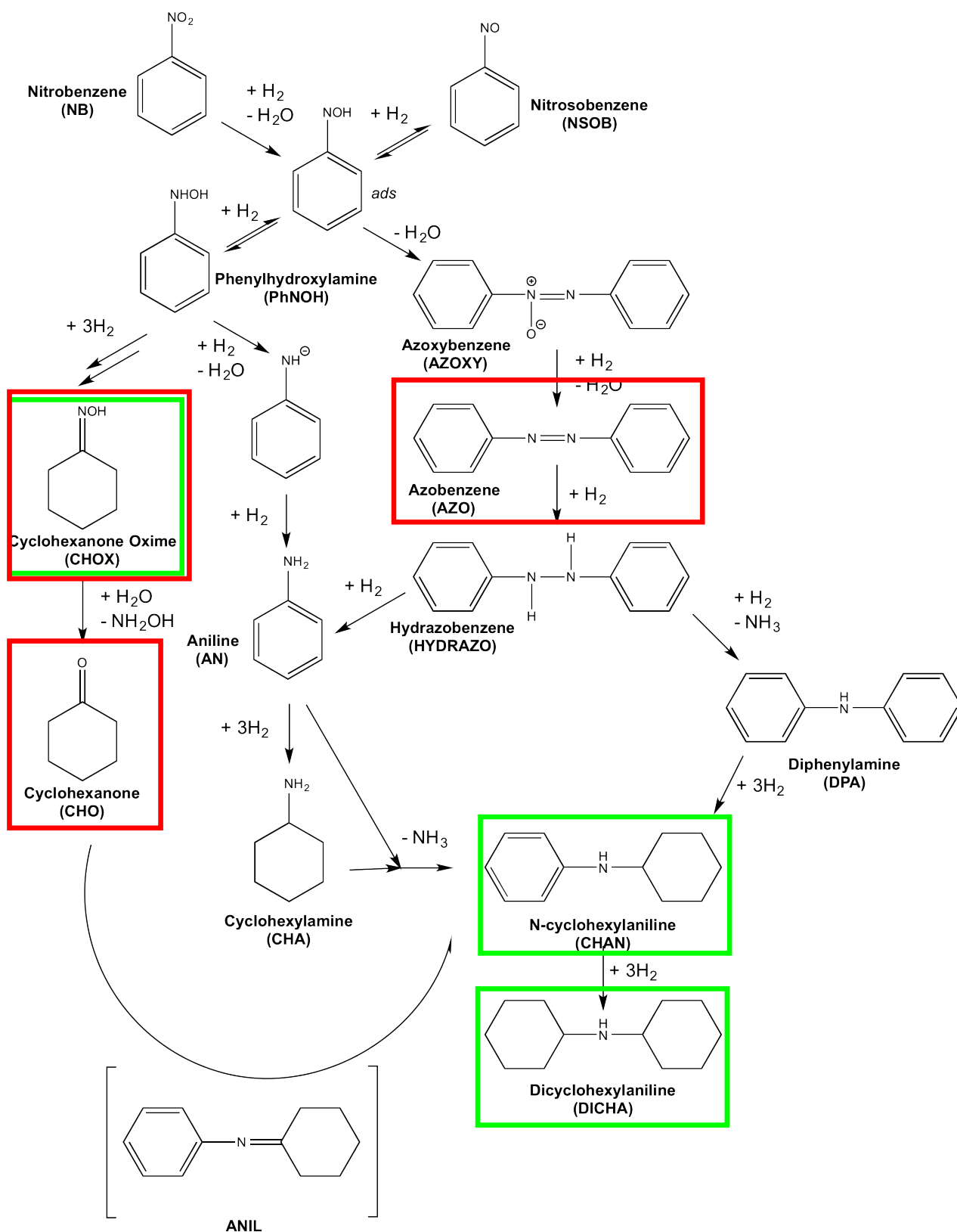
- Catalyst 2 (310/2) showed a high conversion (*ca.* 85%) with a high selectivity towards aniline (99%). At low temperatures, cyclohexanone oxime was produced in a small quantity and that an increase in temperature led to CHAN and DICHA production. This catalyst enabled aniline-derived chemistry by-products.
- Catalyst 3 (143 500) gave a mild conversion (*ca.* 60%) and high selectivity to aniline (99%). At low temperatures, cyclohexanone oxime was produced in larger quantities compared to catalyst 310/2 and over a wider range of temperatures. At higher temperatures, azobenzene and cyclohexanone was observed. This catalyst hence displayed nitrobenzene-derived chemistry.
- As part of the reaction testing, an unknown compound was detected which was successfully identified as cyclohexanone oxime using GC-MS. The discovery of this compound furthered the understanding the provenance of cyclohexanone, which until that point was believed to be produced under aqueous conditions and be linked with phenol. This was detected for the temperature-programmed reaction performed with Sample 1, as seen in **Chapter 3, Section 3.1**.

The characterisation revealed that:

- CO adsorption isotherms revealed that 310/2 catalyst has a modest dispersion of 27%, which indicated that Pd particles were 4 nm in size. Catalyst 143 500 has a higher dispersion (48%), which showed a Pd particle size of roughly 2.5 nm.
- The TEM confirmed the measurements made using CO chemisorptions and highlighted the spherical shape of the 310/2 catalyst and the oblique/prismatic shape of the 143 500 catalyst. The difference of metal distribution throughout the support materials for both catalysts was also noticeable.
- XRD indicated that the 310/2 support was composed of a mixture of delta and theta-alumina, whereas the catalyst 143 500 is made of an alpha-alumina support with a fraction of theta-alumina. These observations are consistent with the BET measurements.

To sum up, the difference of selectivity observed between both catalysts can be explained by the difference in support structure, which may give rise to different particle size and Pd morphologies. The influence of Pd particle size on the selectivity of hydrogenation reactions in general was supported by McInroy *et al.* [99], who determined catalyst morphology using CO probing followed by infrared spectroscopy [85, 97]. This study gave rise to analysing both catalysts using a similar technique methodology, however the low Pd loading may prove to be a challenge. To the best of the authors knowledge, CO probing of low loading catalyst (0.3 w % w) followed by infrared spectroscopy has never been reported and may show detection limitation difficulties.

Finally, the discovery and observations made when reacting both catalysts enabled a better understanding of nitrobenzene hydrogenation. Thus, it was possible to optimise and update the reaction scheme proposed in **Chapters 3 and 4** in **Figures 3.1 and 4.14**. **Scheme 5.5** is reproduced here as a suitable summary of the reaction chemistry observed.



Scheme 5.5: Full reaction scheme of nitrobenzene hydrogenation in a fixed-bed tubular reactor.

Chapter 6

Infrared Spectroscopy + CO

chemisorption

to determine Pd particles

morphology: Samples 2 and 3

The interactions of CO with Pd metal particles supported on an alumina support have been studied extensively in the last 50 years to determine the type of active sites present at the surface of catalysts. The adsorption of CO in surface science is usually followed using electron energy loss spectroscopy, Infrared Spectroscopy and Temperature-Programmed Desorption [86, 77, 124, 125, 101, 126, 127].

6.1 Optimisation Characterisation Rig

6.1.1 CO TPIR of 5 wt % Pd/Al₂O₃ (Sample 1)

The infrared spectroscopy results from the chemisorption using the Spectra-Tech Diffuse Reflectance Infrared Fourier Transform cell on the 5 wt % Pd/Al₂O₃ (Sample 1) are shown in **Figure 6.1**. The chemisorption was carried out as mentioned in **Section 2.4.1**. The saturated spectrum at room temperature displays three characteristic bands for the chemisorption of CO at the surface a Pd/alumina catalyst [85]. The band at 2067 cm⁻¹ is attributed to CO linearly bound on the Pd edge (100)/(111) crystallites. The two other features are attributed to two-fold and three fold chemisorbed CO over Pd low index planes. The band at 1980 cm⁻¹ is assigned to μ_2 bridge bonded CO on Pd (100) and the band at 1922 cm⁻¹ is assigned to μ_3 bridge bonded CO on Pd (111) [74].

Upon heating, all the chemisorbed CO species are totally desorbed and a flat spectra after desorption is observed at 50°C. The reason for such a behaviour is due to an uncomplete

catalyst activation or a re-oxidation due to a leak within the system. CO chemisorbs onto a metallic particle strongly, whilst only binding slightly to an oxidised particle. Hence the desorption at low temperature. This was therefore rendered useless and required experimental development. Nevertheless, it provided an opportunity to verify if the catalyst had been activated properly to chemisorb CO effectively. Carrying out a CO temperature-programmed desorption was found to be very useful in this case.

It was revealed that oxidised Pd/alumina catalysts have been extensively studied upon CO oxidation and are deemed very active [125]. Both palladium and alumina support can undergo CO oxidation if the catalyst is exposed to oxygen.

This type of internal check is necessary to ensure that the temperature-programmed IR measurements are credible.

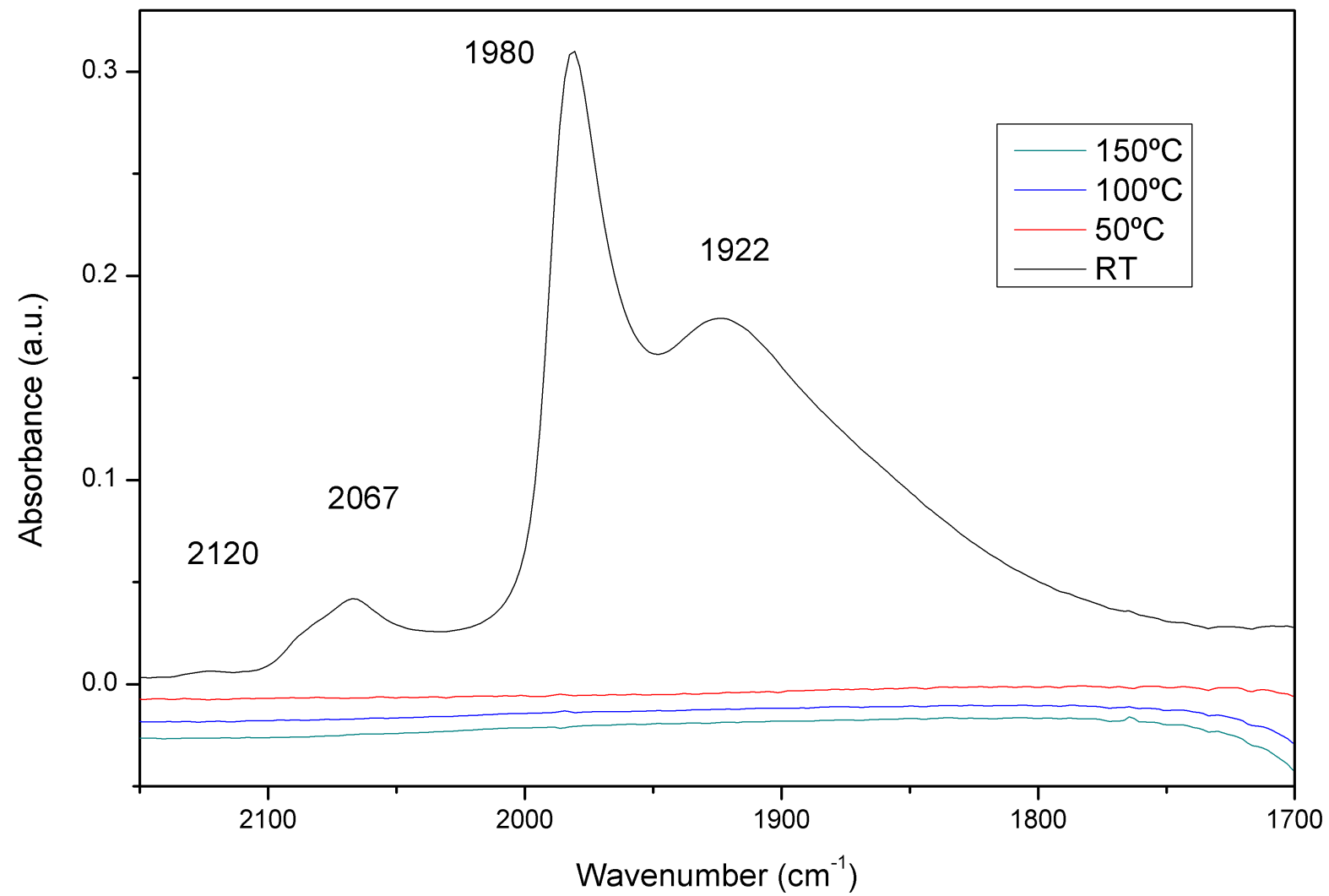


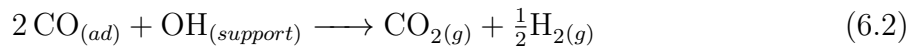
Figure 6.1: Temperature-Programmed Infrared Spectroscopy on 5 wt % Pd/Al₂O₃ catalyst (Sample 1)

6.1.2 CO TPD of 5 wt % Pd/Al₂O₃

6.1.2.1 Before optimisation

Oxidised Pd/alumina catalysts have been extensively studied upon CO oxidation and are deemed very active [125]. Both palladium and alumina supports can then lead to CO oxidation if the catalyst is exposed to oxygen. As a consequence of the issue with the CO TPIR, it was decided that a CO TPD on the 5 wt % Pd/alumina catalyst should be carried out in order to test the purity of the surface after activation. The CO TPD was followed by mass spectrometry and mass 28 and 44 were recorded throughout the experiment.

Lear *et al.* studied the CO TPD on a reduced Pd/alumina catalyst and reported that CO was desorbed mainly around 200°C, and CO₂ around 400°C [86]. The CO TPD carried out on the 5 wt % catalyst is reported in **Figure 6.2**. The black line is mass 28 which corresponds to CO and the red line is mass 44 which corresponds to the CO₂ signal. A large CO₂ peak is observed at 400 K which should not be visible when the catalyst is fully reduced. The peak at 400 K is known to be caused by CO oxidation caused by the presence of hydroxyls at the surface of the alumina catalyst and shown here in **Equation 6.1.2.1**.



The use of CO TPD confirmed that there was in fact a presence of oxygen post activation that re-oxidised the metal particle and the support. The effect on the support led to the desorption of CO₂ at 400 K and the oxygen presence effect on the metal caused a weak adsorption of CO onto the surface of the metal which resulted in a full desorption at 50°C.

As a consequence, the rig was fully inspected using mass spectrometry and leak tested, all faulty parts were replaced to guarantee the purity integrity of the rig.

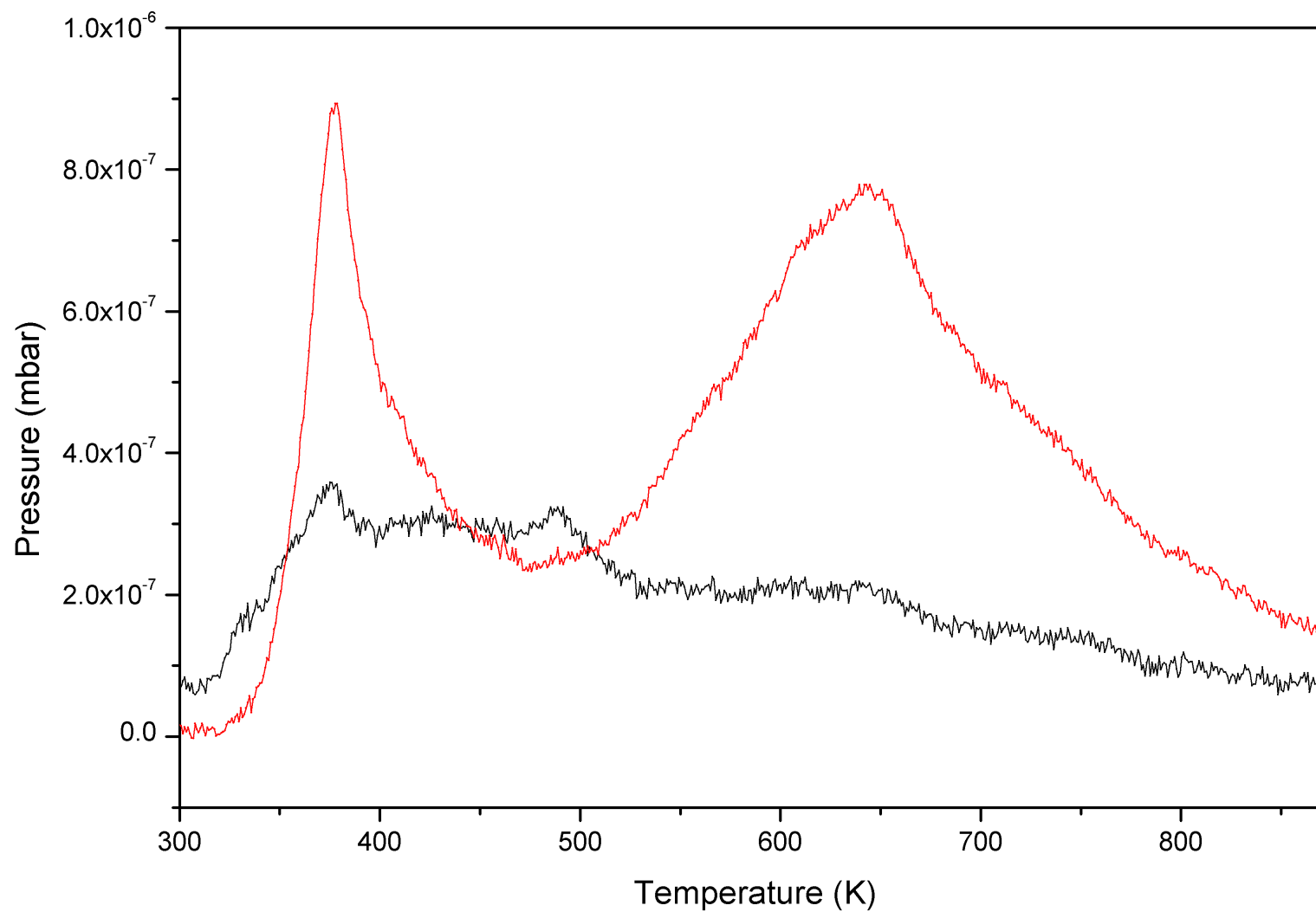


Figure 6.2: Temperature-Programmed Desorption of CO (in black) and CO₂ (in red) for the 5 wt % Pd/Al₂O₃ prior to optimisation of experimental methodology.

6.1.2.2 After optimisation

A second CO TPD was carried out on the 5 wt % catalyst to test the integrity of the rig after extensive procedures were carried out to ensure the purity of reagents was maintained throughout the whole system. Operating conditions were similar to what were shown previously in **Section 6.1.2.1**.

The CO TPD obtained now correspond to the results obtained by Lear *et al.* [86]. The CO was desorbed at around 400 K and the CO₂ signal was composed of a small bump at 400 K and large desorption pattern at 600 K. This result confirms that the rig and flow of helium are clean and that the activation of the catalyst was carried out as required for a CO TPD or a CO TPIR. As a consequence, the CO TPIR measurements were deemed acceptable.

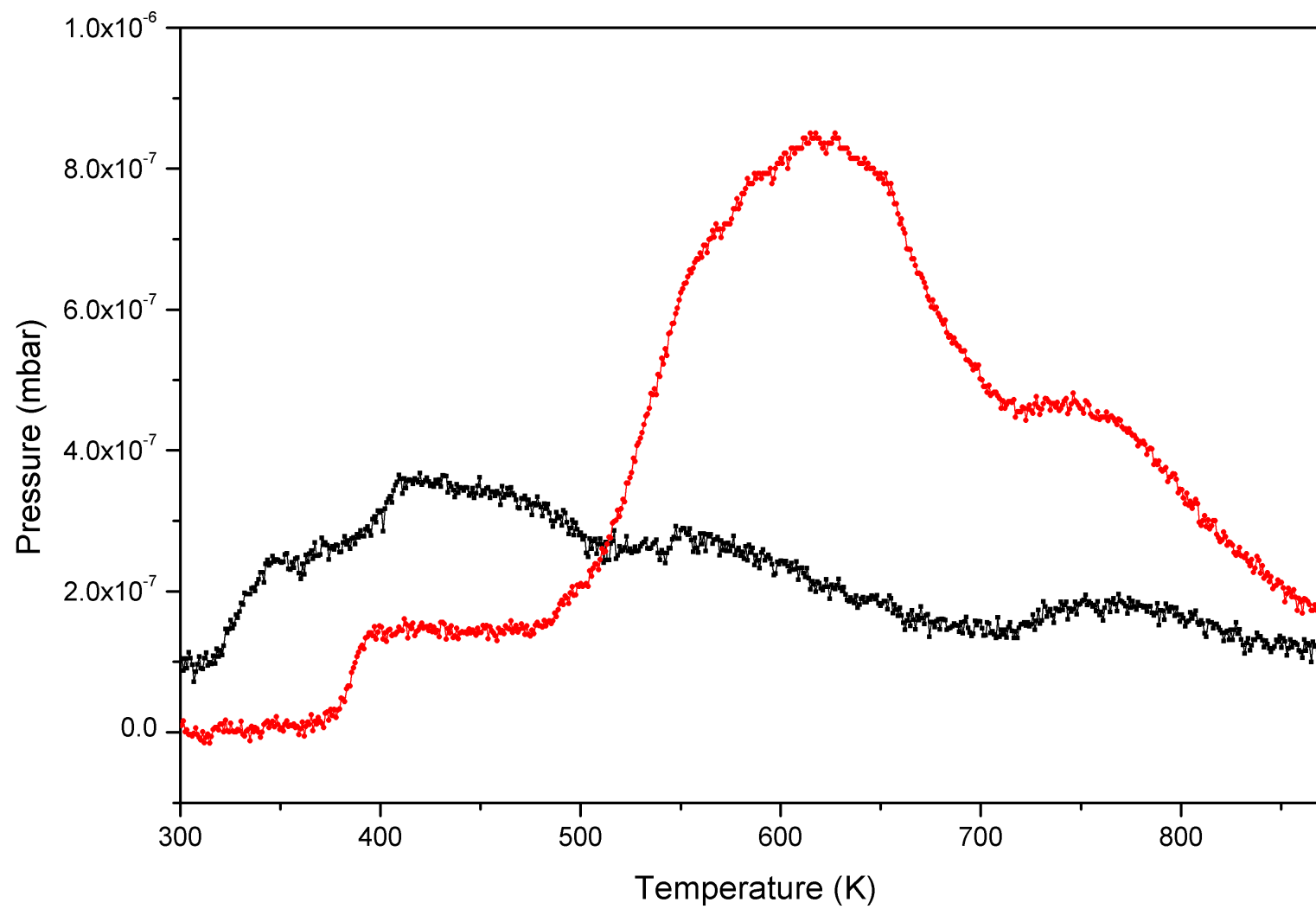


Figure 6.3: Temperature-Programmed Desorption of CO (in black) and CO₂ (in red) for the 5 wt % Pd/Al₂O₃.

6.1.3 CO TPIR of 5 wt % Pd/Al₂O₃ (Sample 1) on Nexus DRIFT cell

The infrared spectroscopy result from the chemisorption using the Spectra-Tech Diffuse Reflectance Infrared Fourier Transform cell on the 5 wt % Pd/Al₂O₃ is shown in **Figure 6.4**. The chemisorption was carried out as mentioned in **Section 2.4.1**.

The saturated spectrum displays four characteristic bands for the chemisorption of CO at the surface a Pd/alumina catalyst as described in **Section 3.4.3**. The shoulder at 2080 cm⁻¹ indicates that a small amount is chemisorbed linearly on the corner site of the palladium crystal. The band at 2057 cm⁻¹ is attributed to CO linearly bound on the Pd edge (100)/(111) crystallites. The two other features are attributed to two-fold and three fold chemisorbed CO over Pd low index planes. The band at 1980 cm⁻¹ is assigned to μ_2 bridge bonded CO on Pd (100) and the band at 1909 cm⁻¹ is assigned to μ_3 bridge bonded CO on Pd (111).

Upon heating **Figure 6.4** shows that the band at 1909 cm⁻¹ decreases in intensity and wavenumber until it reaches 1850 cm⁻¹ (μ_3 bridge bonded CO on Pd (111)). It is still present upon heating to 350°C. The band at 1980 cm⁻¹ (μ_2 bridge bonded CO on Pd (100)) also decreases in intensity and wavenumber upon heating to 350°C and shifted to 1915 cm⁻¹. Both bands are remained after the temperature ramp. It is interesting to note that upon heating to 50°C, the site at 2080 cm⁻¹ (linear CO residing on corner sites) is desorbed. The band at 2055 cm⁻¹ (CO residing on (100)/(111)) decreased in intensity upon heating to 350°C but is still present. Unlike the other bands, the latter does not shift by much upon heating and reached 2060 cm⁻¹ at the final temperature. This can be explained by the fact that the edge site band is a singleton and is not affected as much as the plane bands by the dipole coupling. With increasing temperature, the coverage changes drastically on the low index plane which led to an important change to the intensity stealing phenomena. The μ_1 edge sites located at the intersection of the (111)/(100) and (111)/(111) exhibit a different coordination than the plane sites. These Pd atoms are surrounded by less Pd neighbouring atoms. Hence their d-orbitals are left with more free electrons capable of back bonding with a CO molecule which is explained in **Section 1.4.1**. The d-orbital electron is shared with the anti-bonding orbital of the CO which leads to weakening of the C-O bond. Therefore, the more the electron shared, the stronger the C-M interaction (also known as chemisorption). The μ_1 sites are labelled as high energy sites [71, 97, 85]. The temperature at which the CO desorption occurs for this site is of high importance and enable us to probe the enthalpy of adsorption of the high energy sites.

The quality of the CO TPIR spectra indicates that the experiment is operating in the right conditions and that it is ready to carry out the necessary experiments using the low loading catalyst, with a high degree of purity and reproducibility.

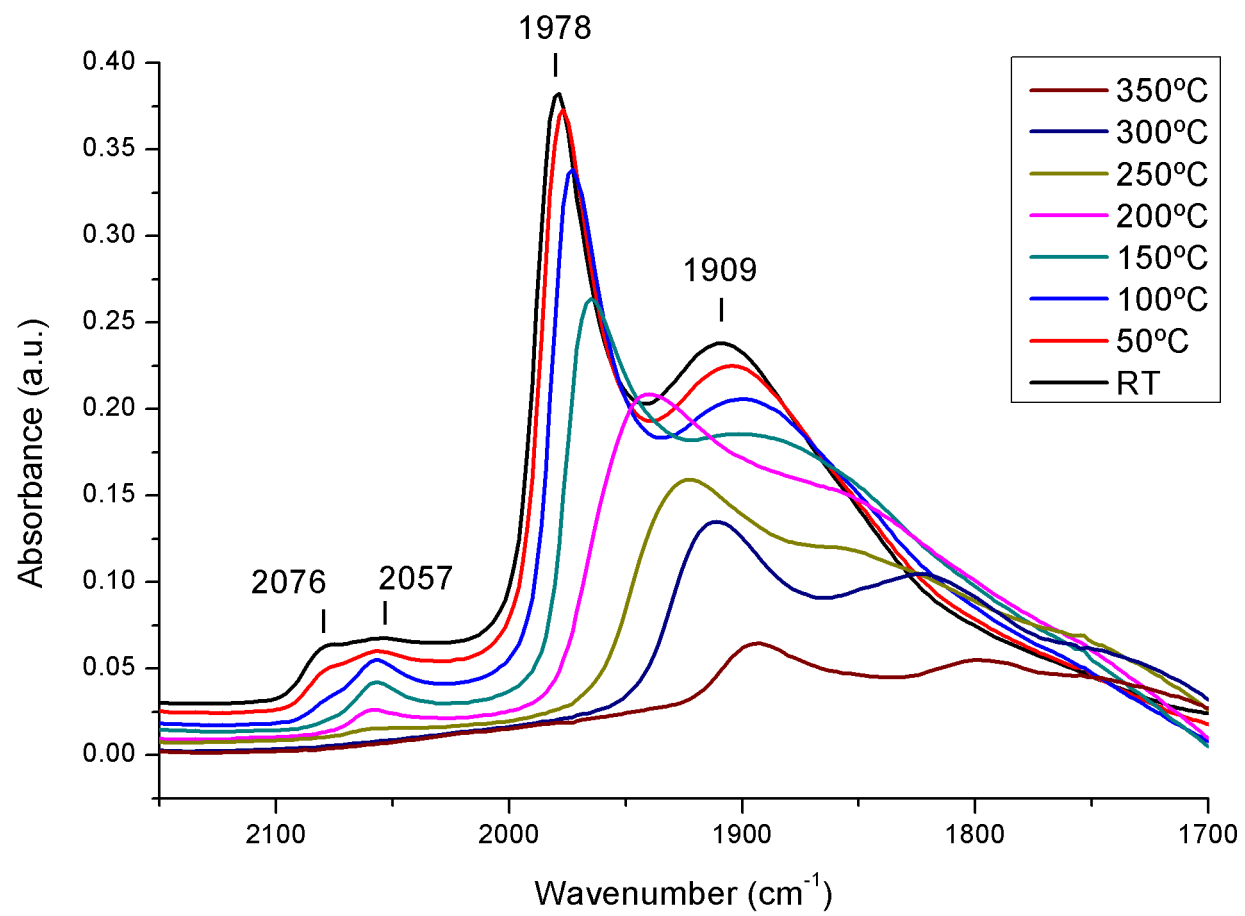


Figure 6.4: Temperature-Programmed Infrared Spectroscopy on the 5 wt % Pd/Al₂O₃ (Sample 1).

6.1.4 CO TPIR of 5 wt % Pd/Al₂O₃ (Sample 1) on Harrick DRIFT cell

The infrared spectroscopy results from the chemisorption using the Spectra-Tech Diffuse Reflectance Infrared Fourier Transform cell on the 5 wt % Pd/Al₂O₃ are shown in **Figure 6.5**. The chemisorption was carried out as mentioned in **Section 2.4.1**.

The saturated spectrum displays four characteristic bands for the chemisorption of CO at the surface a Pd/alumina catalyst. The band at 2060 cm⁻¹ is attributed to CO linearly bound on the Pd edge (100)/(111) crystallites. The two other features are attributed to two-fold and three fold chemisorbed CO over Pd low index planes. The band at 1980 cm⁻¹ is assigned to μ_2 bridge bonded CO on Pd (100) and the band at 1910 cm⁻¹ is assigned to μ_3 bridge bonded CO on Pd (111).

Upon heating **Figure 6.4** shows that the band at 1910 cm⁻¹ decreases in intensity and wavenumber until it reaches 1850 cm⁻¹ (μ_3 bridge bonded CO on Pd (111)), and that it is still present upon heating to 350°C. The band at 1980 cm⁻¹ (μ_2 bridge bonded CO on Pd (100)) also decreases in intensity and wavenumber upon heating to 350°C and shifted to 1920 cm⁻¹. Both bands are still present after the temperature ramp. The band at 2060 cm⁻¹ (CO residing on (100)/(111)) decreases in intensity upon heating to 200°C. With increasing temperature, the coverage changes drastically on the low index plane which led to an important change to the intensity stealing phenomena. The geometry of the DRIFT Harrick cell discussed in the introduction is responsible for the lack of sensitivity. No high energy corner sites were detected and the CO chemisorbed on the edge sites are desorbed faster than the experiment performed in the Nexus DRIFT cell.

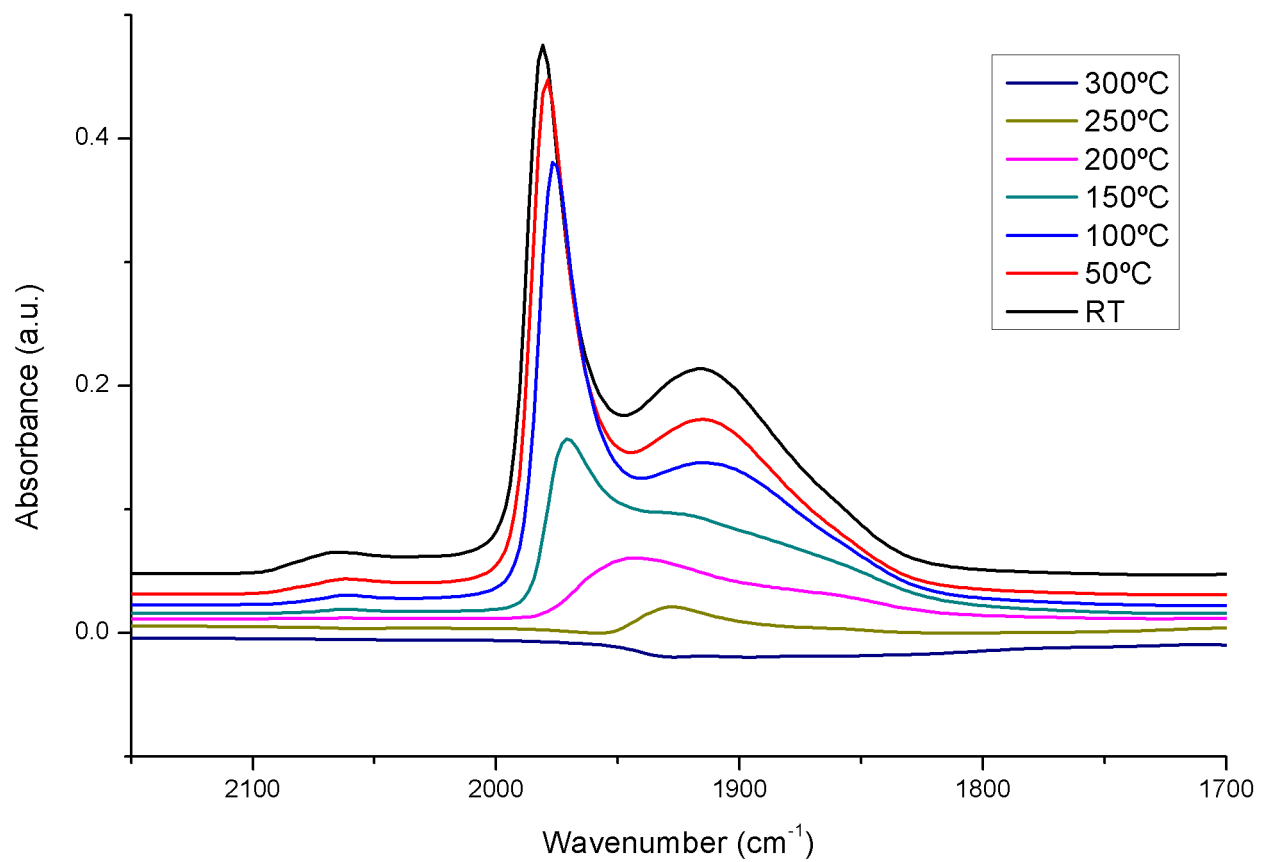


Figure 6.5: Temperature-Programmed Infrared Spectroscopy on the 5 wt % Pd/Al₂O₃ (Sample 1) on Harrick DRIFT cell as showed in **Chapter 1**

6.1.5 CO TPIR of 5 wt % Pd/Al₂O₃ (Sample 1) on Transmission cell

The infrared spectroscopy results from the chemisorption using the Specac transmission Infrared Fourier Transform cell on the 5 wt % Pd/Al₂O₃ are shown in **Figure 6.6**. The chemisorption was carried out as mentioned in **Section 2.4.1**.

The saturated spectrum displays four characteristic bands for the chemisorption of CO at the surface a Pd/alumina catalyst as described in **Section 3.4.3**. The band at 2052 cm⁻¹ is attributed to CO linearly bound on the Pd edge (100)/(111) crystallites. The two other features are attributed to two-fold and three fold chemisorbed CO over Pd low index planes. The band at 1980 cm⁻¹ is assigned to μ_2 bridge bonded CO on Pd (100) and the band at 1905 cm⁻¹ is assigned to μ_3 bridge bonded CO on Pd (111).

Upon heating **Figure 6.6** displays a band at 1905 cm⁻¹ which decreases in intensity and wavenumber until it reaches 1825 cm⁻¹ (μ_3 bridge bonded CO on Pd (111)). It was found to be still present upon heating to 350°C. The band at 1980 cm⁻¹ (μ_2 bridge bonded CO on Pd (100)) also decreases in intensity and wavenumber upon heating to 350°C and shifted to 1905 cm⁻¹. Both bands are still present after the temperature ramp. The band at 2055 cm⁻¹ (CO residing on (100)/(111)) decreases in intensity upon heating to 200°C. Carrying out the TPIR experiment on the transmission cell revealed that the optical conditions in the case of the DRIFT experiment were correct and in accordance with the transmitted spectra. No major distortion of the signal and shift are observed. The intensity of the CO chemisorbed on low index plane is much smaller in intensity than the DRIFT experiments but the location and shape are equivalent. Moreover, with Harrick DRIFT experiment, only the edge sites are detected (no detection of corner sites) and the intensity of the feature at 2050 cm⁻¹ reveals that the diffuse and specular reflectance observed in the DRIFT analysis have not compromised the quality of the spectrum and can be used qualitatively to determine the type of active sites at the surface of the catalyst and the enthalpy of adsorption of these sites.

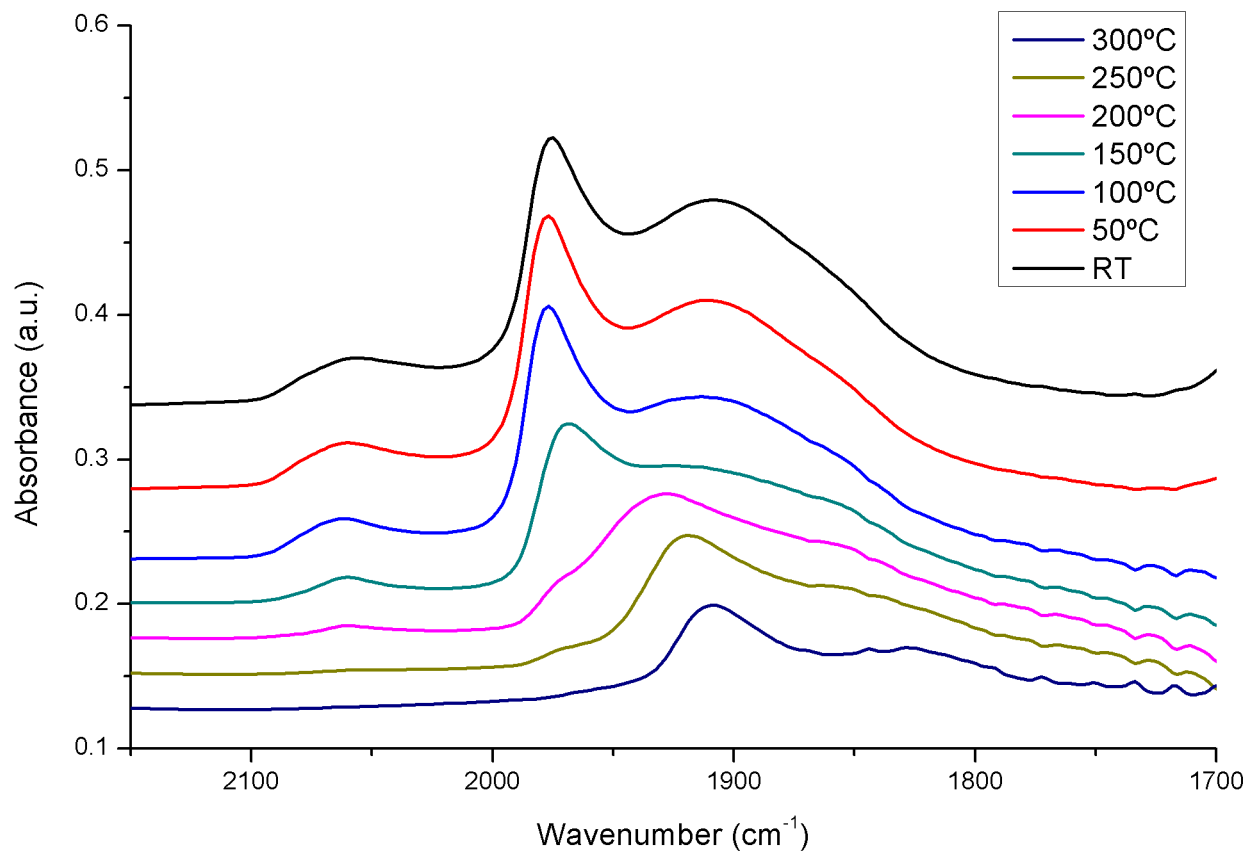


Figure 6.6: Temperature-Programmed Infrared Spectroscopy on the 5 wt % Pd/Al₂O₃ (Sample 1) on Transmission cell as shown in **Chapter 1**

6.2 CO TPIR of the 0.3 wt % Pd/Al₂O₃ (Sample 2, 310/2) catalyst

The infrared spectroscopy results from the chemisorption using the Spectra Tech Diffuse Reflectance Infrared Fourier Transform cell on the 0.3 wt % Pd/Al₂O₃ are shown in **Figure 6.7**. The chemisorption was carried out as mentioned in **Section 2.4.1**.

The scan of the chemisorbed CO at the surface of the catalyst after activation is shown in **Figure 6.7**. We can distinguish three bands for the chemisorption of CO at the surface of this catalyst. The peak at 2061 cm⁻¹ indicates that a small amount of CO is chemisorbed linearly on the corner sites of the palladium crystal. The two other features are attributed to two-fold and three fold chemisorbed CO over Pd low index planes. The band at 1970 cm⁻¹ is assigned to μ_2 bridge bonded CO on Pd (100) and the band at 1913 cm⁻¹ is assigned to μ_3 bridge bonded CO on Pd (111) [74].

Upon heating, the band at 1970 cm⁻¹ and 1913 cm⁻¹ decreased in intensity and merged to form one broad feature which tended to split with an increase in temperature. Literature explained this behaviour as the loss of surface coverage and intensity stealing [74, 104]. The peak at 2061 cm⁻¹, which represents the CO linearly bound to the Pd, is totally desorbed after 100°C indicating a relatively low enthalpy of adsorption for this edge site.

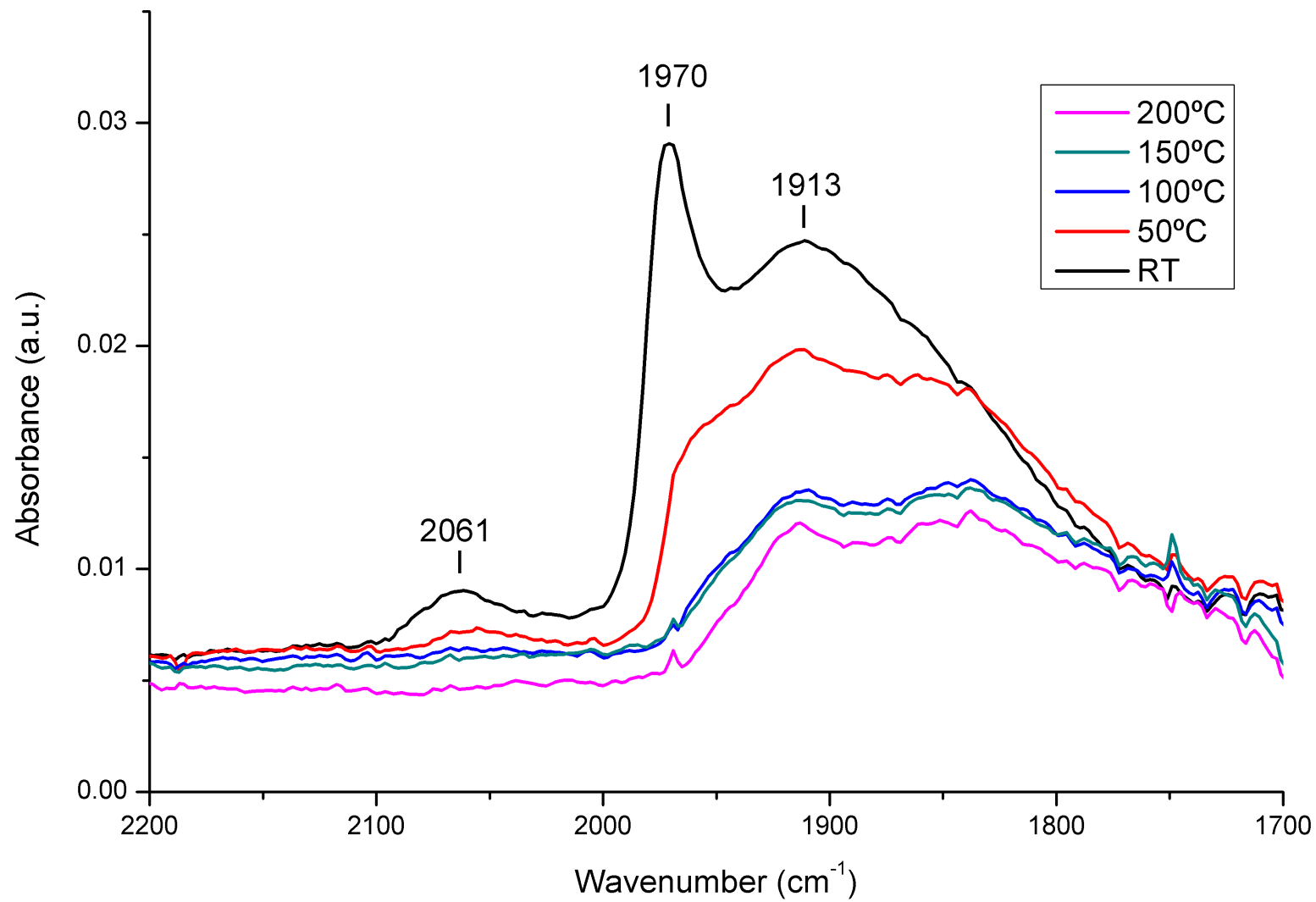


Figure 6.7: Temperature-Programmed Infrared Spectroscopy for CO chemisorption on 0.3 wt % Pd/Al₂O₃ (Sample 2, 310/2).

6.3 CO TPIR of the 0.3 wt % Pd/Al₂O₃ (Sample 3, 143500) catalyst

The infrared spectroscopy results from the chemisorption using the Spectra-Tech Diffuse Reflectance Infrared Fourier Transform cell on the 0.3 wt % Pd/Al₂O₃ are shown in **Figure 6.8**. The chemisorption was carried out as mentioned in **Section 2.4.1**.

The scan of the chemisorbed CO at the surface of the catalyst after activation is shown in **Figure 6.8**. The saturated spectrum displays four characteristic bands for the chemisorption of CO at the surface a Pd/alumina catalyst as described in **Section 3.4.3**. The shoulder at 2082 cm⁻¹ indicates that a small amount is chemisorbed linearly on the corner site of the palladium crystal [85]. The band at 2061 cm⁻¹ is attributed to CO and is linearly bound to the Pd edge (100)/(111) crystallites. The two other features are attributed to two-fold and three fold chemisorbed CO over Pd low index planes. The band at 1976 cm⁻¹ is assigned to μ_2 bridge bonded CO on Pd (100) and the band at 1914 cm⁻¹ is assigned to μ_3 bridge bonded CO on Pd (111).

Upon heating, the band at 1924 cm⁻¹ decreases in intensity and wavenumber and reaches 1900 cm⁻¹ (μ_3 bridge bonded CO on Pd (111)). It is still present upon heating to 300°C. The band at 1982 cm⁻¹ (μ_2 bridge bonded CO on Pd (100)) also decreases in intensity and wavenumber upon heating to 300°C and is seen as a shoulder which shifted to 1950 cm⁻¹. The site at 2082 cm⁻¹ (linear CO residing on corner sites) is present at room temperature, through to 50°C, but is found to fully desorb at 100°C. The band at 2061 cm⁻¹ (CO residing on (100)/(111)) decreases in intensity upon heating and is present up until 200°C, which indicates a relatively strong enthalpy of adsorption of this site. Unlike the bridge-bonded species, the linear species do not shift upon heating. This explained by the fact that the edge site band is a singleton and is not affected as much as the plane bands by the dipole coupling as discussed in **Chapter 3**. With increasing temperature, the coverage changes drastically on the low index plane which leads to an important change to the intensity stealing phenomena discussed by Eischens and Hollins [104, 128].

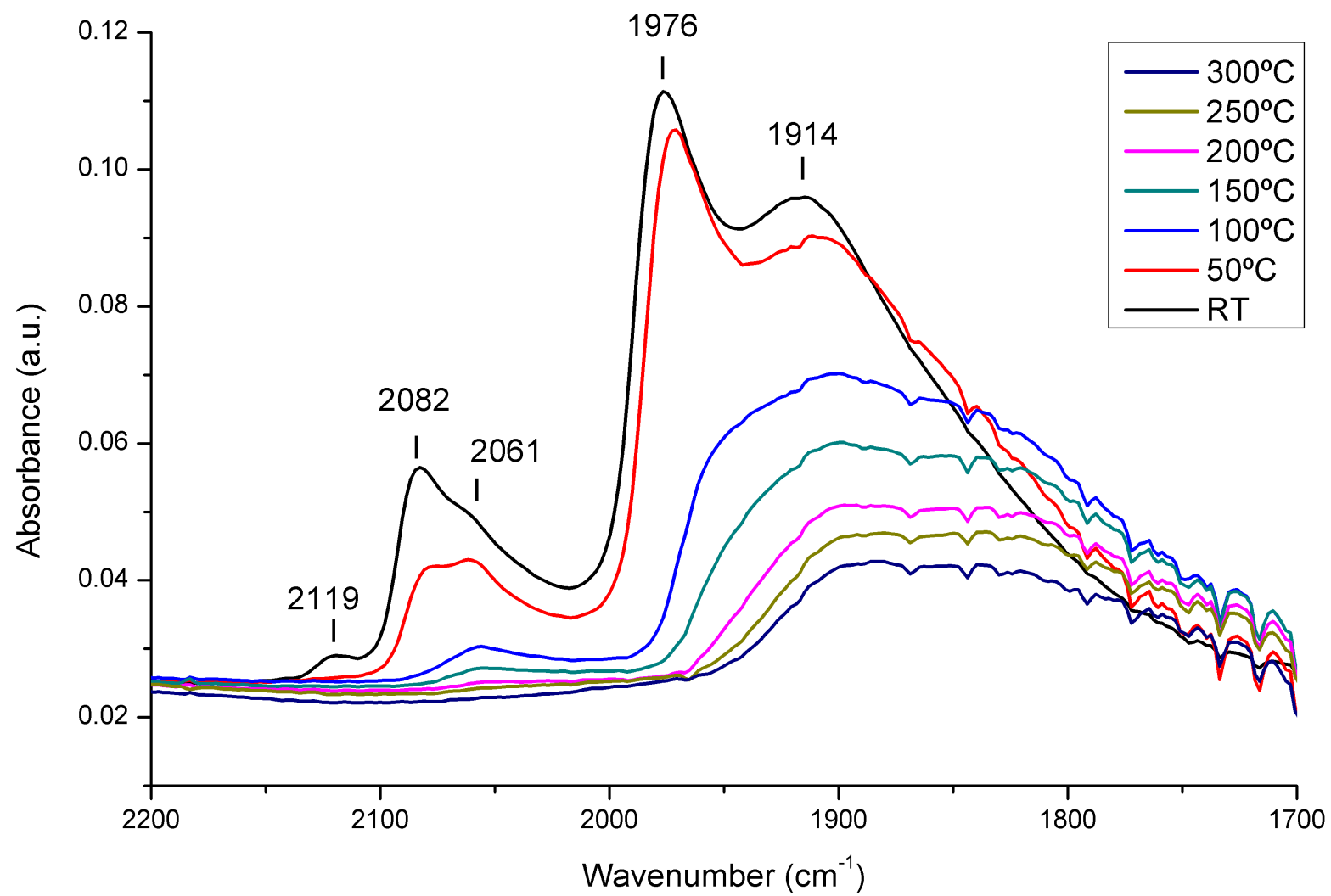


Figure 6.8: Temperature-Programmed Infrared Spectroscopy from CO chemisorption on 0.3 wt % Pd/Al₂O₃ (Catalyst 3, 143 500).

6.3.1 Summary

The CO TPIR measurements on the 5 wt% Pd/alumina in parallel with the CO TPD measurements, enabled the testing of the integrity of the apparatus and determined the right operating conditions to maximise the reduction of the catalyst. This allowed for chemisorption and desorption of CO at the surface of our catalysts to be carried out. Initial difficulties with a small quantity of oxygen thought to be residing on the catalyst was, after extensive refinements, eliminated. The comparison of three different optical IR setups confirmed that the project is working within optimal conditions to analyse low concentrated Pd/alumina catalysts.

The study of the two 0.3 wt % Pd/Al₂O₃ catalysts (Samples 2 and 3) by CO chemisorptions followed by IR spectroscopy revealed:

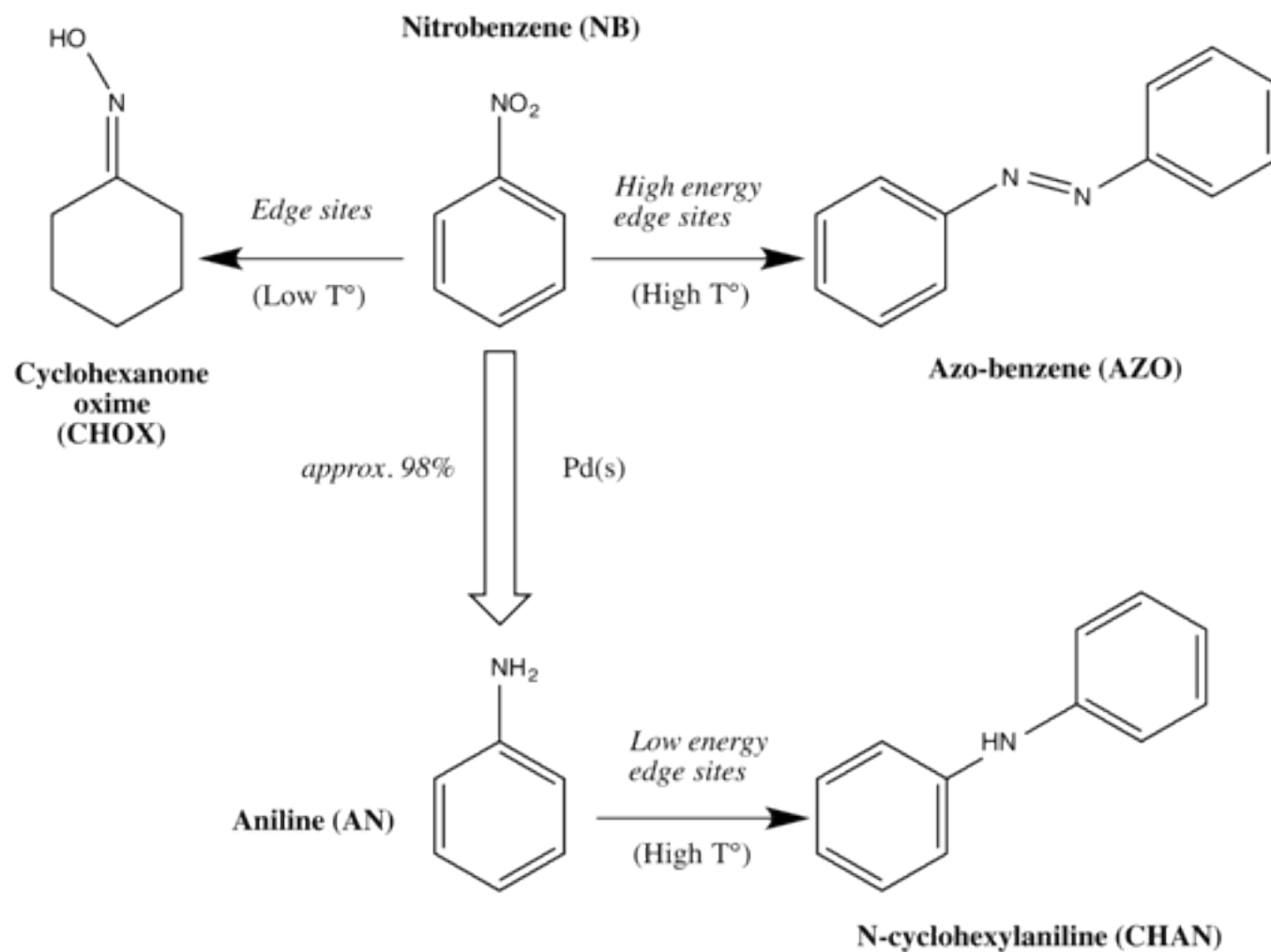
- From previous studies on Pd/alumina, it was believed that the high energy sites such as corner and edges have an impact on the selectivity of a reaction. Thanks to the use of an optically well set-up DRIFT cell (NEXUS), it is possible to qualitatively detect the corner and edge sites and determine their enthalpy of adsorption. This is key for determining the structure/activity relationships of the catalyst used here.
- Sample 2 (310/2) catalyst displays three bands for the chemisorption of CO on the Pd particles. One band for the linear CO chemisorbed on the edge sites and two for the (100) and (111) two-fold and three-fold chemisorbed CO on Pd. Moreover, the enthalpy of adsorption of the high energy sites was investigated using the desorption ramp as an indicator. The CO chemisorbed at the surface of the high energy sites was fully desorbed after 100°C.
- The 143 500 catalyst exhibited four bands. Two due to the low index planes (100) and (111) and two to the linearly chemisorbed CO. Indeed, this catalyst displayed a new band at 2080 wavenumbers which existed for the 310/2. At room temperature, this band was quite sharp and intense, and was assigned to the linear CO sitting on the corner sites of the Pd particles. Alongside this band, there was a shoulder corresponding to the CO chemisorbed to the edge sites. CO population of this site was evident up to 200°C. Thus, the enthalpy of adsorption of this site was found to be significantly greater than that observed for the catalyst 310/2.

As a result, the reaction testing data obtained in **Chapter 5** was analysed using the knowledge of the CO TPIR measurements discussed above. **Scheme 6.1** considers the fact that at low temperature, the presence of these edge sites resulted in the formation of cyclohexanone oxime. At higher temperature, the low energy edge sites (catalyst 310/2) are responsible for the production of aniline-derived chemistry through cleavage of the

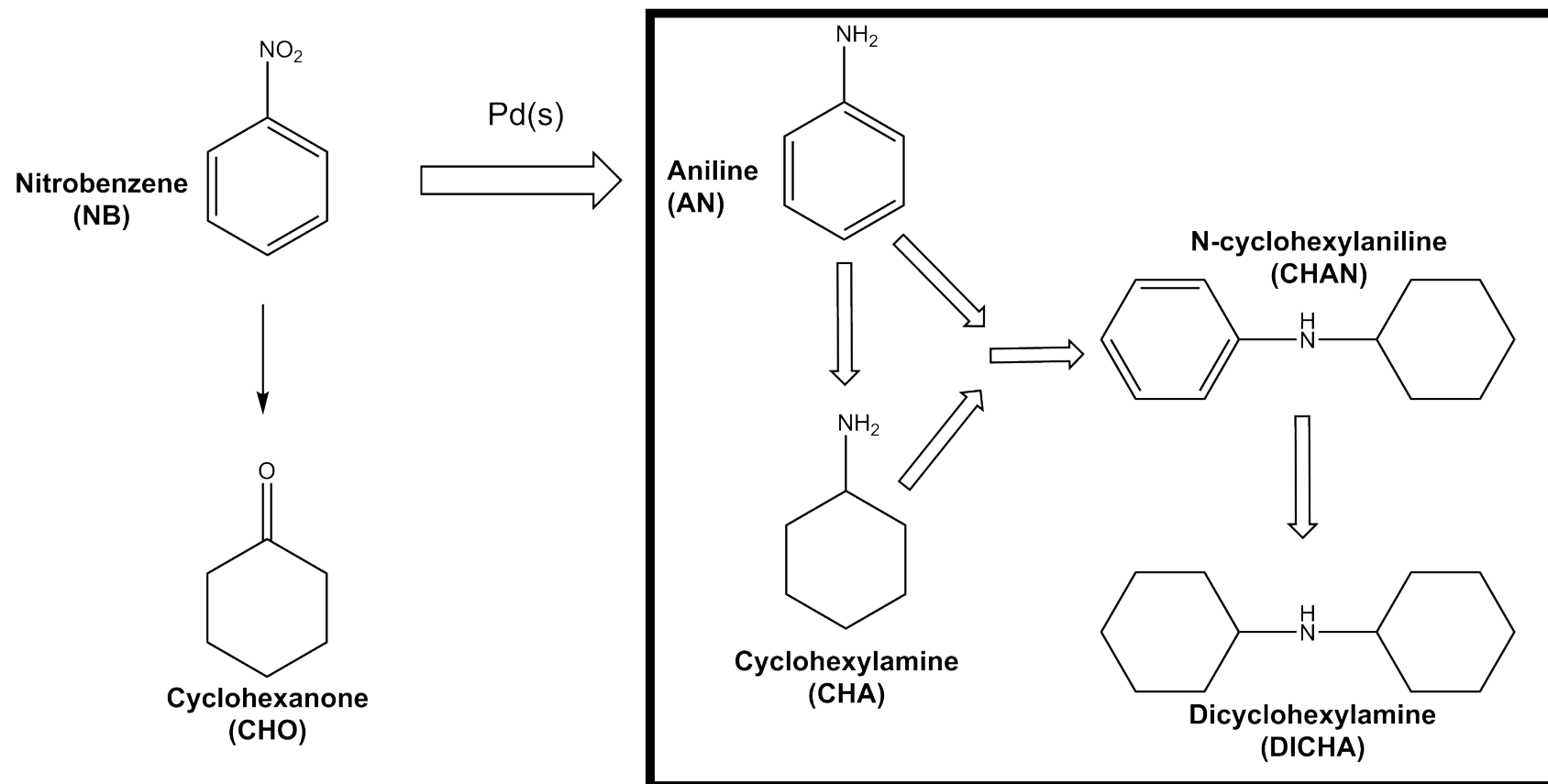
N-H bond. However at high temperatures, the high energy edge sites (catalyst 143 500) are responsible for the production of azobenzene, which is a nitrobenzene derived product obtained through cleavage of the N-O bond.

To conclude, the type of active site determines the shape and morphology of the Pd particles as described in Lear's paper [86]. The desorption of the CO informs us of the enthalpy of adsorption of said high energy sites. Correlating the reaction profiles presented in **Sections 5.4 and 5.7** with the enthalpy of the (111)/(100) and (111)/(111) edge sites, indicates that the high energy edge sites support N-O bond cleavage at high temperature, whereas a lower energy site will cleave a N-H bond on increasing temperature as detailed in **Scheme 6.1**. These conditions only pertain for relatively low concentrations of Pd in the reactor, *i.e.* 0.3 wt % Pd, Samples 2 and 3. The analysis of a high metal loading catalyst (Sample 1, **Chapter 3**), shows that the above deduction does not apply in that instance. Rather, in the presence of high Pd_(s) densities, NB \longrightarrow AN is the preferred reaction where NB is readily consumed by this reaction. High energy edge sites can only access aniline as a feedstock and thus the by-products observed are aniline-derived (*e.g.* CHA, CHAN, DICHA). These deductions force an elaboration of **Scheme 6.1**, (see **Scheme 6.2**) for high loading catalysts.

These trends may be rationalised with respect to bond enthalpies: 391 kJ/mol for -N-H in aniline and 607 kJ/mol for -N=O in nitrobenzene [?]. Hence high energy sites can activate -N=O bond cleavage provided that NB is accessible which is not the case in the presence of high Pd loadings. The lower energy edge sites are unable to activate -N=O bond cleavage but are capable of breaking -N-H bonds. Hence these sites favour the formation of aniline derived by-products at high nitrobenzene conversions. Throughout, it is assumed that any Pd surface site, *e.g.* Pd(111) and Pd(100) planes, have the capability of hydrogenating NB \longrightarrow AN.



Scheme 6.1: Proposed Structure/Activity relationships for the Pd/alumina catalyst in nitrobenzene hydrogenation for low loading catalysts (Samples 2 and 3)



Edge sites with significant enthalpy of adsorption

Scheme 6.2: Proposed Structure/Activity relationships for the Pd/alumina catalyst in nitrobenzene hydrogenation for low loading catalysts (Sample 1). High concentration of Pd in the reactor lead to further hydrogenation to aniline.

Chapter 7

The structure/activity relationship applied to Pd/alumina-silica catalysts (Samples 4, 5 and 6)

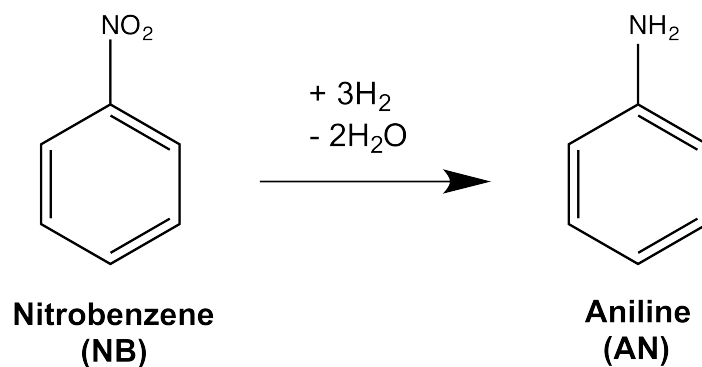
Chapter 3 enabled an experimental protocol to be developed to an extent that permitted CO chemisorption measurements on low loading (0.3%) Pd/Al₂O₃ catalysts. **Chapters 5 and 6** examined reaction profiles and presented characterisation of two prototype hydrogenation catalysts favoured by the industrial collaborator. However, during the course of this study, the industrial partner obtained evidence that the alumina support materials could be meta-stable during reaction conditions (at high temperature in presence of H₂O, see **Section 6.1.2.1**). In an attempt to circumvent this additional complication, a series of alumina-silicas were selected as possible new alternative catalysts. Their performance and characterisation are described in this chapter. As with Samples 2 and 3, these catalysts were supplied by Huntsman Polyurethanes.

7.1 Reaction Testing

7.1.1 M11572 0.3 wt % Pd/Al₂O₃ -30 % SiO₂ (Sample 4) catalyst

Catalyst 4 (M11572) was tested for the nitrobenzene hydrogenation under the same conditions stated in **Section 5.1.1**, so that it would be possible to compare them against Samples 2 (310/2) and 3 (143 500). 20 mg of catalyst was placed in a 1/4 inch tubular reactor and activated as indicated in **Section 2.2**. Nitrobenzene/helium/hydrogen feed (NB 2.03 x 10⁻⁶ mol/min: H₂ 7.83 x 10⁻⁴ mol/min - H₂:NB = 385 : 1) was then passed over the catalyst for approximately 12 hours at 60°C. **Figure 7.1** shows the nitrobenzene conversion (in black) and selectivity towards aniline (in red) calculated using **Equations 2.4 and 2.5**.

The nitrobenzene conversion observed at 60°C is approximately 20%, and was found to decrease with increasing temperature. It reached a minimum of 5% at 140°C and ended at 10% for 160°C. This catalyst lead to a drastic loss in conversion when compared respectively to Samples 2 (310/2) and 3 (143 500) in **Section 5.1**. Moreover, apart from the main product which is aniline, no other compounds were recorded during the temperature-programmed nitrobenzene hydrogenation. As a consequence, the selectivity towards aniline is 100% from 60°C to 160°C. One should note the relationship between using a low conversion and the absence of impurities during the nitrobenzene hydrogenation the 0.3 wt % Pd/Al₂O₃ - 30 wt % SiO₂ catalyst. The industrial requirement seeks high aniline yields, which necessitates high conversions. Thus, due to the reduced nitrobenzene conversion observed in **Figure 7.1**, this catalyst was deemed unsuitable for the industrial application.



Scheme 7.1: Reaction scheme of nitrobenzene hydrogenation in a fixed-bed tubular reactor for the Sample 4 (JM, 0.3 wt% Pd/Al₂O₃ - 30% SiO₂, M11572).

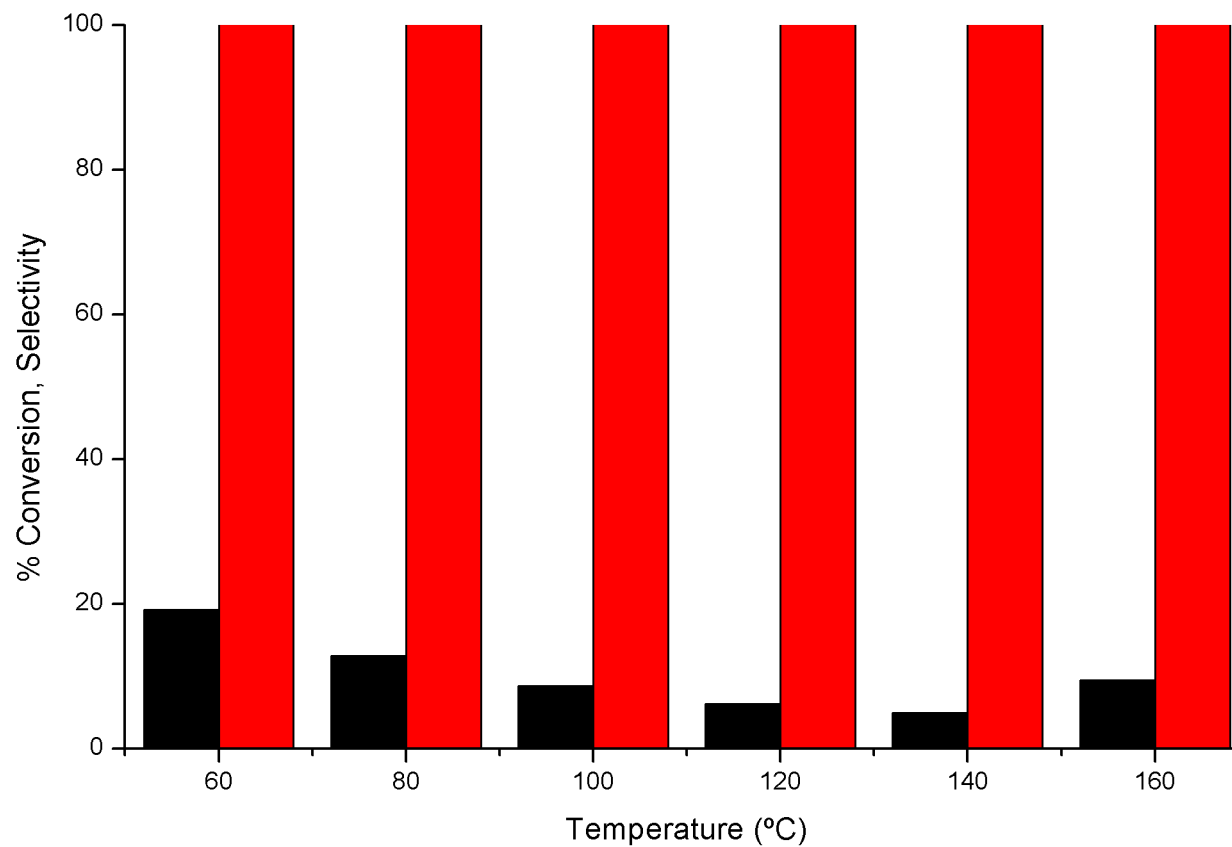


Figure 7.1: Nitrobenzene conversion (black) and aniline selectivity (red) as a function of reaction temperature over 0.3 wt % Pd/alumina-Silica (M11572) catalyst. Catalyst was sieved to 500-250 microns before reaction and 20 mg was placed in the stainless steel 1/4 inch tubular reactor. Nitrobenzene/hydrogen flow was kept constant throughout the reaction. Each temperature was kept for an hour before increasing by 20°C until reaching 160°C (NB 2.03×10^{-6} mol/min: H₂ 7.83×10^{-4} mol/min - H₂:NB = 385 : 1, NB(s⁻¹) : Pd_(s) = 1 : 3.2).

7.1.2 764 0.4 wt % Pd/Al₂O₃ - 1 % SiO₂ (Sample 5) catalyst

Although catalyst 4 exhibited complete selectivity to aniline, the conversions were prohibitively low. This prompted lower silica levels to be examined.

Catalyst 5 (764) was tested for the nitrobenzene hydrogenation under the same conditions stated in **Section 2.2**, so that it would be possible to compare against the 310/2 and 143 500 catalysts. 20 mg of catalyst was placed in a 1/4 inch tubular reactor and activated as indicated in **Section 2.2**. Nitrobenzene/helium/hydrogen feed (NB 2.03 x 10⁻⁶ mol/min: H₂ 7.83 x 10⁻⁴ mol/min - H₂:NB = 385 : 1) was then passed over the catalyst for approximately 12 hours at 60°C. **Figure 7.2** shows the nitrobenzene conversion in black where the selectivity towards aniline (in red) was calculated using **Equations 2.4 and 2.5**.

The 0.4 wt % Pd/Al₂O₃ - 1 wt % SiO₂ catalyst, as opposed to the catalyst 4 (M11572), displayed a radically different trend in relation to nitrobenzene conversion. The conversion presented in **Figure 7.2** oscillated between 95 and 99% across the temperature range. However, the selectivity remained high between 60 and 100°C. There was a decrease in selectivity after 120°C, where it dropped to 95% and reached 85% at 180°C.

The loss of selectivity observed in **Figure 7.2** is reported hereafter in **Figure 7.3** as a % selectivity of impurities against the temperature ramp. Upon increasing temperature, impurities are formed from 80°C and increase with temperature to reach an overall 15% selectivity towards by-products at 180°C.

At 80°C, only N-cyclohexylanilin (CHAN)e in blue and dicyclohexylamine (DICHA) in green are monitored in small quantities. With increasing temperature (to 100°C), we recorded the same impurities but in larger quantity. Cyclohexanone (CHO) (in red) appeared at 120°C alongside the CHAN and DICHA which are both present, with a 2% selectivity. Cyclohexylamine (CHA) (in black) was also produced at 140°C with CHO, CHAN and DICHA. While CHAN and DICHA increased with temperature, cyclohexanone remained at a constant level all the way through from 160°C to 180°C.

The by-product chemistry displayed is aniline derived, as discussed in **Chapter 4**.

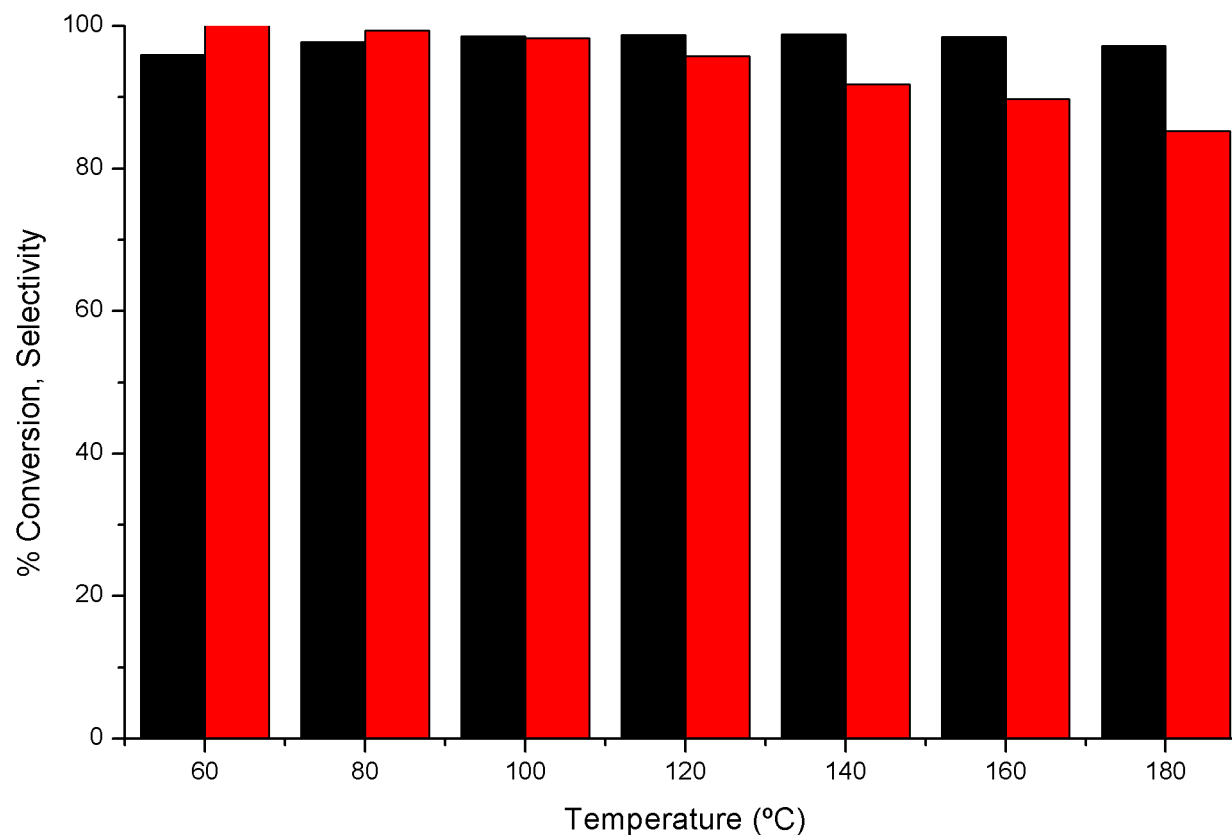


Figure 7.2: Nitrobenzene conversion (black) and aniline selectivity (red) as a function of reaction temperature over 0.4 wt % Pd/alumina-Silica (764) catalyst. Catalyst was sieved to 500-250 microns before reaction and 20 mg was placed in the stainless steel 1/4 inch tubular reactor. Nitrobenzene/hydrogen flow was kept constant throughout the reaction. Each temperature was kept for an hour before increasing by 20°C until reaching 180°C (NB 2.03×10^{-6} mol/min: H₂ 7.83×10^{-4} mol/min - H₂:NB = 385 : 1, NB(s⁻¹) : Pd_(s) = 1 : 6.8).

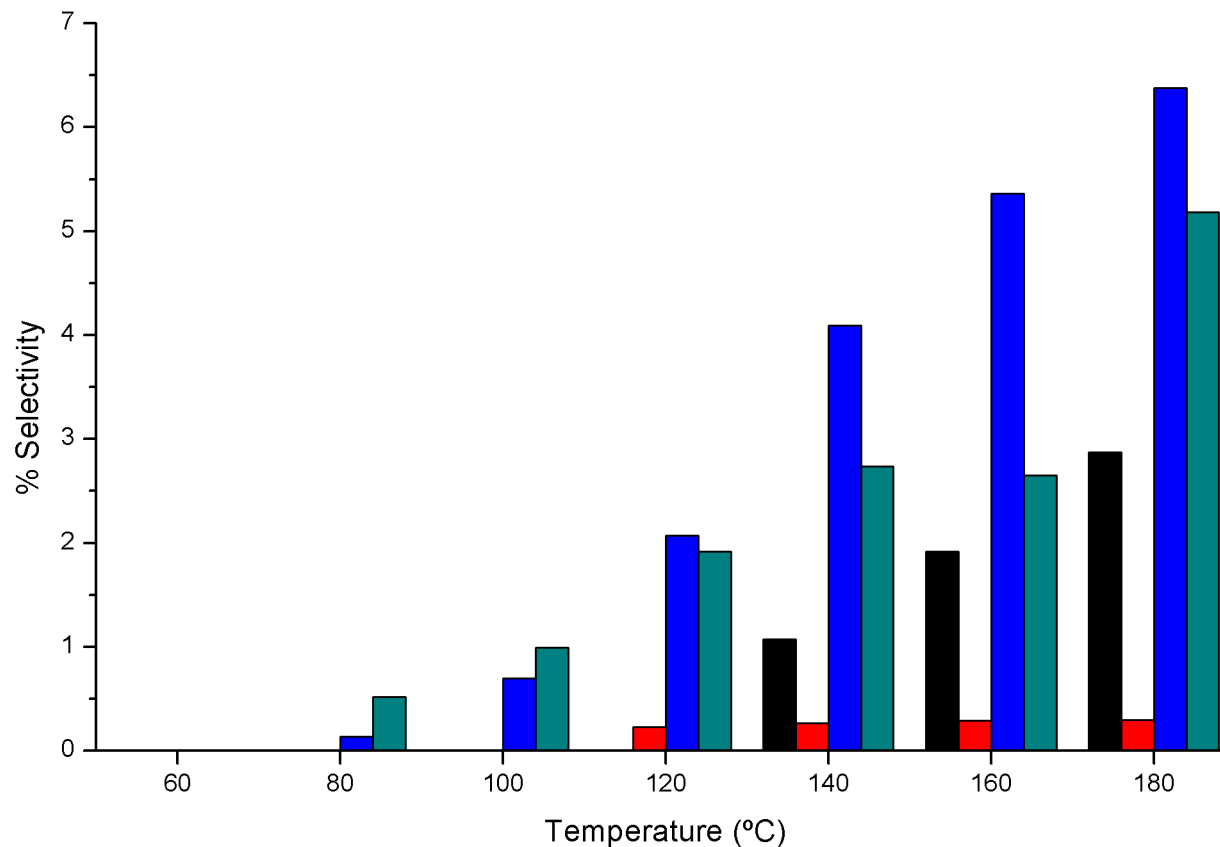


Figure 7.3: Selectivity profile (%) of the by-products produced as a function of reaction temperature over 0.4 wt % Pd/alumina-Silica (764) catalyst. Catalyst was sieved to 500-250 microns before reaction and 20 mg was placed in the stainless steel 1/4 inch tubular reactor. Nitrobenzene/hydrogen flow was kept constant throughout the reaction. Each temperature was kept for an hour before increasing by 20°C until reaching 180°C. Cyclohexylamine (black), cyclohexanone (red) N-cyclohexylaniline (blue) and dicyclohexylaniline (green) are observed.

7.1.3 M12340 0.3 wt % Pd/Al₂O₃ - 1 % SiO₂ (Sample 6) catalyst

This catalyst is analogous to catalyst 5 except, for a slightly reduced metal loading. The M12340 catalyst was tested for the nitrobenzene hydrogenation under the same conditions stated in **Section 2.2**, so that it would be possible to compare against the 310/2 and 143 500 catalysts. 20 mg of catalyst was placed in a 1/4 inch tubular reactor and activated as indicated in **Section 2.2**. Nitrobenzene/helium/hydrogen feed was then flowed over the catalyst for approximately 12 hours at 60°C. **Figure 7.4** shows the nitrobenzene conversion in black and the selectivity towards aniline (in red) was calculated using **Equations 2.4 and 2.5**.

The 0.3 wt % Pd/Al₂O₃ - 1 wt % SiO₂ catalyst compared to the catalyst 5 (764) displayed a superior nitrobenzene conversion. The conversion presented in **Figure 7.4** remained at 100% across the entire temperature range. Although the selectivity remained high from 60°C, it decreased steadily and reached 83% at 160°C.

The loss of selectivity observed in **Figure 7.4** is reported hereafter in **Figure 7.5** as a % selectivity of impurities against the temperature ramp. Upon increasing temperature, impurities are formed from 60°C and are found to increase with temperature. They reach an overall 17% selectivity towards by-products at 180°C. At 60°C, only dicyclohexylamine in green was monitored. Cyclohexanone in red, N-cyclohexylaniline in blue were recorded at 80°C in small amounts. Increasing the temperature to 100°C, showed the same impurities in bigger amounts except for cyclohexanone, which remained at the same level previously recorded at 80°C. Cyclohexylamine (in black) appeared at 120°C alongside the CHO, CHAN and DICHA. From 120 to 160°C, CHA and CHAN increased steadily while DICHA and CHO were constant throughout. As a matter of fact, cyclohexanone, after being detected at 80°C, remained constant across the full temperature range.

The by-product chemistry displayed here is aniline derived as discussed in **Chapters 3, 4 and 5**. The difference of product distribution between 0.3 and 0.4 wt % Pd/Al₂O₃ - 1 wt % SiO₂ depends mostly on the size of the particle. As metal loading does not reflect necessarily on the particle size, CO adsorption isotherms are required on all three catalysts to understand the reactivity differences.

Overall, the catalyst 4 (M11572) is completely selective to aniline, whilst catalysts 5 (764) and 6 (M12340) exhibited the production of similar impurities with differing pro-

portions. With increasing temperature, the 764 selectivity was spread equally between CHAN and DICHA, whereas for the M12340 catalyst it was more pronounced towards the final DICHA product. Full hydrogenation of aniline derived by-products therefore is most favoured over Sample 6.

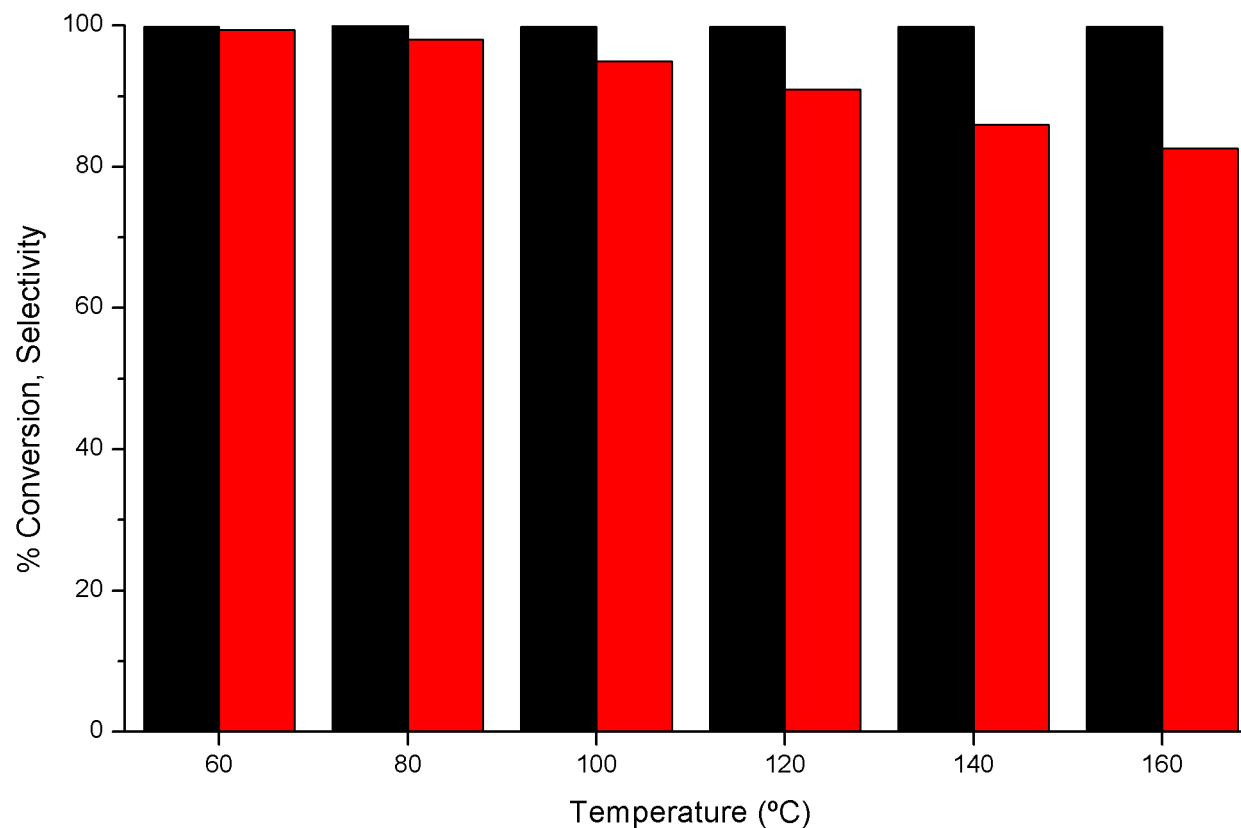


Figure 7.4: Nitrobenzene conversion (black) and aniline selectivity (red) as a function of reaction temperature over 0.3 wt % Pd/alumina-Silica (M12340) catalyst. Catalyst was sieved to 500-250 microns before reaction and 20 mg was placed in the stainless steel 1/4 inch tubular reactor. Nitrobenzene/hydrogen flow was kept constant throughout the reaction. Each temperature was kept for an hour before increasing by 20°C until reaching 160°C (NB 2.03×10^{-6} mol/min: H₂ 7.83×10^{-4} mol/min - H₂:NB = 385 : 1, NB(s⁻¹) : Pd_(s) = 1 : 3.7).

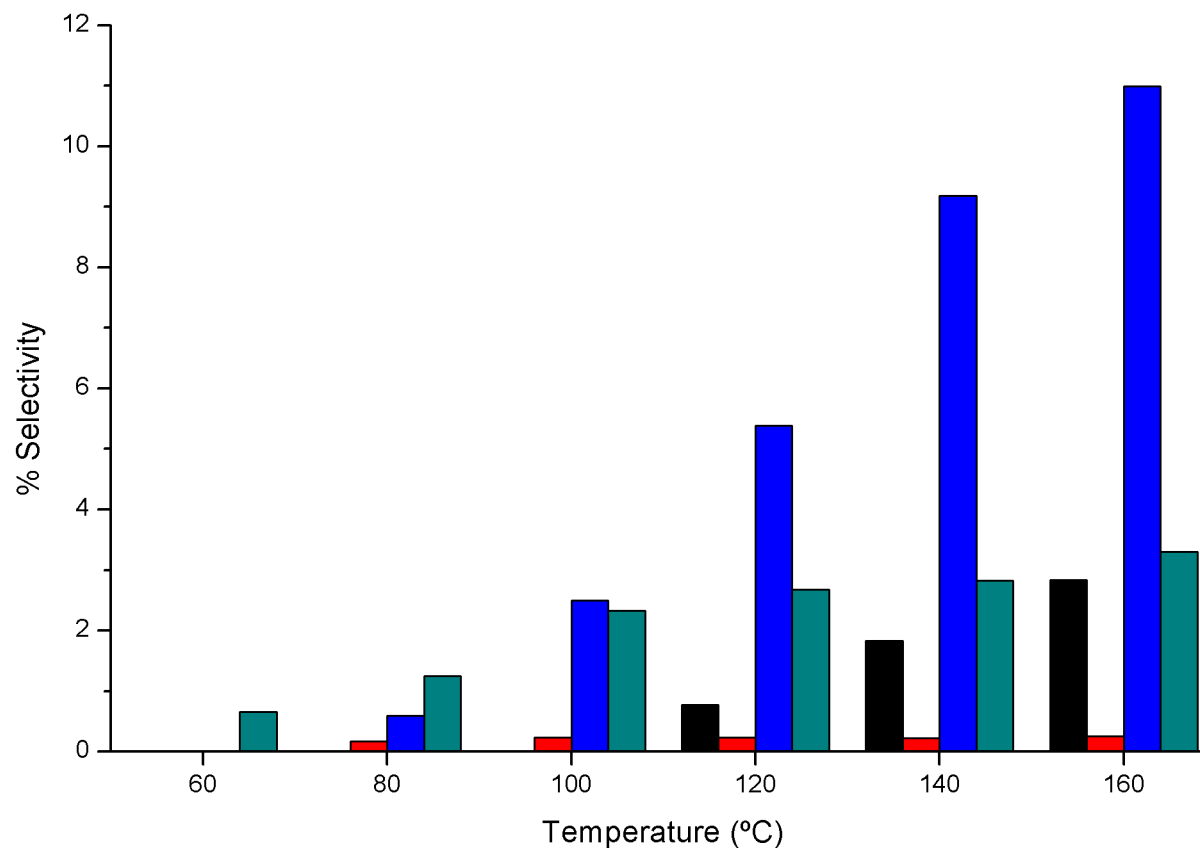


Figure 7.5: Selectivity profile (%) of the by-products produced as a function of reaction temperature over 0.3 wt % Pd/alumina-Silica (M12340) catalyst. Catalyst was sieved to 500-250 microns before reaction and 20 mg was placed in the stainless steel 1/4 inch tubular reactor. Nitrobenzene/hydrogen flow was kept constant throughout the reaction. Each temperature was kept for an hour before increasing by 20°C until reaching 180°C. Cyclohexylamine (black), cyclohexanone (red) N-cyclohexylaniline (blue) and dicyclohexylaniline (green) are observed.

7.2 Characterisation, XRD, BET and CO Chemisorptions.

7.2.1 Atomic Absorption

Catalyst	Actual Weight % Pd Loading
0.3 wt % Pd/Al ₂ O ₃ - 30% SiO ₂ (M11572)	0.23 ±3
0.3 wt % Pd/Al ₂ O ₃ - 1% SiO ₂ (M12340)	0.29 ±3
0.4 wt % Pd/Al ₂ O ₃ - 1% SiO ₂ (764)	0.37 ±3

Table 7.1: Actual Metal Loading From Atomic Absorption Spectroscopy measurements

The value for the 143 500 catalyst was found to be lower than the advertised loading. This may be attributed to the palladium not being properly leached out of the support during the preparation stages of the solution.

7.2.2 CO adsorption isotherms

CO chemisorption was carried out as discussed in **Section 2.4.7**, assuming that the stoichiometry of CO:Pd was 1:2. CO isotherm plots for catalysts 4, 5 and 6 are respectively shown in **Figures 7.6a, 7.6b and 7.6c**. All saturation values and subsequent calculated dispersions and estimated particle sizes are presented here in **Table 7.2**.

Catalyst		CO uptake (mol CO / g catalyst)	Dispersion (%)	Particle size (nm)	BET S.A. (m ² .g ⁻¹)
M11572	1	2.70 x 10 ⁻⁶	19.1	5.7	273
	2	2.95 x 10 ⁻⁶	20.9	5.2	
764	1	6.0 x 10 ⁻⁶	32	3.4	107
M12340	1	3.3 x 10 ⁻⁶	23	4.5	115

Table 7.2: Table of Dispersions for CO Pulsed Chemisorptions.

It is visible that there are some differences in the Pd distribution, which prompts the need for further characterisation work to be undertaken. As discussed in **Chapter 6**, difference in particle size can lead to drastic changes in catalyst selectivity. This is shown in the model found in **Chapter 6 and Figure 6.1**.

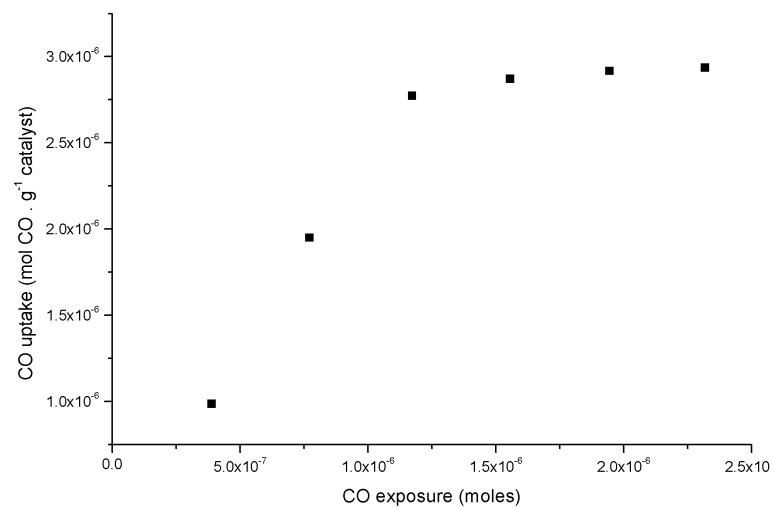
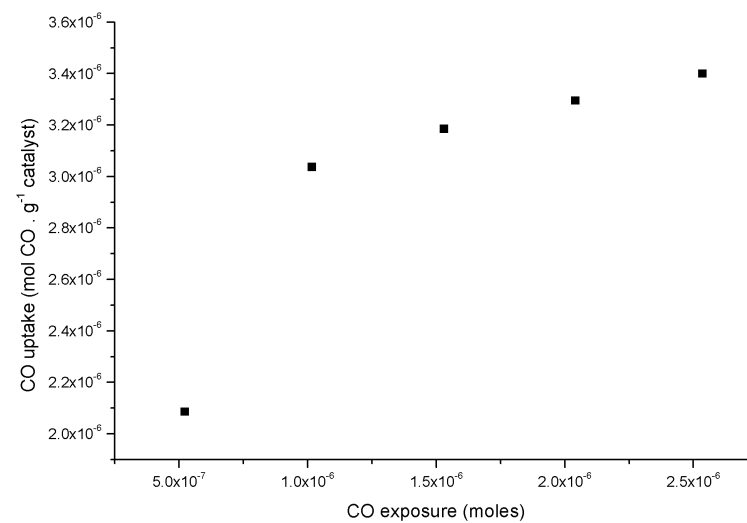
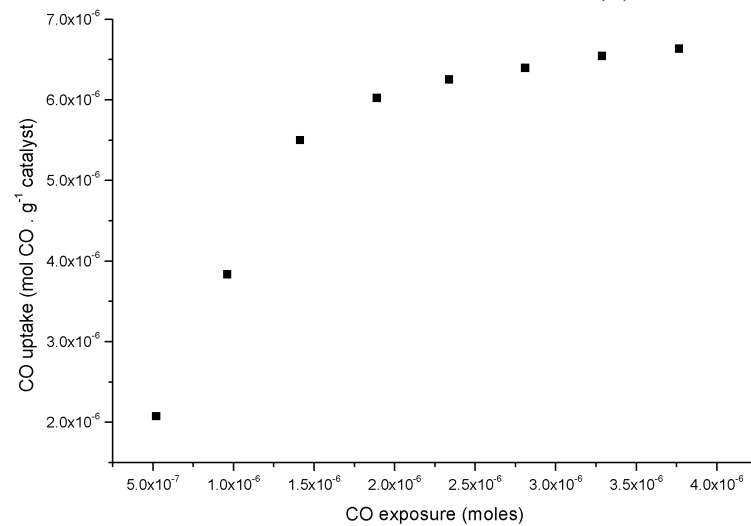
(a) M11572 - 0.3 wt % Pd/Al₂O₃ - 30% SiO₂(b) M12340 - 0.3 wt % Pd/Al₂O₃ - 1% SiO₂(c) 764 - 0.4 wt % Pd/Al₂O₃ - 1% SiO₂

Figure 7.6: Pulsed CO Chemisorption Isotherm on Pd/alumina-Silica catalysts 4, 5 and 6.

7.2.3 X-ray powder Diffraction

Figure 7.7 represents the diffractogram of the catalyst 4 (M11572) carried out as specified in **Section 2.4.3**. The XRD pattern displays a high amorphous character with few broad bands assigned to γ -alumina, as reported in **Table ??** [121]. As shown by Rajagopal *et al.* [129], when silica is mixed with alumina, the resulting XRD pattern displays a highly amorphous broad band as the silica content increases. Moreover, the catalyst formulation stipulates that the support contains as much as 30% of silica which correlates with the diffractogram observed.

Figure 7.8 shows the diffractogram obtained for the non-reduced catalyst 6 (M12340) which contains 0.3 wt % of palladium is composed of alumina and 1% of silica. Firstly, the sample is not more amorphous but resembles the diffractogram obtained from catalyst 2 (310/2) shown in **Section 5.2.4**. These two catalysts come from the same supplier so it can be assumed that the support used is identical if it were not for the added silica. The assignments made for the catalyst 2 (310/2) in **Table 5.4** are similar to those of catalyst 6 (M12340) and are shown in **Table 7.4** and **Figure 7.7**. It can be concluded that the 1% silica added to the support is too low to induce a significant structural transformation, hence the diffractogram looks identical to catalyst 2. The support is composed of δ and θ -alumina.

The diffractogram of catalyst 5 (764) is presented in **Figure 7.9**. This catalyst is supposedly prepared identically to catalyst 6 (M12340) but contains 0.4 wt % of palladium. As expected, a change of 0.1 wt % in palladium loading did not affect the XRD pattern recorded as it looks similar to that given for catalyst 6 (M12340). Therefore, the assignment reported in **Table 7.4** is valid for catalyst 5 (764) as well. Catalyst 5 is also supported on a mixture of δ and θ -alumina.

To sum up, the addition of 30 % silica to the support leads to a loss in the crystallinity of the sample and showed a γ -alumina/silica support. However, the addition of 1 % silica to the alumina support induced the formation of a δ,θ -alumina/silica support with a much higher crystallinity. Moreover, the BET data presented in **Section 7.2** is consistent with the type of transition alumina phases observed, as discussed earlier in **Chapter 5, Section 5.2**.

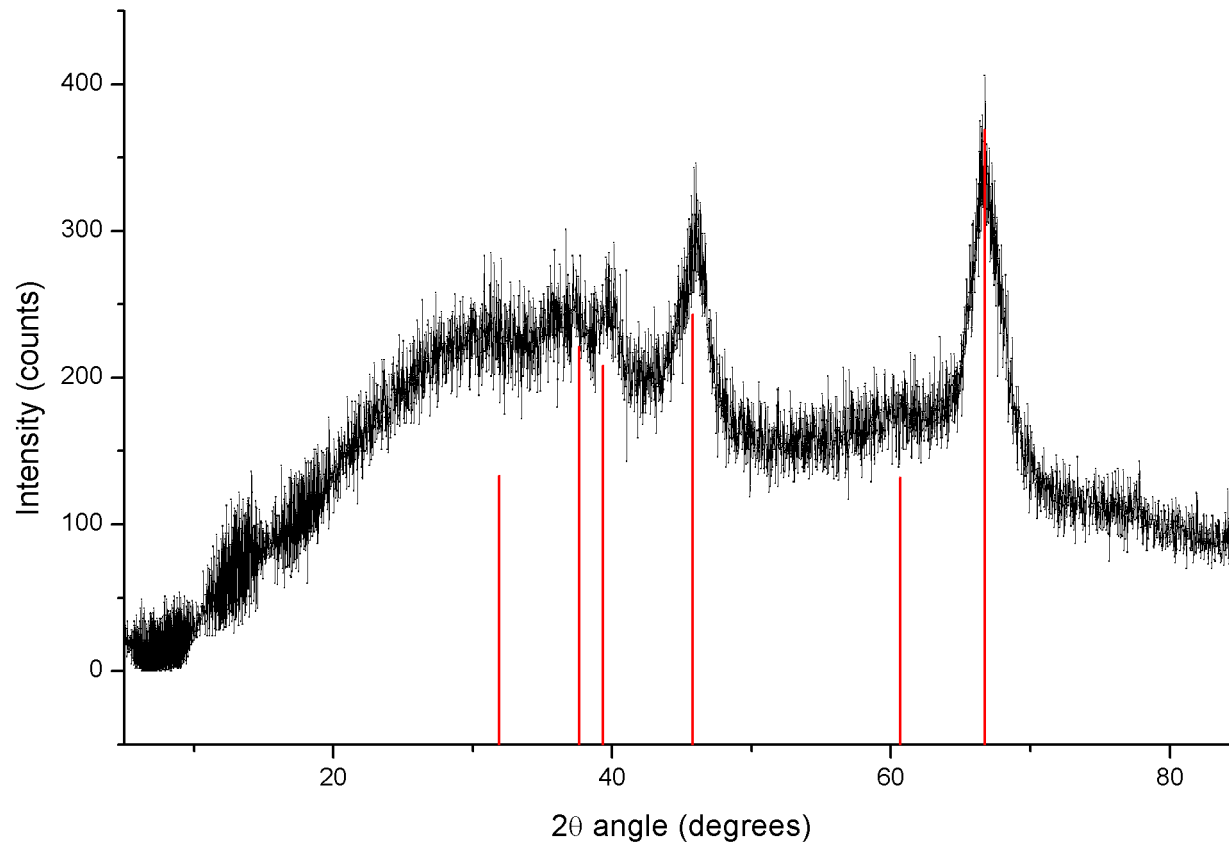


Figure 7.7: X-ray Powder Diffraction pattern recorded for the 0.3 wt % Pd/alumina-30%Silica (M11572) catalyst. The red drop lines represent the reference γ -alumina diffractogram [95].

Gamma-alumina		
2 Θ Angle (degrees)	d spacing (\AA)	h k l
37.618	2.38918	311
39.358	2.28746	222
45.765	1.981	400
60.679	1.52497	511
66.721	1.40078	440

Table 7.3: XRD assignments for the M11572 catalyst based on the gamma-alumina main reflections [95].

2 Θ Angle (degrees)	Theta-alumina		Delta-alumina	
	d spacing (\AA)	h k l	d spacing (\AA)	h k l
31.44	2.82737	400		
32.74	2.729	202	2.73067	222
36.8	2.44529	111		
39	2.3121	401		
39.52			2.28062	226
45.12	2.02006	311		
45.52			1.99028	400
46.84			1.94955	0.0.12
47.5			1.90956	318
50.72	1.79866	510		
57.38	1.62049	203		
60.06	1.54207	313		
63.98	1.45505	020		
64.18			1.44991	440
66.77			1.39986	4.0.12
67.14	1.38721	712		

Table 7.4: XRD assignments for the 764 and M12340 catalyst based on the main reflections of θ and δ -alumina transition phases [95].

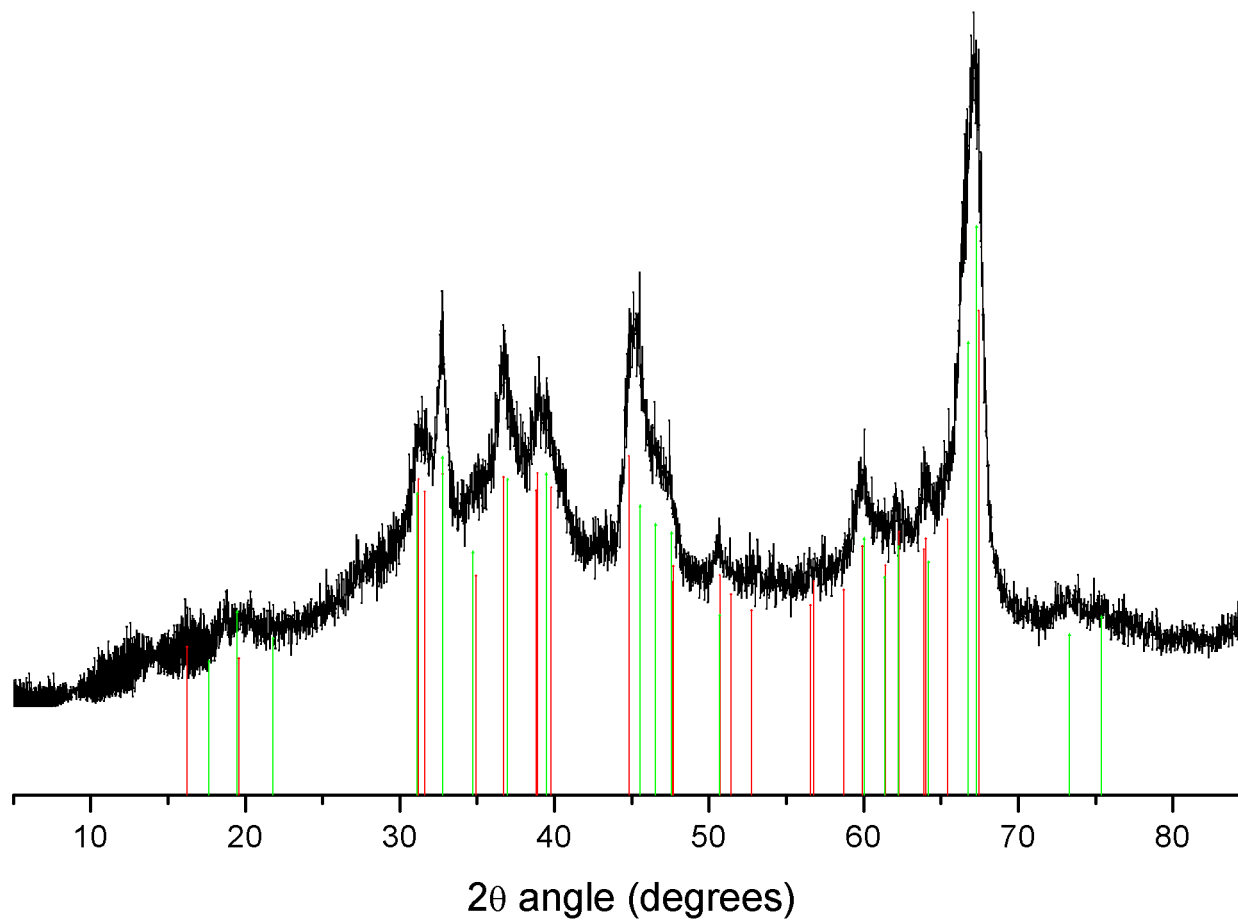


Figure 7.8: X-ray Powder Diffraction pattern recorded for the 0.3 wt % Pd/Al₂O₃ - 1% SiO₂ (M12340) catalyst. The red drop lines represent the δ -alumina main reflections and the green drop lines the θ -alumina [95].

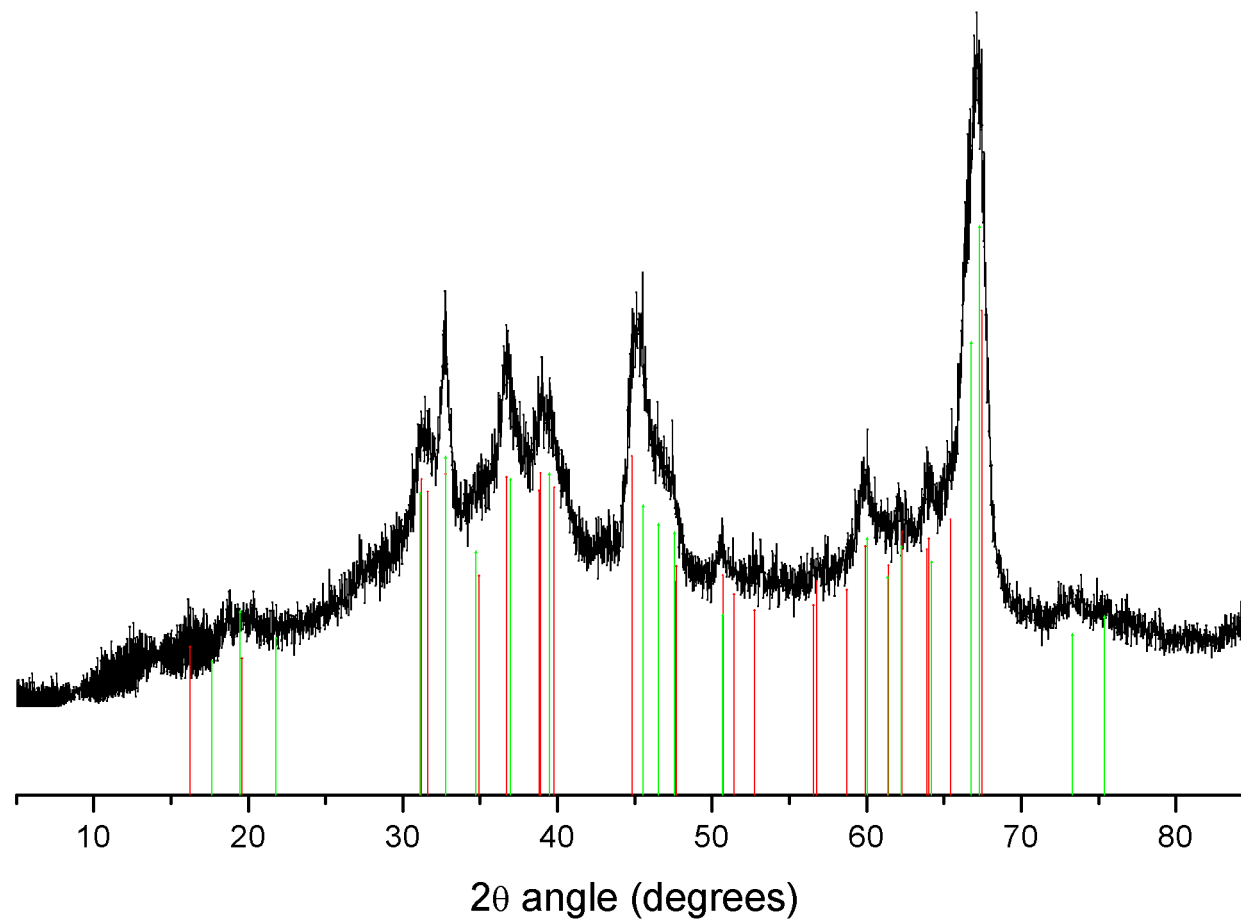


Figure 7.9: X-ray Powder Diffraction pattern recorded for the 0.4 wt % Pd/Al₂O₃ - 1% SiO₂ (764) catalyst. The red drop lines represent the δ-alumina main reflections and the green drop lines the θ-alumina [95].

7.3 CO Temperature-programmed Infrared Spectroscopy (Samples 4, 5 and 6)

7.3.1 M11572 0.3 wt % Pd/Al₂O₃-30 % SiO₂ (Sample 4) catalyst

The infrared spectroscopy results from the chemisorption using the Spectra Tech Diffuse Reflectance Infrared Fourier Transform cell on the 0.3 wt % Pd/Al₂O₃ - 30% SiO₂ are shown in **Figure 7.10**. The chemisorption was carried out as mentioned in **Section 2.4.1**.

The scan of the chemisorbed CO at the surface of the catalyst after activation is shown in **Figure 7.10**. The saturated spectrum displayed here is quite unusual. Three bands for the chemisorption of CO at the surface of this catalyst are distinguishable. The peak at 2082 cm⁻¹ indicates that a small amount is chemisorbed linearly on the corner sites of the palladium crystal [85]. The broad noisy peaks present at lower wavenumbers correspond to CO chemisorbed over Pd low index planes. The peak at 1985 cm⁻¹ is attributed to CO μ_2 bridge bonded CO on Pd (100) and the band at 1930 cm⁻¹ is assigned to μ_3 bridge bonded CO on Pd (111) [74].

Upon heating, the band at 1985 cm⁻¹ and 1930 cm⁻¹ decrease slightly in intensity and merge to form one broad feature still present at 50°C but which totally desorbed at 100°C. The signal to noise ratio and the unusual shape of the peaks possibly reflects the lack of probed dipoles (Pd-CO) by the IR beam (note that this catalyst possesses the lowest metal surface area for the silica doped catalysts, see **Table 7.2**). The later could be due to the Pd particles being encapsulated in the 30 % silica present in the support, which may have blocked the low index plane sites. CO adsorption isotherm measurements indicate however that this not the case. The peak at 2082 cm⁻¹ represents the linear chemisorption at the surface and shows it has a low enthalpy of adsorption as well considering that only a fraction of it is left at 50°C. It fully desorbs at 100°C. It is surmised that the T_{max} seen for the $\nu_1(\text{CO})$ band (<100°C), means that these edge sites are below the enthalpic value required to break either a N-H (bond enthalpy of 391 kJ/mol) or a N=O (bond enthalpy of 607 kJ/mol) bond. Hence, no by-product formation is possible with this catalyst. It is also acknowledged that silica-aluminas exhibit atypical properties [130]. A detailed study of the silica-alumina modified Pd catalysts is beyond the scope of the current work of the project.

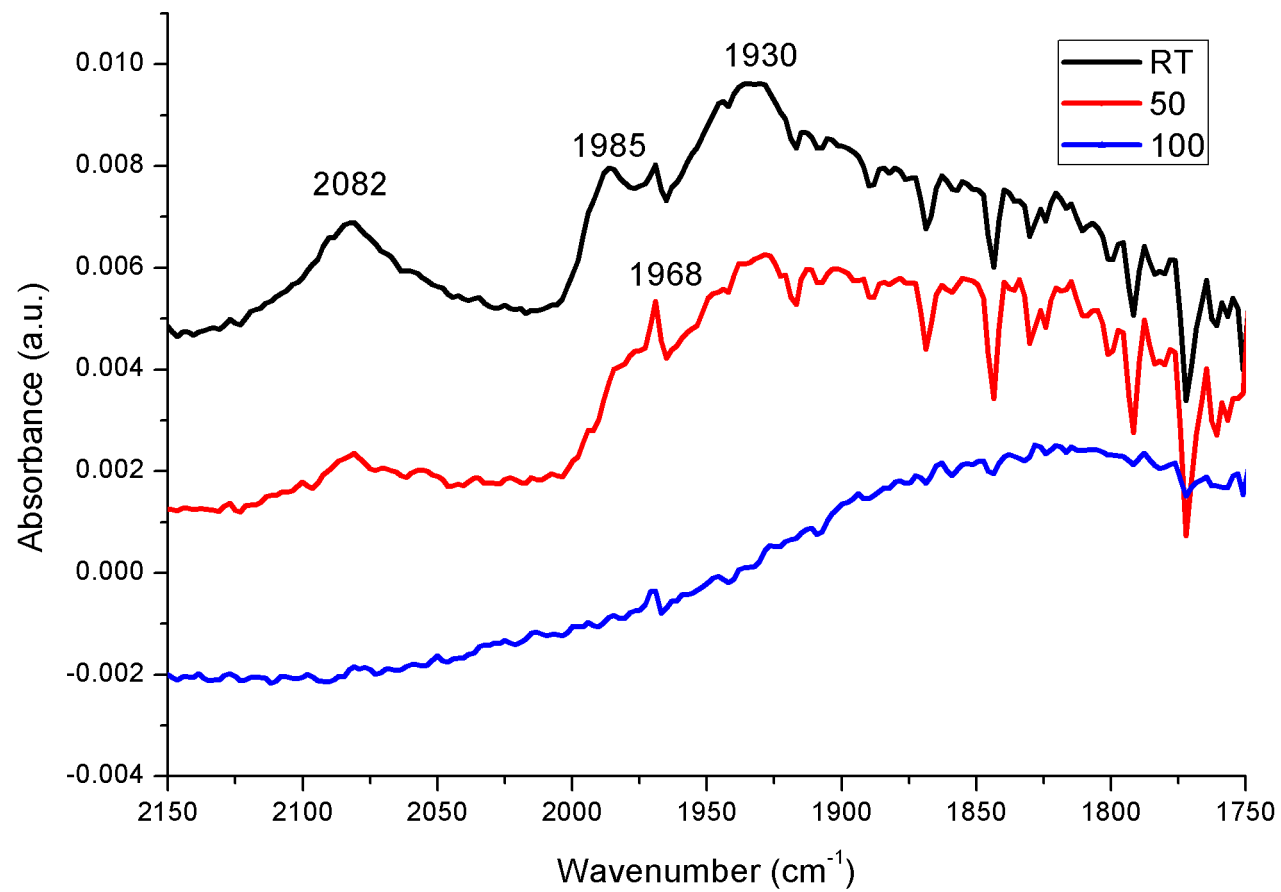


Figure 7.10: Temperature-Programmed Infrared Spectroscopy on 0.3 wt % Pd/Al₂O₃ - 30% SiO₂ (M11572).

7.3.2 764 0.4 wt % Pd/Al₂O₃- 1 % SiO₂ (Sample 5) catalyst

The infrared spectroscopy results from the chemisorption using the Spectra-Tech Diffuse Reflectance Infrared Fourier Transform cell on the 0.4 wt % Pd/Al₂O₃ - 1% SiO₂ are shown in **Figure 7.11**. The chemisorption was carried out as mentioned in **Section 2.4.1**.

The scan of the chemisorbed CO at the surface of the catalyst after activation is shown in **Figure 7.11**. The saturated spectrum displays four characteristic bands for the chemisorption of CO at the surface of a Pd/alumina catalyst as discussed in **Section 6.3**. The shoulder at 2082 cm⁻¹ indicates that a small amount has chemisorbed linearly on the corner site of the palladium crystal [85]. The band at 2061 cm⁻¹ is attributed to CO linearly bound to the Pd edge (100)/(111) crystallites. The two other features are attributed to two-fold and three fold chemisorbed CO over Pd low index planes. The band at 1982 cm⁻¹ is assigned to μ_2 bridge bonded CO on Pd (100) and the band at 1924 cm⁻¹ is assigned to μ_3 bridge bonded CO on Pd (111).

Upon heating, the band at 1924 cm⁻¹ decreases in intensity and wavenumber and reaches 1900 cm⁻¹ (μ_3 bridge bonded CO on Pd (111)). It is still present upon heating to 200°C. The band at 1982 cm⁻¹ (μ_2 bridge bonded CO on Pd (100)) also decreases in intensity and wavenumber upon heating to 200°C and is seen as a shoulder which shifts to 1940 cm⁻¹. The site at 2082 cm⁻¹ (linear CO residing on corner sites) is present at room temperature, although still present 50°C, at 100°C it is found to fully desorb. The band at 2061 cm⁻¹ (CO residing on (100)/(111)) decreases in intensity upon heating and is present up until 150°C, which indicates a relatively strong enthalpy of adsorption of this site (see the comparison with catalyst 3 (143 500 in) **Section 6.3**). Unlike the Bridge-bonded species seen in **Section 6.3**, the linear species does not shift upon heating. The desorption temperature of 150°C places the enthalpy of these edge sites as being intermediate between the low enthalpy ($T_{max} = 100^\circ\text{C}$, Sample 2) and high ($T_{max} = 200^\circ\text{C}$, Sample 3) enthalpic edge sites. Thus, these sites have insufficient energy to break a N=O bond, hence the by-product distribution as observed in **Section 7.1.2** is aniline-derived.

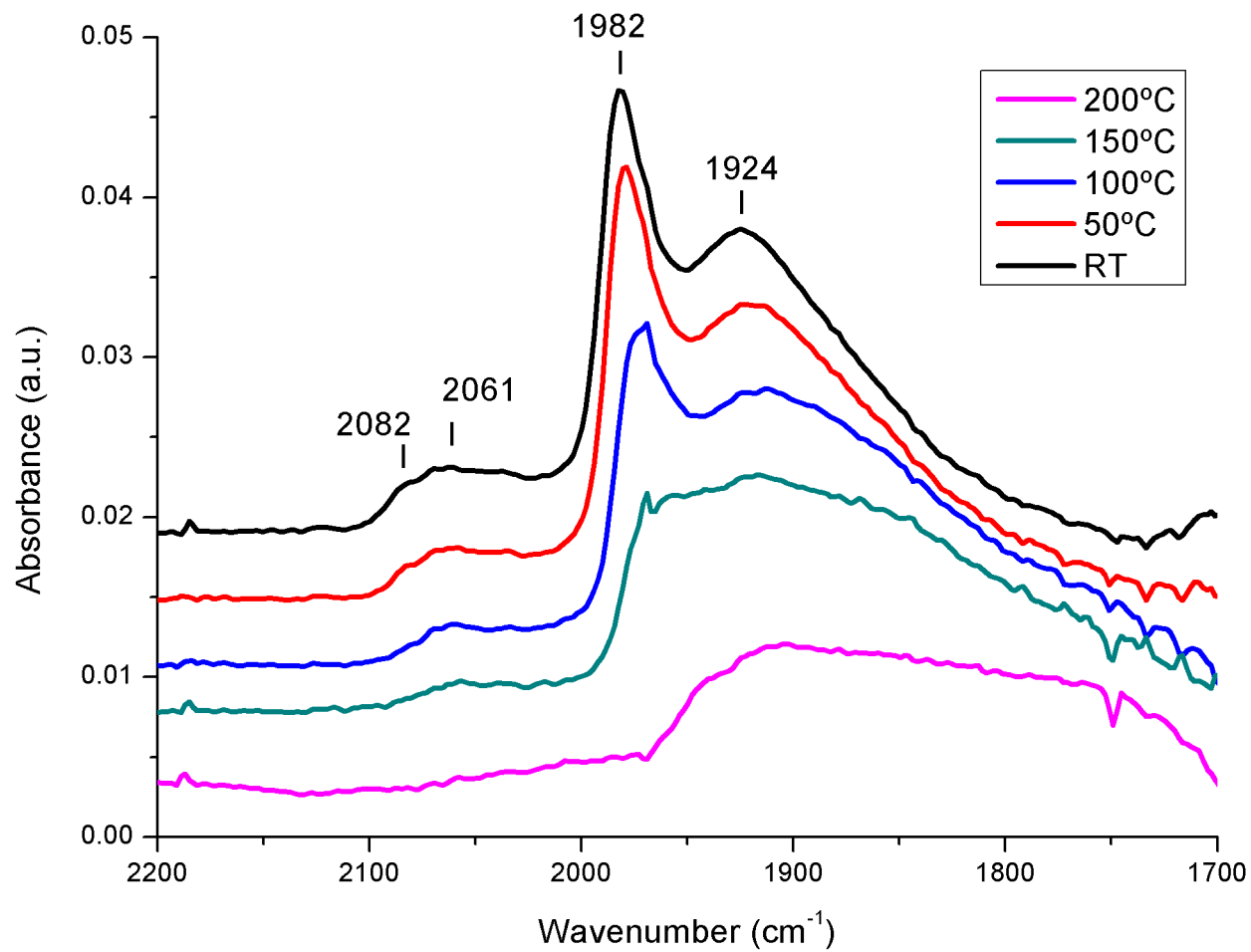


Figure 7.11: Temperature-Programmed Infrared Spectroscopy on 0.4 wt % Pd/Al₂O₃ - 1% SiO₂ (764).

7.3.3 M12340 0.3 wt % Pd/Al₂O₃- 1 % SiO₂ catalyst (Sample 6)

The infrared spectroscopy results from the chemisorption using the Spectra-Tech Diffuse Reflectance Infrared Fourier Transform cell on the 0.3 wt % Pd/Al₂O₃ - 1% SiO₂ are shown in **Figure 7.11**. The chemisorption was carried out as mentioned in **Section 2.4.1**.

The scan of the chemisorbed CO at the surface of the catalyst after activation is shown in **Figure 7.11**. The saturated spectrum displays three characteristic bands for the chemisorption of CO at the surface a Pd/alumina catalyst. The broad band at 2055 cm⁻¹ is attributed to CO linearly bound to the Pd edge (100)/(111) crystallites. The two other features are attributed to two-fold and three fold chemisorbed CO over Pd low index planes. The band at 1978 cm⁻¹ is assigned to μ_2 bridge bonded CO on Pd (100) and the band at 1924 cm⁻¹ is assigned to μ_3 bridge bonded CO on Pd (111) [74].

Upon heating, the band at 1924 cm⁻¹ decreases in intensity and wavenumber and reaches 1875 cm⁻¹ (μ_3 bridge bonded CO on Pd (111)), and loses definition after 150°C. The band at 1978 cm⁻¹ (μ_2 bridge bonded CO on Pd (100)) also decreases in intensity and wavenumber upon heating to 100°C. The band at 2055 cm⁻¹ (CO residing on (100)/(111)) decreases in intensity upon heating and is present up until 100°C which indicates a weaker enthalpy of adsorption of this site than Sample 5 (see the comparison with catalyst 3 (143 500) in **Section 6.3**).

The small variation of intensity from 764 to M12340 catalyst is due to the difference of metal loading which result in the small differences of particle size. These influence the density of edge and corner sites at the surface of the catalyst. Sample 5 exhibits slightly higher enthalpic adsorption than Sample 6 but nevertheless, the Sample 5 edge sites are of insufficient magnitude to induce nitrobenzene derived chemistry. For Sample 6, a T_{max} of 100°C defines a low enthalpy for the edge sites, insufficient to break a N=O bond and hence, as illustrated in **Section 7.1.3**, only aniline-derived products are seen.

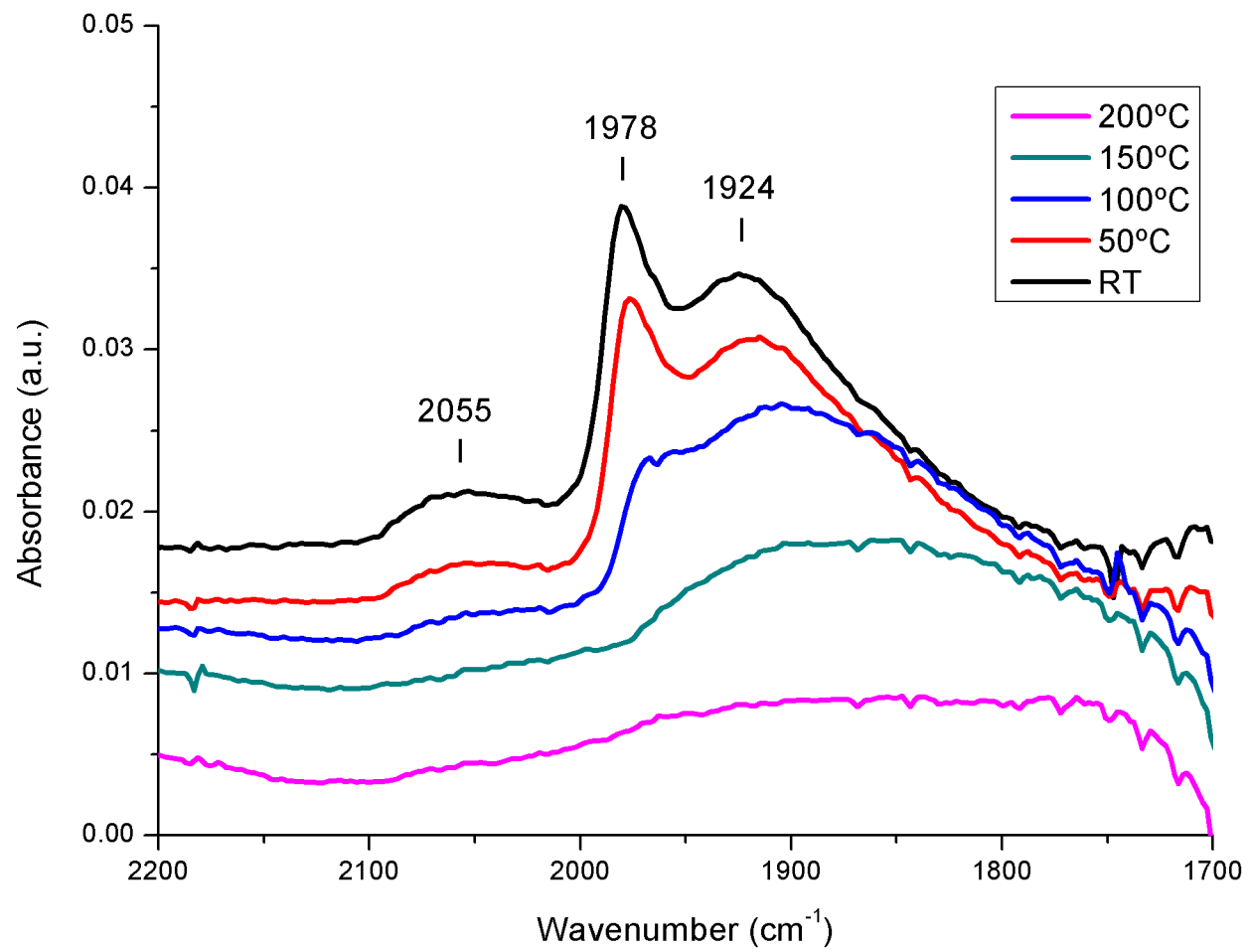


Figure 7.12: Temperature-Programmed Infrared Spectroscopy on 0.3 wt % Pd/Al₂O₃ - 1% SiO₂ (M12340).

7.4 Discussion

After establishing the model presented in **Chapter 6** regarding the production of impurities linked to the shift and energetics of the CO chemisorbed IR bands at the surface of Pd/Al₂O₃ catalysts, it seemed interesting to test the validity of the model using different catalysts where the support material has been modified in an attempt to overcome structural problems recently reported by the industrial collaborator [11]. The addition of silica was not meant to change the reactivity of the said catalysts.

The reaction testing revealed:

- The addition of 30% silica to the support led to a substantial decrease in nitrobenzene conversion to 10%. This was found to be far lower than all other catalysts. The low conversion resulted in a 100% selectivity towards aniline.
- The other two catalysts containing 1% silica showed a much higher activity, proving to be more active than the 310/2 and 143 500 catalysts. They exhibit a high loss of selectivity and production of aniline derived by-products.

The characterisation revealed:

- The total surface area of the 30% silica catalyst was higher than the other two modified catalysts, plus XRD pattern suggested the support to be γ -alumina support which is consistent with BET surface area. The other two catalysts exhibited the exact same support characteristics as catalyst 2 (310/2). 1% silica did not seem to be enough to drastically influence the alumina support. Both support were composed of a mixture of δ/θ -alumina.
- The CO adsorption isotherms revealed that the low conversion catalyst (Sample 4) exhibited particles of a size 5-6 nm. Catalyst 5 (0.4% Pd) and 6 (0.3% Pd) respectively exhibited particle size of 3.4 nm and 4.5 nm. It is usual for a higher loading to show larger particle sizes. Therefore, the preparation process of the catalyst may have been altered.
- The CO TPIR of the 30% catalyst was quite interesting because it did not display well formed CO chemisorption bands for any of the Pd sites expected. It also desorbed at a relatively low temperature. It was suggested that the low enthalpic value of the edge sites of this catalyst is insufficient to activate either N=O or N-H bonds and hence, only NB \longrightarrow AN chemistry is seen.
- The TPIR for the 0.3 and 0.4% Pd/alumina-1% Silica catalyst are quite similar. They both revealed a substantial amount of edge sites with relatively high enthalpy

of adsorption. However, the enthalpy of these sites is insufficient to activate a N=O bond cleavage and therefore the product distribution is dominated by aniline-derived chemistry.

Chapter 8

Conclusion

Nitrobenzene hydrogenation to produce aniline is a highly important industrial process because it accounts for most of the aniline produced in the world, with 75% of it reacted further as part of the MDI process to produce polyurethanes. The polyurethane market is growing by 5% every year and is estimated to grow even more in years to come.

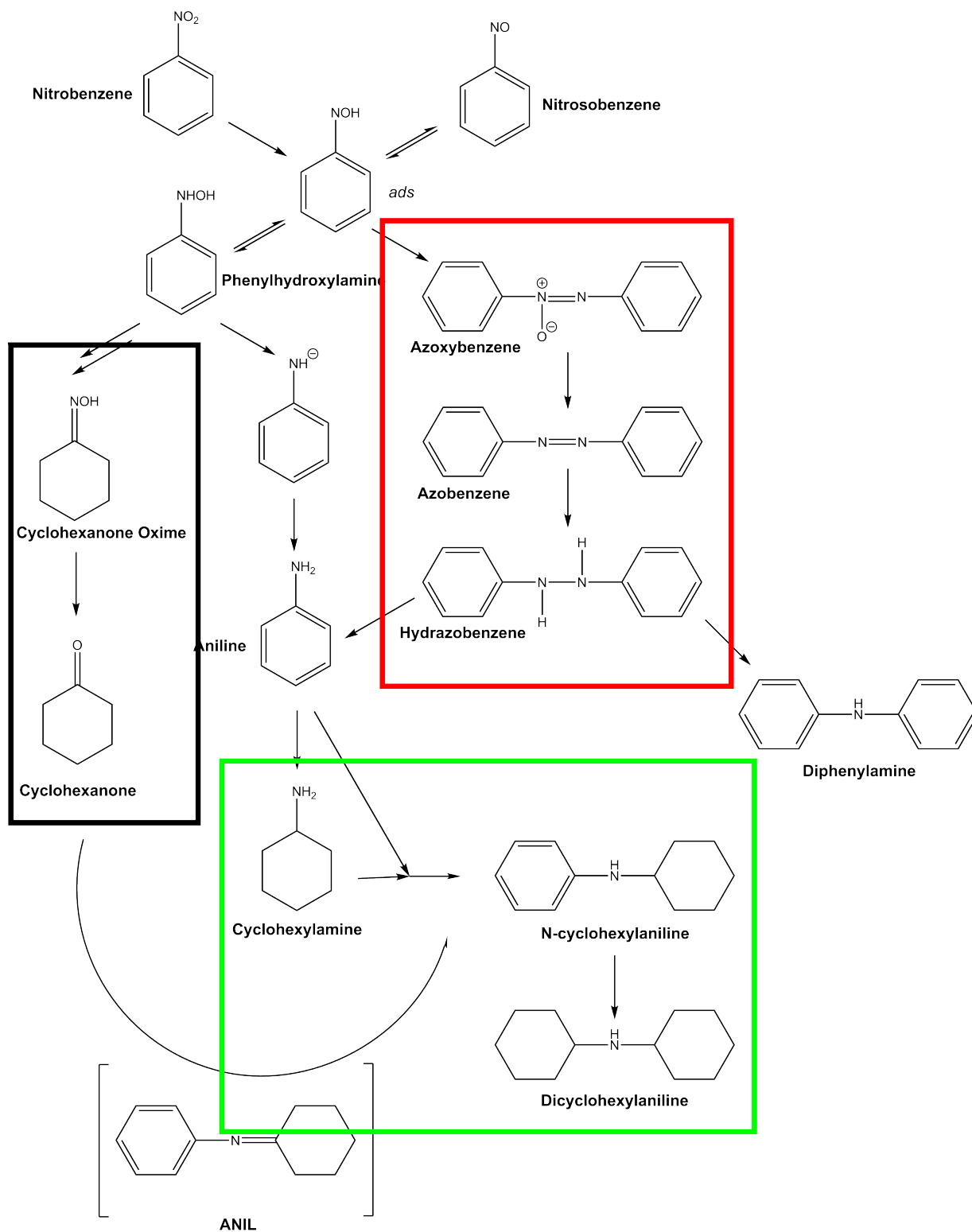
Industrial demand for cleaner, greener processes is a key requirement nowadays for economical and environmental reasons and as a consequence, industry are constantly pushed to improve their processes by taking all of these factors into consideration. In an attempt to do this, Huntsman Polyurethane has upgraded their aniline production plant to a trickle-bed reactor which operates under a gas-liquid-solid phase and uses an active Pd/alumina catalyst of low metal loading. However the change has resulted in the production of undesirable by-products being formed during the reaction. Such by-products are acceptable if they are consistently produced and can be treated and removed from the reaction mixture. It was found that different catalysts screened of the same formulation resulted in the production of diverse impurities without any logical sense, and here lies the project objectives.

To conclude:

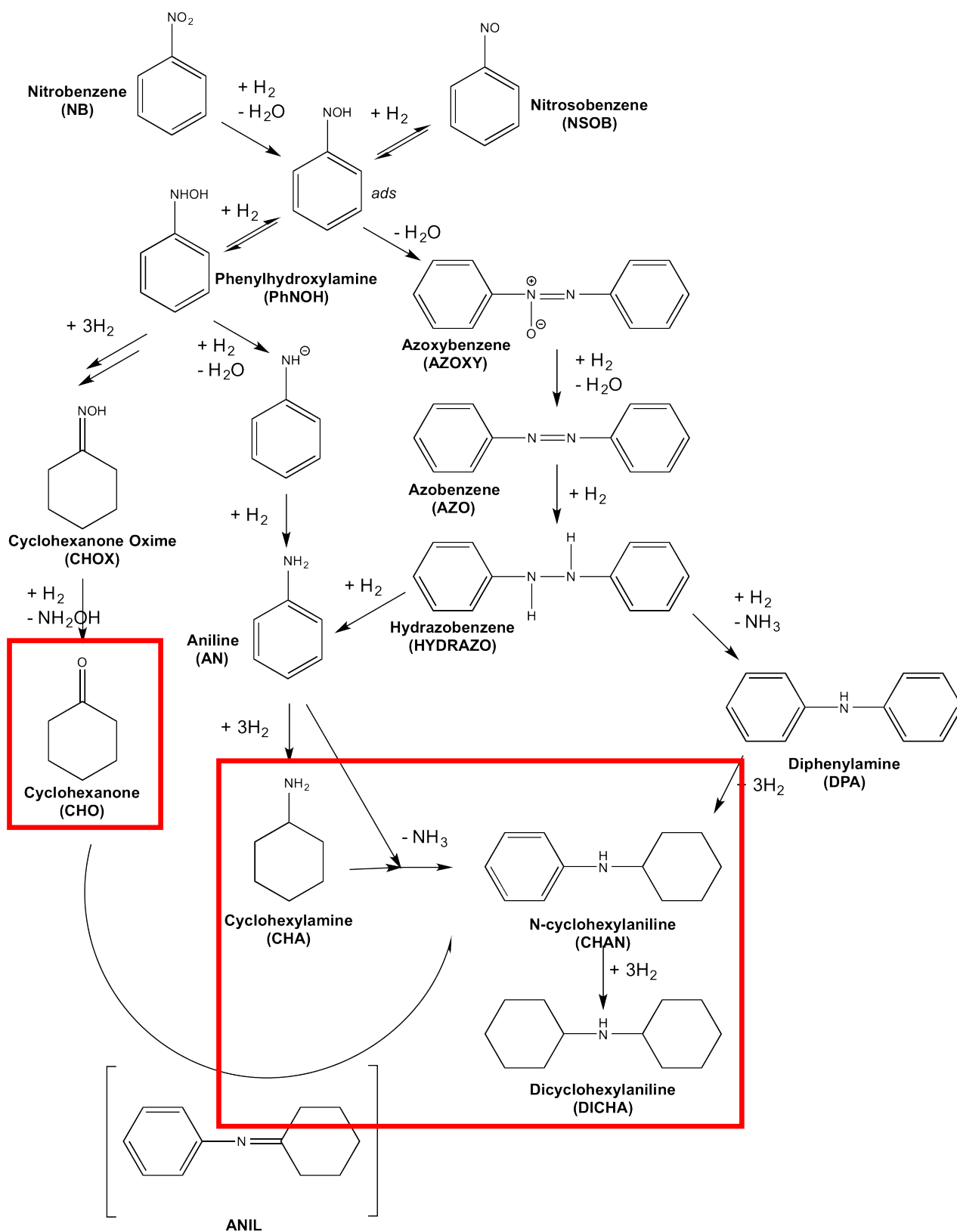
1. The testing of industrial grade catalysts in our lab-scale reactor led to a large range of impurities produced during the reaction in the form of azobenzene, azoxybenzene, diphenylamine, cyclohexanone to cyclohexylamine, N-cyclohexylaniline and dicyclohexylamine. As part of the reaction testing, an unknown compound was produced and identified to be cyclohexanone oxime using GCMS. Integration of the cyclohexanone oxime into the general scheme of nitrobenzene hydrogenation enabled the linkage and a better understanding of the different molecules present such as cyclohexanone, phenol and the intermediate ANIL. The full scheme is reported in **Figure 5**.

2. The reaction of the as-received Sample 2 (310/2) enabled us to understand the behaviour of nitrobenzene hydrogenation with respect to contact time over the catalyst. Although these catalysts are deemed selective for the hydrogenation reaction, it was found that by increasing the temperature or contact time, it consequently led to a loss in aniline selectivity. However, one should note that the reaction was carried out in the gas phase with a high excess of hydrogen so there was no mass transfer limitation.
3. Characterisation of the catalysts, namely, TEM and CO adsorption isotherms, played a big part in the understanding the morphology of the palladium particles. The two techniques were consistent with each other and could be used closely with CO TPIR results to explain differences in the catalyst composition.
4. BET measurements linked with XRD revealed that the alumina support used in the industrial selective hydrogenation catalysts was substantially different and may have an effect on the size of particle and dispersion observed elsewhere.
5. CO TPIR provided an insight on the energetics and the morphology of palladium particles at the surface of Pd/alumina. It is the only technique able to give a reproducible and informative result. When linked with the general scheme for the nitrobenzene hydrogenation, we were able to predict the behaviour of a Pd/alumina in nitrobenzene hydrogenation reaction for given reaction conditions (see **Schemes 8.1 and 8.2**).

With respect to future work, it would be interesting to study the reactions of the different branches of the mechanism using different reactants and isotopic labels. This would develop the scheme further regarding the interaction of the by-products with different catalysts. The synthesis of our own catalytic samples may be useful to study the role of the alumina support played in the morphology of palladium crystals, plus the role of the preparative method and the role of silica played.



Scheme 8.1: Nitrobenzene reaction scheme for *low loading Pd catalysts*. It was possible to discern between nitrobenzene-derived chemistry (in red) and aniline-derived chemistry (in green).



Scheme 8.2: Nitrobenzene reaction scheme for *high loading Pd catalysts*. The presence of high concentration of Pd leads to aniline-derived product in high quantity.

Appendices

Appendix A

A.1 Nitrobenzene Calibration

The number of moles of the calibration standards injected and the corresponding peak areas measured by the GC are displayed in **table A.1** and the calibration plot in **figure A.1**.

Concentration ($mol.L^{-1}$)	Peak Area (counts)			Average
	1	2	3	
0	0	0	0	
1.08×10^{-9}	195	188	199	194
4.33×10^{-9}	760	780	781	767
8.14×10^{-9}	1751	1687	1634	1691
1.08×10^{-8}	2230	1953	2133	2105

Table A.1: Nitrobenzene calibration data obtained manual injection on GC.

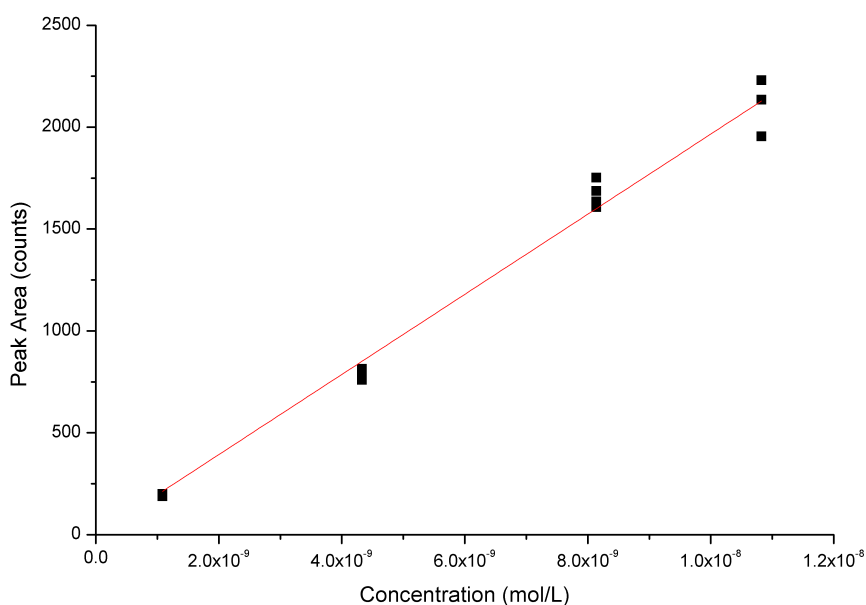


Figure A.1: Nitrobenzene calibration plot.

A.2 Aniline Calibration

The number of moles of the calibration standards injected and the corresponding peak areas measured by the GC are displayed in Table 3 and the calibration graph in Figure 4.

Concentration (mol.L^{-1})	Peak Area (counts)			Average
	1	2	3	
0	0	0	0	0
6.77×10^{-10}	113	112	112	112
1.81×10^{-9}	282	294	292	289
2.47×10^{-9}	451	433	431	438
3.76×10^{-9}	657	673	685	671
4.84×10^{-9}	858	880	917	885
1.13×10^{-8}	2409	2300		2354

Table A.2: Aniline calibration data obtained manual injection on GC.

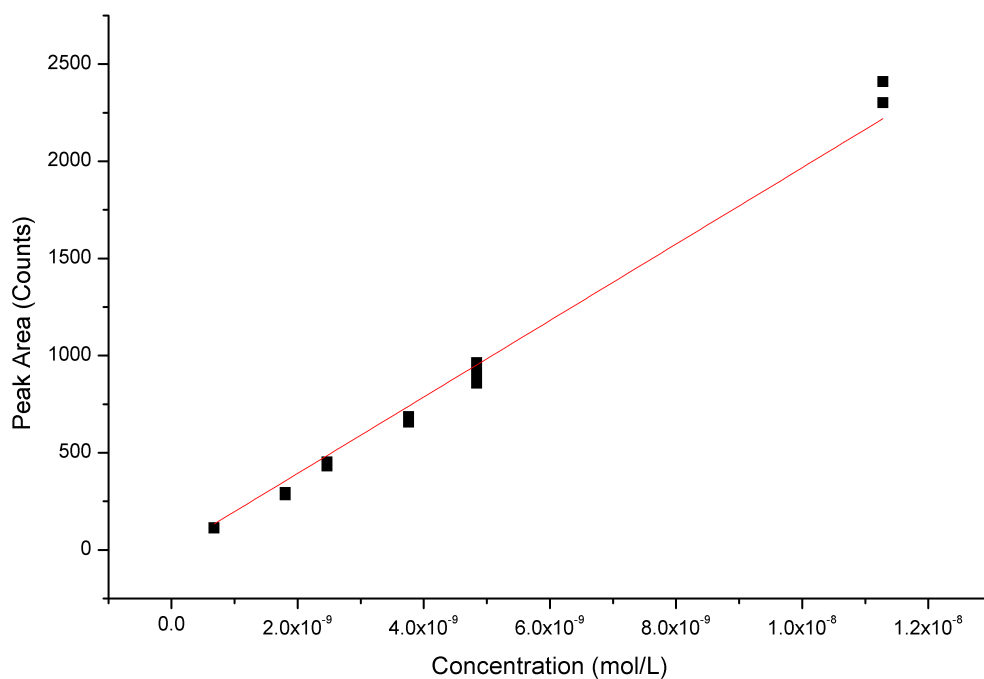


Figure A.2: Aniline calibration plot.

A.3 Cyclohexylamine (CHA) Calibration

The number of moles of the calibration standards injected and the corresponding peak areas measured by the GC are displayed in **table A.3** and the calibration plot in **figure A.3**.

Concentration ($mol.L^{-1}$)	Peak Area (counts)			Average
	1	2	3	
0	0	0	0	0
1.19×10^{-9}	29	34	57	40
8.53×10^{-9}	1345	1341	1295	1327
1.98×10^{-8}	3422	3300	3267	3329

Table A.3: Cyclohexylamine calibration data obtained manual injection on GC.

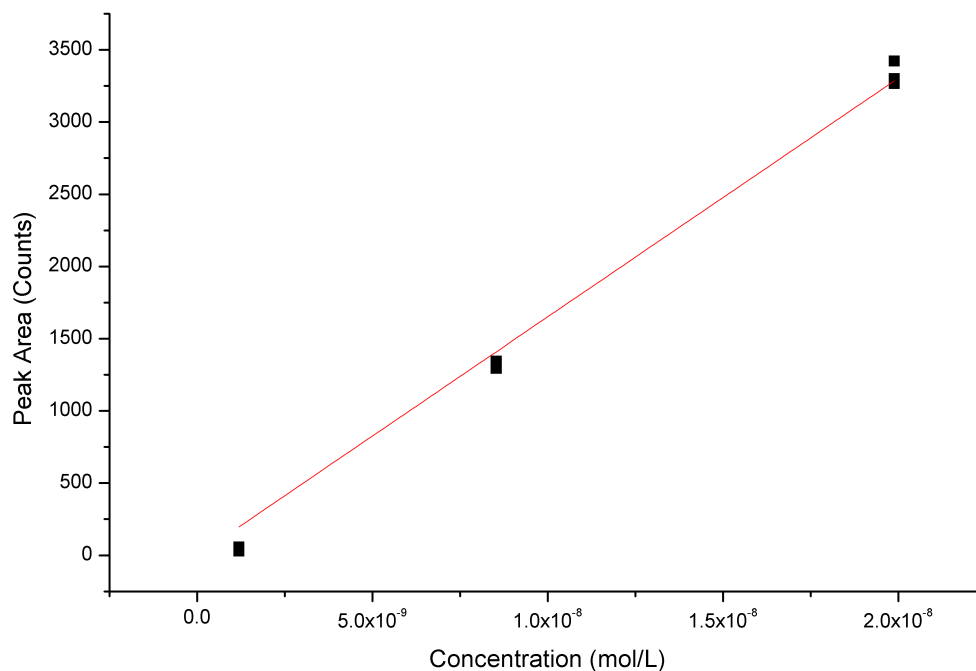


Figure A.3: Cyclohexylamine calibration plot.

A.4 Dicyclohexylamine (DICHA) Calibration

The number of moles of the calibration standards injected and the corresponding peak areas measured by the GC are displayed in **table A.4** and the calibration plot in **figure A.4**.

Concentration ($mol.L^{-1}$)	Peak Area (counts)			Average
	1	2	3	
0	0	0	0	0
6.55×10^{-10}	223	228	228	226
4.68×10^{-9}	1797	1747	1710	1751
1.09×10^{-8}	3944	3975	3833	3917

Table A.4: Dicyclohexylamine calibration data obtained manual injection on GC.

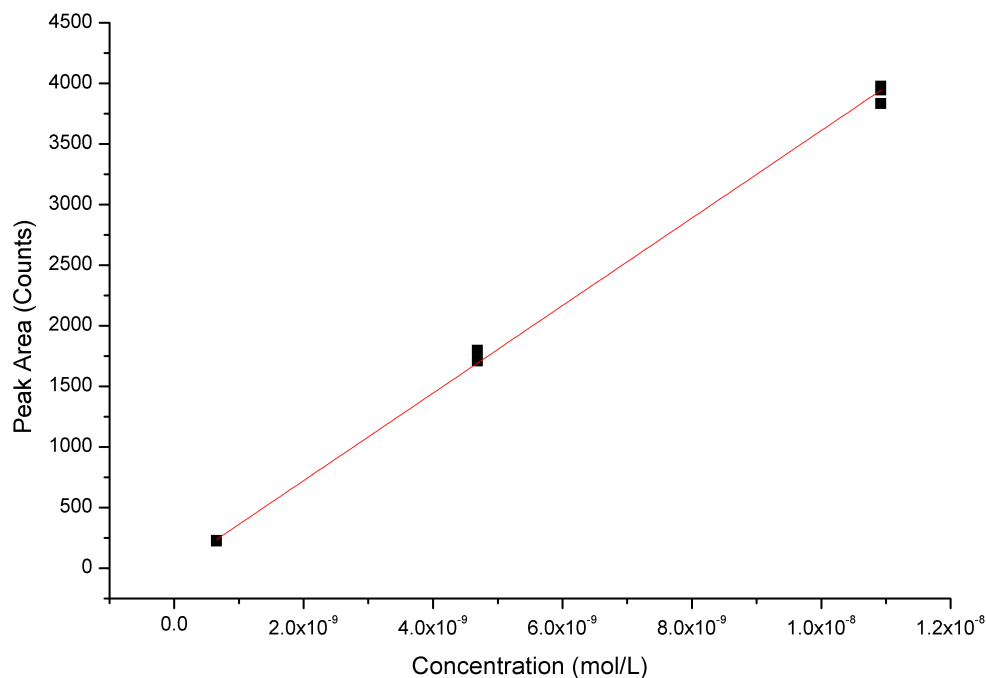


Figure A.4: Dicyclohexylamine calibration plot.

A.5 Diphenylamine (DPA) Calibration

The number of moles of the calibration standards injected and the corresponding peak areas measured by the GC are displayed in **table A.5** and the calibration graph in **figure A.5**.

Concentration ($mol.L^{-1}$)	Peak Area (counts)			Average
	1	2	3	
0	0	0	0	0
6.72×10^{-10}	209	183	200	197
4.81×10^{-9}	1178	1200	1243	1207
1.12×10^{-8}	3200	3321	3210	3243

Table A.5: Diphenylamine calibration data obtained manual injection on GC.

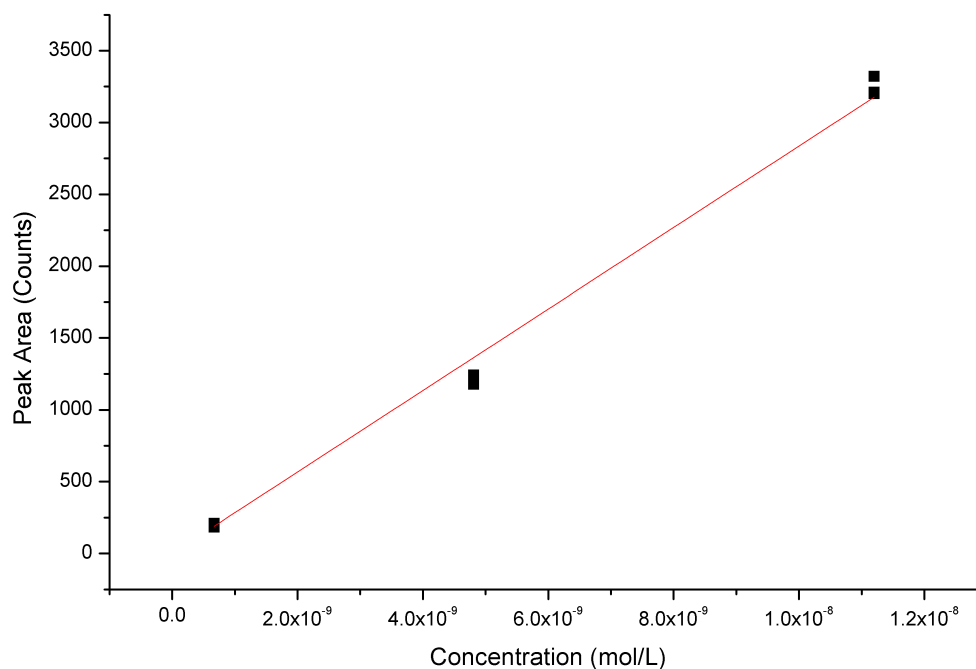


Figure A.5: Diphenylamine calibration plot.

A.6 Azobenzene (AZO) Calibration

The number of moles of the calibration standards injected and the corresponding peak areas measured by the GC are displayed in **table A.6** and the calibration plot **figure A.6** .

Concentration ($mol.L^{-1}$)	Peak Area (counts)			Average
	1	2	3	
0	0	0	0	0
6.91×10^{-10}	237	238	232	235
4.95×10^{-9}	1769	1715	1750	1744
1.15×10^{-8}	3700	3926	3851	3825

Table A.6: Azobenzene calibration data obtained manual injection on GC.

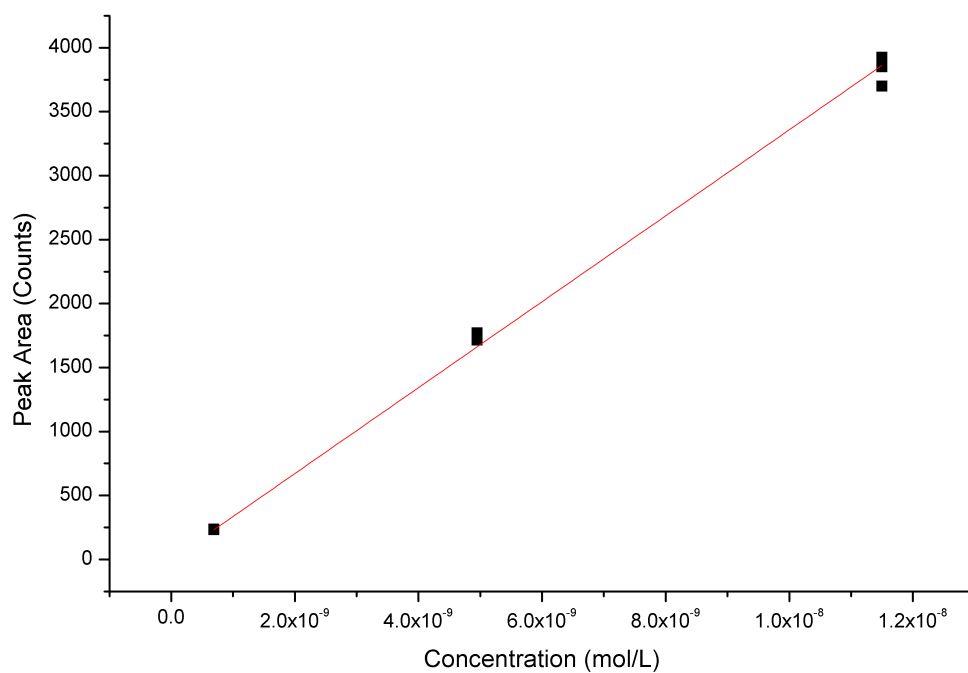


Figure A.6: Azobenzene calibration plot.

A.7 N-cyclohexylaniline (CHAN) Calibration

The number of moles of the calibration standards injected and the corresponding peak areas measured by the GC are displayed in **table A.7** and the calibration plot **figure A.7**.

Concentration (<i>mol.L</i> ⁻¹)	Peak Area (counts)			Average
	1	2	3	
0	0	0	0	0
6.37 x 10 ⁻¹⁰	219	220	221	220
4.55 x 10 ⁻⁹	1503	1400	1436	1446
1.06 x 10 ⁻⁸	3620	3699	3701	3673

Table A.7: N-cyclohexylaniline calibration data obtained manual injection on GC.

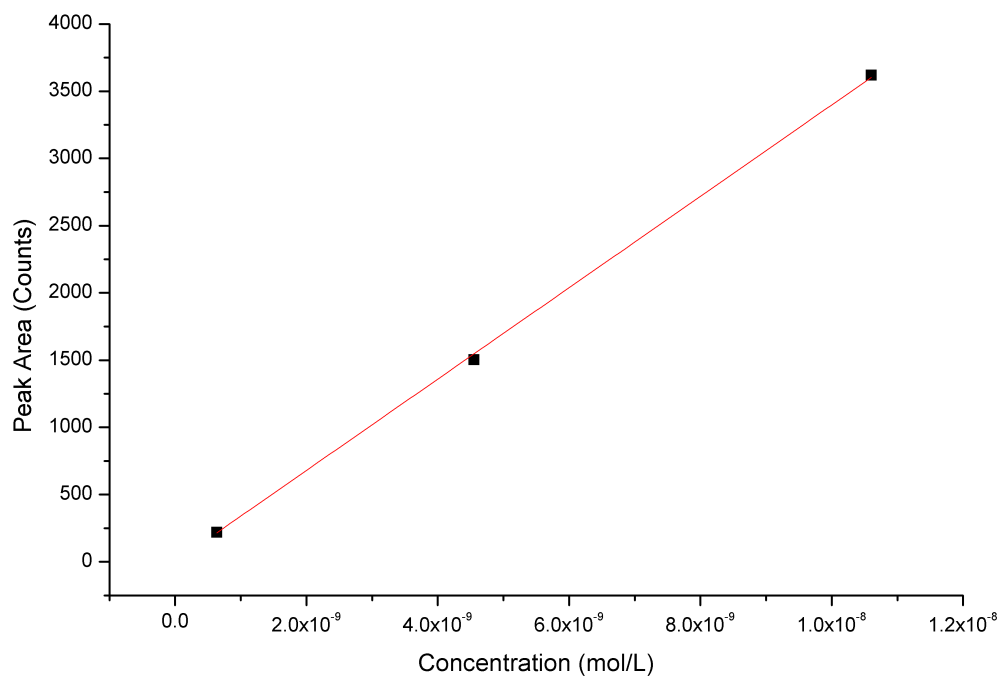


Figure A.7: N-cyclohexylaniline calibration plot.

Bibliography

- [1] F. Zaera. New advances in the use of infrared absorption spectroscopy for the characterization of heterogeneous catalytic reactions. *Chem. Soc. Rev.*, 2014.
- [2] J. C. Michaelson. Aniline in history and technology. *Endeavour*, 17(3):121 – 126, 1993.
- [3] mcgroups.co.uk/researches/aniline.
- [4] <http://www.marketsandmarkets.com/market-reports/mdi-tdi-polyurethane-market-381.html>.
- [5] S. Lee D. Randall. The polyurethanes book. *Wiley*, 2003.
- [6] M. A. Bechamp. De l'action des protosels de fer. *Annales de Chimie et de Physique*, 42:186–196, 1854.
- [7] W. Burow, W. Oehlert, U. Pitzer, and H. Bade. Use of synthetic, iron raw materials for preparing iron oxide pigments. 2000. US Patent 6,086,846.
- [8] J. Wisniak and M. Klein. Reduction of nitrobenzene to aniline. *Industrial and Engineering Chemistry Product Research and Development*, 23(1):44–50, 1984.
- [9] M. Dugal, F.U. von Gehlen, S. Wershofen, A. Lago, P. Lehner, and B. Marotz. hydrogenating nitrobenzene in presence of catalyst; single-step or multi-step distillation. 2007. US Patent App. 11/706,444.
- [10] A.J. Zeeuw and M.G. Bent. Chemical installation. 2010.
- [11] C. Mitchell. Private communication. *Huntsman Polyurethanes*, November 2010.
- [12] N. S. Abo-Ghander, F. Logist, J. R. Grace, J. F. M. Van Impe, S. S. E. H. Elnashaie, and C. J. Lim. Optimal design of an autothermal membrane reactor coupling the dehydrogenation of ethylbenzene to styrene with the hydrogenation of nitrobenzene to aniline. *Chemical Engineering Science*, 65(10):3113–3127, 2010.

- [13] N. S. Abo-Ghander, F. Logist, J. R. Grace, J. F. M. Van Impe, S. S. E. H. El-nashaie, and C. J. Lim. Comparison of diffusion models in the modeling of a catalytic membrane fixed bed reactor coupling dehydrogenation of ethylbenzene with hydrogenation of nitrobenzene. *Computers and Chemical Engineering*, 38:11–23, 2012.
- [14] M. R. Rahimpour, R. Vakili, E. Pourazadi, D. Iranshahi, and K. Paymooni. A novel integrated, thermally coupled fluidized bed configuration for catalytic naphtha reforming to enhance aromatic and hydrogen productions in refineries. *International Journal of Hydrogen Energy*, 36(4):2979–2991, 2011.
- [15] M. R. Rahimpour, Z. A. Aboosadi, and A. H. Jahanmiri. Differential evolution (de) strategy for optimization of methane steam reforming and hydrogenation of nitrobenzene in a hydrogen perm-selective membrane thermally coupled reactor. *International Journal of Energy Research*, 37(8):868–878, 2013.
- [16] Gheorghe Maria and Dragos-Nicolae Stefan. Variability of operating safety limits with catalyst within a fixed-bed catalytic reactor for vapour-phase nitrobenzene hydrogenation. *Journal of Loss Prevention in the Process Industries*, 23(1):112–126, 2010.
- [17] T. Fujii E. Nishikawa K. Akagawa M. Ozawa S. Ishigai, S. Nakanishi. Steam power engineering, thermal and hydraulic design principles. *Univeristy of Osaka*, 1999.
- [18] F. Haber. Elektrolytische darstellung von phenyl- β -hydroxylamin. *Zeitschrift für Elektrochemie*, 5(6):77–78, 1898.
- [19] J. A. Makaryan and V. I. Savchenko. n-aryllhydroxylamines transformation in the presense of heterogeneous catalysts. *Studies in Surface Science and Catalysis*, Volume 75:2439–2442, 1993.
- [20] F. Visentin, G. Puxty, O. M. Kut, and K. Hungerbuhler. Study of the hydrogenation of selected nitro compounds by simultaneous measurements of calorimetric, ft-ir, and gas-uptake signals. *Industrial and Engineering Chemistry Research*, 45(13):4544–4553, 2006.
- [21] A. Corma, C. Gonzalez-Arellano, M. Iglesias, and F. Sanchez. Gold complexes as catalysts: Chemoselective hydrogenation of nitroarenes. *Applied Catalysis a-General*, 356(1):99–102, 2009.
- [22] A. Corma, P. Concepcion, and P. Serna. A different reaction pathway for the reduction of aromatic nitro compounds on gold catalysts. *Angewandte Chemie-International Edition*, 46(38):7266–7269, 2007.

- [23] E. A. Gelder, S. D. Jackson, and C. M. Lok. A study of nitrobenzene hydrogenation over palladium/carbon catalysts. *Catalysis Letters*, 84(3-4):205–208, 2002.
- [24] E. A. Gelder, S. D. Jackson, and C. M. Lok. The hydrogenation of nitrobenzene to aniline: a new mechanism. *Chemical Communications*, (4):522–524, 2005.
- [25] M. Freifelder and G. R. Stone. Reductions with ruthenium catalyst .3. hydrogenation of nuclear substituted anilines. *Journal of Organic Chemistry*, 27(10):3568–and, 1962.
- [26] H. Greenfield. Hydrogenation of aniline to cyclohexylamine with platinum metal catalysts. *Journal of Organic Chemistry*, 29(10):3082–and, 1964.
- [27] German patent: Dt 24 61 615 a1.
- [28] Uk patent: Gb 2 024 643 a.
- [29] C. F. Winans. Hydrogenation of aniline. *Industrial and Engineering Chemistry*, 32:1215–1216, 1940.
- [30] E. L. Pitara, B. Nzemba, J. Barbier, F. Barbot, and Miginiac. Catalytic hydrogenation of aniline in aqueous media. *Journal of Molecular Catalysis a-Chemical*, 106(3):235–240, 1996.
- [31] S. Narayanan and R. P. Unnikrishnan. Comparison of hydrogen adsorption and aniline hydrogenation over co-precipitated co/al₂o₃ and ni/al₂o₃ catalysts. *Journal of the Chemical Society-Faraday Transactions*, 93(10):2009–2013, 1997.
- [32] S. Narayanan, R. Unnikrishnan, and V. Vishwanathan. Nickel-alumina prepared by constant and varying ph method - evaluation by hydrogen-oxygen chemisorption and aniline hydrogenation. *Applied Catalysis a-General*, 129(1):9–19, 1995.
- [33] G. Mink and L. Horvath. Hydrogenation of aniline to cyclohexylamine on naoh-promoted or lanthana supported nickel. *Reaction Kinetics and Catalysis Letters*, 65(1):59–65, 1998. Mink, G Horvath, L.
- [34] A. J. Tench and R. L. Nelson. Adsorbed nitro-compounds and electron donor properties of magnesium oxide. *Transactions of the Faraday Society*, 63(537P):2254–and, 1967.
- [35] S. Meijers and V. Ponec. Infrared spectroscopic study of the adsorption of nitro-compounds and amines on cobalt oxide. *Journal of Catalysis*, 149(2):307–316, 1994.
- [36] S. Meijers, T. P. P. vanderHoeven, V. Ponec, J. P. Jacobs, and H. H. Brongersma. The active sites in the selective reduction of nitrobenzene by cobalt aluminum oxide catalysts. *Journal of Catalysis*, 161(1):459–464, 1996.

- [37] Q. Chen, S. Haq, B. G. Frederick, and N. V. Richardson. Adsorption of nitrobenzene and some simple derivatives on the cu110 surface. *Surface Science*, 368:310–317, 1996. 8th International Conference on Vibrations at Surfaces Jun 23-27, 1996 Univ birmingham, birmingham, england.
- [38] N. V. Richardson and P. Hofmann. A spectroscopic investigation of the adsorption of phenol on cu(110). *Vacuum*, 33(10-1):793–796, 1983.
- [39] M. X. Yang, M. Xi, H. J. Yuan, B. E. Bent, P. Stevens, and J. M. White. Nexafs studies of halobenzenes and phenyl groups on cu(111). *Surface Science*, 341(1-2):9–18, 1995.
- [40] M. Xi and B. E. Bent. Iodobenzene on cu(111) - formation and coupling of adsorbed phenyl groups. *Surface Science*, 278(1-2):19–32, 1992.
- [41] P. R. Davies, D. Edwards, and D. Richards. Stm and xps studies of the oxidation of aniline at cu(110) surfaces. *Journal of Physical Chemistry B*, 108(48):18630–18639, 2004.
- [42] P. R. Davies, D. Edwards, and D. Richards. Aromatic interactions in the close packing of phenyl-imides at cu(110) surfaces. *Surface Science*, 573(2):284–290, 2004.
- [43] S. X. Huang, D. A. Fischer, and J. L. Gland. The correlation of the structure and reactivity of aniline on the ni(111) surface. *Abstracts of Papers of the American Chemical Society*, 207:321–PHYS, 1994. 2.
- [44] S. X. Huang, D. A. Fischer, and J. L. Gland. In-situ kinetic-studies of aniline on nickel single-crystal surfaces. *Abstracts of Papers of the American Chemical Society*, 207:152–COLL, 1994. 1.
- [45] S. X. Huang, D. A. Fischer, and J. L. Gland. Aniline hydrogenolysis on nickel - effects of surface hydrogen and surface-structure. *Catalysis Letters*, 34(3-4):365–374, 1995.
- [46] S. X. Huang, D. A. Fischer, and J. L. Gland. In situ studies of cyclohexylamine dehydrogenation and hydrogenation on the ni(111) surface. *Journal of Physical Chemistry*, 100(32):13629–13635, 1996.
- [47] S. X. Huang, D. A. Fischer, and J. L. Gland. The role of hydrogen in the hydrogenation and hydrogenolysis of aniline on nickel single-crystal surfaces - implications for the mechanisms of hdn reactions. *Abstracts of Papers of the American Chemical Society*, 208:38–PETR, 1994. 2.

- [48] S. X. Huang, D. A. Fischer, and J. L. Gland. Aniline adsorption, hydrogenation, and hydrogenolysis on the ni(100) surface. *Journal of Physical Chemistry*, 100(24):10223–10234, 1996.
- [49] S. X. Huang and J. L. Gland. Cyclohexylamine adsorption and hydrogenolysis on the ni(100) surface. *Journal of Physical Chemistry*, 100(6):2206–2212, 1996.
- [50] S. X. Huang, D. A. Fischer, and J. L. Gland. Correlation between the surface configurations and hydrogenolysis - aniline on the pt(111) surface. *Journal of Vacuum Science and Technology A*, 12(4):2164–2169, 1994. 2.
- [51] E. Gelder. The hydrogenation of nitrobenzene over metal catalysts. *Thesis*, 2005.
- [52] H. C. Yao and P. H. Emmett. Kinetics of catalytic liquid phase hydrogenation .1. the hydrogenation of aromatic nitrocompounds over colloidal rhodium and palladium. *Journal of the American Chemical Society*, 81(16):4125–4132, 1959. Times Cited: 56.
- [53] H. C. Yao and P. H. Emmett. Kinetics of liquid phase hydrogenation .2. hydrogenation of aromatic and aliphatic nitrocompounds over a colloidal platinum catalyst. *Journal of the American Chemical Society*, 83(4):796, 1961. Times Cited: 23.
- [54] H. C. Yao and P. H. Emmett. Kinetics of liquid phase hydrogenation .3. nature of platinum oxide catalysts. *Journal of the American Chemical Society*, 83(4):799, 1961. Times Cited: 15.
- [55] H. C. Yao and P. H. Emmett. Kinetics of liquid phase hydrogenation .4. hydrogenation of nitrocompounds over raney nickel and nickel powder catalysts. *Journal of the American Chemical Society*, 84(7):1086, 1962. Times Cited: 38.
- [56] A. Metcalfe and M. W. Rowden. Hydrogenation of nitrobenzene over palladium-silver catalysts. *Journal of Catalysis*, 22(1):30–and, 1971.
- [57] D. N. Rihani, Narayana.Tk, and Doraiswa.Lk. Kinetics of catalytic vapor-phase hydrogenation of nitrobenzene to aniline. *Industrial and Engineering Chemistry Process Design and Development*, 4(4):403–and, 1965.
- [58] K. H. Gharda and C. M. Sliepcevich. Copper catalysts in hydrogenating nitrobenzene to aniline. *Industrial and Engineering Chemistry*, 52(5):417–420, 1960.
- [59] F Stoessel. Experimental study of thermal hazards during the hydrogenation of aromatic nitro compounds. *Journal of Loss Prevention in the Process Industries*, 6(2):79 – 85, 1993.

- [60] R. Zapf K. K. Yeong, A. Gavriilidis and V. Hessel. Experimental studies of nitrobenzene hydrogenation in a microstructured falling film reactor. *Chemical Engineering Science*, 59(16):3491 – 3494, 2004.
- [61] J. M. Chalmers and G. Dent. Industrial analysis with vibrational spectroscopy. *RSC Analytical Spectroscopy Monographs*, 1997.
- [62]
- [63] P. R. Griffiths and J. A. de Haseth. Fourier transform infrared spectrometry. *Wiley*, 2007.
- [64] R. P. Eischens and W. A. Pliskin. The infrared spectra of adsorbed molecules. *Advances in Catalysis*, 10:1–56, 1958.
- [65] J. De Paula P. Atkins. Physical chemistry. *Oxford Press*, 2006.
- [66] Hariharan P. Basics of interferometry. *Elsevier*, 2007.
- [67] T. H. Ballinger, J. C. S. Wong, and J. T. Yates. Transmission infrared spectroscopy of high area solid surfaces. a useful method for sample preparation. *Langmuir*, 8:1676–1678, 1992.
- [68] C. L. Angell and Paul C. Schaffer. Infrared spectroscopic investigations of zeolites and adsorbed molecules. ii. adsorbed carbon monoxide1. *The Journal of Physical Chemistry*, 70:1413–1418, 1966.
- [69] N.S. Hush and M.L. Williams. Carbon monoxide bond length, force constant and infrared intensity variations in strong electric fields: Valence-shell calculations, with applications to properties of adsorbed and complexed co. *Journal of Molecular Spectroscopy*, 50(1–3):349 – 368, 1974.
- [70] R. P. Eischens. Infrared methods applied to surface phenomena. *Journal of Physics and Chemistry of Solids*, 14:56, 1960. Times Cited: 3.
- [71] Blyholde.G and M. C. Allen. Infrared spectra and molecular orbital model for carbon monoxide adsorbed on metals. *Journal of the American Chemical Society*, 91(12):3158, 1969. Times Cited: 101.
- [72] V. M. Browne, S. G. Fox, and P. Hollins. Infrared-spectroscopy as an insitu probe of morphology. *Catalysis Today*, 9(1-2):1–14, 1991.
- [73] J. C. Tracy and P. W. Palmberg. Structural influences on adsorbate binding energy - carbon monoxide on (100) palladium. *Journal of Vacuum Science and Technology*, 6(5):926–and, 1969.

- [74] W. K. Kuhn, J. Szanyi, and D. W. Goodman. Co adsorption on pd(111) - the effects of temperature and pressure. *Surface Science*, 274(3):L611–L618, 1992.
- [75] G. Blyholder. Molecular orbital view of chemisorbed carbon monoxide. *Journal of Physical Chemistry*, 68(10):2772, 1964. Times Cited: 1401.
- [76] A. M. Bradshaw and F. M. Hoffmann. Chemisorption of carbon-monoxide on palladium single-crystal surfaces - ir spectroscopic evidence for localized site adsorption. *Surface Science*, 72(3):513–535, 1978.
- [77] B. Bourguignon, S. Carrez, B. Dragnea, and H. Dubost. Vibrational spectroscopy of imperfect co/pd(111) surfaces obtained by adsorption between 150 and 230 k. *Surface Science*, 418(1):171–180, 1998.
- [78] R. P. Eischens, W. A. Pliskin, and S. A. Francis. Infrared spectra of chemisorbed carbon monoxide. *Journal of Chemical Physics*, 22(10):1786–1787, 1954. Times Cited: 184.
- [79] R. P. Eischens. Infrared-spectra of chemisorbed molecules. *Accounts of Chemical Research*, 5(2):74, 1972. Times Cited: 33.
- [80] A. M. Bradshaw and F. M. Hoffmann. Chemisorption of carbon-monoxide on palladium single-crystal surfaces - ir spectroscopic evidence for localized site adsorption. *Surface Science*, 72(3):513–535, 1978. Times Cited: 565.
- [81] M. Baumer and H. J. Freund. Metal deposits on well-ordered oxide films. *Progress in Surface Science*, 61(7-8):127–198, 1999.
- [82] W. K. Kuhn, J. W. He, and D. W. Goodman. Studies of bimetallic surfaces using infrared reflection absorption-spectroscopy. *Journal of Vacuum Science and Technology a-Vacuum Surfaces and Films*, 10(4):2477–2480, 1992.
- [83] B. Coq. *Metal-support interaction in catalysis: Generalities, basic concepts and some examples in hydrogenation and hydrogenolysis reactions*, volume 546, pages 49–71. 1999.
- [84] Nist database.
- [85] T. Lear, R. Marshall, J. A. Lopez-Sanchez, S. D. Jackson, T. M. Klapotke, M. Baumer, G. Rupprechter, H. J. Freund, and D. Lennon. The application of infrared spectroscopy to probe the surface morphology of alumina-supported palladium catalysts. *J Chem Phys*, 123(17):174706, 2005.

- [86] T. Lear, N. G. Hamilton, and D. Lennon. The application of temperature-programmed desorption, adsorption isotherms and temperature-programmed oxidation to investigate the interaction of CO with alumina-supported palladium catalysts. *Catalysis Today*, 126(1-2):219–227, 2007.
- [87] B. Welz and Michael S. Atomic absorption spectrometry. *Wiley-VCH*, 2005.
- [88] G. Fagerlund. Determination of specific surface by the BET method. *Matériaux et Construction*, 6:239–245, 1973.
- [89] S. D. Jackson and N. J. Casey. Hydrogenation of propyne over palladium catalysts. *J. Chem. Soc. Faraday Trans.*, 91:3269–3274, 1995.
- [90] R. J. Farrauto C. H. Bartholomew. Fundamentals of industrial catalytic processes, 2nd edition. *Wiley*, 2005.
- [91] P. Aranyi, G. Raksi, J. Petro, I. Fekete, J. Forstner, B. Jover, L. Leder, M. Nyari, E. Szabo, and S. Szoboszlay. Cyclo-hexylamine prepn.—by catalytic hydrogenation of aniline.
- [92] E. Echigoya, H. Hagiwara, and A. Sakurai. Catalytic hydrogenation of aniline in fluidized beds. *Bulletin of the Chemical Society of Japan*, 39(11):2527–and, 1966.
- [93] P. Rubio-Marques, A. Leyva-Perez, and A. Corma. A bifunctional palladium/acid solid catalyst performs the direct synthesis of cyclohexylanilines and dicyclohexylamines from nitrobenzenes. *Chemical Communications*, 49(74):8160–8162, 2013.
- [94] H. D. Burge, D. J. Collins, and B. H. Davis. Intermediates in the raney-nickel catalyzed hydrogenation of nitrobenzene to aniline. *Industrial and Engineering Chemistry Product Research and Development*, 19(3):389–391, 1980.
- [95] P. S. Santos, H. S. Santos, and S.P. Toledo. Standard transition aluminas. electron microscopy studies. *Materials Research*, 3:104 – 114, 2000.
- [96] R. Divakar and V.S. Raghunathan. Characterisation of interfaces in nanocrystalline palladium. *Sadhana*, 28(1-2):47–62, 2003.
- [97] T. Lear, R. Marshall, E. K. Gibson, T. Schott, T. M. Klapotke, G. Rupprechter, H.-J. Freund, J. M. Winfield, and D. Lennon. A model high surface area alumina-supported palladium catalyst. *Physical Chemistry Chemical Physics*, 7(4):565, 2005.
- [98] R. van Hardeveld and F. Hartog. Influence of metal particle size in nickel-on-aerosil catalysts on surface site distribution, catalytic activity, and selectivity. volume 22, pages 75 – 113. 1972.

- [99] A. R. McInroy, A. Uhl, T. Lear, T. M. Klapotke, S. Shaikhtudinov, S. Schauer-
mann, G. Rupprechter, H. J. Freund, and D. Lennon. Morphological and chemical
influences on alumina-supported palladium catalysts active for the gas phase hy-
drogenation of crotonaldehyde. *J Chem Phys*, 134(21):214704.
- [100] H. Dropsch and M. Baerns. Co adsorption on supported pd catalysts studied by ad-
sorption microcalorimetry and temperature programmed desorption. *Applied Catal-
ysis A: General*, 158(1-2):163 – 183, 1997.
- [101] P. D. Holmes, G. S. McDougall, I. C. Wilcock, and K. C. Waugh. Diffuse reflectance
infrared-spectroscopy of adsorbates on supported metal-catalysts. *Catalysis Today*,
9(1-2):15–22, 1991.
- [102] F. C. Meunier, A. Goguet, S. Shekhtman, D. Rooney, and H. Daly. A modified
commercial drifts cell for kinetically relevant operando studies of heterogeneous
catalytic reactions. *Applied Catalysis A: General*, 340(2):196–202, 2008.
- [103] A. R. McInroy, D. T. Lundie, J. M. Winfield, C. C. Dudman, P. Jones, and
D. Lennon. Improved atom efficiency via an appreciation of the surface activity
of alumina catalysts: Methyl chloride synthesis. *Applied Catalysis B: Environmen-
tal*, 70(1-4):606–610, 2007.
- [104] R. M. Hammaker, S. A. Francis, and R. P. Eischens. Infrared study of intermolecular
interactions for carbon monoxide chemisorbed on platinum. *Spectrochimica Acta*,
21(7):1295, 1965. Times Cited: 280.
- [105] H. U. Blaser, C. Malan, B. Pugin, F. Spindler, H. Steiner, and M. Studer. Selective
hydrogenation for fine chemicals: Recent trends and new developments. *Advanced
Synthesis and Catalysis*, 345(1-2):103–151, 2003.
- [106] H.-U. Blaser. A golden boost to an old reaction. *Science*, 313(5785):312–313, 2006.
- [107] F. Cardenas-Lizana, D. Lamey, S. Gomez-Quero, N. Perret, L. Kiwi-Minsker, and
M. A. Keane. Selective three-phase hydrogenation of aromatic nitro-compounds
over beta-molybdenum nitride. *Catalysis Today*, 173(1):53–61, 2011. 9th Congress
on Catalysis Applied to Fine Chemicals (CAFC9) Sep 13-16, 2010 Zaragoza, SPAIN
Spanish Natl Res Council (CSIC); Univ Zaragoza; Govt Aragon.
- [108] F. Cardenas-Lizana, D. Lamey, N. Perret, S. Gomez-Quero, L. Kiwi-Minsker, and
Mark A. Keane. Au/mo₂n as a new catalyst formulation for the hydrogenation
of p-chloronitrobenzene in both liquid and gas phases. *Catalysis Communications*,
21:46–51, 2012.

- [109] D. J. Collins, R. P. Schneider, M. C. Wolf, and B. H. Davis. Nitrobenzene hydrogenation - poisoning effect of tin dichloride on a platinum catalyst. *Journal of Molecular Catalysis*, 62(1):57–60, 1990.
- [110] S. G. Diao, W. Z. Qian, G. H. Luo, F. Wei, and Y. Wang. Gaseous catalytic hydrogenation of nitrobenzene to aniline in a two-stage fluidized bed reactor. *Applied Catalysis a-General*, 286(1):30–35, 2005.
- [111] F. Figueras and B. Coq. Hydrogenation and hydrogenolysis of nitro-, nitroso-, azo-, azoxy- and other nitrogen-containing compounds on palladium. *Journal of Molecular Catalysis a-Chemical*, 173(1-2):223–230, 2001.
- [112] D. A. Dotzauer, S. Bhattacharjee, Y. Wen, and M. L. Bruening. Nanoparticle-containing membranes for the catalytic reduction of nitroaromatic compounds. *Langmuir*, 25(3):1865–1871, 2009.
- [113] N. Frikha, E. Schaer, and J.-L. Houzelot. Methodology of multiphase reaction kinetics and hydrodynamics identification: Application to catalyzed nitrobenzene hydrogenation. *Chemical Engineering Journal*, 124(1-3):19–28, 2006.
- [114] A. Corma, P. Serna, P. Concepcion, and J. Juan Calvino. Transforming nonselective into chemoselective metal catalysts for the hydrogenation of substituted nitroaromatics. *J Am Chem Soc*, 130(27):8748–8753, 2008.
- [115] Temirbulatova A.E. Ualikhanova A. Sokol'skij, D.V. Liquid-phase hydrogenation of aniline in the presence of deposited ruthenium and rhodium catalysts. *Zhurnal Prikladnoj Khimii*, 56(7):1610–1614, 1983.
- [116] V. M. H. Govindarao and K. V. Ramana Murthy. Liquid phase hydrogenation of aniline in a trickle bed reactor. *Journal of Applied Chemistry and Biotechnology*, 25(3):169–181, 1975.
- [117] H. Egberink and C. Vanheerden. The mechanism of the formation and hydrolysis of cyclohexanone oxime in aqueous-solutions. *Analytica Chimica Acta*, 118(2):359–368, 1980.
- [118] D. Goldsmith, D. Becher, Shelia Sample, and Carl Djerassi. Mass spectrometry in structural and stereochemical problems-xcvii : A study of the fragmentation processes of oximes. *Tetrahedron*, 22(0):145 – 173, 1966.
- [119] Paula Rubio-Marques, Juan Carlos Hernandez-Garrido, Antonio Leyva-Perez, and Avelino Corma. One pot synthesis of cyclohexanone oxime from nitrobenzene using a bifunctional catalyst. *Chem. Commun.*, 50:1645–1647, 2014.

- [120] L. Kiwi-Minsker, E. Joannet, and A. Renken. Solvent-free selective hydrogenation of 2-butyne-1,4-diol over structured palladium catalyst. *Industrial and Engineering Chemistry Research*, 44(16):6148–6153, 2005.
- [121] R. S. Zhou and R. L. Snyder. Structures and transformation mechanisms of the eta, gamma and theta transition aluminas. *Acta Crystallographica Section B-Structural Science*, 47:617–630, 1991. 5.
- [122] A. Boumaza, L. Favaro, J. Ledion, G. Sattonnay, J. B. Brubach, P. Berthet, A. M. Huntz, P. Roy, and R. Tetot. Transition alumina phases induced by heat treatment of boehmite: An x-ray diffraction and infrared spectroscopy study. *Journal of Solid State Chemistry*, 182(5):1171–1176, 2009.
- [123] P. Ptáček. *Strontium Aluminate - Cement Fundamentals, Manufacturing, Hydration, Setting Behaviour and Applications*, 2014.
- [124] F. Di Gregorio, L. Bisson, T. Armaroli, C. Verdon, L. Lemaitre, and C. Thomazeau. Characterization of well faceted palladium nanoparticles supported on alumina by transmission electron microscopy and ft-ir spectroscopy of co adsorption. *Applied Catalysis A: General*, 352(1-2):50–60, 2009.
- [125] R. F. Baddour, M. Modell, and U. K. Heusser. Simultaneous kinetic and infrared spectral studies of carbon monoxide oxidation on palladium under steady-state conditions. *Journal of Physical Chemistry*, 72(10):3621–and, 1968.
- [126] M. A. Chesters, G. S. McDougall, M. E. Pemble, and N. Sheppard. The chemisorption of co on pd(110) at 110 and 300-k studied by electron-energy loss spectroscopy. *Surface Science*, 164(2-3):425–436, 1985. Times Cited: 63.
- [127] H. Conrad, G. Ertl, J. Kupperts, W. Sesselmann, and H. Haberland. Electron-spectroscopy of surfaces by impact of metastable he atoms - co on pd(110). *Surface Science*, 121(1):161–180, 1982. Times Cited: 65.
- [128] P. Hollins. The influence of surface defects on the infrared spectra of adsorbed species. *Surface Science Reports*, 16(2):51 – 94, 1992.
- [129] J.A. Marzari R. Miranda S. Rajagopal, H.J. Marini. Silica-alumina-supported acidic molybdenum catalysts - tpr, xrd characterization. *Journal of Catalysis*, 147(2):417 – 428, 1994.
- [130] W Daniell, U Schubert, R Glöckler, A Meyer, K Noweck, and H Knözinger. Enhanced surface acidity in mixed alumina–silicas: a low-temperature ftir study. *Applied Catalysis A: General*, 196(2):247 – 260, 2000.